

**A structural and metamorphic study of the southern  
Menderes Massif (Western Turkey)**

Dissertation zur Erlangung des Grades  
"Doktor der Naturwissenschaften"

am Fachbereich Geowissenschaften  
der Johannes Gutenberg Universität in Mainz

Jean-Luc Régnier, geboren am 26.05.1972 in St-Clotilde de la Réunion (France)

Mainz, December 2004

## **Erklärung**

Ich versichere hiermit, die vorliegende Arbeit selbständig und nur unter Verwendung der angegebenen Quellen und Hilfsmittel verfaßt zu haben.

All views and results presented in this thesis are those of the author unless stated otherwise.

Mainz, December 2004

"La logique mène à tout à condition d'en sortir, dit un sage..."

Alphonse ALLAIS.

A ma maman, Aysun and "iosephs"

## **Acknowledgements**

My first thanks go to my supervisor Uwe Ring and Cees Passchier, who have been there when I needed them -in the field and in Mainz. Talip Güngör has been a great help either in the field or about regional geology of the Menderes Massif.

I want to thank Igor I. Likhanov, Khalid Najoui, André Leyreloup, and Paul Bons for the important discussions that we have had throughout my Phd.

Moa Zahid, David Iacopini, Philippe Turpaud, Stéphanie Brichau, Arzu Arslan are thanked for their help and tolerance during the three years spent in Mainz.

My special thanks go to Jochen Mezger for his inestimable help at the end of this thesis.

Beyond Geology, I thanks my family which always believed in me. This thesis is also a little bit theirs.

## Summary

*P-T* conditions, paragenetic studies and the relation between mineral growth, deformation and - when possible- isograd minerals have been used to describe the type of metamorphism involved within lower units of the southern Menderes Massif of the Anatolide Belt in western Turkey. The study areas mainly consist of Proterozoic orthogneiss and surrounding schists of presumed Paleozoic age. Both units are seen as nappes in the southern study area, the Çine and the Selimiye nappe, on the whole corresponding to Proterozoic orthogneiss and surrounding schists, respectively. The Çine and Selimiye nappes are part of a complex geological structure within the core series of the Menderes Massif. Their emplacement under lower greenschist facies conditions, would result from closure of the northern Neo-Thethys branch during the Eocene. These two nappes are separated by a major tectonic structure, the Selimiye shear zone, which records top-to-the-S shearing under greenschist facies conditions. Amphibolite to upper amphibolite facies metamorphism is widely developed within the metasedimentary rocks of the Çine nappe whereas no metamorphism exceeding lower amphibolite facies has been observed in the Selimiye nappe.

In the southern margin of the Çine Massif, around Selimiye and Millas villages, detailed sampling has been undertaken in order to map mineral isograds within the Selimiye nappe and to specify *P-T* conditions in this area. The data collected in this area reveals a global prograde normal erosion field gradient from south to north and toward the orthogneiss. The mineralogical parageneses and *P-T* estimates are correlated with Barrovian-type metamorphism. A jump of *P-T* conditions across the Selimiye shear zone has been identified and estimated *c.* 2 kbar and 100 °C which evidences the presence of amphibolite facies metasedimentary rocks near the orthogneiss. Metasedimentary rocks from the overlying Selimiye nappe have maximum *P-T* conditions of *c.* 4-5 kbar and *c.* 525 °C near the base of the nappe. Metasedimentary rocks from the Çine nappe underneath the Selimiye shear zone record maximum *P-T* conditions of about 7 kbar and >550 °C. Kinematic indicators in both nappes consistently show a top-S shear sense. Metamorphic grade in the Selimiye nappe decreases structurally upwards as indicated by mineral isograds defining the garnet-chlorite zone at the base, the chloritoid-biotite zone and the biotite-chlorite zone at the top of the nappe. The mineral isograds in the Selimiye nappe run parallel to the regional  $S_R$  foliation.  $^{40}\text{Ar}/^{39}\text{Ar}$  mica ages indicate an Eocene age of metamorphism in the Selimiye nappe and underneath the Çine nappe in this area.

Metasedimentary rocks of the Çine nappe 20-30 km north of the Selimiye shear zone record maximum *P-T* conditions of 8-11 kbar and 600-650 °C. Kinematic indicators show mainly top-N shear sense associated with prograde amphibolite facies metamorphism. An age of about 550 Ma could be indicated for amphibolite facies metamorphism and associated top-N shear in the orthogneiss and metasedimentary rocks of the Çine nappe. However, there is no evidence for polymetamorphism in the

metasedimentary rocks of the Çine nappe, making tectonic interpretations about late Neoproterozoic to Cambrian and Tertiary metamorphic events speculative.

In the western margin of the Çine Massif metamorphic mineral parageneses and pressure–temperature conditions lead to similar conclusion regarding the erosion field gradient, prograde normal toward the orthogneiss. The contact between orthogneiss and surrounding metasedimentary rocks is mylonitic and syn-metamorphism. *P-T* estimates are those already observed within the Selimiye nappe and correlated with lower amphibolite facies parageneses.

Finally additional data in the eastern part and a general paragenetic study within the Menderes Massif lower units, the Çine and the Selimiye nappes, strongly suggest a single Barrovian-type metamorphism predating Eocene emplacement of the high pressure–low temperature Lycean and Cycladic blueschist nappes. Metamorphic mineral parageneses and pressure–temperature conditions do not support the recently proposed model of high pressure–low temperature metamorphic overprinting, which implies burial of the lower units of the Menderes Massif up to depth of 30 km, as a result of closure of the Neo-Tethys.

According to the geochronological problem outlined during this thesis, there are two possible schemes: either Barrovian-type metamorphism is Proterozoic in age and part of the sediments from Selimiye nappe (lower amphibolite facies) has to be proterozoic of age too, or Barrovian-type metamorphism in Eocene of age. In the first case the structure observed now in the core series would correspond to simple exhumation of Proterozoic basement. In the latter case a possible correlation with closure of Neo-Tethys (*sensu stricto*, southern branch) is envisaged.

## Résumé

Les conditions pression-température, l'étude des paragenèses et des isogrades ainsi que les relations cristallisation-déformation ont été utilisées pour contraindre le type de métamorphisme observé au sein des unités cristallines du Massif du Menderes en Turquie occidentale. Les zones étudiées sont principalement constituées de deux unités : un méta-granite orthogneissifié d'âge d'intrusion protérozoïque et d'une couverture schisteuse dont l'âge de dépôt présumé paléozoïque est incertain. Dans la partie méridionale ces deux unités sont considérées dans un premier temps comme des nappes dont l'emplacement résulterait de la fermeture septentrionale de la Néotéthys à l'Eocène. Ces deux nappes sont en contact tectonique le long de la zone de cisaillement de Selimiye, en extension vers le sud. Cette zone de cisaillement a principalement joué lors d'un métamorphisme en faciès schistes verts, postdatant la croissance minéralogique au sein des deux nappes. La nappe de Çine montre des paragenèses dans le faciès amphibolitique -et au-delà en température- alors que les conditions du métamorphisme au sein de la nappe de Selimiye n'excèdent pas la limite supérieure en température du faciès des schistes verts.

Un échantillonnage resserré a été effectué dans la partie sud du Massif de Çine, au alentour des villages de Millas et de Selimiye, afin de cartographier les zones du métamorphisme et de spécifier les conditions pression-température dans cette zone. Les résultats ont montré globalement la présence d'un gradient de température prograde normal sur la surface d'érosion, du sud vers le nord en direction du contact orthogneiss/schistes. Les paragenèses minéralogiques et les conditions pression-température sont typiquement celles observées durant un métamorphisme de type Barrovian. Au sein de l'unité schisteuse, et le long de la zone de cisaillement de Selimiye, une saute en température et en pression a été identifiée, et estimée de l'ordre de 2 kbar et 100 °C. Cette zone de cisaillement sépare ainsi les schistes de faciès amphibolitique de la nappe de Çine (7 kbar et >550 °C) de ceux de moindre degré métamorphique appartenant à la nappe de Selimiye (4-5 kbar et *c.* 525 °C). Cependant, au sein des deux nappes, les critères cinématiques sont similaires et montrent, durant le métamorphisme, un cisaillement du toit vers le sud.

Différentes zones du métamorphisme ont été cartographiées au sein de la nappe de Selimiye. Du plus faible au plus fort degré nous avons observé : une zone à chlorite-biotite, une zone à chloritoïde-biotite et finalement une zone à grenat-chlorite. Les isogrades sont globalement parallèles à la foliation régionale et les données  $^{40}\text{Ar}/^{39}\text{Ar}$  sur mica indiqueraient un âge Eocène pour le métamorphisme dans cette zone.

Au sein de la nappe de Çine, 20 à 30 km au nord de Selimiye, des enclaves schisteuses ont été également étudiées en détail, afin de contraindre les conditions pression-température (P-T) et le sens de cisaillement durant le métamorphisme. Les résultats montrent des conditions P-T aux alentours de 8-11 kbar et 600 à 650 °C, bien supérieures à celles observées au sein de la nappe de Selimiye. Les critères de cisaillement diffèrent également, et sont ici en accord avec un déplacement du toit vers le nord. Un âge protérozoïque a été proposé pour ce métamorphisme de faciès amphibolitique. Cependant les preuves en faveur d'une histoire métamorphique polyphasée sont inexistantes, ne permettant en aucun cas d'affirmer la présence de deux événements métamorphiques ; l'un très ancien au Protérozoïque et, l'autre beaucoup plus récent à l'Eocène.

Dans la partie ouest du Massif de Çine, l'étude paragéométrique et thermodynamique conduit aux mêmes conclusions concernant les conditions P-T que celles déduites de l'étude pétrologique au sein de la nappe de Selimiye. Dans cette zone le métamorphisme est également de type Barrovian et, le gradient thermique de terrain également prograde normal sur la surface d'érosion en direction du contact orthogneiss/schistes.

Globalement, l'étude paragéométrique au sein des deux unités étudiées, la nappe de Çine et de Selimiye, est en bon accord avec la présence d'un seul événement métamorphique de type Barrovian, prédatant la mise en place à l'Eocène des nappes métamorphisées sous le faciès des schistes bleus (schistes bleus des Cyclades et nappes lyciennes) et ultérieurement charriées sur les unités inférieures du Menderes Massif. Dans ce cadre, le récent modèle géodynamique proposant l'enfouissement des nappes de Çine et de Selimiye à des profondeurs de 30 km, résultant de la fermeture septentrionale de la Néotéthys à l'Eocène n'est en aucun cas conforté par notre étude pétrologique.

Malgré le caractère problématique -souligné tout au long de cette thèse- des données géochronologiques dans cette zone, il nous semble cependant possible de proposer deux schémas possibles pour expliquer la succession des paragenèses observées au sein des nappes de Çine et de Selimiye : Soit le métamorphisme de type Barrovian est Protérozoïque est dans ce cas une partie des schistes étudiés est protérozoïque, soit le métamorphisme est Eocène et, éventuellement corrélé avec la fermeture de la Néotéthys *sensu stricto* au sud du Massif.



## Foreword

The work presented in this thesis aims to clarify and to discriminate the type of metamorphism recorded by the lower units of the southern Menderes Massif of the Anatolide Belt in western Turkey. Sampling have been undertaken in the Çine Massif which mainly consists of Proterozoic orthogneiss and Proterozoic-Paleozoic metamorphic rocks showing Gondwana stratigraphic affinities.

This thesis is divided into four Chapters: the introductory Chapter 1 is followed by two Chapters which make up the body of this thesis. Chapter 2 and 3 are self-consistent research manuscripts. Chapter 2 has been published in *Journal of Metamorphic Geology* in September 2003, but not in the exact form presented here. Chapter 3 has been submitted to *Journal of Metamorphic Geology* in March 2004. Chapter 4 summarizes the conclusions of Chapters 2 and 3 and links back to the introduction. Three Appendices are available at the end of this thesis showing the location of the samples for Chapter 2 and parageneses of the samples studied throughtout this thesis. Finally, a summary of the methods used to specify  $P$ - $T$  conditions with THERMOCALC software and mineral activity models are displayed in the latter Appendix.

In the Chapter 1 an overview on paleocontinental reconstructions in the eastern Mediterranean is presented. The Problems concerning metamorphism within the Anatolide-Tauride block basement is emphasized.

In chapter 2, two areas are described in detail from a petrological and structural point of view involving metasedimentary enclaves in the orthogneiss and surrounding schists of the Selimiye nappe. In this chapter structural field observations, quantitative and qualitative petrological data pose the base of preliminary assumptions. In this Chapter we put forward the theory that Barrovian-type metamorphism expressed within the core series of the Menderes Massif may result from a polyorogenic history. Chapter 2 is almost identical to the manuscript published in *Journal of Metamorphic Geology* entitled “Contrasting metamorphic evolution of metasedimentary rocks from the Çine and Selimiye nappes in the Anatolide belt, western Turkey”. Co-authors are Uwe Ring, Cees W. Passchier, Klauss Gessner and Talip Güngör. However, the version presented here differs slightly from the published version because of some new data described in Chapter 3.

In chapter 3, new petrological data from the western and eastern part of the Çine massif argue for a single Barrovian-type metamorphism within the lower units Menderes Massif. We propose that Barrovian-type metamorphism predates Eocene emplacement of the high pressure–low temperature (HP-LT) Lycean and Cycladic blueschist nappes. Correlation between emplacement of HP-LT nappes and widely expressed retrograde metamorphism in the Selimiye nappe is also envisaged. Chapter 3 is

largely identical with a manuscript submitted to *Journal of Metamorphic Geology* entitled “Mineralogical parageneses and *P-T* conditions of Precambrian-Paleozoic schists of the Çine Massif in the Anatolide belt of western Turkey”. Co-authors are Jochen E. Mezger and Cees W. Passchier.

Finally, some important remarks must be added here concerning the progress this work. The setup of this thesis has been unfortunately hampered by unexpected technical problems. Indeed, originally we planned to perform  $^{40}\text{Ar}/^{39}\text{Ar}$  dating on mica and amphibole in order to specify the Barrovian-type metamorphism age. Minerals have been previously separated, irradiated and sent to Henri Maluski (University of Montpellier, France). Preliminary results yielded Mesozoic ages on mica for the Çine nappe but technical problems and finally total breakdown of laser spectrometer avoided us to present any unequivocal ages. New measurements are under way and will hopefully be available soon. We also attempted to perform Rb/Sr measurements on mica, garnet and whole rock, which yielded apparently Tertiary ages. But results are not accurate enough to be presented here.

# Table of Contents

## Acknowledgements

## Summary

## Résumé

## Foreword

CHAPTER 1 .....	13
<b>INTRODUCTION.....</b>	<b>13</b>
<b>The Hercynian and Eocimmerian chains in the eastern Mediterranean .....</b>	<b>14</b>
<b>The recent Alpine chain in the eastern Mediterranean Anatolide belt (western Turkey) .....</b>	<b>16</b>
<b>Presentation of the problem .....</b>	<b>16</b>
CHAPTER 2 .....	20
<b>POSSIBLE CONTRASTING METAMORPHIC EVOLUTION OF METASEDIMENTARY ROCKS FROM THE ÇİNE AND SELIMIYE NAPPES IN THE ANATOLIDE BELT, WESTERN TURKEY.....</b>	<b>20</b>
<b>Abstract.....</b>	<b>20</b>
<b>Introduction.....</b>	<b>21</b>
<b>Setting.....</b>	<b>23</b>
<b>Structure .....</b>	<b>29</b>
Southern study area .....	29
Northern study area .....	31
<b>Scope of metamorphic study and analytical procedures .....</b>	<b>33</b>
<b>Mineralogy and relationships between deformation and mineral growth .....</b>	<b>35</b>
Southern study area .....	35
Selimiye nappe .....	35
Metasedimentary rocks of the Çine nappe .....	36
Northern study area .....	37
Summary .....	39
<b>Parageneses and thermobarometry.....</b>	<b>40</b>
Southern study area .....	40
Selimiye nappe .....	40
Metasedimentary rocks of Çine nappe .....	43
Northern study area .....	45
<b>Discussion.....</b>	<b>49</b>
Results of the metamorphic study .....	49
Implications for the nature of the Selimiye shear zone .....	49
Cause of Eocene metamorphism across the Selimiye shear zone .....	50
Orogenic implications .....	51
Alpine top-N shearing in the Anatolide belt .....	54
<b>Conclusions .....</b>	<b>56</b>
CHAPTER 3 .....	58
<b>METAMORPHIC PARAGENESSES AND P-T CONDITIONS OF PRECAMBRIAN-PALEOZOIC SCHISTS OF THE ÇİNE MASSIF IN THE ANATOLIDE BELT OF WESTERN TURKEY. NATURE OF THE CONTACT SCHISTS/PROTEROZOIC ORTHOGNEISS AND GEODYNAMIC IMPLICATIONS. ....</b>	<b>58</b>
<b>ABSTRACT.....</b>	<b>58</b>
<b>INTRODUCTION.....</b>	<b>58</b>

<b>Geological SETTING .....</b>	<b>60</b>
<b>Structural study and NATURE OF CONTACT BETWEEN ORTHOGNEISS AND METASEDIMENTARY ROCKS.....</b>	<b>61</b>
Southern Selimiye area: summary of main conclusions of chapter 2.....	61
Western area.....	65
Northern and Eastern area.....	68
Primarily conclusions on structural observations.....	68
<b>SCOPE OF the METAMORPHIC STUDY AND ANALYTICAL PROCEDURES.....</b>	<b>72</b>
<b>Mineral chemistry of metasedimentary rocks of the Çine Massif .....</b>	<b>73</b>
<b>Implications of mineral composition and parageneses .....</b>	<b>75</b>
<b>PSEUDOSECTIONS AND P-T ESTIMATES .....</b>	<b>79</b>
Sample SE3.....	79
Sample SE12.....	80
Sample T6.....	84
Sample Z12.....	87
Sample GU1T.....	87
Sample Z8.....	88
<b>P-T field gradient, nature of tectonic contact and Possible origin of Barrovian metamorphism in the Menderes Massif .....</b>	<b>95</b>
<b>Discussion.....</b>	<b>101</b>
<b>CONCLUSIONS .....</b>	<b>103</b>
<b>CHAPTER 4 .....</b>	<b>105</b>
<b>SUMMARY AND GENERAL CONCLUSIONS .....</b>	<b>105</b>
<b>RECOMMENDATIONS FOR FURTHER STUDY .....</b>	<b>107</b>
<b>APPENDIX 1 &amp; 2 .....</b>	<b>109</b>
<b>APPENDIX 3.....</b>	<b>121</b>
<b>THERMODYNAMIC IN PETROLOGY &amp; THERMOCALC SOFTWARE.....</b>	<b>121</b>
<b>INTRODUCTION.....</b>	<b>121</b>
<b>THERMOCALC SOFTWARE .....</b>	<b>122</b>
<b>activity-composition relationship.....</b>	<b>123</b>
Calcul of end-member proportions .....	124
Activity models.....	126
Activity models used with THERMOCALC v3.1 for the KFMASH system .....	127
Activity models used with THERMOCALC v3.2.1 for the NCKFMASH system.....	132
Activity models used with THERMOCALC v3.2.1 for the MnNCKFMASH system .....	135
<b>REFERENCES .....</b>	<b>137</b>

# Chapter 1

## Introduction

The Anatolide belt of western Turkey formed during recent Alpine collision due to closure of northern branch of the Neothethys (Izmir-Ankara suture; Sengör & Yilmaz, 1981). Proterozoic basement and recent Alpine cover have been amalgamated and associated with a complex and still controversial metamorphic history.

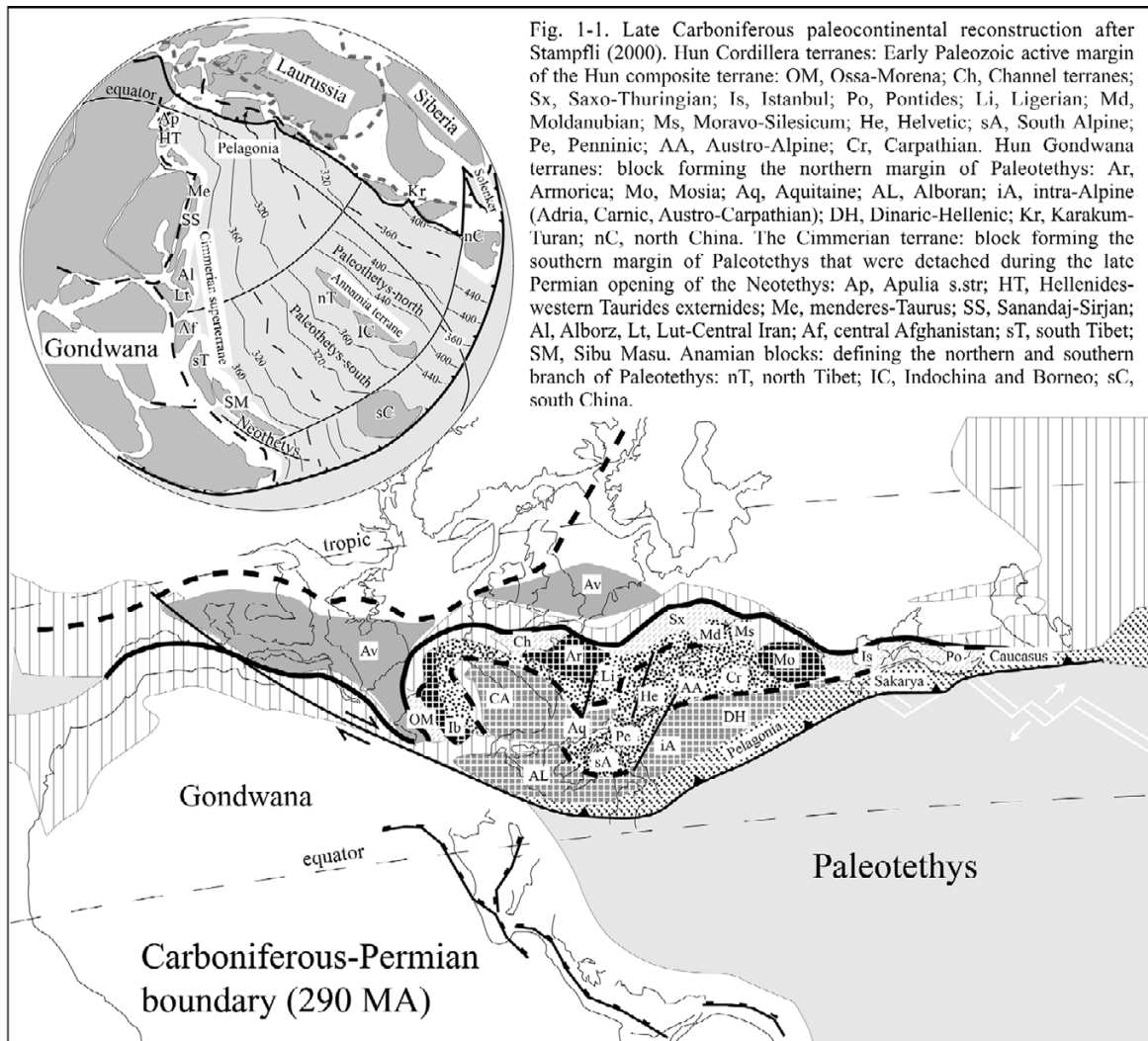
Although Alpine cover series (Cycladic Blueschist unit and Lycean nappes) shown widespread evidence for Eocene HP-LT metamorphism (Oberhänsli *et al.*, 1997; Rimmelé *et al.*, 2003), Proterozoic orthogneiss basement and concomitant Paleozoic schists only displayed Barrovian-type metamorphism overprinting. Hetzel *et al.* (1998) propose an Alpine contractional event associated with top-to-the-N kinematic fabric elements under greenschist to amphibolite facies conditions to explain the presence of Barrovian metamorphism and an inverted metamorphic field gradient across the northern central area of the Anatolide belt. There, Lips *et al.* (2001) additionally provided Eocene  $^{40}\text{Ar}$ – $^{39}\text{Ar}$  ages on mica during this top-to-the-N event.

Ring *et al.* (1999a; 2001), and Gessner *et al.*, (2001a, 2001b) argued for a top-to-the-S emplacement of Proterozoic orthogneiss and associated schists preliminary metamorphosed under amphibolite facies conditions during the Proterozoic. They based their inference on SHRIMP zircon age of  $566 \pm 9$  Ma for a metagranite (only affected by greenschist shear bands) crosscutting regional-scale amphibolitic facies foliation in the orthogneiss (Gessner *et al.*, 1999a & 2004). According to these authors, Paleozoic schists would be only affected by a single greenschists metamorphism during top-to-the-S nappe emplacement. In the latter case metamorphism and deformation are mainly discriminated via top-to-the-N/S senses of shear and respectively Proterozoic amphibolite/Eocene greenschist facies metamorphism.

The Anatolide belt of western Turkey therefore has a tectonic and metamorphic history since the Proterozoic which makes up one of the most misunderstood parts of the Alpine-Himalayan orogen. It seems important here and even essential to present a short but helpful overview of actual knowledge about paleocontinental reconstructions since the Paleozoic in the eastern Mediterranean.

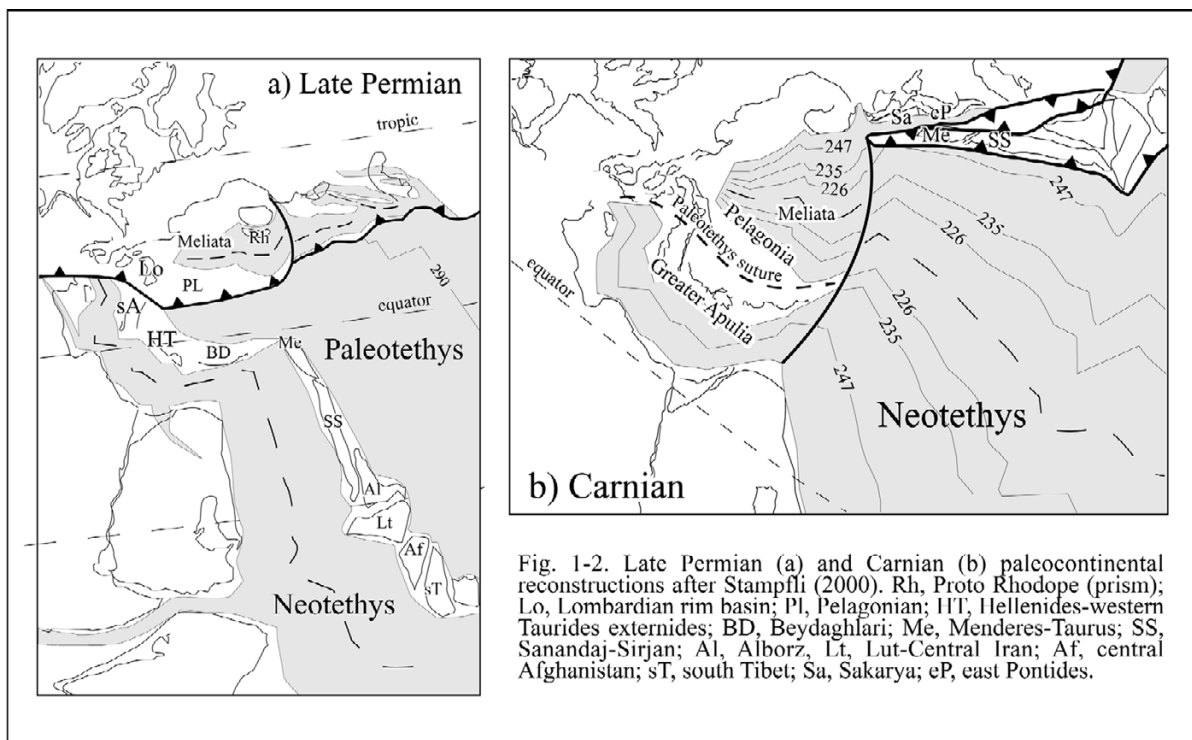
## THE HERCYNIAN AND EOCIMMERIAN CHAINS IN THE EASTERN MEDITERRANEAN

Paleocontinental reconstructions in the eastern Mediterranean display a complex architecture according to the closure and the opening of different oceans and back-arc oceans since the Carboniferous period. During this time the Hercynian chain in the eastern Mediterranean results from the closure of the Rheic ocean involving accretion of different units from the Hun superterrane (Hun Cordillera and Hun Gondwana terranes, Fig. 1-1).



Subduction of the Paleotethys beneath the Laurasia continent which was coeval with the opening of the Neothethys along the Gondwanan margin in the south (Fig. 1-2a), allowed northward drifting of the Cimmerian terranes including the Menderes Massif (Fig. 1-1 & 1-2). Subsequently, the juxtaposition to Laurasia of Apulia, Hellenides-western Taurides externides and, Menderes-Taurus terranes, at least for our interested area, would occur during the Carnian (Şengör, 1979; Stampfli *et al.*, 1998; Stampfli, 2000), allowing the welding of the Tauric plate to the Sakarya zone (Fig. 1-2b). However, recently Stampfli & Borel (2002), proposed a new interpretation where the east

Mediterranean domain would be a part of the Neotethyan oceanic system since the Late Paleozoic (Fig. 1-3a & 1-3b). In this scheme, the Tauric plate (southern Turkey) would only welded to the Pontides area (Laurasia) during the Palaeogene.



The Eocimmerian orogenesis likely did not produce any substantial crustal thickening and so far, no Triassic collisional type metamorphism is reported in the eastern Mediterranean. This can be explained by the presence of an oceanic plateau located between the Cimmerian and Eurasian Plates, which reduced the effect of crustal thickening (Stampfli, 2000; Okay, 2000). However, the partial subduction of this oceanic plateau produced a high-pressure, low-temperature (HP-LT) metamorphism during the late Triassic (Monod *et al.*, 1996; Okay & Monié, 1997). According to Stampfli and Borel (2002), during the Carnian-Early Norian, the Tauric plate was located 2000 km west of the Pontides area, welded to Pelagonia after the closure of the Paleotethys (Fig. 1-3b). This has some implication for the Tauric plate which stayed isolated from the Neo-Tethys subduction until the late Cretaceous. Moreover, the presence of an oceanic plateau located between the Tauride block and the Sakarya zone in the present-day, should be only related to an oceanic plateau-continent collision during the Carnian. The important consequence from lack of collisional metamorphism during the Eocimmerian event, is the juxtaposition of Hun Gondwanan terranes with Cimmerian terranes including respectively Panafrican and Hercynian basement in the eastern Mediterranean (Loos & Reischmann, 1999; Gessner *et al.*, 2001a; Ring *et al.*, 1999a, 2001). This collage would be followed by the subduction of Neotethys and the opening of back-arc oceans along ancient suture of the Paleotethys (Fig. 1-4a & 1-4b).

## **THE RECENT ALPINE CHAIN IN THE EASTERN MEDITERRANEAN ANATOLIDE BELT (WESTERN TURKEY)**

Sediments accumulated in the back arc ocean along ancient sutures of the Paleotethys during the subduction of the Neo-Tethys (Fig. 1-5), or sediments from the Meliata Ocean formed before the Cimmerian chain (Permian-Triassic boundary), will be overprinted by a Alpine HP-LT metamorphism during the closure of the Vardar, Meliata and Lycian oceans (Pelagonian-Cycladic zone in Greece, Cycladic blueschist unit and Lycian nappes in Turkey) and subsequently overthrust southward onto the Taurid-block in western Turkey (Collins & Robertson, 2003). There, the remain of this neothetyssian back arc is well documented as the Izmir-Ankara suture. Sediments overlapping this HP-LT metamorphism involve comformable serie from the late Permian-Triassic to the Late Cretaceous. The Climax for this HP-LT metamorphism is reffered to as Eocene in age (Oberhänsli *et al.*, 1998, 2001; Sherlock *et al.*, 1999; Ring & Layer, 2002).

### **PRESENTATION OF THE PROBLEM**

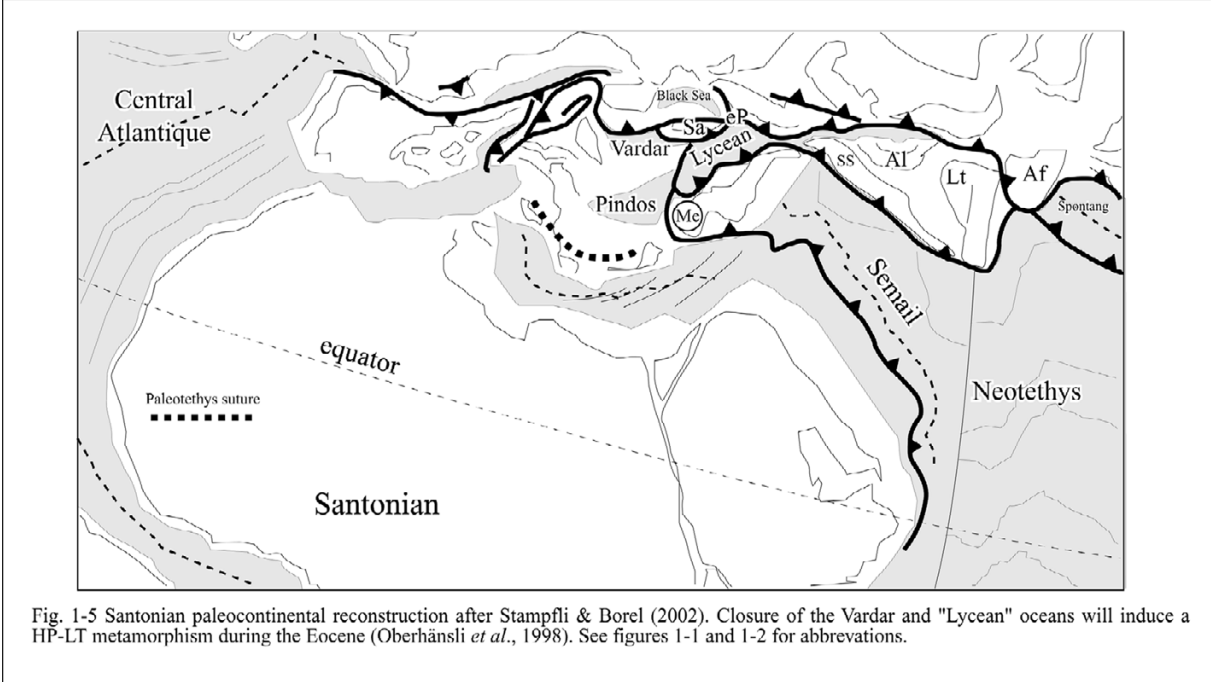
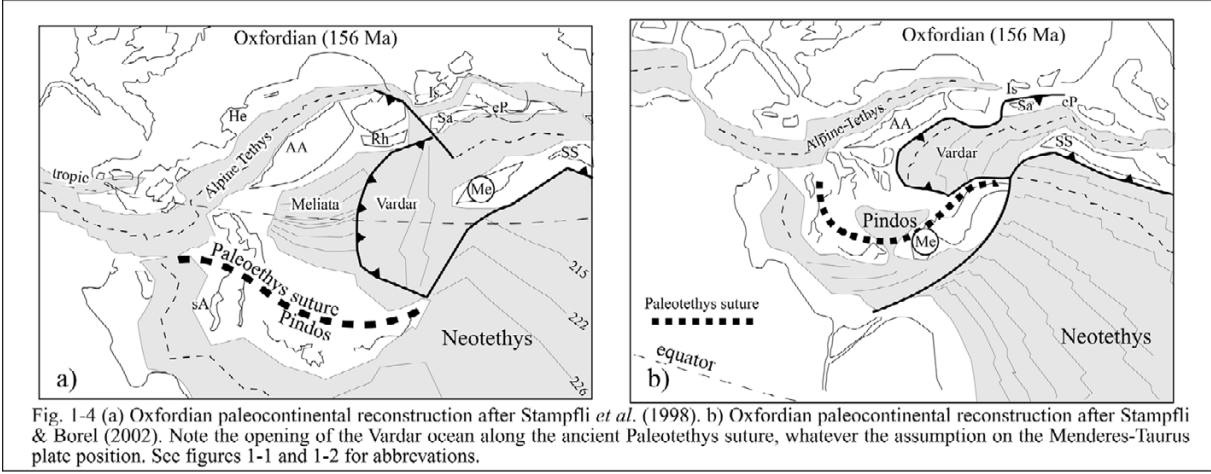
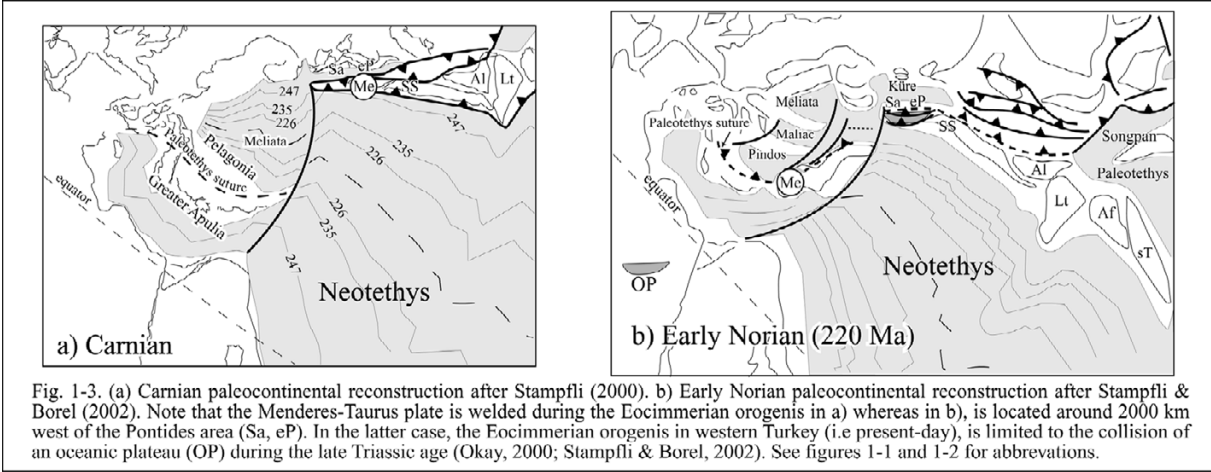
Figure 1-6a attempts to summarize the geodynamic evolution from the Anisian to the Eocene in the eastern Mediterranean. Though geodynamic evolution in the eastern Mediterranean is relatively well constrained, two important points remain problematic. The first one concerns the continuation of the Neo-Tethys active margin in western Turkey. Stampfli (2000) proposes a possible extension of this Late Cretaceous-Palaeogene active margin westward under the Lycean nappes, linking up the Antalya Suture with the Axios Vardar Zone (Fig. 1-6b). Indeed, the Eastern Mediterranean subduction zone (Aegean active margin) is likely not older than Miocene and does not represent the western continuation of the Neo-Tethys active margin (Stampfli, 2000; Fig. 1-6b). The second important point concerns the previously described Barrovian-type metamorphism within the Taurid-block basement and its possible relation with the recent Alpine history. The Taurid-block Basement in western Turkey mainly consists of Proterozoic orthogneiss and Proterozoic?-Paleozoic metasedimentary rocks and has been studied in detail throughout this thesis.

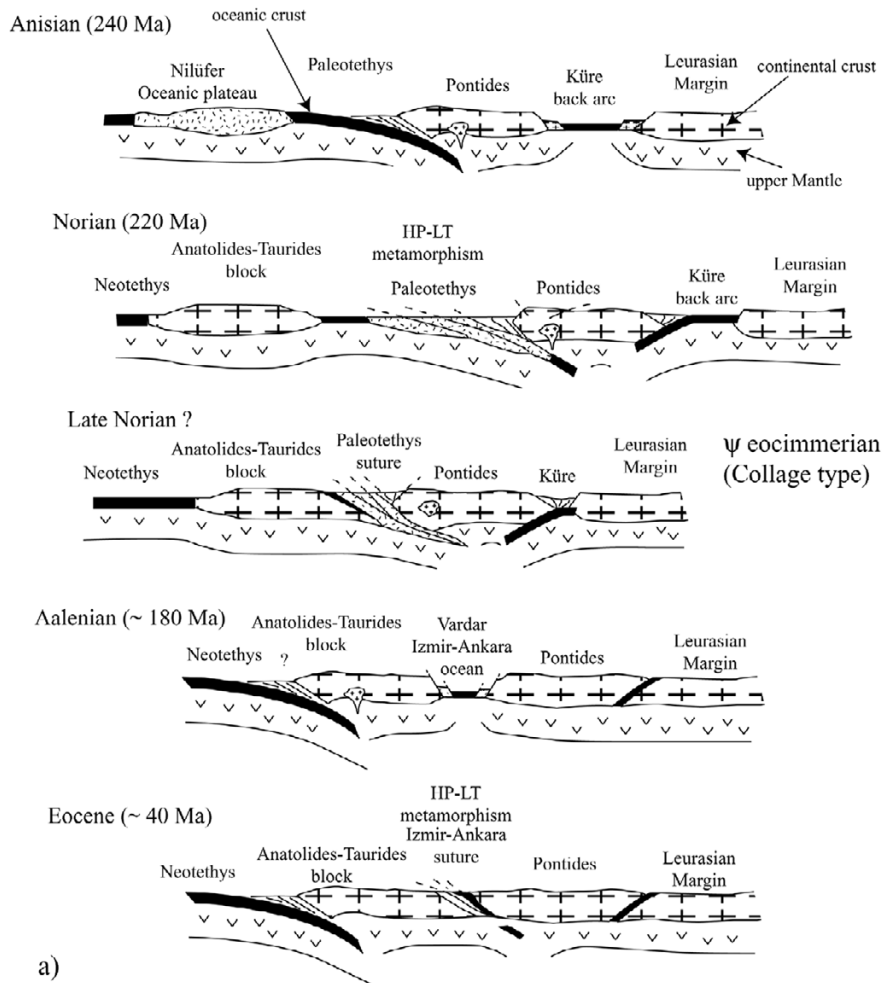
So far, different assumptions have been proposed to explain the presence of Barrovian-type metamorphism within the basement of the western Anatolide belt, traditionally referred to as the Menderes Massif. Bozkurt & Park (1994) proposed direct correlation between top-to-the-S emplacement of the HP-LT nappe (Cycladic blueschist unit and Lycian nappes) and Barrovian-Type metamorphism displayed in the core series. Contact-type metamorphism has been also envisaged in the south Menderes Massif (Çine Massif) associated with exhumation of an incipient metamorphic core complex (Bozkurt *et al.*, 1993; Bozkurt & Park, 1994). Polyorogenic history involving



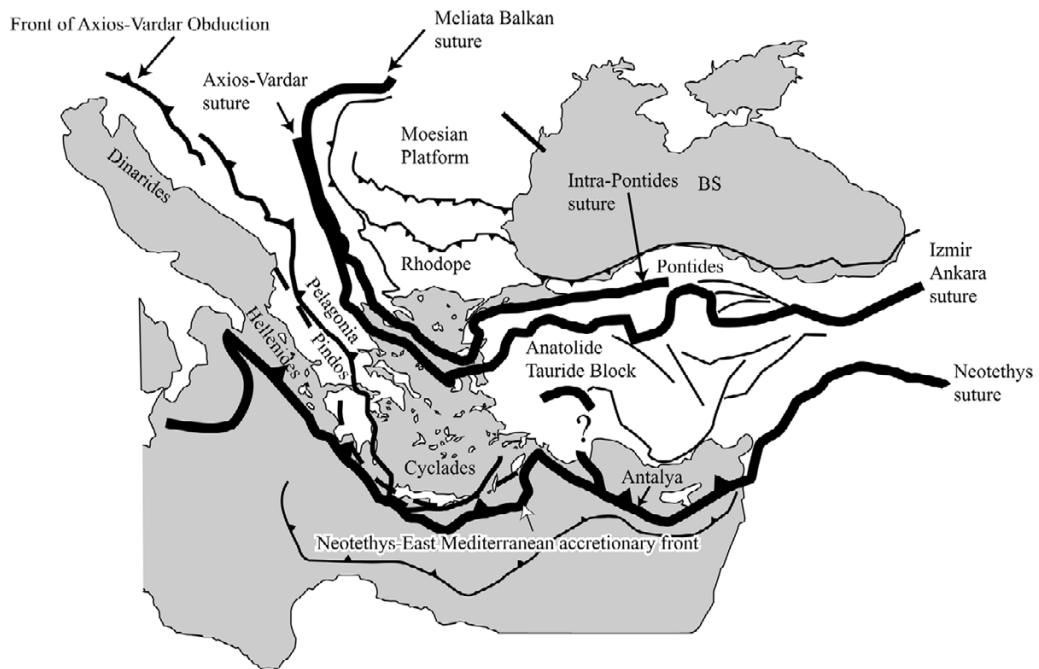
Proterozoic and Eocene metamorphism during emplacement of lower Menderes nappes has been also suggested (Ring *et al.*, 1999a; Gessner *et al.*, 2001a).

All these suggestions however are not supported by any detailed metamorphic study. Indeed, *P-T* conditions are often inferred and not precisely quantified. The terms amphibolite or greenschists facies are used without significative paragenesis analysis, making the relationship between different metamorphism speculative. The main aim of this thesis is therefore to discriminate the type of metamorphism recorded within the core series of western Anatolide belt and to propose a geodynamic model linking up Proterozoic with recent Alpine history.





a)



b)

Fig. 1-6. a) Different sketches at the lithospheric scale summing up the geodynamic evolution from the Anisian to the Eocene in the eastern Mediterranean. Note that the welding of the Anatolide-Taurides block during the late Trias is not so far well constrained. b) Simplified tectonic map of eastern Mediterranean after Stampfli (2000).

## Chapter 2

# Possible contrasting metamorphic evolution of metasedimentary rocks from the Çine and Selimiye nappes in the Anatolide belt, western Turkey

### ABSTRACT

*P-T* conditions, mineral isograds, the relation of the latter to foliation planes and kinematic indicators are used to elucidate the metamorphism and evolution of a shear zone in an orogen exhumed from mid-crustal depths in western Turkey. Furthermore, we discuss whether simple monometamorphic fabrics of rock units from different nappes result from one single orogeny or are related to different orogenies. Metasedimentary rocks from the Çine and Selimiye nappes at the southern rim of the Anatolide belt of western Turkey record different metamorphic conditions. The Eocene Selimiye shear zone separates both nappes. Metasedimentary rocks from the Çine nappe underneath the Selimiye shear zone record maximum *P-T* conditions of about 7 kbar and >550 °C. Metasedimentary rocks from the overlying Selimiye nappe have maximum *P-T* conditions of *c.* 4-5 kbar and *c.* 525 °C near the base of the nappe. Kinematic indicators in both nappes consistently show a top-S shear sense. Metamorphic grade in the Selimiye nappe decreases structurally upwards as indicated by mineral isograds defining the garnet-chlorite zone at the base, the chloritoid-biotite zone and the biotite-chlorite zone at the top of the nappe. The mineral isograds in the Selimiye nappe run parallel to the regional  $S_R$  foliation, which suggest that the prograde greenschist to lower amphibolite facies metamorphic event is not of contact type.  $^{40}\text{Ar}/^{39}\text{Ar}$  mica ages indicates an Eocene age of metamorphism in the Selimiye nappe. Our preferred interpretation is that metamorphism in the metasedimentary rocks of the Çine nappe directly below the Selimiye shear zone is of the same age.

Metasedimentary rocks of the Çine nappe 20-30 km north of the Selimiye shear zone record maximum *P-T* conditions of 8-11 kbar and 600-650 °C. Kinematic indicators show mainly top-N shear sense associated with prograde amphibolite facies metamorphism. An age of about 550 Ma has been proposed for amphibolite facies metamorphism and associated top-N shear in the orthogneiss and metasedimentary rocks of the Çine nappe. However, there is no evidence for polymetamorphism in the metasedimentary rocks of the Çine nappe, making tectonic interpretations about late Neoproterozoic to Cambrian and Tertiary metamorphic events speculative. Our study shows a simple monophase tectonometamorphic fabrics and indicate a simple orogenic development during Barrovian-type metamorphism.

**Keywords:** Metamorphism, geothermobarometry, *P-T* grid, shear zone, Anatolide belt, Turkey.

## INTRODUCTION

An interesting problem in polyorogenic settings is that some rocks preserve tectonometamorphic fabrics of an older orogeny extremely well, and that these fabrics are not altered during a severe younger orogenic overprint. A stunning example is recorded in metasedimentary rocks from the Sesia zone in the Italian Alps, which experienced a regional Alpine high-pressure (HP) metamorphism of 500-600 °C and >13 kbar (Pognante, 1989) and associated deformation in the Alpine subduction zone. At Monte Mucrone, metapelite of the Sesia zone shows a Variscan amphibolite facies tectonometamorphic fabric with a pronounced mineral elongation lineation expressed by sillimanite and no signs of Alpine HP metamorphism (Compagnoni, 1977). This metapelite is locally crosscut by cm-wide veins, which contain cm-sized omphacite crystals. In other parts of the Sesia zone, Variscan sillimanite was statically transformed to kyanite (Compagnoni, 1977). Both omphacite and kyanite grew during Alpine HP metamorphism. This Alpine HP metamorphism and associated heterogeneous deformation in the Alpine subduction zone left parts of the Sesia zone mineralogically and/or structurally completely unaffected.

The phenomenon that closely juxtaposed rocks record completely different tectonometamorphic histories, is an important issue for researchers studying orogenic processes. The tectonic significance of faults and shear zones, deduced from the different *P-T* paths of the rocks above and below the tectonic discontinuity, can be overestimated, when it is automatically assumed that the metamorphic history of the rocks resulted from the same orogenic event.

The Anatolide belt of western Turkey (also referred to as the Menderes Massif), which is part of the Alpine Hellenide-Anatolide orogen in the eastern Mediterranean, also shows evidence for a polyorogenic history including metamorphism and deformation at the Neoproterozoic/Cambrian boundary (Candan *et al.*, 2001; Gessner *et al.*, 2001a; 2004; Ring *et al.*, 2001). During the Alpine orogeny, the Anatolide belt was assembled; stacking of nappes with different tectonometamorphic evolutions occurred in the Late Cretaceous and Tertiary (Şengör *et al.*, 1984; Ring *et al.*, 1999a; Gessner *et al.*, 2001a). Nappe tectonism in the western Anatolide belt occurred initially under HP conditions in the upper tectonometamorphic units. Subsequently, the HP units were thrust onto the non-high-pressure Menderes nappes (including the Selimiye and Çine nappes) along the Cyclades-Menderes thrust in the Eocene (Gessner *et al.*, 2001b).

The metasedimentary rocks at the southern margin of the Anatolide belt, the Selimiye nappe of Ring *et al.* (1999a), show a simple monometamorphic greenschist to lower amphibolite facies

development during the Tertiary orogeny (Ashworth & Evirgen, 1984).  $^{40}\text{Ar}/^{39}\text{Ar}$  dating of mica from directly below the Selimiye shear zone (Hetzl & Reischmann, 1996) corroborates an Eocene age for this metamorphism (Gessner *et al.*, 2001b).

In contrast to the Tertiary tectonometamorphic development in the Selimiye nappe, the underlying Çine nappe shows widespread evidence for late Neoproterozoic orogenic activity at *c.* 550 Ma (Loos & Reischmann, 1999; Gessner *et al.*, 2001a; Ring *et al.*, 2001). Gessner *et al.* (2001a, 2004) showed that weakly deformed granite, yielding a  $^{207}\text{Pb}/^{206}\text{Pb}$  single-zircon evaporation age of  $547\pm 1$  Ma and a SHRIMP zircon age of  $566\pm 9$  Ma, cuts a penetrative regional-scale amphibolite facies foliation and stretching lineation with associated top-N kinematic indicators in orthogneiss. These data would indicate that the main tectonometamorphic development, at least in Çine nappe orthogneiss, is of late Neoproterozoic age. This age for penetrative deformation in the Çine nappe seems corroborated by  $^{207}\text{Pb}/^{206}\text{Pb}$  garnet ages from garnet-bearing orthogneiss, which yielded an age of  $518\pm 10$  Ma for a second garnet generation (Ring *et al.*, 2004a). A fundamental question is how the metasedimentary rocks of the Çine nappe above the orthogneiss and directly below the Selimiye shear zone, which seems to record late Neoproterozoic to Cambrian metamorphism in other parts of the western Anatolide belt (Ring *et al.*, 2001), responded to Eocene nappe stacking in the western Anatolide belt. It seems possible that the anhydrous orthogneiss preserved an old tectonometamorphic fabric (the  $S_{\text{PA}}$  foliation of Gessner *et al.*, 2001b; the suffix 'PA' indicates a pre-Alpine age), whereas the more hydrous metasedimentary rocks may have been at least locally re-equilibrated during the Alpine orogeny.

The Selimiye shear zone separates the Selimiye nappe from the Çine nappe. The tectonic significance of the Selimiye shear zone is debated. Bozkurt & Park (1994) regarded it as a metamorphic-core-complex-type normal fault of Oligocene age.  $^{40}\text{Ar}/^{39}\text{Ar}$  white mica dating by Hetzel & Reischmann (1996) showed that the Selimiye shear zone is of Eocene age and that orthogneiss of the Çine nappe in its footwall cooled slowly after shearing. Fission-track dating indicates accelerated cooling in the Early Miocene at 23-20 Ma (Gessner *et al.*, 2001c; Ring *et al.*, 2004b). This cooling has been attributed to extensional reactivation of the basal thrust of the Lycian nappes, which occurs tectonically above the Selimiye shear zone (Fig. 2-1). Ring *et al.* (1999a) and Gessner *et al.* (2001b) proposed that the Selimiye shear zone is a thrust, which operated during Eocene nappe stacking, the  $D_{\text{A3}}$  event of Gessner *et al.* (2001b; the suffix 'A' indicates an Alpine age). The  $D_{\text{A3}}$  event would have assembled the western Anatolide belt and juxtaposed tectonic units with different tectonometamorphic evolutions.

Recently, Whitney & Bozkurt (2002) carried out a tectonometamorphic pilot study at the orthogneiss/schist contact at the southern rim of the Anatolide belt. They proposed that the orogenic

development resulted from a single Tertiary event, which caused syn-metamorphic top-N thrusting followed by top-S normal faulting during retrograde metamorphism. They based their inference of Alpine top-N shearing on top-N kinematic indicators observed in the schist sequence. The assumption of an early Tertiary event causing northward-directed translation has also been invoked by Bozkurt & Park (1994) and Hetzel *et al.* (1998).

There are still different ideas and strong controversy about emplacement of the nappes, and metamorphism itself. In other words it still remains unclear if the metamorphism expressed in the lower units pre-dates or has been initiated during emplacement of nappes. Large-scale tectonic models of the Aegean/western Turkish area argue against Tertiary top-N thrusting during emplacement of nappes (Şengör *et al.*, 1984; Collins & Robertson, 1997, 1998, 2003). Likewise, kinematic studies in the adjacent Aegean do not support early Tertiary top-N transport (Ridley, 1984; Ring *et al.*, 1999b) but movement during metamorphism itself remain a conjecture.

We have studied metapelite from the Selimiye nappe and also metapelite from the Çine nappe during three field seasons in order to determine *P-T* conditions, to map mineral isograds, to determine the type of metamorphism recorded by both nappes in order to find possible evidence for a polymetamorphism as recorded in the Sesia zone, since HP-LT metamorphism is also present in our area. Another major aim is to establish the relationship between isograds, the regional foliation and the Eocene Selimiye shear zone to shed more light on the disputed tectonic nature of the Selimiye shear zone. Special emphasis is put on careful examination of shear-sense indicators in the field and in thin section. We focus on two main areas (Fig. 2-1): a schist unit southeast of Lake Bafa (southern study area) in which the Selimiye shear zone is developed, and a schist unit at the northern rim of the Çine submassif southwest of Aydın (northern study area).

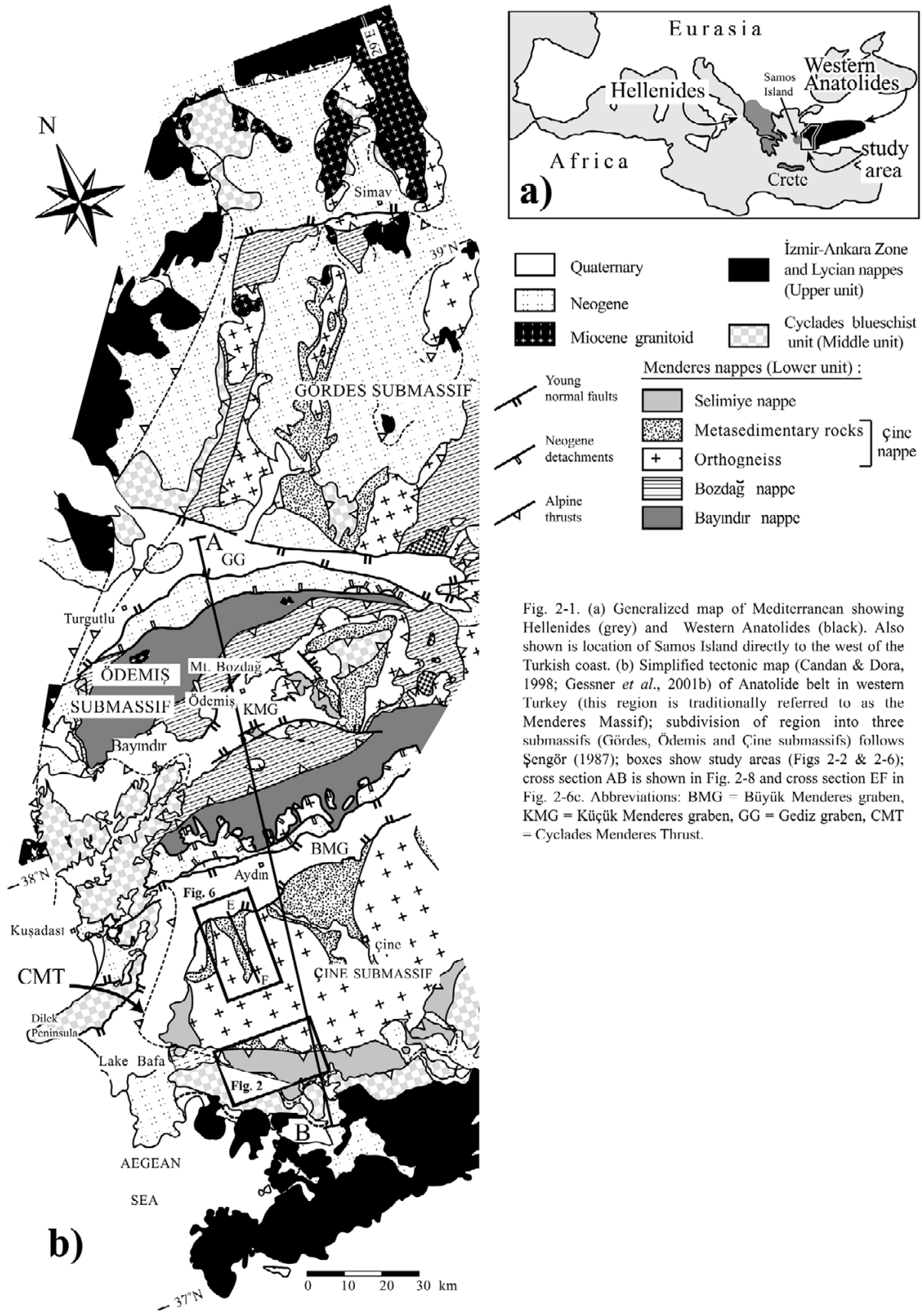
## SETTING

The architecture of the Anatolide belt of western Turkey comprises three major tectonometamorphic units (Fig. 2-1). The Lycian nappes and the İzmir-Ankara suture zone represent the upper tectonometamorphic unit. The middle tectonometamorphic unit consists of the Cycladic blueschist unit. These two units were affected only by a single orogeny undergoing a Late Cretaceous to Eocene HP metamorphism during the closure of Neo-Tethys (northern branch) and were subsequently thrust onto the underlying Menderes nappes (Oberhänsli *et al.*, 1998, 2001; Sherlock *et al.*, 1999; Ring & Layer, 2003). The lowermost tectonometamorphic unit of the Anatolide belt, the Menderes nappes, comprises from top to bottom: (1) The Selimiye nappe, (2) the Çine nappe, (3) the Bozdağ nappe, and (4) the Bayındır nappe (Ring *et al.*, 1999a; Gessner *et al.*, 2001b). The Çine and Bozdağ nappes have a polyorogenic history (Candan *et al.*, 2001; Gessner *et al.*, 2001a). The

Menderes nappes are separated from the overlying HP units by the Eocene out-of-sequence Cyclades-Menderes thrust. Above the Menderes nappes, structures related to this huge thrust developed during lower greenschist facies metamorphism (Gessner *et al.*, 2001*b*).

The Selimiye nappe contains metapelite, calcschists, metamarl, marble and quartzite. Fossil evidence indicates Devonian and Carboniferous protolith ages for some of the metasedimentary rocks (Lower greenschists facies metamorphism, Schuiling, 1962; Çağlayan *et al.*, 1980). Ring *et al.* (1999*a*) regarded the entire metasediment sequence above the orthogneiss of the Çine nappe as belonging to the lowermost parts of the Selimiye nappe. However, detailed re-mapping of the Selimiye shear zone in the course of this study indicated that some of the metasedimentary rocks directly south of the orthogneiss occur below the Selimiye shear zone (Fig. 2-2) and must therefore be part of the Çine nappe. Furthermore, the metasedimentary rocks directly south of the orthogneiss and east of Lake Bafa were intruded by the protolith of a metagranite, which yielded a SHRIMP  $^{206}\text{Pb}/^{238}\text{U}$  age of  $541\pm 14$  Ma (Gessner *et al.*, 2004), indicating a Precambrian protolith age for the surrounding metapelite (Fig. 2-3). Because these metasedimentary rocks occur below the Selimiye shear zone and because no Precambrian sediments have so far been reported from the Selimiye nappe, we regard the lowermost part of the metasedimentary sequence east of Lake Bafa to be part of the Çine nappe as indicated in Figs 2-1 and 2-2 and discussed further below.





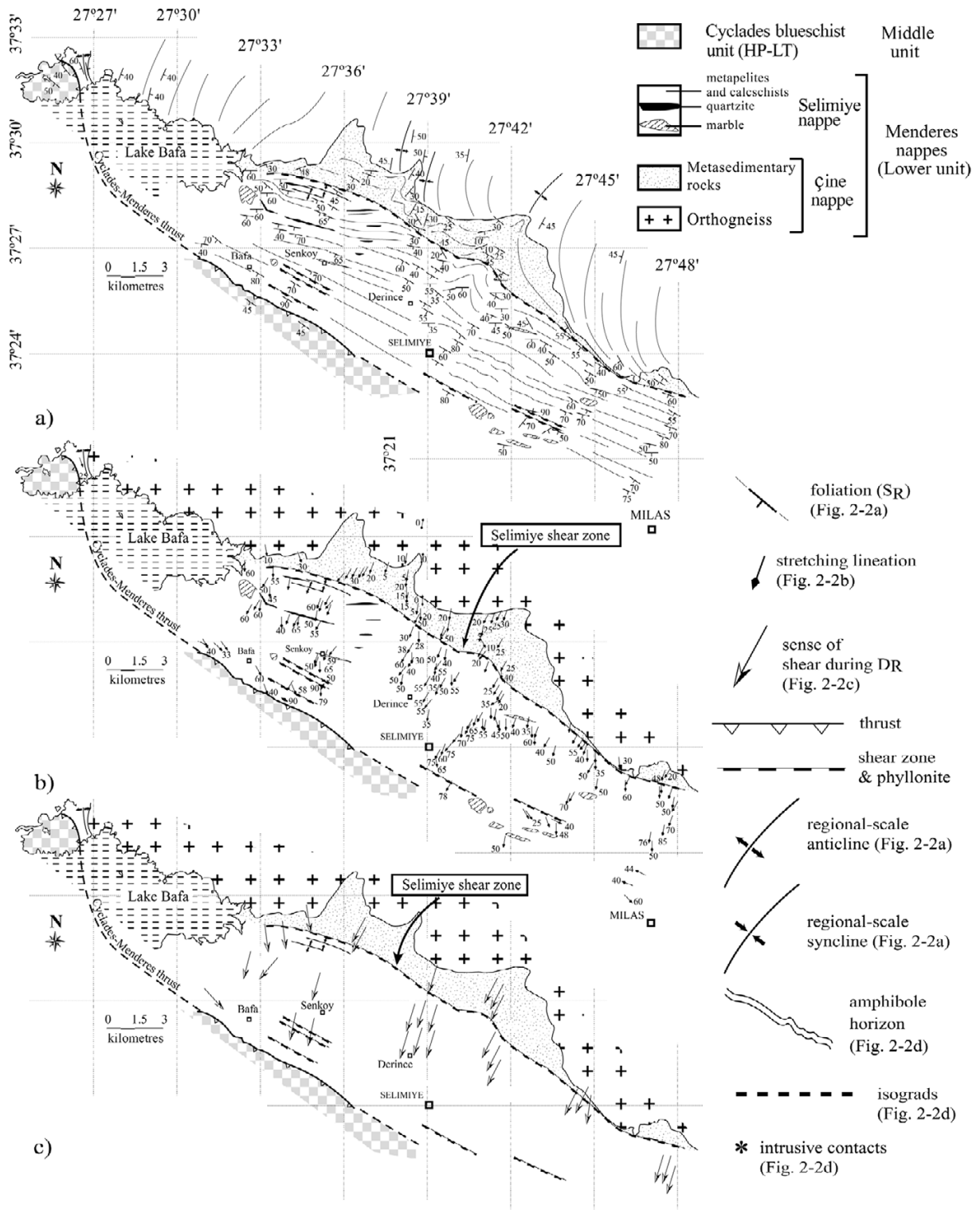


Fig. 2-2. Southern study area: (a) Map of main foliation, SR, after De Graciansky (1966), Bozkurt & Park (1994) and this study; note that foliation swings from a northerly strike in Çine nappe orthogneiss into a west-northwesterly strike in the Selimiye nappe. (b) Stretching lineation map; lineations swing from a NNE trend into a SE/ESE trend near the Cyclades-Menderes thrust. (c) Shear senses associated with SR as deduced from rotated garnet, S-C fabrics, shear bands and asymmetric quartz veins; arrows indicate movement direction of tectonic top.

Most of the Çine nappe consists of deformed orthogneiss and weakly deformed metagranite. Metasedimentary rocks, which in part show migmatitic fabrics, eclogite and amphibolite also occur (Oberhänsli *et al.*, 1997; Candan *et al.*, 2001). Protoliths to all dated orthogneisses are intruded at *c.* 560-540 Ma (Hetzl & Reischmann, 1996; Dannat, 1997; Hetzel *et al.*, 1998; Loos & Reischmann, 1999; Gessner *et al.*, 2004). Some metagranites have protolith ages of *c.* 540-530 Ma (Dannat, 1997; Loos & Reischmann, 1999).  $^{206}\text{Pb}/^{207}\text{Pb}$  single-zircon evaporation dating of migmatites from the Ödemiş and Gördes submassifs generally yielded ages of *c.* 550-540 Ma for migmatization (Dannat & Reischmann, 1999). Ring *et al.* (2001) estimated peak-metamorphic conditions from the lowermost Çine nappe of 670-730 °C and *c.* 6.0-6.5 kbar. Prograde garnet (grt I) growth occurred largely before and during the formation of the regional foliation. Formation of a second garnet generation, which discordantly overgrew grt I, followed at 550-620 °C and *c.* 6.0-6.5 kbar.

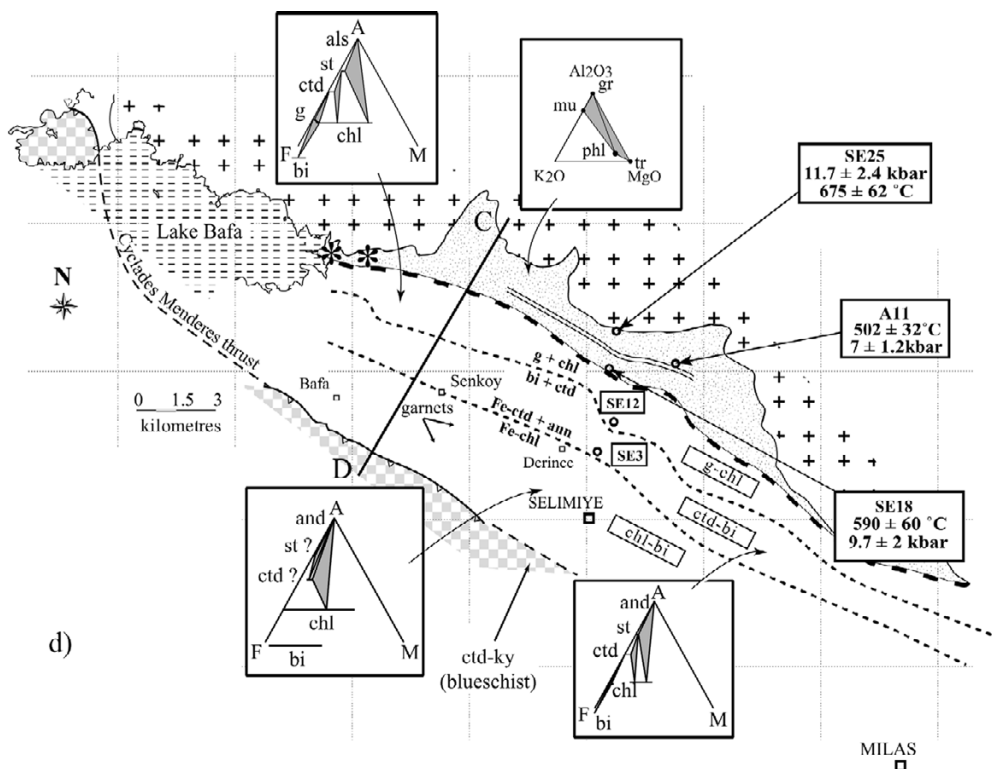


Fig. 2-d. Isograd map; isograds parallel  $S_R$  foliation in Selimiye nappe; AFM and AKM projections for metapelite of the Selimiye nappe and calcschist of Çine nappe (amphibolite facies); see text for abbreviations.

The Bozdağ nappe that structurally underlies the Çine nappe is made up of metapelite with intercalated metapsammite, marble, amphibolite and eclogite lenses (Candan *et al.*, 2001). Protolith ages of all rock types are unknown, but a Precambrian age for at least parts of these rocks has been proposed (Candan *et al.*, 2001; Gessner *et al.*, 2001a). Peak-metamorphic conditions vary from 480-540 °C and 6.1-7.6 kbar at the base to 610-660 °C and 8.5-10.8 kbar at the top of the nappe and attest to an inverted metamorphic field gradient in the Bozdağ nappe (Ring *et al.*, 2001). Differential

thermodynamic modelling by the Gibbs method yielded a prograde path for garnet growth during metamorphism (Ring *et al.*, 2001). A  $^{207}\text{Pb}/^{206}\text{Pb}$  garnet age from metapelite provided an age of  $512\pm 56$  Ma (Ring *et al.*, 2004a). Shear-sense indicators, especially rotated garnet and associated asymmetric strain shadows around garnet, yielded a consistent top-N sense of shear during prograde amphibolite facies metamorphism. In summary, both the Çine and Bozdağ nappes are characterized by systematically top-N ductile shear structures that developed apparently during late Neoproterozoic to Cambrian amphibolite facies metamorphism.

The Bayındır nappe contains phyllite, quartzite, marble and greenschist of inferred Mesozoic age (Özer & Sözbilir, 2003). The rocks were affected by a single low greenschist facies metamorphism. Syn-metamorphic kinematic indicators yielded a consistent top-S sense of shear (Gessner *et al.*, 2001b).

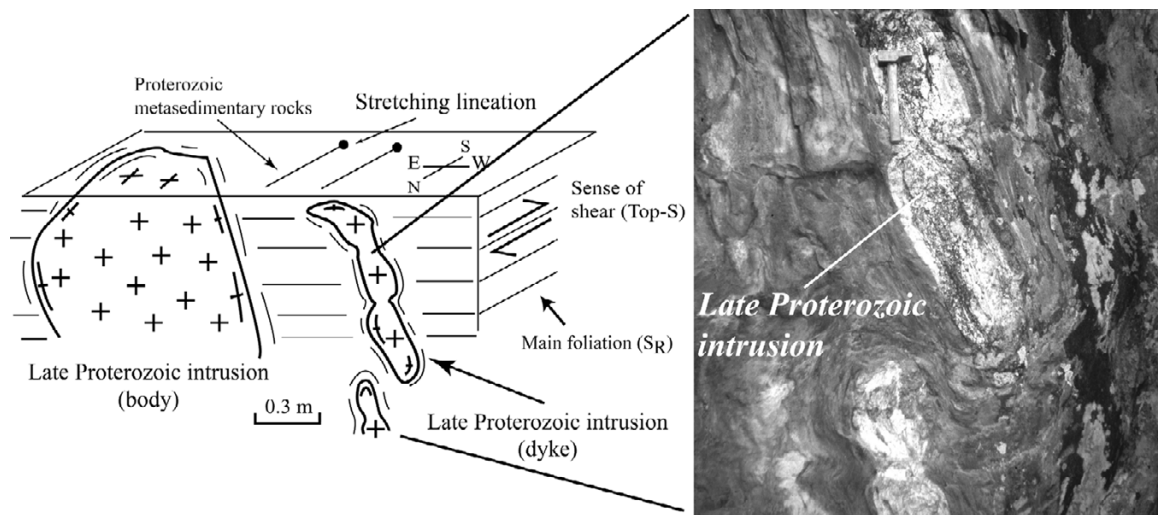


Fig. 2-3. Field photograph and interpretative drawing of deformed intrusive contact in metasedimentary rocks of the Çine nappe east of Lake Bafa.

## STRUCTURE

### Southern study area

The Eocene Selimiye shear zone consists of strongly to mylonitically deformed metasedimentary rocks, and separates schist of the Selimiye nappe above from schist of the Çine nappe below (Fig. 2-2). These two schist units strongly resemble each other in the field but record different  $P$ - $T$  conditions, which will be discussed in detail below, and are separated by a major shear zone. These are the main reasons why we distinguish both schist units in Fig. 2-2.

Regional-foliation trajectories vary significantly across the Selimiye shear zone (Fig. 2-2a) (de Graciansky, 1966). The regional foliation in orthogneiss of the Çine nappe is N-S oriented and folded about large-scale N-trending synforms and antiforms. In metasedimentary rocks of the Çine nappe directly below the Selimiye shear zone, the regional foliation swings into a WNW-ESE orientation parallel to the shear zone (Fig. 2-2a). In the Selimiye nappe, the regional foliation also strikes WNW-ESE.

Multiple foliations occur in schist of the Selimiye nappe. The penetrative regional foliation is termed  $S_R$  and is related to the  $D_R$  deformation. An older foliation is only locally preserved in microlithons between the penetrative  $S_R$  foliation (Fig. 2-4a). The major metamorphic minerals (garnet, chloritoid, amphibole, epidote and mica) grew in  $S_R$ . However, where the older foliation is preserved, the same minerals that form  $S_R$  also grew parallel to this older foliation. A "post- $S_R$ " foliation crosscuts  $S_R$  at a low angle. Thin-section work reveals that these low-angle planes are  $C'$  shear bands associated with  $S_R$ . In addition,  $S_R$  is locally deformed by a weak crenulation cleavage, which is associated with late folding (see below).

On  $S_R$  a prominent mineral stretching lineation,  $L_R$ , formed.  $L_R$  is expressed by stretched quartz aggregates, strain shadows around garnet and by the alignment of micas.  $L_R$  plunges SSW in the lower parts of the Selimiye nappe and swings in the vicinity of the Cyclades-Menderes thrust into an ESE-WNW trend (Fig. 2-2b). Shear-sense indicators associated with  $S_R$  and  $L_R$  are the above mentioned shear bands, asymmetric veins, S-C fabrics as well as rotated garnet, epidote and plagioclase and asymmetric strain shadows around these minerals (Fig. 2-4a-c). In a number of outcrops shear-sense indicators are imperfectly developed and do not allow an unambiguous determination of the shear sense. Where the kinematic indicators are well developed, they yielded a top-S shear sense (Figs 2-2c, 2-4a, 2-4b & 2-5a), as has been previously reported by Hetzel & Reischmann (1996) and Gessner *et al.* (2001a). However, occasionally the same shear-sense indicators show a top-N sense of shear (see below). Kinematic indicators in the upper Selimiye nappe and the overlying Cycladic blueschist unit

yielded a top-SE/ESE shear sense. In the Cycladic blueschist unit, the top-SE/ESE kinematic indicators developed during retrograde blueschist facies metamorphism. This is best expressed by pronounced chloritization of various minerals. Chloritization during retrogression also characterizes the kinematic indicators in discrete shear zones in the upper Selimiye nappe (phyllonite zones in Fig. 2-2).

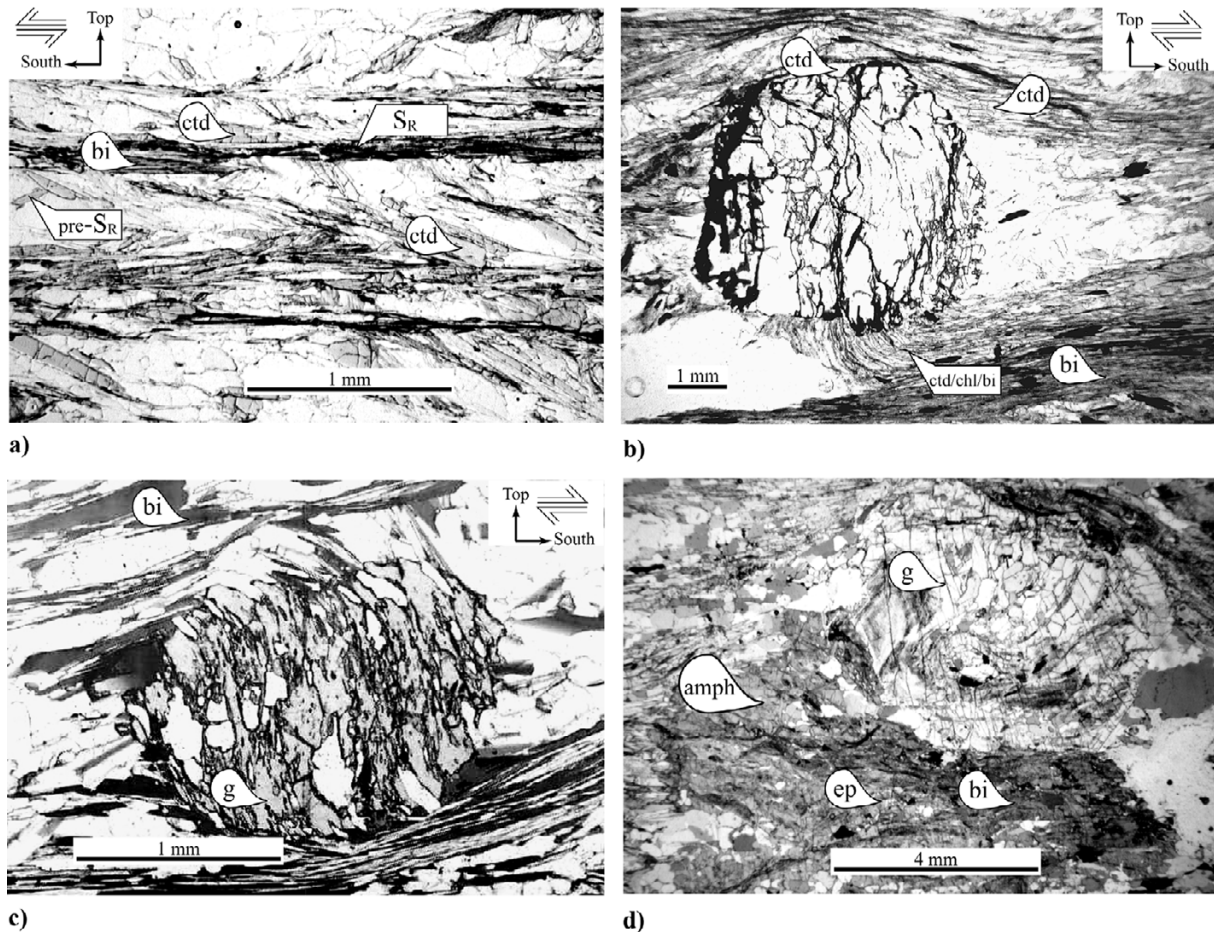


Fig. 2-4. Microphotographs from the southern study area: (a) Sample SE3, Selimiye nappe; penetrative regional  $S_R$  foliation separating microlithons in which pre- $S_R$  foliation is locally preserved; chloritoid grew in  $S_R$  and pre- $S_R$  foliation. Note that most foliation planes in microlithons appear to be related to  $S_R$  and form S-C fabrics indicating a top-S shear sense. (b) Sample SE12, garnet-chlorite zone, Selimiye nappe; rotated garnet indicating a top-S sense of shear. (c) Sample O5, Çine nappe; rotated garnet showing a top-S shear sense. (d) Sample N7, Çine nappe; garnet-epidote-amphibole-biotite-muscovite-plagioclase (+ calcite + quartz + fluids) assemblage in calcschist.

A number of larger scale tight to isoclinal folds with WNW-trending axes occur in the upper Selimiye nappe below the Cyclades-Menderes thrust. These folds fold the  $S_R$  foliation and because of their tight to isoclinal character their axial planes are subparallel to the  $S_R$  foliation. The relationships between the long and short limbs of the asymmetric folds are consistent with a apparent top-S shearing.

In addition to the open, tight to isoclinal folds, the  $S_R$  foliation in the Selimiye shear zone is folded about tight to isoclinal folds at the centimetre to metre scale. A weak crenulation cleavage is

associated with the folds. The axes of the folds are parallel to the  $L_R$  stretching lineations (Fig. 2-5b). These post- $D_R$  folds formed after the peak of the metamorphism and folded the  $D_R$  shear-sense indicators. Detailed field work revealed that the top-S shear-sense indicators occur in the upright limbs of the post- $D_R$  tight to isoclinal folds, whereas the top-N fabrics occur in the inverted limbs of the folds (Fig. 2-5b). Therefore, the top-N shear-sense indicators are folded structures, which originally had a top-S shear sense.

The metasedimentary rocks of the Çine nappe directly below the Selimiye shear zone display similar structures as the schist of the Selimiye nappe; a penetrative foliation and a SSW-plunging stretching lineation associated with top-S kinematic indicators (Fig. 2-2c). The shear-sense indicators are rotated garnet (Fig. 2-4c), asymmetric strain shadows around garnet and shear bands. Intrusive late Neoproterozoic orthogneiss at the northeastern end of Lake Bafa displays, together with the surrounding metapelite, two sets of isoclinal folds. The second generation of these folds have the  $S_R$  foliation as an axial-plane cleavage. In structurally deeper levels of the orthogneiss, widespread top-N shear-sense indicators occur (Fig. 2-5a). The top-N kinematic indicators are asymmetric feldspar porphyroclasts in which K-feldspar was dynamically recrystallized.

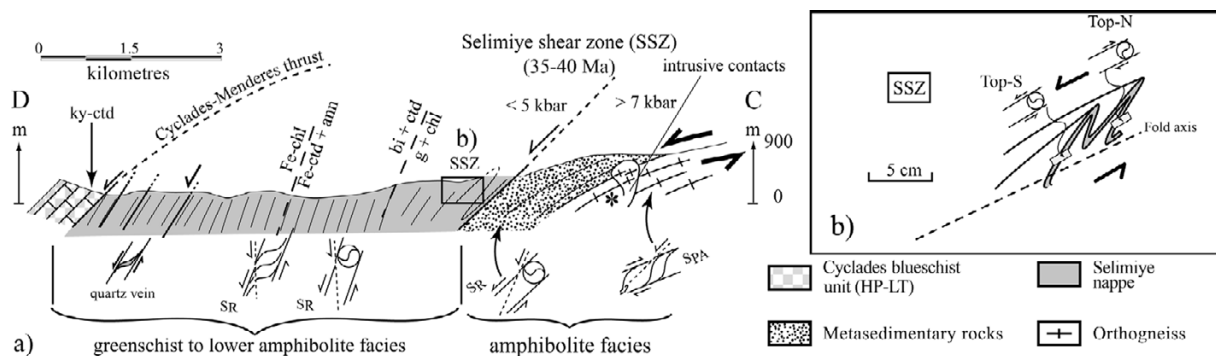


Fig. 2-5. Cross section DC (for location see Fig. 2-2d); top-S-displacing Selimiye shear zone (SSZ) separates metasedimentary rocks of the Çine nappe from those of the Selimiye nappe; insert show that SSZ and  $S_R$  are folded about N-trending isoclinal folds, which inverted top-S kinematic indicators in overturned limbs (a-type folds; Malavieille, 1987).  $S_{PA}$  foliation after Gessner *et al.*, 2001b; the suffix 'PA' indicates a pre-Alpine age.

Above, we have shown that metamorphism in the Selimiye nappe is of Tertiary age. Therefore, the syn-metamorphic WNW-striking foliation in the Selimiye nappe also has to be of Tertiary age. The Selimiye shear zone formed after top-S shearing associated with the  $S_R$  foliation.

### Northern study area

In the metasedimentary rocks in the northern part of the Çine nappe southwest of Aydın (Fig. 2-1), two foliations occur. The main foliation, which we term  $S_M$ , is parallel in the surrounding orthogneiss to the main foliation in the metasedimentary rocks ( $S_M$  would correspond to  $S_{PA}$  of

Gessner *et al.*, 2001b). On  $S_M$  a pronounced stretching lineation,  $L_M$ , occurs (Fig. 2-6a & b). In orthogneiss,  $L_M$  is marked by strongly elongated quartz-feldspar aggregates, whereas in the schist  $L_M$  is characterized by an alignment of biotite and stretched quartz aggregates. In the metasedimentary rocks, numerous symmetric foliation-boudinage structures occur, which attest to coaxial deformation (Fig. 2-6c). Nonetheless, rotated garnet and shear bands are common and indicate top-N shear associated with  $S_M$  and  $L_M$  in large parts of the metasedimentary rocks of the northern study area (Figs 2-6c & 2-7a). In the surrounding orthogneiss, top-N kinematic indicators are common and expressed by asymmetric recrystallized feldspar tails around feldspar porphyroclasts. This top-N shear sense is in marked contrast to the top-S shear sense in the metasedimentary rocks in the southern area (Figs 2-5 to 2-8).

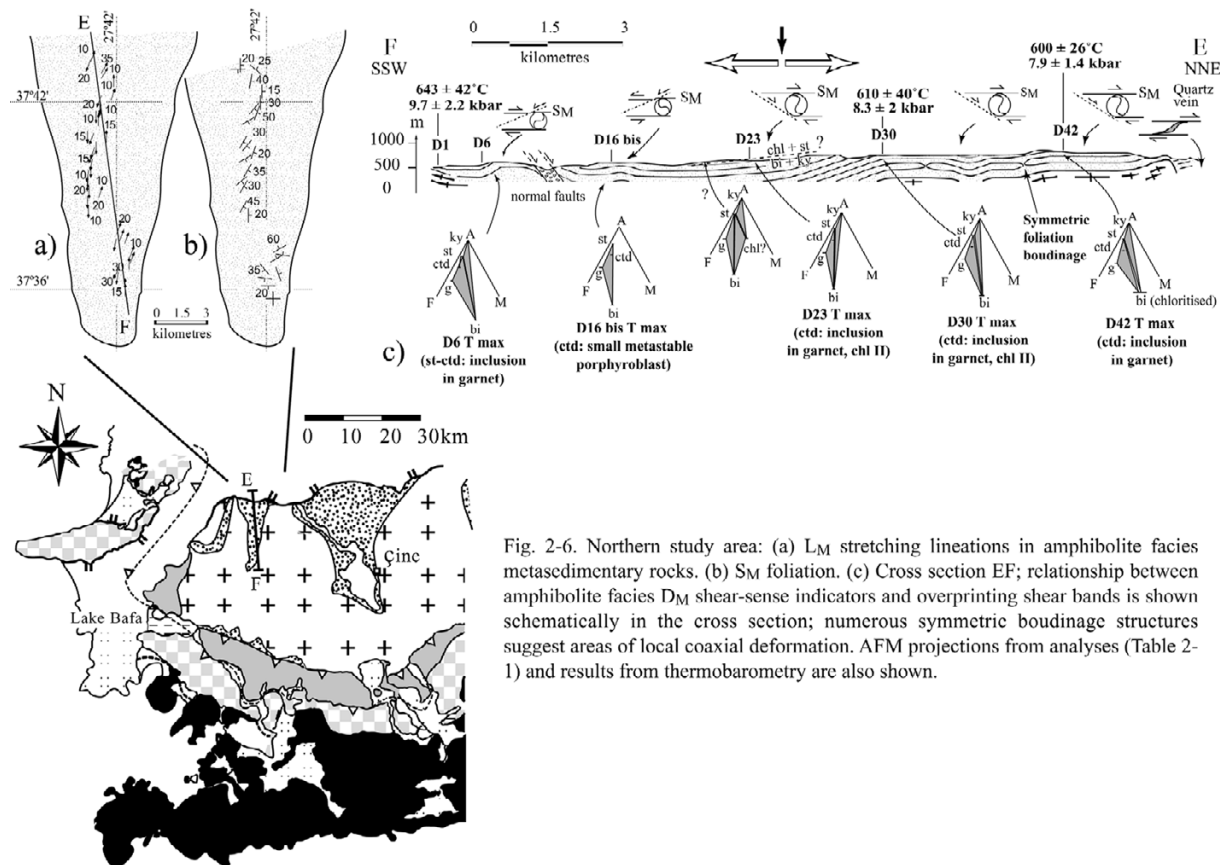


Fig. 2-6. Northern study area: (a)  $L_M$  stretching lineations in amphibolite facies metasedimentary rocks. (b)  $S_M$  foliation. (c) Cross section EF; relationship between amphibolite facies  $D_M$  shear-sense indicators and overprinting shear bands is shown schematically in the cross section; numerous symmetric boudinage structures suggest areas of local coaxial deformation. AFM projections from analyses (Table 2-1) and results from thermobarometry are also shown.



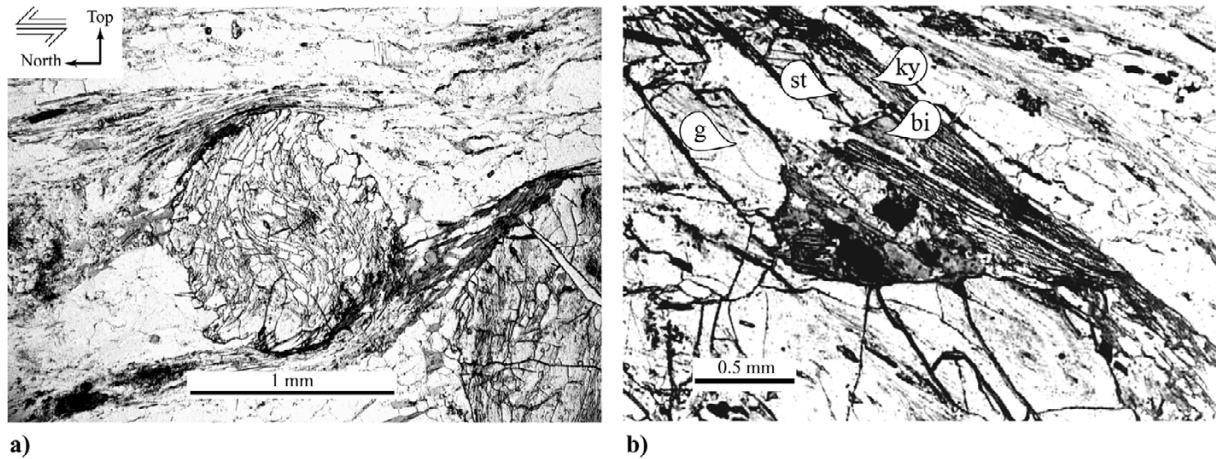
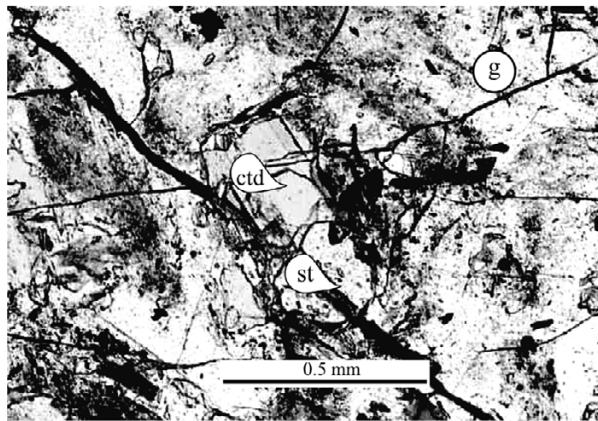


Fig. 2-7. Northern study area: (a) Sample D13; rotated garnet indicating top-N shear sense. (b) Sample D6; staurolite biotite-kyanite paragenesis. (c) Sample D6; chloritoid and staurolite inclusions in garnet.



c)

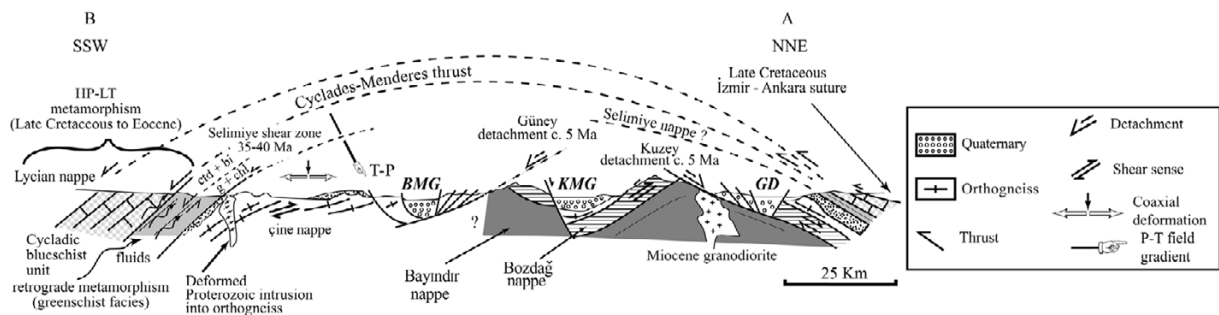


Fig. 2-8. (a) Interpretative cross section AB modified after Lips *et al.* (2001) (for location of section and patterns see Fig. 2-1); ages for the Selimiye shear zone are  $^{40}\text{Ar}/^{39}\text{Ar}$  white mica ages (Hetzel & Reischmann, 1996), and those for the Güneç and Kuzey detachment are fission track ages (Gessner *et al.*, 2001c, Ring *et al.*, 2004b). *P-T* field gradient for Selimiye and Çine nappes according to this study.

## SCOPE OF METAMORPHIC STUDY AND ANALYTICAL PROCEDURES

Metasedimentary rocks in the southern study area were formerly thought to belong entirely to the Selimiye nappe (Ring *et al.*, 1999a). However, as discussed above, the Selimiye shear zone developed within this metasedimentary section and therefore the upper part of this section belongs to the Selimiye nappe, whereas the underlying metasedimentary rocks belong to the Çine nappe. If so, differences in the metamorphic evolution of both metasedimentary units are likely. Metasedimentary rocks of the Çine nappe in the northern and southern study area preserve different kinematic indicators

(top-S in the south and top-N in the north) and the question arises whether or not the different structures are associated with different metamorphic events.

More than 350 samples were collected in the two study areas in order to map mineral isograds and their relationship to the regional foliation and the Eocene Selimiye shear zone. Location of samples and parageneses are respectively shown in Appendix 1 & 2. The extensive sampling also allows us to compare in detail metamorphic development of the different schist units.

The mineral analyses were obtained with a Jeol Superprobe (JXA 8900RL) at Johannes Gutenberg-Universität Mainz, Germany. Operating conditions were an acceleration voltage of 15 kV, a beam current of 15 nA and 20 s counting time per element. Standards are: wollastonite for Si, corundum for Al, pyrophanite for Ti, hematite for Fe, MgO for Mg, wollastonite for Ca, albite for Na, orthoclase for K, Cr<sub>2</sub>O<sub>3</sub> for Cr, rhodochrosite for Mn. A ZAF procedure was used for matrix correction. The mineral analyses are considered to be accurate within a range of *c.* 3% (relative) on any given grain.

Abbreviations used in text, figures and tables are adopted from Powell et al. (1998): als = aluminosilicate, amph = amphibole, bi = biotite, carb = carbonate, cd = cordierite, chl = chlorite, ctd = chloritoid, ep = epidote, fsp = plagioclase, g = garnet, ky = kyanite, mu = muscovite, q = quartz, st = staurolite, tr = tremolite, dol = dolomite, cc = calcite, cz = clinozoisite, an = anorthite, gr = grossular, py = pyrope, alm = almandine, andr = andradite, spss = spessartine, phl = phlogopite, clin = clinocllore.

*P-T* grids have been calculated with the THERMOCALC software (version 3.1) (Powell *et al.*, 1998), and using the internally consistent thermodynamic data set of Holland & Powell (1998) (update September 1999). For geothermobarometry, we calculated multivariant reactions using mode "average P-T" of the THERMOCALC software (Powell & Holland, 1988, 1994; Worley & Powell, 2000). Activities of the end-members were calculated from microprobe analyses (Tables 2-1 & 2-2) using the AX software (Holland, 2000). The calculated *P-T* data are listed in Table 2-3.

## MINERALOGY AND RELATIONSHIPS BETWEEN DEFORMATION AND MINERAL GROWTH

### Southern study area

#### *Selimiye nappe*

Garnet has a general grain size of about 5 mm but can be >1 cm in diameter. Garnet composition is almandine (60-70%), pyrope (1-10%), spessartine (1-10%) and grossular (10-30%). Most garnet lacks zoning, while some displays exchange between Ca and Mg-Fe from core to rim (Fig. 2-9a, sample SE12) as previously observed by Whitney & Bozkurt (2002). Mineral formulae do not show significant Fe<sup>3+</sup> and therefore we assumed that Fe<sup>2+</sup> = Fe<sup>total</sup>.

In all assemblages white mica shows a solid solution between paragonite, muscovite and celadonite depending on whole rock composition, degree of metamorphism and probably retrograde reactions. Margarite occurs in calcschists and occasionally in metapelites as inclusions in garnet. Phengitic substitution (Massonne & Schreyer, 1987) increases from 2.9 to 3.17 per formula unit (pfu) towards the orthogneiss but changes unsystematically from one sample to another. Secondary white mica occasionally occurs and has a lower Si content than primary white mica.

Primary chlorite occurs in all assemblages (Appendix 2) but secondary chlorite is ubiquitous. Garnet is often totally retrograded to chlorite, which implies an important stage of fluid circulation. Secondary chlorite porphyroblasts cut the main S<sub>R</sub> foliation and secondary chlorite replaced biotite that grew in the S<sub>R</sub> foliation.

Biotite is present in all samples, even in the calcschists, and in general is severely chloritized. Biotite is also found as inclusions in garnet.

Chloritoid is in equilibrium with biotite and chlorite in the upper parts of the nappe (samples SE2, SE3, C7, G12, G14, G16, E3, E4, E5, O28, Fig. 2-4a). At the base of the Selimiye nappe, chloritoid is stable with garnet, chlorite and biotite (Fig. 2-4b) (Appendix 2). Inclusions of chloritoid in garnet suggest that chloritoid grew before garnet during prograde metamorphism. On the basis of 6-oxygen structural formula, the mole fraction of Mg in chloritoid increases from the SSW to the NNE (Mg content varies from 0.132 to 0.213 pfu), and is related to an increase in temperature (Table 2-1, samples SE3 and SE12).

Plagioclase appears as albite in the pelitic schists but as oligoclase (An<sub>30</sub>) in the calcschists (Table 2-2, sample C9P and SE14). In the calcschists, we focused our study on impure layers in which

carbonate minerals mainly consist of solid solutions between dolomite, calcite and subordinate siderite or magnesite. Epidote minerals are zoisite and clinozoisite. Carbonate minerals and epidote are commonly present as inclusions in garnet. Accessory minerals in the Selimiye nappe are opaques (rutile, ilmenite, hematite, graphite), titanite, apatite, zircon and tourmaline.

Deformation/metamorphism relationships indicate that top-S shearing during  $D_R$  occurred during prograde to peak metamorphism. Rotated garnet consistently indicates top-S shear. Asymmetric strain shadows around garnet contain primary chlorite, primary white mica and biotite. These sheet silicates also grew in  $D_R$  shear bands.

Secondary white mica and biotite cut across the  $S_R$  foliation in some places. Secondary chlorite porphyroblasts also cut across  $S_R$ , but also occasionally replace biotite that grew in the  $S_R$  foliation suggesting that fluids circulated along  $S_R$  planes during this retrograde phase of metamorphism. Retrograde chlorite-forming reactions in  $S_R$  are in part associated with top-S shearing. Phyllonite zones with top-S kinematic indicators developed in metapelite of the chlorite-biotite zone and are characterized by very fine-grained layers of quartz and plagioclase interlayered with biotite and chlorite. Small porphyroblasts of chlorite occasionally appear in the matrix.

In a quartzite conglomerate with intercalated pelitic layers of the Cycladic blueschists unit directly above the Selimiye nappe south of Selimiye (Fig. 2-2d), chloritoid, kyanite, chlorite, white mica, quartz and opaques occur (T. Will, written communication 2002). Similar rocks with the same mineral assemblage yielded  $P-T$  conditions of 15 kbar and 500 °C on nearby Samos Island in the Aegean Sea (Will *et al.*, 1998). Moreover, recently Rimmelé *et al.*(2003) showed the presence of carpholite-kyanite-chlorite assemblages in the Mesozoic marble (blueschists unit, Fig 2-2d). They proposed minimum pressure-temperature conditions about 10-12 kbar and 440 °C. On Samos Island and on Dilek Peninsula, the minerals of this HP assemblage form a penetrative foliation (Fig. 2-1). In the mylonite zone of the Cyclades-Menderes thrust, this HP assemblage is completely retrograded and zones enriched in the secondary chlorite are common.

#### *Metasedimentary rocks of the Çine nappe*

Pelitic gneiss directly beneath the Selimiye shear zone shows assemblages of quartz, muscovite, plagioclase, biotite, garnet and accessory minerals (tourmaline, rutile, ilmenite, hematite, apatite, zircon). Tourmaline can be strongly concentrated forming black layers parallel to the foliation. Chloritoid has never been observed in these assemblages.

Garnet has a similar composition as in the Selimiye nappe but appears more homogeneous in both pelitic gneisses and in the calcschists. Garnet composition is almandine (63%), pyrope (8%), spessartine (2%) and grossular-andradite (25%) (Fig. 2-9b & c). Primary chlorite only occurs in calcschists (Appendix 2) and secondary chlorite is absent. Phengitic substitution in white mica (Massonne & Schreyer, 1987) is up to 3.3 pfu but changes unsystematically from one sample to another. Biotite is not altered and can be used for thermodynamic calculations.

In the pelitic gneisses, plagioclase zoning does not show obvious disequilibrium between core and rim but does show a slight compositional core-to-rim variation from An<sub>14</sub> to An<sub>16</sub> (Sample SE25, Table 2-2) in relationship to the degree of metamorphism. Sample SE18 shows coexisting albite and oligoclase in equilibrium (peristerite gap, Table 2-2) (Ashworth & Evirgen, 1985).

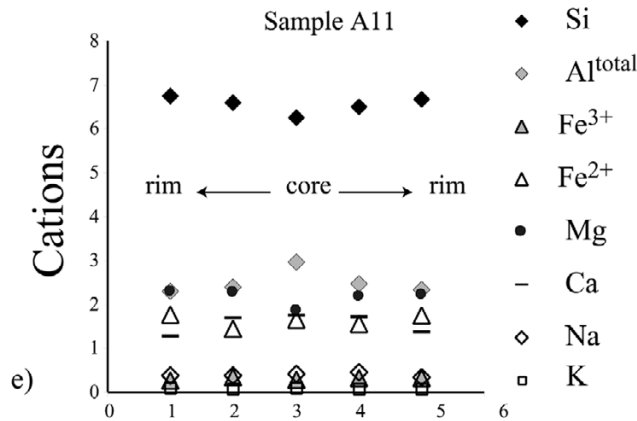
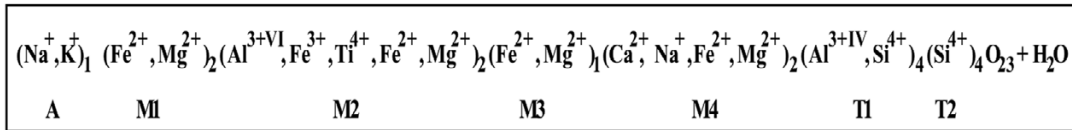
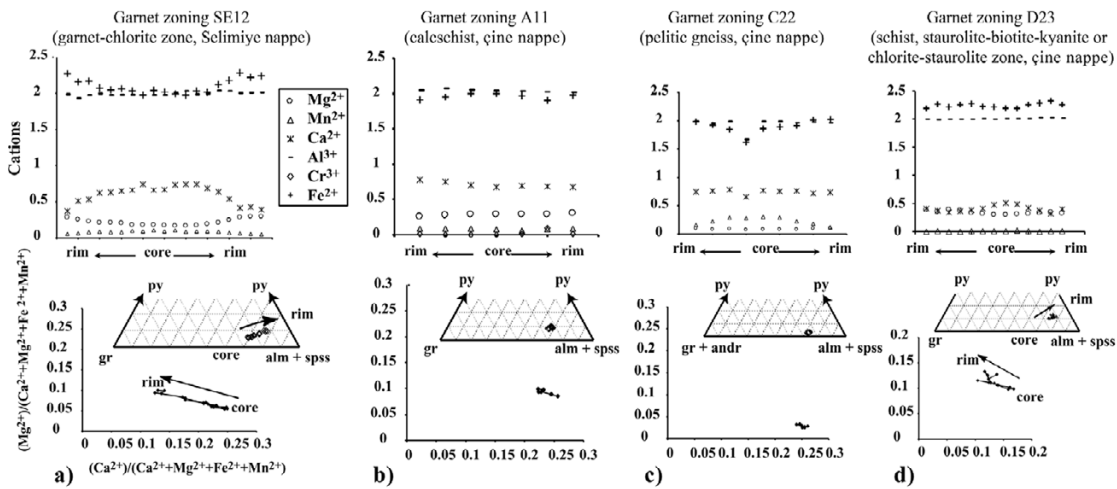
Amphibole appears in calcschists as tschermakite or magnesiohornblende (Leake *et al.*, 1997) and coexists with andesine, white mica, biotite, garnet, epidote, quartz and carbonate (Fig. 2-4d). The occurrence of amphibole has been observed along a horizon, which extends for 7 km along strike (Fig. 2-2d). On the basis of 23-oxygen structural formula, total Al content varies from 3 (core) to 2.5 pfu (rim; for instance sample A11, Table 2-1 & Fig. 2-9e). This variation is mainly correlated with an increase of Si in the T1 tetrahedral site (Fig. 2-9f). Mg increases from 1.8 (core) to 2.3 pfu (rim), whereas Ca and Fe<sup>2+</sup> decrease in the octahedral sites. Epidote minerals are zoisite and clinozoisite. In the calcschists plagioclase shows zoning from oligoclase (core) to andesine (rim, An<sub>37</sub>, Sample A11, Table 2-2). Accessory minerals are opaques (rutile, ilmenite, hematite, graphite), titanite, apatite, zircon and tourmaline.

Rotated garnet crystals show a top-S sense of shear associated with S<sub>R</sub> (Fig. 2-2c). Asymmetric top-S strain shadows around garnet and plagioclase with oligoclase rims contain white mica with high Si values and biotite. In shear bands in S<sub>R</sub> white mica with the highest Si contents and biotite grew. In calcschists, primary chlorite also occurs in these shear bands. These relationships indicate that top-S shearing occurred during prograde to peak metamorphism.

### **Northern study area**

The most notable difference between metasedimentary rocks of the Çine nappe in the north and those in the southern study area is the occurrence of kyanite and staurolite in the north. In addition, calcschists do not contain amphibole (series D, Appendix 2). The retrograde reactions are again less important than in the Selimiye nappe and only sporadic secondary chlorite is observed. Chloritoid appears only as inclusions in garnet except for one sample (Appendix 2-2, sample D16bis), where chloritoid occurs with biotite in the matrix (the Mg content of this chloritoid is around 0.225 pfu or

XMg = 0.225). Garnet has the same chemistry as in the southern study area, with a slight exchange between Ca and Mg from core to rim (Fig. 2-9d, sample D23). Plagioclase is oligoclase or andesine and does not show variations from core to rim (e.g sample D42, Table 2-1).



Calcic Amphibole ( $\text{Ca} + \text{Na}^{\text{M4}} > 1$ ,  $\text{Na}^{\text{A}} + \text{K}^{\text{A}} < 0.5$ )

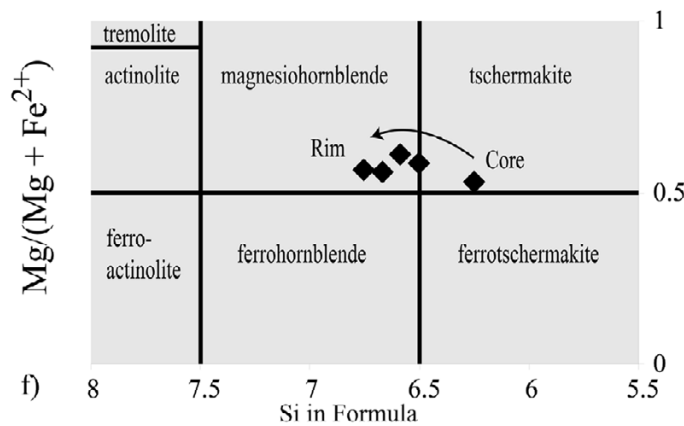


Fig. 2-9. Garnet zoning patterns from different metamorphic zones in Selimiye (a) and Çine nappe (b-d); zoning is depicted by profiles across garnet (diagrams at the top), pyrope-grossular/andradite-almandine/spessartine distribution (diagrams in the centre), and  $X_{\text{Mg}}$  vs  $X_{\text{Ca}}$  (diagrams at the bottom); cations are given on the basis of 12-oxygen structural formula. All garnet is close to almandine end member; some show a slight exchange between Ca and Mg indicating prograde metamorphism. Sample A11: e) Amphibole zoning pattern, f) Amphibole composition on a  $(\text{Mg}/\text{Mg} + \text{Fe}^{2+})$  vs  $(\text{Si}^{\text{total}})$  diagram (Leake *et al.*, 1997).

Staurolite is in equilibrium with biotite, garnet and kyanite (sample D6, Fig. 2-7b) and also with chloritoid as inclusions in garnet (sample D6, Fig. 2-7c). Therefore, staurolite grew during prograde metamorphism and is also stable with garnet at the peak of metamorphism (equilibrium at  $T_{\max}$  with garnet, kyanite and biotite). Epidote and opaques are common in calcschist and appear in metapelite as inclusions in garnet.

In contrast to the southern study area, rotated garnet, locally with staurolite inclusions, depict a top-N sense of shear (see below) associated with  $S_M$ . Staurolite in the matrix grew after the main  $S_M$  foliation formed. The relationships between garnet rotation during the formation of  $S_M$  and later growth of staurolite indicates that  $S_M$  formed during prograde amphibolite facies metamorphism and that peak metamorphic conditions were attained after the  $S_M$ -forming deformation.

## Summary

The mineralogical development in both study areas is characterized by a single prograde metamorphism. This is shown in the southern study area by an increase in Mg from core to rim in garnet and amphibole, and a weak increase in Ca from the core to rim in plagioclase (Sample A11 & SE25, Table 2-2). Inclusion of chloritoid in garnet in the northern study area also indicates a prograde metamorphism. No evidence for polymetamorphism has been found in either study area.

Deformation/metamorphism relationships in the southern Çine nappe are the same as those in the Selimiye nappe and indicate top-S shearing during prograde amphibolite facies metamorphism. Along the Cyclades-Menderes thrust top-S shearing took place during lower to middle greenschist facies conditions and phyllonite zones developed. Shearing in the metasedimentary rocks of the northern Çine nappe also developed during prograde metamorphism; however, here the sense of shear is mostly top-N.

In the Selimiye nappe, secondary chlorite, biotite and white mica cut across the regional  $S_R$  foliation, and garnet was retrograded to chlorite after the formation of  $S_R$ . This is interpreted to be the result of retrograde metamorphism associated with pronounced fluid circulation after  $D_R$ . Evidence has been given that top-S shearing in the Selimiye nappe locally continued during retrogression (see also Whitney & Bozkurt, 2002). This retrogression complicates thermodynamic considerations and necessitates the study of single subsystem models and Schreinemakers' rules. The coexistence of oligoclase with albite (peristerite gap) described from metasedimentary rocks of the Çine nappe also make  $P$ - $T$  estimations in the southern study area problematic (Evirgen & Ataman, 1982; Evirgen & Ashworth, 1984; Ashworth & Evirgen, 1984; Ashworth & Evirgen, 1985; Whitney & Bozkurt, 2002).

In the northern study area, parageneses and mineral analyses are more suitable for estimating  $P$ - $T$  conditions of amphibolite facies metamorphism.

## PARAGENESES AND THERMOBAROMETRY

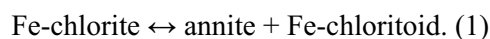
### Southern study area

#### *Selimiye nappe*

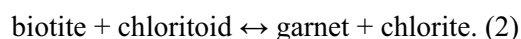
Analysis of the metamorphic parageneses (Appendix 2) allows mapping of three isometamorphic zones in the Selimiye nappe (Fig. 2-2d): the chlorite-biotite zone in the upper Selimiye nappe, the chloritoid-biotite zone and the garnet-chlorite zone at the base of the nappe. However, two samples containing garnet (G2 & G8) have been found in the chlorite-biotite zone close to the Cyclades-Menderes thrust and will be discussed further below. The boundaries of the different metamorphic zones are parallel to  $S_R$  over a distance of about 30 km between Lake Bafa and Milas (Fig. 2-2d).

The calcschists always display the same quartz-muscovite-plagioclase-biotite-chlorite-epidote-carbonate ( $\pm$ garnet) assemblage, which is not suitable to distinguish different metamorphic zones. Therefore, the KFMASH system has been used because it provides a framework to study both calcschists and metapelites in a comparable fashion. Minerals used are chlorite, biotite, garnet, staurolite, cordierite, chloritoid and aluminosilicates. They are projected into an AFM diagram from quartz, muscovite and  $H_2O$ . Fluid ( $H_2O$ ) pressure is assumed to be equal to total pressure. Accessory minerals are not taken into account in the reactions observed. Structural formulae and activity models are shown in Appendix 3. The resulting  $P$ - $T$  grid for the KFMASH system is given in Fig. 2-10a.

The occurrence of chloritoid in the KFMASH system is related to the continuous reaction:



This reaction appears around 500 °C allowing for the occurrence of the chlorite-biotite-chloritoid paragenesis in the KFMASH system (Sample SE3, Figs 2-2d, 2-4a & 2-10a). In samples SE2, SE3, C7, G12, G14, G16, E3, E4, E5 and O28 chloritoid is in equilibrium with chlorite and biotite. The occurrence of garnet (e.g. sample SE12, Figs 2-2d, 2-4b & 2-10a) is assumed to be related to the discontinuous reaction in the KFMASH system:



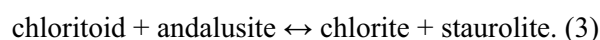


Numerous chloritoid inclusions in garnet corroborate the inference (Appendix 2-2) that chloritoid grew before garnet during increasing temperature. The position of reaction (2) in  $P$ - $T$  space essentially depends on the invariant [cd, als] point (Fig. 2-10a), the position of which is subject to considerable uncertainty and has either been placed in the andalusite field (Powell *et al.*, 1998) or in the kyanite field (Spear & Cheney, 1989). The coexistence of minerals involved in reaction (2) with the different aluminosilicates should be deduced in thin sections but unfortunately no aluminosilicates have been found in the Selimiye nappe (in this area). Therefore, metamorphic pressure is poorly constrained. Recently, Likhonov *et al.* (2001) described reaction (2) in the andalusite field at around 3 kbar. This would move the position of the invariant [cd, als] point close to the  $\text{Al}_2\text{SiO}_5$  triple point. If so, a pressure of about 4 kbar and a temperature around 500 °C would be implied for the Selimiye nappe.

According to the phengitic substitution observed in metapelite of the Selimiye nappe (mostly between 2.90 and 3.17 pfu), pressure can be estimated around 4 kbar (Massonne & Schreyer, 1987). Therefore, it seems probable that the  $P$ - $T$  conditions in the lower Selimiye nappe are around 500 °C and 4 kbar as previously suggested by Ashworth & Evirgen (1984) and Whitney & Bozkurt (2002). However, phengitic substitution depends on bulk rock composition (Wei & Powell, 2003) and estimate of pressure is given here in first approximation.

The occurrence of the paragenesis chloritoid-biotite before garnet-chloritoid with increasing temperature could be related to Fe-rich and Mn-poor bulk compositions of the rocks (e.g. low Mn contents in garnet in sample SE12, Table 2-1). It has been shown by a number of studies that the occurrence of garnet in greenschist facies pelites may be a factor of the Mn content of the rock (Spear & Cheney, 1989; Droop & Harte, 1995; Tinkham *et al.*, 2001). However, two samples (G2 & G8) in the chlorite-biotite zone contain garnet (without chloritoid inclusions). These may be explained either by a local Mn-rich bulk composition allowing the stability of garnet, or by thrust imbrication of slices from the overlying Cycladic blueschist unit.

According to the  $P$ - $T$  grid (Fig. 2-10a) the continuous reaction (1) appears at the high- $T$  side of the discontinuous reaction:



Despite this, staurolite is not observed in these rocks. Whitney & Bozkurt (2002) argued that the absence of staurolite is a temperature indicator rather than a bulk-compositional effect. However, staurolite is stable in KFMASH at considerably lower temperatures than the 560 °C suggested by these

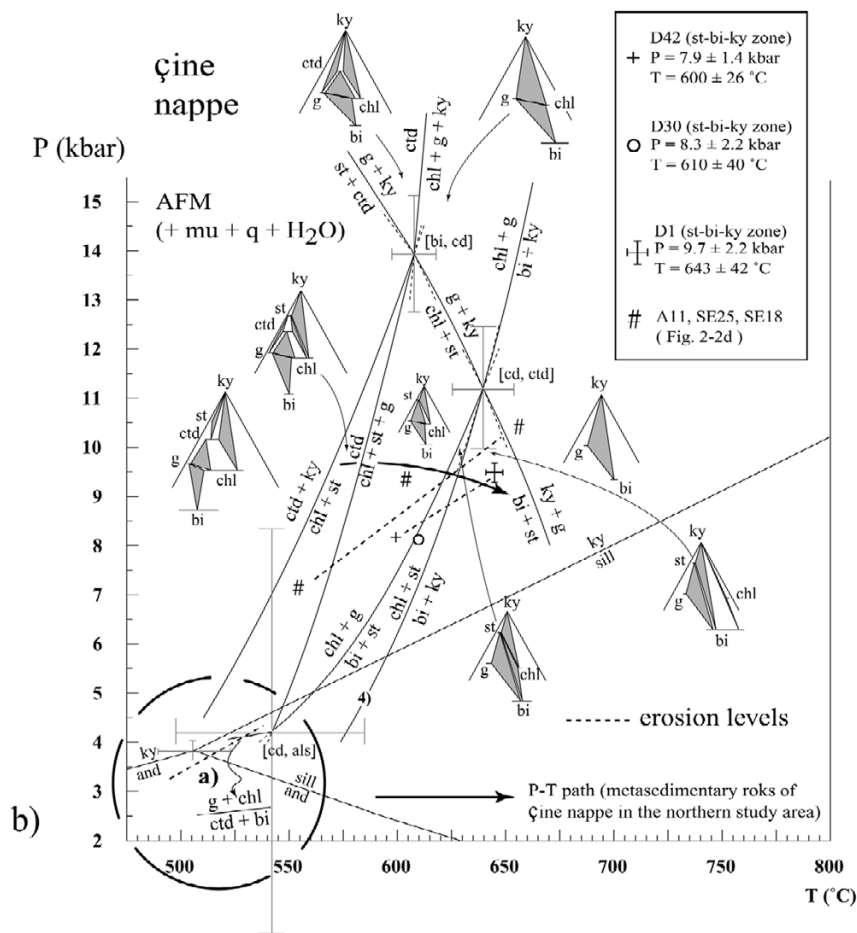
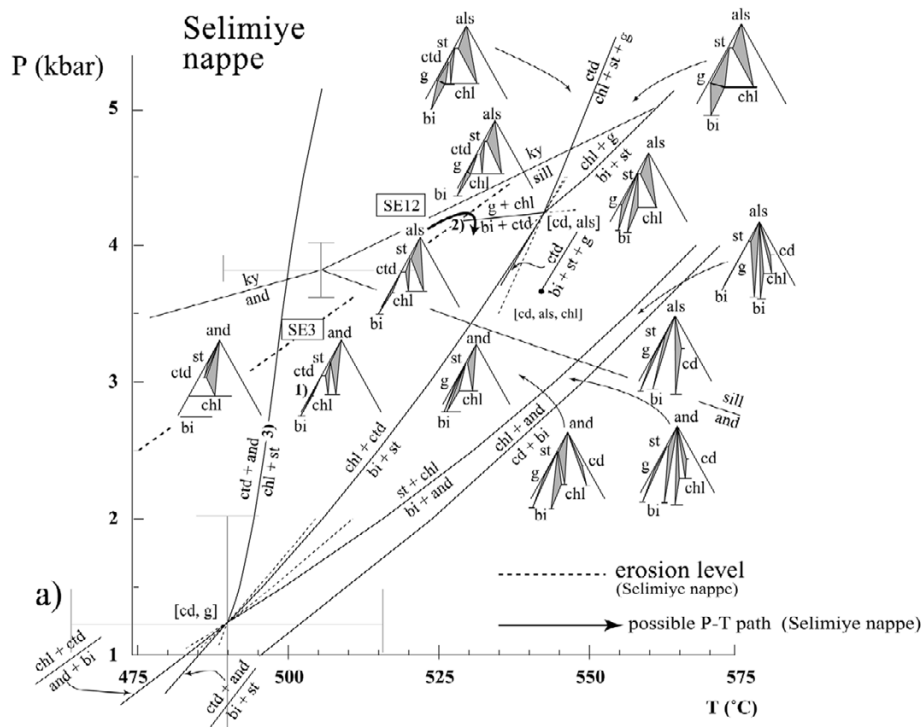


Fig. 2-10. *P-T* grids calculated with THERMOCALC v3.1 (Powell *et al.*, 1998), KFMASH system. H<sub>2</sub>O = fluid ( $\mu$ ,  $q$ , H<sub>2</sub>O in excess). [bi, cd]:  $P = 13.93 \pm 1.2$  kbar,  $T = 607.8 \pm 10$  °C. [cd, ctd]:  $P = 11.2 \pm 1.4$  kbar,  $T = 639.6 \pm 14$  °C. [cd, g]:  $P = 1.25 \pm 1.6$  kbar,  $T = 490 \pm 26$  °C. [cd, als]:  $P = 4.22 \pm 4.2$  kbar,  $T = 542.3 \pm 46$  °C. Aluminosilicate invariant point:  $P = 3.8 \pm 0.2$  kbar,  $T = 505 \pm 16$  °C. (a) *P-T* grid for rocks of Selimiye nappe. (b) *P-T* grid for rocks of Çine nappe (northern and southern study area). Reactions discussed in the text have been labelled.

authors (Fig. 2-10a). We therefore suggest that the absence of staurolite is likely related to a compositional effect rather than a consequence of lower temperatures than the 560 °C.

Finally, chloritoid inclusions in the garnet-chlorite zone (for instance samples SE6, SE18, SE11, A20, A18, B22) could be indicative for a clockwise  $P$ - $T$  path: chlorite-biotite followed first by chloritoid-biotite, then garnet-chloritoid at higher pressure, and finally by garnet-chloritoid-chlorite-biotite at  $T_{\max}$  (Fig. 2-10a). Nevertheless, given the thermodynamic uncertainties, the  $P$ - $T$  path is not well constrained by the parageneses in the metapelites. In conclusion, it seems likely that the temperature increases from 350 °C to 525 °C towards the garnet-chlorite zone and that the pressure can be estimated at about 4 kbar at the base of the Selimiye nappe. Observed  $P$ - $T$  conditions are likely to be near the kyanite-andalusite transition, close to the aluminosilicate invariant point and so more likely related with Barrovian-type metamorphism.

#### *Metasedimentary rocks of Çine nappe*

Thermodynamic calculations using independent sets of reactions have been carried out for samples SE18 and SE25. Sample SE25 belongs to pelitic gneiss above the orthogneiss and sample SE18 is from metapelite directly below the Selimiye shear zone. Analyses and results are reported in Tables 2-1 and 2-3. Temperatures of  $590 \pm 54$  °C (sample SE18) and  $675 \pm 62$  °C (sample SE25) have been obtained for a pressure of *c.* 10 kbar. However, the pressure is probably overestimated, because mineral analyses from sample SE18 show the coexistence of oligoclase with albite (peristerite gap, Table 2-2) and  $X_{\text{ca}}$  in plagioclase from sample SE25 is low (Table 2-1).

In the vicinity of the orthogneiss, tschermakitic-magnesiohornblende amphibole occurs in calcschist (samples A11, A13, N6, N7) and coexists with andesine, white mica, biotite, garnet, epidote, quartz and carbonate. The plane marking the initial growth of amphibole in the calcschists parallels  $S_R$  over a distance of about 7 km (Fig. 2-2d). We used this amphibole horizon to constrain  $P$ - $T$  conditions (sample A11, Table 2-1). The temperature has been estimated using the Ca-amphibole-plagioclase thermometer (Blundy & Holland, 1990; Holland & Blundy, 1994). Temperature estimates are between 500 °C and 640 °C for a pressure range of 6-9 kbar. Pressure has been estimated with the calibration of Johnson & Rutherford (1989) related to the  $Al^{\text{total}}$  content of amphibole (3-2.5 pfu). Pressure estimates range from *c.* 9 kbar for amphibole cores to *c.* 6.3 kbar for the rims.

Because  $\text{CO}_2$  fluids play an important role in the calcschists, we attempted to determine  $P$ - $T$  conditions related to the occurrence of amphibole, using THERMOCALC software in the  $\text{K}_2\text{O}$ - $\text{CaO}$ - $\text{MgO}$ - $\text{Al}_2\text{O}_3$ - $\text{SiO}_2$ - $\text{CO}_2$ - $\text{H}_2\text{O}$  subsystem (KCMAS-CH). The end-member minerals used are grossular, phlogopite, dolomite, tremolite, clinocllore, anorthite, clinozoisite and muscovite. These minerals are

projected into the  $\text{Al}_2\text{O}_3\text{-K}_2\text{O-MgO}$  diagram from quartz, calcite, and fluids ( $\text{H}_2\text{O-CO}_2$ ). Fluid pressure ( $\text{H}_2\text{O, CO}_2$ ) is assumed to be equal to total pressure.

Before considering  $P$ - $T$  conditions related to amphibole crystallisation, the mole fraction of  $\text{CO}_2$  in the rocks needs to be estimated. We determined  $X_{\text{CO}_2}$  using a  $P$ - $X_{\text{CO}_2}$  pseudosection. Activities of the end members were calculated from the analyses using the AX software (Holland, 2000) (Table 2-1, sample A11). A minimum temperature of about 500 °C can be estimated via the Ca-amphibole-plagioclase thermometer used herein. Figure 2-11a displays the  $P$ - $X_{\text{CO}_2}$  pseudosection grid for a pressure range of 2-10 kbar. The inset in Fig. 11a shows the occurrence of all phases except clinocllore around the invariant points [clin, mu, phl, tr, dol] and [clin, cz, tr] at  $X_{\text{CO}_2} = 0.1$  and around 7 kbar. This is consistent with the complex parageneses observed in thin section (Appendix 2-2). At 600 °C only the invariant point [clin, cz, tr] is stable and moves to higher  $X_{\text{CO}_2}$  while the reaction tremolite  $\leftrightarrow$  dolomite is shifted to higher pressure where clinozoisite becomes unstable. We believe that the  $P$ - $X_{\text{CO}_2}$  pseudosection below 500 °C provides a good estimate for the mole fraction of  $\text{CO}_2$  ( $X_{\text{CO}_2} = 0.1$ ), which appears reasonable for the stabilization of garnet (grossular end member). Given this  $\text{CO}_2$  mole fraction and the activities of the end members from the analyses, a  $P$ - $T$  grid has been drawn (Fig. 2-11b). The stability of clinozoisite-grossular-anorthite around the invariant point [clin, mu, phl, tr, dol] for sample A11 can be estimated at about 7 kbar and 500 °C. Tremolite appears at 540 °C resulting from the reaction in the KCMAS-CH subsystem:



In addition, thermodynamic calculations using independent sets of reactions have been carried out using the same activities for the end members. Temperature and pressure obtained are  $502 \pm 32$  °C and  $7 \pm 1.2$  kbar (Table 2-3). An increase in  $X_{\text{CO}_2}$  up to 0.5 yielded a temperature and pressure of *c.* 550 °C and *c.* 8 kbar but increased the uncertainties of the estimates. It appears that amphibole in the calcschists near the orthogneiss formed at higher pressure than reaction (2) in the KFMASH subsystem which we estimated to be >7 kbar. Therefore, thermobarometric calculations from sample SE18 probably yielded too high pressures (peristerite gap) but temperatures in the metasedimentary rocks of the Çine nappe close to the orthogneiss are likely to be higher than 550 °C (e.g. sample SE25). The lack of staurolite in the metasedimentary rocks of the Çine nappe in the southern study area, as well as in the schists of the Selimiye nappe, has been used by Whitney & Bozkurt (2002) to indicate temperatures <560°C. We think, especially in the metasedimentary rocks of the Çine nappe, that the lack of staurolite (as well as the lack of aluminosilicates) is related to bulk composition.

In conclusion,  $P$ - $T$  estimates from the metasedimentary rocks of the Çine nappe below the Selimiye shear zone are likely on the order of 7 kbar and >550 °C. These  $P$ - $T$  estimates are higher than

those from the metasedimentary rocks of the Selimiye nappe above the shear zone (*c.* 4-5 kbar and <525 °C). This finding supports our structural observations in the field that both units are separated by a tectonic contact (Figs 2-2 & 2-5a).

### **Northern study area**

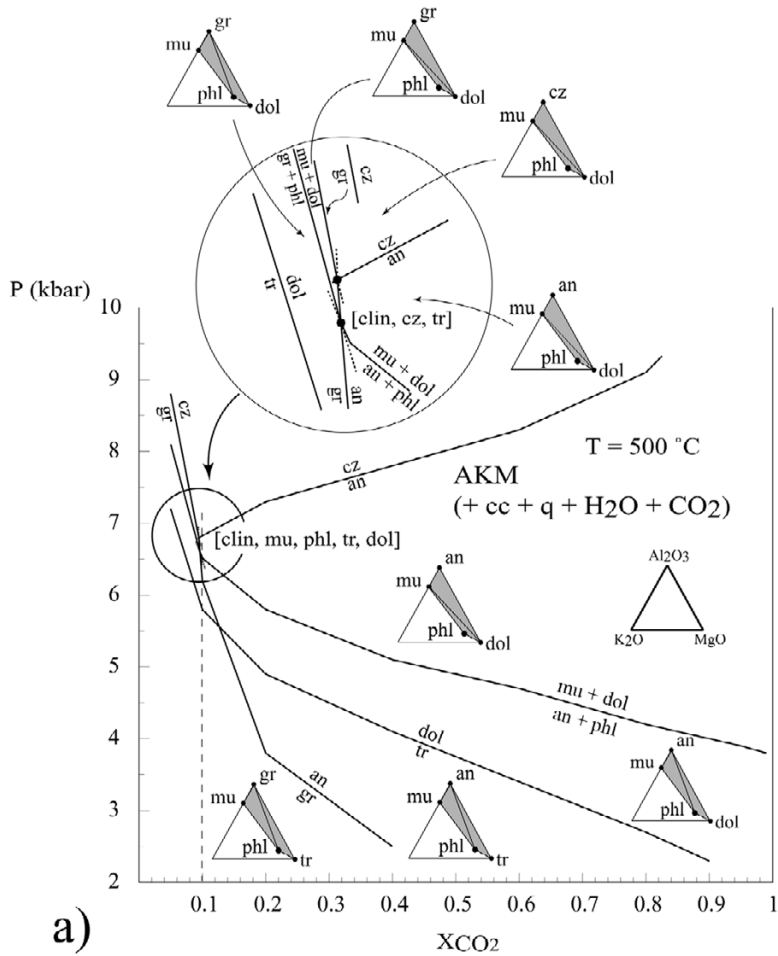
Due to the occurrence of kyanite and staurolite, metamorphic conditions in this area are better constrained than in the southern study area. We again used the KFMASH system to describe the petrogenetic relationships. The resulting *P-T* grid is shown in Fig. 2-10b. Analysis of the parageneses (Appendix 2) shows that kyanite-biotite-staurolite is a critical paragenesis in this area. Considering the *P-T* grid and this critical paragenesis, we estimated a temperature of >600 °C and a pressure between 8 and 11 kbar.

As already noticed, the retrograde reactions are less important than in the southern part and only mica shows retrograde alteration. Indeed analyses sometimes point to lower potassium contents in biotite (Table 2-1, samples D6, D16bis) than those expected (*c.* 10% of K<sub>2</sub>O). Chloritoid always appears as inclusions in garnet, occasionally in textural equilibrium with staurolite (samples D6, D8, D19). This indicates prograde metamorphism (Figs 2-6c, 2-7c & 2-10b). In sample D16bis, one small porphyroblast of chloritoid was found in contact with biotite in the matrix. Because of the paragenesis garnet-biotite-staurolite in the same thin section, this mineral should be considered as relic and therefore metastable. The occurrence of kyanite in sample D23 could be due to the discontinuous reaction in the KFMASH subsystem:

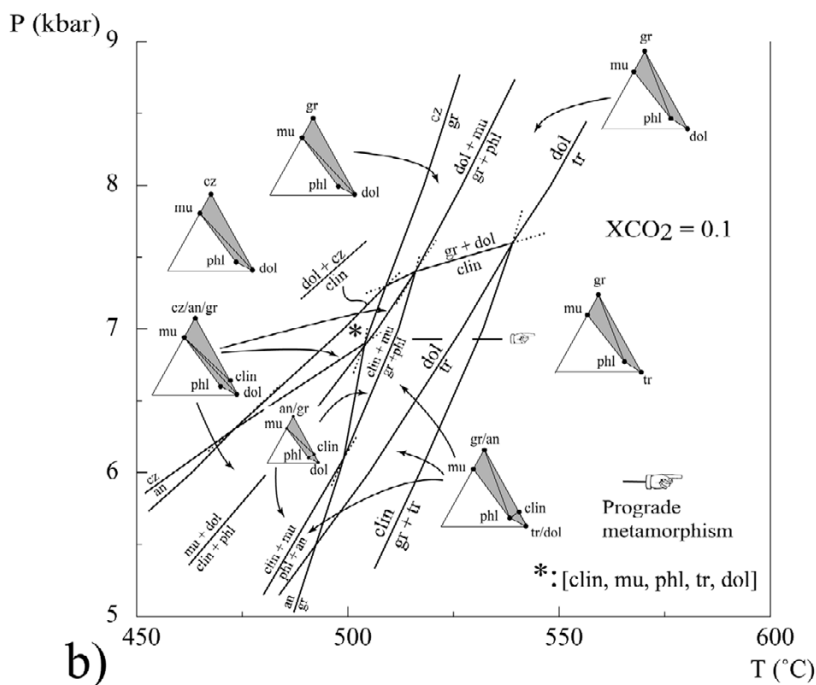


Reaction (4) allows the stability of the paragenesis staurolite-biotite-kyanite in the KFMASH system and the disappearance of chlorite towards the Mg-chlorite end member (Fig. 2-10b). Because of the low Mg contents of chlorite in samples D23 and D30 (Table 2-1), these minerals are considered to be secondary.

The inclusion of staurolite-chloritoid in garnet (e.g sample D6) imply a compositional fractionation in the KFMASH system with increase of Mg proportion due to the growth of garnet. Indeed garnet-chloritoid-staurolite represent an anterior equilibrium before occurrence of biotite-staurolite-kyanite paragenesis at  $T_{\text{max}}$  (textural equilibrium in matrix).



a)

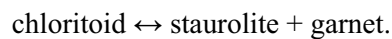


b)

Fig. 2-11. (a) P- $X_{CO_2}$  pseudosection calculated for calcschist sample A11, THERMOCALC v3.1 (Powell *et al.*, 1998), KCMAS-H-CO<sub>2</sub> system. See text for abbreviations of end members; H<sub>2</sub>O-CO<sub>2</sub> = fluids (cc, q, and fluids in excess). Activities calculated with the AX software (Holland, 2000) (Table 2-1): gr = 0.02, dol = 0.7, tr = 0.1, clin = 0.05, phl = 0.07, an = 0.5, cz = 0.7, mu = 0.7 (q = 1, cc = 1). Note that  $X_{CO_2}$  is about  $X_{CO_2} = 0.1$  for this sample. (b) P-T grid corresponding to calculated  $X_{CO_2}$  of 0.1; position of the invariant point [clin, mu, phl, tr, dol] is assumed to give equilibrium pressure whereas T<sub>max</sub> is related to amphibole growth at around 540°C (prograde metamorphism).

This can be seen in a  $T-X_{Mg}$  pseudosection where Fe is concentrated in garnet core followed during its nucleation and prograde metamorphism by an increase of Mg proportion from garnet-chloritoid-staurolite to biotite-staurolite-kyanite paragenesis (Fig. 2-12a). Ca and Mn have been as well mostly concentrated in the garnet (grossular, spessartine, epidote inclusion). The whole composition was likely near MnCKFMASH, but after compositional fractionation, the parageneses at  $T_{max}$  can be described in the KFMASH system (effective composition).

In KFMASH system garnet-chloritoid-staurolite paragenesis depends on the divariant reaction:



This reaction albeit dependent on temperature is restricted to very Fe-rich whole rock composition at low pressure (Fig. 2-12b) almost lacking Mg. However the stability field will be expanded around 8 kbar and more (Fig. 2-12a). We believe that the paragenesis garnet-chloritoid-staurolite represents a paragenesis at  $P_{max}$  around 8 kbar or even more for temperature around 575 °C (Fig. 2-10). This also imply a  $P-T$  path in decompression from  $P_{max}$  to  $T_{max}$  during exhumation process.

Thermodynamic calculations using independent sets of reactions have been undertaken for samples D1, D30, and D42. Analyses and results are reported in Tables 2-1 and 2-3. Temperatures of 600 to 650 °C and pressures of 8-11 kbar were obtained. The results are consistent with the  $P-T$  grid.

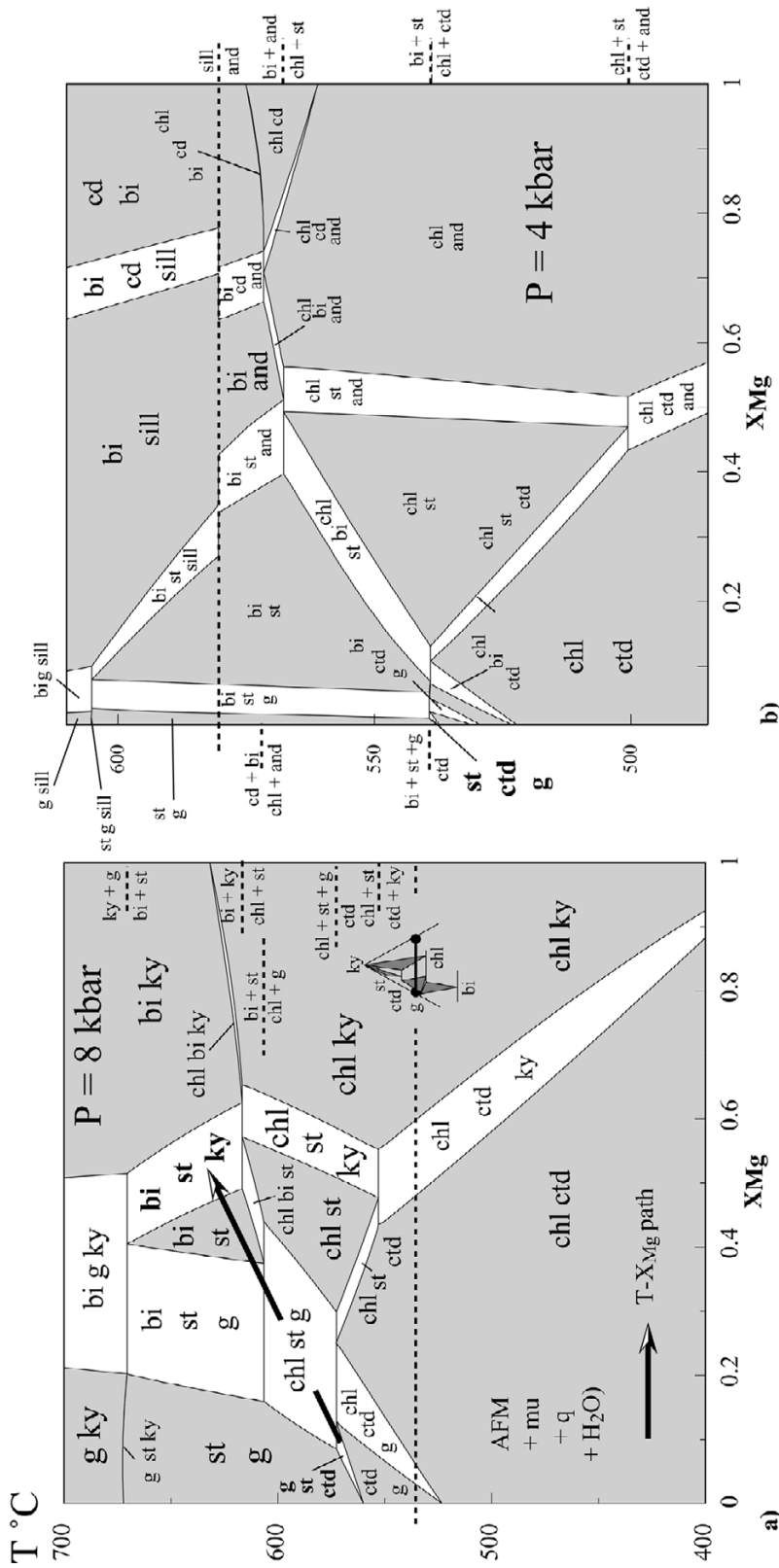


Fig. 2-12. (a)  $T$ - $X_{Mg}$  pseudosection at 8 kbar for the sample D6 (calculated with THERMOCALC v3.1).  $Al_2O_3$  : 48.81, (FeO +MgO) : 42.24,  $K_2O$  : 8.95 (in mol%). Composition of the whole rock has been calculated from a theoretical point of view allowing the occurrence of chloritoid-staurolite-garnet paragenesis at  $P_{max}$  (staurolite-chloritoid inclusion) and biotite-kyanite-staurolite paragenesis at  $T_{max}$ . Stability field for the paragenesis staurolite-chloritoid-garnet is very narrow. The  $T$ - $X_{Mg}$  path show an increase in Mg proportion from the garnet core to the paragenesis observed at  $T_{max}$ . Other cations (mainly Ca and Mn) have been concentrated during growth of garnet. This fractionation is correlated with an increase of temperature during prograde metamorphism. (b)  $T$ - $X_{Mg}$  pseudosection at 4 kbar using the same composition. Stability field for the paragenesis staurolite-chloritoid-garnet is extremely narrow. Both pseudosections demonstrates that although the divariant reaction  $ctd = st + g$  in KFMASH is dependent on temperature, stability field at low pressure is extremely narrow and limited to rock without Mg. Stability field for the paragenesis staurolite-chloritoid-garnet start to become suitable albeit narrow at 8 kbar and will be expanded at higher pressure.



## DISCUSSION

### Results of the metamorphic study

East of Lake Bafa, the Selimiye shear zone separates two metasedimentary units, which record different  $P$ - $T$  conditions but largely similar structures. Metasedimentary rocks of the Çine nappe experienced amphibolite facies metamorphism shown by the occurrence of the amphibole-garnet paragenesis and  $P$ - $T$  conditions of about 7 kbar and  $>550$  °C. This schist sequence is overlain by lower grade metasedimentary rocks with maximum  $P$ - $T$  conditions of about 4 kbar and 525 °C. These greenschist to lower amphibolite facies rocks belong tectonically to the Selimiye nappe. Prograde metamorphism in the Selimiye nappe decreases structural upwards as indicated by mineral isograds defining the garnet-chlorite zone at the base, the chloritoid-biotite zone and the biotite-chlorite zone at the top of the nappe. Due to uncertainties in the thermodynamic calculations, the metamorphic break between the metasedimentary rocks of the Çine and Selimiye nappe is not very well defined but appears to be on the order of 2 kbar. The  $P$ - $T$  break indicates that about 7 km of metamorphic section is missing and therefore a tectonic contact is responsible, the Selimiye shear zone. This  $P$ - $T$  break demonstrates that movement along the Selimiye shear zone developed after peak and/or retrograde metamorphism (see also Whitney & Bozkurt, 2002).

Amphibolite facies schists in the northern study area southwest of Aydın record maximum  $P$ - $T$  conditions of 8-11 kbar and 600-650 °C. The chloritoid inclusions in garnet indicate prograde metamorphism and a clockwise  $P$ - $T$ -path. Because the schists southwest of Aydın and those east of Lake Bafa both occur below the Selimiye shear zone and no major tectonic contact occurs between the two studied schists units, we propose that these two schist sequences belong to the same tectonic unit, the Çine nappe. However, the metasedimentary rocks in the northern study area record different structures than those in the south. We have found no evidence for regional-scale polymetamorphism in the metasedimentary rocks of either the Çine or Selimiye nappes. Within both nappes,  $P$ - $T$  conditions are correlated with Barrovian-type metamorphism.

### Implications for the nature of the Selimiye shear zone

In the southern study area, mineral isograds in the Selimiye nappe are parallel to the regional  $S_R$  foliation and formed during prograde metamorphism. The  $S_R$  foliation and associated isograds with top-S kinematic indicators suggests that metamorphism in the Selimiye nappe is related to N-S crustal shortening during Barrovian-type metamorphism. The Selimiye shear zone post-date metamorphism expressed in Çine and Selimiye nappes.

The break in metamorphism across the Selimiye shear zone with lower grade rocks occurring tectonically above higher grade rocks is often considered to be evidence that the tectonic contact results of extensional process. However, it is important to note that a number of detailed studies (Wheeler & Butler, 1994; Ring & Brandon, 1994; Ring, 1995; Ring *et al.*, 1999c) showed that this type of metamorphic break is not always indicative for normal faulting. Indeed, Gessner *et al.* (2001b) proposed that Eocene stacking of nappes in the western Anatolide belt was out-of-sequence thrusting, which can explain the occurrence of lower grade rocks tectonically above higher-grade rocks.

Strong evidence against an interpretation that the Selimiye shear zone is a metamorphic-core-complex-type normal fault, as proposed by Bozkurt & Park (1994), comes from the absence of contact-type metamorphism in the Selimiye nappe. Mineral isograds are parallel to the regional  $S_R$  foliation- and slow cooling recorded in the footwall of the Selimiye shear zone (Hetzl & Reischmann, 1996). The footwalls of core-complex-bounding normal faults show extremely fast cooling rates (Foster & John, 1999; Ring *et al.*, 2003). Rapid cooling at 23-20 Ma at the southern rim of the Anatolide belt as recorded by fission-track ages is remarkably similar to the pattern and timing of cooling at the northern end of the Anatolide belt (Ring *et al.*, 2004b). In the north, fast cooling was caused by Early Miocene extensional faulting along the Simav detachment (Işık & Tekeli, 2001; Ring *et al.*, 2004b). The Simav detachment reactivated the basal thrust of the Cycladic blueschist unit. The similarities of the fission-track cooling pattern suggests that there should also be an Early Miocene extensional detachment at the southern rim of the Anatolide belt and it has been speculated that the basal thrust of the Lycian nappe was reactivated as an extensional fault (Ring *et al.*, 2004b). It might be feasible that some of the retrograde top-S shear-sense indicators in the upper Selimiye nappe formed during the proposed Early Miocene extensional reactivation of the Lycian nappes. Alternatively, the retrograde top-S kinematic indicators might be due to out-of-sequence thrusting along the Cyclades-Menderes thrust (see below).

### **Cause of Eocene metamorphism across the Selimiye shear zone**

In the Cycladic blueschist unit of Dilek Peninsula,  $^{40}\text{Ar}/^{39}\text{Ar}$  dating on phengite yielded an Eocene age of  $40.1 \pm 0.4$  Ma (Oberhänsli *et al.*, 1998), which is most probably related to movement on deep-seated parts of the Cyclades-Menderes thrust (Gessner *et al.*, 2001b; Ring & Layer, 2003). The age for greenschist to lower amphibolite facies metamorphism in the Selimiye nappe is also Eocene ( $>43$ -37 Ma; Hetzel & Reischmann, 1996). The source of heating could be related to a complicated redistribution of the isotherms during the stacking of the Menderes nappes (lower units) involving lower and middle crustal levels. However, since the Selimiye shear zone postdate the metamorphism, it seems possible that metamorphism expressed in the Selimiye nappe pre-date emplacement of the lower nappes. Subsequently, emplacement of the middle and upper tectonometamorphic units (H-P)

onto the Menderes nappes would have caused the retrograde metamorphism observed and possibly the general development of shear bands top to the south in all nappes. In contrast to the Sesia zone - example outlined above- no evidence for HP-LT metamorphism has been found. We so think that the total lack of Tertiary HP-LT overprint in the Menderes nappes indicates that the middle and upper units were significantly exhumed before emplacement onto the Menderes nappes.

### **Orogenic implications**

The most fundamental question concerns the age of the described tectonometamorphic fabrics in the Çine nappe. Above it was shown that prograde metamorphism in the Selimiye nappe has to be Tertiary in age. However, the age of metamorphism in the underlying Çine nappe is much less clear. The total lack of evidence for polymetamorphism suggest that metamorphism in the entire Çine nappe has the same age as that in the Selimiye nappe. Gessner *et al.* (2001a, 2004) proposed that the amphibolite facies  $S_{PA}$  foliation and associated top-N kinematic indicators in orthogneiss are of late Neoproterozoic to Cambrian age and the  $^{207}\text{Pb}/^{206}\text{Pb}$  garnet ages (Ring *et al.*, 2004a) from the orthogneiss and from underlying metapelite of the Bozdağ nappe seems to support this conclusion.

A possible interpretation is that amphibolite facies metamorphism in the metasedimentary rocks of the southern Çine nappe, directly below the Selimiye nappe is also of Tertiary age and thus unrelated to the tectonometamorphic fabrics in the orthogneiss below these rocks. The  $D_R$  structures with their consistent top-S kinematic indicators and the deformation/metamorphism relationships, which show that the kinematic indicators developed during prograde metamorphism related to the Eocene Selimiye nappe metamorphism. The variation in foliation strike between the schist units in the hanging wall and footwall of the Selimiye shear zone and the orthogneiss (Fig. 2-2a) would then imply that the N-S-striking foliation in the orthogneiss is of late Neoproterozoic to Cambrian age and the WNE-striking foliation in the schist is of Eocene age.



Table 2-2. Plagioclase analyses for different metamorphic zones. C9P: schist, Selimiye nappe. SE14: calcschist, Selimiye nappe. SE25: pelitic gneiss, Çine nappe. SE18: schist, Çine nappe (fsp1 – oligoclase; fsp2 – albite). Mineral formulae have been calculated with AX software (Holland, 2000).

Sample	C9P	C9P	C9P	SE14	SE14	SE14	SE25	SE25	SE25	SE18	SE18	SE18	SE18	SE18	A11	A11	
Min	fsp/rim	fsp/core	fsp/rim	fsp/rim	fsp/core	fsp/rim	fsp/core	fsp	fsp/rim	fsp1	fsp1	fsp2	fsp2	fsp2	fsp/core	fsp/rim	
SiO <sub>2</sub>	68.04	68.17	68.21	59.90	60.50	60.66	61.95	64.19	63.85	62.92	62.96	66.86	66.77	66.52	67.38	59.38	56.79
TiO <sub>2</sub>	-	0.01	0.01	0.01	0.02	-	0.04	0.01	0.02	-	-	0.01	-	-	-	0.03	-
Al <sub>2</sub> O <sub>3</sub>	19.28	19.17	19.30	24.69	24.49	24.80	20.62	21.77	21.99	23.61	22.75	19.08	19.33	19.23	19.10	23.43	25.42
Cr <sub>2</sub> O <sub>3</sub>	0.15	-	0.07	0.06	0.02	-	1.16	0.09	-	0.22	0.05	-	0.04	0.46	0.23	0.07	0.08
Fe <sub>2</sub> O <sub>3</sub>	-	0.08	0.11	0.10	0.01	0.05	0.73	0.04	0.05	0.12	0.09	-	0.07	0.10	0.16	0.04	0.01
FeO	-	-	-	-	-	-	-	-	-	-	-	-	-	-	-	-	-
MnO	0.03	0.01	0.05	-	-	-	-	-	0.03	0.03	0.04	0.05	0.04	-	-	0.05	-
MgO	0.01	-	-	-	-	-	0.31	-	-	0.02	-	-	-	-	-	-	0.01
CaO	0.16	0.16	0.14	6.68	6.25	6.31	2.84	3.13	3.38	4.29	4.07	0.11	0.24	0.13	0.13	5.62	7.55
Na <sub>2</sub> O	11.96	11.87	12.07	7.87	8.11	7.94	9.05	9.72	9.87	8.11	8.86	11.61	11.69	11.51	11.46	8.31	7.28
K <sub>2</sub> O	0.05	0.06	0.02	0.04	0.05	0.05	0.37	0.07	0.07	0.07	0.07	0.07	0.01	0.07	0.08	0.08	0.07
Totals	99.69	99.52	99.97	99.34	99.45	99.82	97.06	99.03	99.26	99.40	98.88	97.79	98.19	98.02	98.54	97.01	97.20
Oxygen	8	8	8	8	8	8	8	8	8	8	8	8	8	8	8	8	8
Si	2.99	3.00	2.99	2.69	2.70	2.70	2.83	2.86	2.84	2.79	2.81	2.99	2.98	2.97	2.99	2.72	2.61
Ti	-	-	-	-	-	-	-	-	-	-	-	-	-	-	-	-	-
Al	1.00	0.99	1.00	1.31	1.29	1.30	1.11	1.14	1.15	1.23	1.20	1.01	1.02	1.01	1.00	1.27	1.38
Cr	0.01	-	-	-	-	-	0.04	-	-	0.01	-	-	-	0.02	0.01	-	-
Fe <sup>3+</sup>	-	-	-	-	-	-	0.03	-	-	-	-	-	-	-	0.01	-	-
Fe <sup>2+</sup>	-	-	-	-	-	-	-	-	-	-	-	-	-	-	-	-	-
Mn	-	-	-	-	-	-	-	-	-	-	-	-	-	-	-	-	-
Mg	-	-	-	-	-	-	0.02	-	-	-	-	-	-	-	-	-	-
Ca	0.01	0.01	0.01	0.32	0.30	0.30	0.14	0.15	0.16	0.20	0.20	0.01	0.01	0.01	0.01	0.28	0.37
Na	1.02	1.01	1.03	0.68	0.70	0.69	0.80	0.84	0.85	0.70	0.77	1.01	1.01	1.00	0.99	0.74	0.65
K	-	-	-	-	-	-	0.02	-	-	-	-	-	-	-	-	0.01	-
Sum	5.02	5.01	5.02	5.00	5.00	4.99	4.99	4.99	5.01	4.94	4.98	5.01	5.02	5.01	5.00	5.01	5.02

Another possibility is that amphibolite facies metamorphism in the metasedimentary rocks of the southern Çine nappe is of the same late Neoproterozoic to Cambrian age as amphibolite facies metamorphism in the orthogneiss. Support for this interpretation would be that the schist and the orthogneiss record a single amphibolite facies metamorphism. However, because the kinematic indicators in the orthogneiss indicate top-N shear with local coaxial deformation and those in the metasedimentary rocks consistently indicate top-S shear, this interpretation does not appear likely.

The age of amphibolite facies metamorphism in the metasedimentary rocks of the northern Çine nappe is even more problematic. Because the metasedimentary units in the south and in the north record amphibolite facies metamorphism and occur above the orthogneiss, one could assume that their metamorphism is of the same age, and, according to our interpretation given above, of Tertiary age. However, in this case it is necessary to explain the different kinematic indicators associated with garnet growth, i.e. top-N rotated garnet in the north and top-S rotated garnet in the south. Furthermore, the main foliation in the northern metasedimentary rocks does not show a discordant pattern with the underlying orthogneiss. Because of this, and because the orthogneiss and the northern metasedimentary rocks depict the same prograde top-N kinematic indicators, it is possible that amphibolite facies metamorphism in the metasedimentary rocks of the northern Çine nappe is of late Neoproterozoic to Cambrian age. This inference is supported by the metamorphic study of Ring *et al.* (2001) from the lowermost Çine nappe and the Bozdağ nappe. These authors proposed that deformation/metamorphism relationships between staurolite and garnet growth in these two nappes are very similar to those in the metasedimentary rocks of the Çine nappe in our northern SE study area. Ring

*et al.* (2001) concluded that the staurolite-garnet relationships resulted from late Neoproterozoic to Cambrian metamorphism, which is corroborated by the  $^{207}\text{Pb}/^{206}\text{Pb}$  garnet ages (Ring *et al.*, 2004a).

This latter interpretation implies that both studied metasediment outcrops in the Çine nappe have a monometamorphic amphibolite facies overprint of different age. Earlier studies (Candan *et al.*, 2001; Gessner *et al.*, 2001a; Ring *et al.*, 2001) showed that the Çine and Bozdağ nappes have widespread evidence of amphibolite, and local eclogite and granulite facies metamorphism of late Neoproterozoic to Cambrian age. Nappe stacking during the Tertiary orogeny caused pronounced retrogression along the nappe boundaries during greenschist facies metamorphism. Locally, deformation zones associated with top-S kinematic indicators formed during this greenschist facies retrogression within the Çine and Bozdağ nappes. Apart from these localised zones at the nappe boundaries and within the nappes, the Çine and Bozdağ nappes were not affected by Tertiary deformation and metamorphism. According to this interpretation the metasedimentary rocks of the Çine nappe directly below the Selimiye shear zone were severely affected by Alpine shearing. Note that only these southern metasedimentary rocks are close to a Tertiary thrust (Fig. 2-8). It can be proposed that deformation-related fluid flow obliterated evidence for older metamorphism in the metasedimentary rocks of the Çine nappe immediately below the Selimiye nappe.

Although this interpretation is speculative, it is based on a detailed metamorphic and microstructural study of more than 350 samples and a number of age constraints. This interpretation highlights that simple tectonometamorphic fabrics do not *a priori* indicate a simple orogenic development of a heterogeneous nappe stack. Preservation in some areas and complete overprinting of those fabrics in other areas could be controlled by deformation-related fluid flow associated with Tertiary nappe stacking. Detailed dating of tectonometamorphic fabrics is essential to constrain the orogenic history more closely.

### **Alpine top-N shearing in the Anatolide belt**

A number of workers (Bozkurt & Park, 1994; Hetzel *et al.*, 1998; Whitney & Bozkurt, 2002) interpreted top-N amphibolite facies shearing in the Bozdağ and Çine nappes as an early phase of Tertiary deformation related to northward nappe movement. Gessner *et al.* (2001a, 2004) showed that the top-N kinematic indicators in orthogneiss were cut by granite yielding an age of *c.* 550 Ma (see above).  $^{207}\text{Pb}/^{206}\text{Pb}$  garnet dating in both nappes (Ring *et al.*, 2004a) also yielded ages of >500 Ma. These data would indicate that amphibolite facies shearing in the Bozdağ nappe and in orthogneiss of the Çine nappe is of latest Neoproterozoic to Cambrian age and is not related to the Alpine orogeny.

For the amphibolite facies top-N shearing event in the metasedimentary rocks of the Çine nappe in our northern study area a pre-Tertiary age is also possible. However, there are no geochronological data for this rock sequence to substantiate this inference, but Tertiary age for top-N shearing cannot be ruled out. For instance evidences for a lower amphibolite facies metamorphism (as in the Selimiye nappe) associated with top-to-the-N fabrics, would change our assumption about different metamorphism events. If so, a more complex deformation history has to be proposed taking in account different senses of shear and metamorphism associated.

Bozkurt & Park (1994) and Whitney & Bozkurt (2002) based their inference of Tertiary top-N shearing in part on work in the Selimiye nappe. It has been shown in this study that occasional top-N sense-of-shear indicators in the Selimiye shear zone are inverted top-S kinematic indicators and are therefore not indicative for an early Tertiary phase of top-N shear in this area. Furthermore, there is no evidence in the Selimiye shear zone, that the top-N shear-sense indicators formed before the top-S kinematic indicators as assumed by Bozkurt & Park (1994) and Whitney & Bozkurt (2002).

Bozkurt & Park (1994) also mentioned early north-verging folds in the Selimiye nappe. We have also mapped tight to isoclinal folds with WNW-trending axes and S-dipping axial planes. The structural facing direction of these asymmetric folds is unknown. The relationships between long and short limbs favour a top-S shear sense.

In summary, it is concluded that top-N metamorphism in the western Anatolide belt seems reduced to amphibolite facies metamorphism and associated proterozoic age. Early Alpine metamorphism would be more correlated with top-S movement and greenschist metamorphism. Large-scale tectonic models also do supply hint for such an event (Şengör *et al.*, 1984; Collins & Robertson, 1997, 1998, 2003).

## CONCLUSIONS

The major conclusions are:

- The Selimiye shear zone developed after a prograde greenschist- to lower amphibolite facies metamorphism. Metamorphism in the Selimiye nappe itself may have resulted from burial below the upper and middle tectonometamorphic units of the Anatolide belt in the Eocene.

- Metamorphism in the Selimiye nappe is of Barrovian-type and decreases structurally upwards as indicated by mineral isograds defining the garnet-chlorite zone at the base, the chloritoid-biotite zone and the biotite-chlorite zone at the top of the nappe.

- There is no evidence for a HP-LT metamorphism overprint indicating that middle and upper units were significantly exhumed before emplacement onto the Menderes nappes.

- Despite the very fact that the metamorphism in the underlying Çine nappe is relatively simple and monophasic it appears still possible that all studied metasedimentary rocks in the Çine nappe do not record the same Eocene metamorphism. Our study emphasises that rocks, which have relatively simple metamorphic fabrics, may reflect complex tectonic evolutions resulting from more than one single orogeny. A detailed geochronologic and metamorphic study is needed to constrain the age of metamorphism in the Çine nappe. Meanwhile evidences for top-to-the-N fabrics during lower amphibolite facies metamorphism might also change our assumption about different metamorphism events.



Table 2-3.  $P$ - $T$  calculations. Abbreviations : an = anorthite, ab = albite, phl = phlogopite, ann = annite, cast = eastonite, py = pyrope, gr = grossular, alm = almandine, mu = muscovite, pa = paragonite, cel = celadonite, mst = Mg-staurolite, fst = Fe-staurolite, ky = kyanite, cc = calcite, dol = dolomite, cz = clinozoisite, tr = tremolite, clin = clinoclone, q = quartz, sd = standard deviation, cor = correlation, sigfit =  $\chi^2$  test. Activities have been calculated with the AX software using following models (Holland, 2000; Holland & Powell, 1998): amphibole: non-ideal mixing model for Ca-amphiboles (Holland & Blundy, 1994), plagioclase: model 1 from Holland & Powell (1992), biotite: Al-M1 ordered; site-mixing model; symmetric formalism (Powell & Holland, 1993, 1999), garnet: 2-site mixing; regular solution gammas, muscovite: non ideal interactions (Holland & Powell, 1998), epidote: symmetric formalism, carbonate: disordered calcite structure, 1-site mixing, chlorite: Al-M4 ordered model (Holland *et al.*, 1998), staurolite: ideal Fe-Mg mixing.

**Sample SE18** (Selimiye nappe, garnet-chlorite zone),  $T_{\max}$ :  
Activities and their uncertainties from analyses (Table 1):

	an	ab	phl	ann	east	py	gr
a	0.400	0.780	0.0464	0.0530	0.0350	0.00217	0.0160
sd(a)/a	0.10800	0.05000	0.36935	0.35086	0.39650	0.68205	0.50357

	alm	mu	pa	cel	q	H2O
a	0.280	0.660	0.970	0.0250	1.00	1.00
sd(a)/a	0.15357	0.10000	0.09979	0.42526	0	

Independent set of reactions

3east + 6q = phl + py + 2mu  
 phl + east + 6q = py + 2cel  
 py + gr + mu = 3an + phl  
 gr + alm + mu = 3an + ann  
 py + 2pa + 3cel = 2ab + 3east + 9q + 2H2O

**results :**

$T = 590^\circ\text{C}$ ,  $sd(T) = 27$ ,  $P = 9.7$  kbar,  $sd(P) = 1.0$ ,  $cor = 0.820$ ,  $sigfit = 0.51$

**Sample D1** (northern study area, staurolite-biotite-kyanite zone),  $T_{\max}$ :  
Activities and their uncertainties from analyses (Table 1):

	phl	ann	east	py	gr	alm	mu
a	0.0800	0.0250	0.0570	0.00400	0.00240	0.360	0.670
sd(a)/a	0.30859	0.45063	0.34770	0.63695	0.67514	0.15000	0.15000

	pa	cel	an	ab	ky	H2O	q
a	0.940	0.0170	0.350	0.810	1.00	1.00	1.00
sd(a)/a	0.10000	0.58824	0.12675	0.05000	0		0

Independent set of reactions

gr + 2ky + q = 3an  
 pa + 3an = gr + ab + 3ky + H2O  
 3east + 6q = phl + py + 2mu  
 phl + east + 6q = py + 2cel  
 3east + 5q = 2phl + mu + 2ky  
 ann + 2ky + q = alm + mu

**results :**

$T = 643^\circ\text{C}$ ,  $sd(T) = 21$ ,  $P = 9.7$  kbar,  $sd(P) = 1.1$ ,  $cor = 0.773$ ,  $sigfit = 0.75$

**Sample SE25** (southern study area, pelitic gneiss),  $T_{\max}$ :  
Activities and their uncertainties from analyses (Table 1):

	mu	pa	cel	py	gr	alm	an
a	0.630	0.542	0.0400	0.00279	0.00850	0.300	0.280
sd(a)/a	0.10000	0.10000	0.38400	0.66444	0.57014	0.15000	0.15552

	ab	phl	ann	east	q	H2O
a	0.840	0.0370	0.0620	0.0340	1.00	1.00
sd(a)/a	0.05012	0.39138	0.32856	0.39913	0	

Independent set of reactions :

2east + 6q = mu + cel + py  
 3east + 6q = 2mu + py + phl  
 3an + phl = mu + py + gr  
 3an + ann = mu + gr + alm  
 2pa + py + 3ann + 9q = 3cel + 3alm + 2ab + 2H2O

**results :**

$T = 675^\circ\text{C}$ ,  $sd(T) = 31$ ,  $P = 11.7$  kbar,  $sd(P) = 1.2$ ,  $cor = 0.790$ ,  $sigfit = 0.93$

**Sample D30** (northern study area, staurolite-biotite-kyanite zone),  $T_{\max}$ :  
Activities and their uncertainties from analyses (Table 1):

	mu	pa	cel	an	ab	py	gr
a	0.710	0.930	0.0170	0.590	0.670	0.00660	0.00440
sd(a)/a	0.10000	0.10011	0.45374	0.05043	0.05000	0.59403	0.62921

	alm	phl	ann	east	ky	q	H2O
a	0.320	0.0650	0.0390	0.0520	1.00	1.00	1.00
sd(a)/a	0.15000	0.33306	0.39308	0.35756	0	0	

Independent set of reactions :

gr + 2ky + q = 3an  
 pa + 3an = ab + gr + 3ky + H2O  
 mu + 2phl + 6q = 3cel + py  
 2east + 6q = mu + cel + py  
 7cel + 4east + 12ky = 11mu + 5py  
 ann + 2ky + q = mu + alm

**results :**

$T = 610^\circ\text{C}$ ,  $sd(T) = 19$ ,  $P = 8.3$  kbar,  $sd(P) = 0.9$ ,  $cor = 0.750$ ,  $sigfit = 0.38$

**Sample A11** (southern study area, calc schist),  $T_{\max}$ :  
Activities and their uncertainties from analyses (Table 1):

	clin	mu	an	gr	cz	phl	tr
a	0.0500	0.700	0.500	0.0200	0.700	0.0700	0.100
sd(a)/a	0.36167	0.10000	0.07500	0.47772	0.05000	0.32451	0.28053

	dol	cc	H2O	CO2
a	0.700	1.00	0.900	0.100
sd(a)/a	0.05000	0		

Independent set of reactions

5clin + 49an + 3gr + 40cc = 38cz + tr + 20dol  
 clin + 6an + 10cc = gr + 4cz + 5dol + 2H2O  
 clin + 12an + 12cc = gr + 8cz + 5dol + 2CO2  
 3an + phl + 6cc = mu + 2gr + 3dol

**results :**

$T = 502^\circ\text{C}$ ,  $sd(T) = 16$ ,  $P = 7.0$  kbars,  $sd(P) = 0.6$ ,  $cor = 0.884$ ,  $sigfit = 0.75$

**Sample D42** (northern study area, staurolite-biotite-kyanite zone),  $T_{\max}$ :  
Activities and their uncertainties from analyses (Table 1):

	an	ab	py	gr	alm	pa	mst
a	0.640	0.640	0.00600	0.00580	0.320	0.880	0.000140
sd(a)/a	0.05000	0.05016	0.60264	0.60565	0.15000	0.10000	71.42857

	fst	q	ky	H2O
a	0.630	1.00	1.00	1.00
sd(a)/a	0.20000	0	0	

Independent set of reactions

gr + q + 2ky = 3an  
 23gr + 6mst + 48q = 69an + 8py + 12H2O  
 23gr + 6fst + 48q = 69an + 8alm + 12H2O  
 gr + 2pa + 3q = 3an + 2ab + 2H2O

**results :**

$T = 600^\circ\text{C}$ ,  $sd(T) = 13$ ,  $P = 7.9$  kbar,  $sd(P) = 0.7$ ,  $cor = 0.567$ ,  $sigfit = 0.49$

## Chapter 3

# Metamorphic parageneses and P-T conditions of Precambrian-Paleozoic schists of the Çine Massif in the Anatolide belt of western Turkey. Nature of the contact schists/Proterozoic orthogneiss and geodynamic implications.

### ABSTRACT

The nature of the contact between Proterozoic orthogneiss of the Çine Massif and surrounding metasedimentary rocks of presumed Paleozoic age, representing a part of the lower units of the southern Menderes Massif of the Anatolide Belt in western Turkey is re-evaluated in light of new petrological and structural data. In the southern part of the Çine Massif, Proterozoic orthogneiss and Paleozoic metasedimentary rocks are separated by a major tectonic structure, the Selimiye shear zone, which records top-to-the-S shearing under greenschist facies conditions. In the western part of the Çine Massif, mylonitic shear zone situated at the base of the Proterozoic orthogneiss near the contact with the metasedimentary rocks shows top-to-the-N movement. Pressure-temperature conditions obtained with THERMOCALC constraints this top-to-the-N movement during a lower-amphibolite facies metamorphism. Metamorphic mineral parageneses and pressure-temperature conditions do not support a recently proposed model of high pressure-low temperature metamorphic overprinting, which implies burial of the lower units of the Menderes Massif up to depth of 30 km, as a result of closure of the Neo-Tethys. The observed parageneses and the lack of polymetamorphism within the lower Menderes Massif units, the Çine and the Selimiye nappes, are consistent with a single Barrovian-type metamorphism predating Eocene emplacement of the high pressure-low temperature Lycean and Cycladic blueschist nappes.

**Keywords:** Metamorphism, *P-T* pseudosections, Selimiye shear zone, Menderes Massif, Anatolide belt, western Turkey

### INTRODUCTION

The structural evolution and associated metamorphism of the Menderes Massif, the structurally lowest succession of nappes of the Alpine Anatolide belt of western Turkey, has been subject to ongoing controversial debates. The main problem involves the timing of amphibolite facies metamorphism of the main tectonometamorphic units that comprise the Menderes Core series, the

Proterozoic basement of the Çine Massif and the overlying Paleozoic metasedimentary Selimiye and underlying Bozdağ nappes. Related to that is the unsolved nature of the contact between these tectonometamorphic units during metamorphism.

Greenschist to lower amphibolite facies metamorphism of the Paleozoic metasedimentary units (Selimiye nappe) is constrained to the Eocene (Satır & Friedrichen, 1986; Hetzel & Reischmann, 1996). Régnier *et al.* (2003) proposed a different timing for amphibolite facies metamorphism in the Çine nappe. In the southern Çine nappe, metamorphism is coeval with that of the overlying Selimiye nappe and Tertiary of age. In the northern Çine nappe a  $566 \pm 9$  Ma old metagranite crosscutting amphibolite facies foliation is seen as evidence for Neoproterozoic age for metamorphism (Gessner *et al.*, 2001a, 2004; Ring *et al.* 2001, 2004a). In addition kinematic indicators within metasedimentary rocks of the Çine nappe show different sense of shear, top-to-the-N in north and top-to-the-S in the south (Régnier *et al.*, 2003). The discussion in Régnier *et al.* (2003) has revealed that this interpretation, based on existing evidence, is far from satisfactory. The main concern is that there is no convincing evidence for polymetamorphism in the Menderes Massif, except in eclogite enclaves within orthogneiss affected by an amphibolite facies metamorphism and localized retrograde greenschist facies overprinting (Candan & Dora, 1993; Whitney & Bozkurt, 2002; Régnier *et al.*, 2003). Bozkurt & Park (1994, 1997) argued for a single Barrovian-type metamorphic event, the so-called Main Menderes Metamorphism, that overprinted Proterozoic basement and overlying Paleozoic sedimentary rocks during Eocene thrusting of HP–LT units onto the underlying core series. However, timing and cause of Barrovian-type metamorphism and its relation with Eocene HP–LT metamorphism remain a conjecture (Rimmelé *et al.*, 2003).

The nature of the contact between the Proterozoic basement and the overlying Paleozoic metasedimentary rocks has been interpreted as either tectonic, termed the Selimiye shear zone (De Graciansky, 1966; Ring *et al.*, 1999a; Gessner *et al.*, 2001a; Régnier *et al.*, 2003), or intrusive (Bozkurt *et al.*, 1993).

The incentive of this study is to develop a geodynamic model of the Menderes Massif and the Anatolide belt by differentiating timing and origin of metamorphism. An extensive data base already exists through studies by Evirgen & Ataman (1982), Evirgen & Ashworth (1984), Ashworth & Evirgen (1984, 1985), Candan & Dora (1993), Whitney & Bozkurt (2002). Our own research in the northern and southern Çine Massif (Régnier *et al.*, 2003) is augmented by additional detailed structural and petrological studies of the western Çine Massif near Lake Bafa, which connects the previously studied areas, and representative areas of the eastern part near Karacasu (Figs. 1-3). The contact between Proterozoic basement and Paleozoic cover units is especially well exposed in the

western Çine Massif.  $P$ - $T$  conditions were then calculated with the program THERMOCALC (Powell *et al.*, 1998) and compared with a previous study (Régnier *et al.*, 2003).

The new structural data and thermobarometric results are discussed with existing data and previously postulated tectonometamorphic models. We will propose a new synthesis of the evolution of the Menderes Massif based on a succession of parageneses from the greenschist to amphibolite facies metamorphism through the contact of the orthogneiss with the surrounding metasedimentary rocks.

## GEOLOGICAL SETTING

The Anatolide belt of western Turkey comprises three major tectonometamorphic units (Figs. 3-1 & 3-2). From top to bottom it includes the Lycian nappes and the İzmir-Ankara suture zone with the Bornova Flysch Zone, as the uppermost unit, comprising ophiolitic mélange and Late Paleozoic to Mesozoic rift succession deposited during opening of the northern branch of the Neo-Tethys ocean (Collins & Robertson, 1999; Stampfli, 2000). The middle unit includes the Cycladic blueschist unit composed of Mesozoic metabauxite-bearing platform carbonates and metaolistostrome. Both units were affected by a single HP-LT metamorphic event resulting from the closure of the Neo-Tethys (*sensu lato*, northern branch) during the Late Cretaceous to Eocene, and were subsequently thrust southward along the Cyclades Menderes thrust onto the structurally deepest tectonometamorphic unit, the Menderes core series (Oberhänsli *et al.*, 1998, 2001; Sherlock *et al.*, 1999; Collins & Robertson, 2003; Rimmelé *et al.*, 2003).

The Menderes core series has been interpreted as an Eocene out-of-sequence stacking of nappes that includes from top to bottom, the Selimiye, the Çine, the Bozdağ and the Bayındır nappes (Fig. 3-1 & 3-2) (Ring *et al.*, 1999a; Gessner *et al.*, 2001a; Régnier *et al.*, 2003). The Selimiye nappe comprises low-grade phyllite, metapelite, calc-schist, metamarl, marble and quartzite of locally (within low-grade phyllites) Paleozoic age (Devonian to Carboniferous; Schuiling, 1962; Çağlayan *et al.*, 1980). The Selimiye nappe experienced a greenschist to lower amphibolite facies metamorphism in the Eocene (Sattir & Friedrichen, 1986; Hetzel & Reischmann, 1996; Régnier *et al.*, 2003).

Underlying the Paleozoic metasediments of the Selimiye nappe are deformed orthogneiss, weakly deformed to undeformed metagranite of the Çine Massif, forming the Çine nappe. Interlayered mica schist and sillimanite-bearing paragneiss, partially migmatized, as well as enclaves of eclogite also occur (Schuiling, 1962; De Graciansky, 1966; Hetzel & Reischmann, 1996; Oberhänsli *et al.*, 1997; Loos & Reischmann, 1999; Candan *et al.*, 2001; Dora *et al.*, 2001). The metasedimentary rocks display amphibolite facies metamorphism and, eclogites show amphibolite facies metamorphic

overprinting (Schuiling, 1962; Ashworth & Evirgen, 1985; Oberhänsli *et al.*, 1997; Dora *et al.*, 2001; Ring *et al.*, 2001; Gessner *et al.*, 2001a; Régnier *et al.*, 2003). The intrusion age of the orthogneiss is assigned to the late Proterozoic, 560–540 Ma (Hetzl & Reischmann, 1996; Hetzel *et al.*, 1998; Loos & Reischmann, 1999; Gessner *et al.*, 2004).

Structurally underlying the Çine nappe are metapelites of the Bozdağ nappe with intercalated metapsammite, marble, amphibolite and eclogite of unknown age (Candan *et al.*, 2001). The Bozdağ and Çine nappe locally form klippen on low-grade phyllite, quartzite, and marble of the Bayındır nappe (Figs. 3-1 & 3-2). Deformation within the Bayındır nappe shows consistent top-to-the-S sense of shear (Ring *et al.*, 1999a; Gessner *et al.*, 2001a). Recent discovery of rudist fossils assigns the protolith age of the Bayındır nappe to the late Cretaceous (Özer & Sözbilir, 2003), constraining top-to-the-S shearing and lower greenschist facies metamorphism at the base of the core series to the Tertiary or younger (Fig. 3-1 & 3-2).

The Bozdağ and Çine nappes display amphibolite facies metamorphism associated with top-to-the-N shearing, whereas Selimiye nappe is characterized by greenschist to lower amphibolite facies metamorphism, respectively, coeval with top-to-the-S shearing. All nappes are affected by greenschist facies top-to-the-S shear bands. Amphibolite facies metamorphism is assigned to the Proterozoic, due to a SHRIMP zircon age of  $566 \pm 9$  Ma obtained from a metagranite crosscutting the penetrative amphibolite facies foliation in orthogneiss (Gessner *et al.* 2001a, 2004). The stacking of the nappes would occur during the Tertiary under lower greenschist facies conditions (Gessner *et al.* 2001a, 2004).

## **STRUCTURAL STUDY AND NATURE OF CONTACT BETWEEN ORTHOGNEISS AND METASEDIMENTARY ROCKS**

### **Southern Selimiye area: summary of main conclusions of chapter 2**

Determining the nature of the contact between orthogneiss of the Çine nappe and metasedimentary rocks of the Selimiye nappe is complicated by the uncertainty of the correlation of the metasedimentary rocks immediately north of the Selimiye nappe. Régnier *et al.* (2003) assigned metasedimentary rocks outcropping east of Lake Bafa to Çine nappe due to a late Proterozoic metagranite crosscutting the schistosity. Bozkurt *et al.* (1993) describe intrusive relationships near the village of Selimiye. These intrusions are weakly deformed and situated near the orthogneiss, implying preservation of Proterozoic intrusive relationships (Hetzl & Reischmann, 1996; Loos & Reischmann, 1999). However, original intrusive contact between metasedimentary rocks and orthogneiss do not

lead to the conclusion that the observed amphibolite facies metamorphism is of contact metamorphic origin and related to the intrusion.

In the orthogneiss of the Çine nappe foliation strikes N–S, approximately perpendicular to the WNW–ESE-striking schistosity observed in the Selimiye nappe, indicating the presence of an important disharmonic structure (De Graciansky, 1966; see also paragraphe 2 & fig. 2-2a). Synkinematic garnet porphyroblasts in equilibrium with chloritoid, biotite and chlorite in schist of the Selimiye nappe indicate top-to-the-S shearing during prograde metamorphism. An increase of  $P$ – $T$  conditions toward the contact with the orthogneiss, from greenschist to amphibolite facies, and a jump of 2 kbar and *c.* 100 °C across the contact between the Selimiye and the Çine nappes are recognized (Régnier *et al.*, 2003). Régnier *et al.* (2003) proposed that the contact between both nappes is originally of tectonic origin, and occurred along the Selimiye shear zone. Subparallelism of the shear zone, mineral isograds and the main schistosity within the Selimiye nappe, correlated with a top-to-the-S sense of shear, indicates that the Selimiye shear zone has been likely initiated during metamorphism. However jump of the  $P$ – $T$  conditions mentioned above evidence mainly a post-peak metamorphism movement throughout the Selimiye shear zone.

From a metamorphic point of view, mapped mineral isograds involve the following reactions in the KFASH and KFMASH system: Fe-chlorite  $\rightleftharpoons$  Fe-chloritoid + annite and biotite + chloritoid  $\rightleftharpoons$  garnet + chlorite.  $P$ – $T$  estimations yield 350–500 °C and 4–5 kbar toward the Selimiye shear zone and observed parageneses correlate with Barrovian-type metamorphism, prograde normal ( $P$  and  $T$  increasing together) on the erosional level (Ashworth & Evirgen, 1984). These  $P$ – $T$  conditions are in contrast to those encountered within the Çine Massif near the orthogneiss and behind the Selimiye shear zone, or further north south of Korçalı, where metasedimentary enclaves in orthogneiss contain staurolite–biotite–kyanite (+ garnet) paragenesis, corresponding to  $P$ – $T$  conditions of *c.* 9 kbar and 650 °C in the KFMASH system (Régnier *et al.*, 2003). The prograde character of amphibolite facies metamorphism during regional top-to-the-N shearing is supported by the presence of chloritoid–staurolite inclusions in garnet (Régnier *et al.*, 2003).

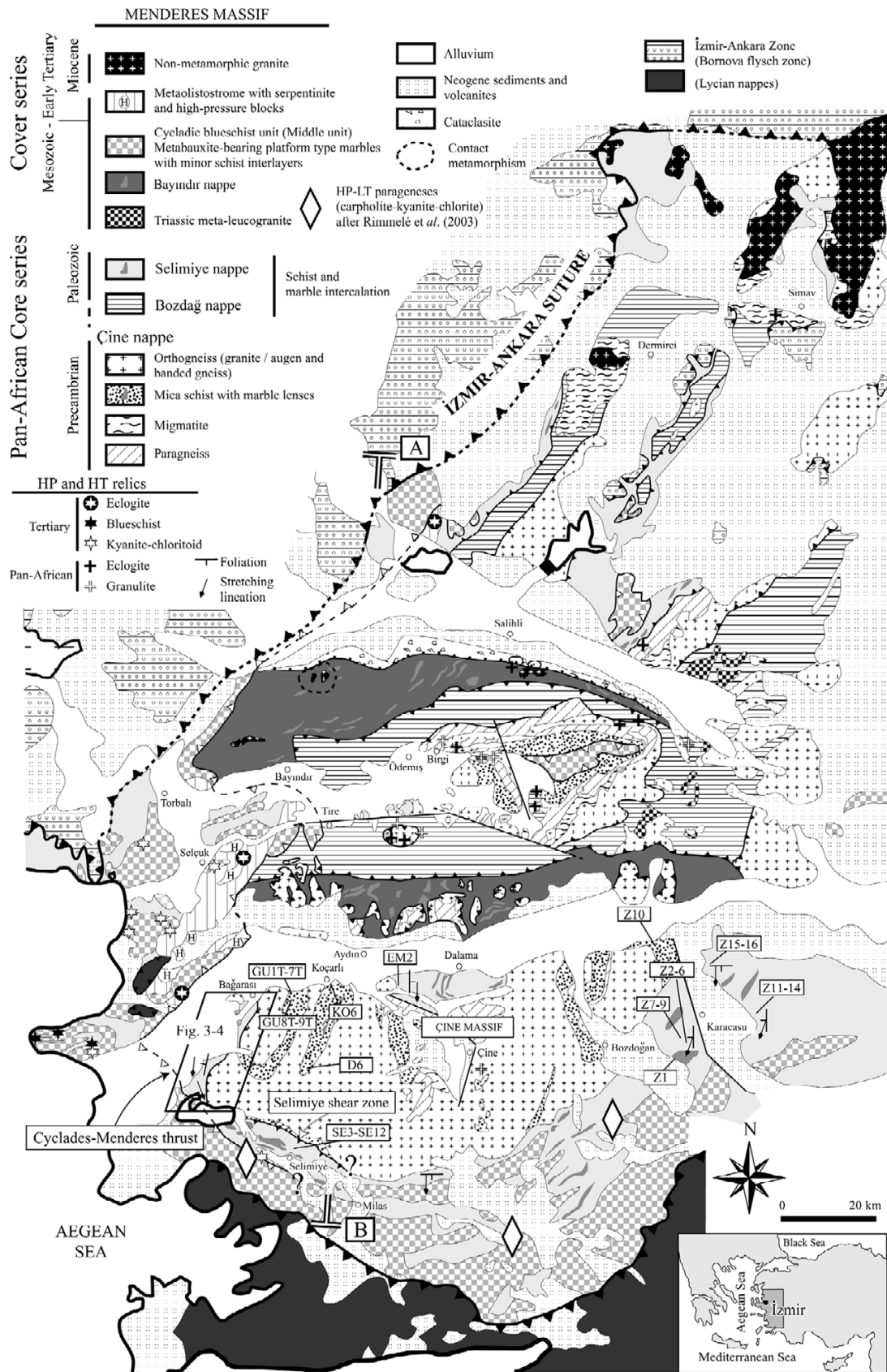


Fig. 3-1. Generalized geologic map of the Menderes Massif in western Turkey modified after Candan & Dora (1998) and Gessner *et al.*, (2001a). Sample localities are shown. Detailed map of Figure 3-4 (western Çine massif) is localized by the box. AB depicts location of cross section in Figure 3-2.

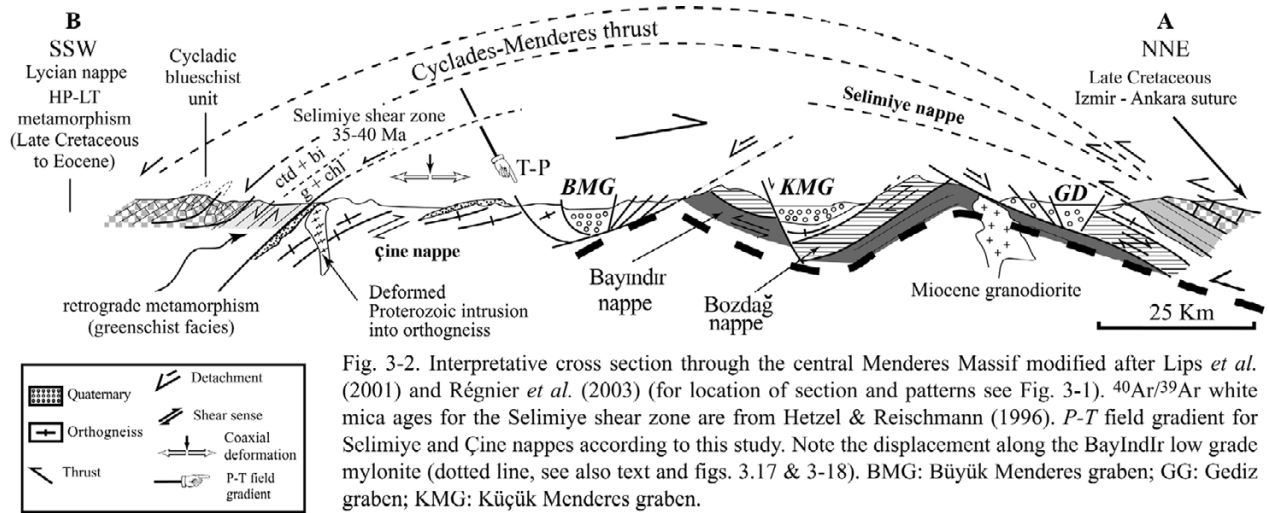


Fig. 3-2. Interpretative cross section through the central Menderes Massif modified after Lips *et al.* (2001) and Régnier *et al.* (2003) (for location of section and patterns see Fig. 3-1).  $^{40}\text{Ar}/^{39}\text{Ar}$  white mica ages for the Selimiye shear zone are from Hetzel & Reischmann (1996). *P-T* field gradient for Selimiye and Çine nappes according to this study. Note the displacement along the Bayındır low grade mylonite (dotted line, see also text and figs. 3.17 & 3-18). BMG: Büyük Menderes graben; GG: Gediz graben; KMG: Küçük Menderes graben.

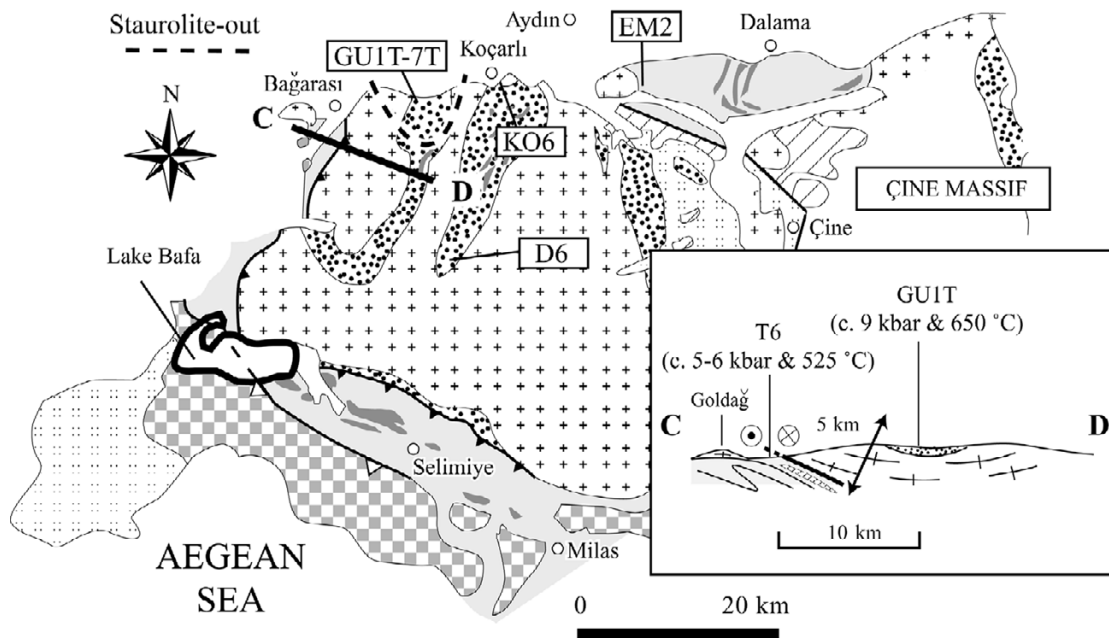


Fig. 3-3. Location and sketch of cross section CD (for patterns see Fig. 3-1). The isograd staurolite-out has been represented. Structural distance between T6 and GUIT is estimated around 5 km (perpendicular to the main foliation).



## Western area

In the western part of the Çine Massif the contact between Proterozoic orthogneiss and assumed Paleozoic schists is best exposed (Figs. 3-1, 3-3 & 3-4). North of Lake Bafa, orthogneiss is also present within metasedimentary rocks along the same foliation trend (Fig 3-4, samples YE9-YE11). There, Late Cretaceous metacarbonates overlying Paleozoic schist were overprinted by Eocene HP–LT metamorphism (Özer *et al.*, 2001; Rimmelé *et al.*, 2003). The contact between Cycladic blueschist and underlying metasedimentary rocks is tectonic near Lake Bafa (Fig. 3-4).

The Cross section CD (Fig. 3-3) displays the structural position of the orthogneiss compared to the surrounding metasedimentary rocks and will be discussed below. The regional strike of the foliation in the orthogneiss is N–S oriented and folded by large-scale N-trending syn- and antiforms. Foliation in the metasedimentary rocks possesses a similar orientation (Fig. 3-4, cross section HG), except northeast of Çalıköy where NW-trending folds affect the schistosity. Stretching lineation in the metasedimentary rocks are NNE-trending in the northern part of the study area, SSE-trending in the southern part around Bafa Lake, while mostly NNE in the orthogneiss.

In metasedimentary rocks a complex deformation has been observed at the outcrop scale. Sigmoid quartz aggregates and greenschists S-C' fabrics indicate a predominant top-to-the-SSW sense of the shear in the most western part (Sample R1 & R8 Figs. 3-5a & 3-5b). In the northern part near the orthogneiss metasedimentary rocks show mainly top-to-the N structures again expressed by sigmoid quartz pebbles (Fig. 5c). Boudinage foliation is also widespread. All metasedimentary rocks are affected by top-to-the-S greenschists shear bands (Fig. 5c).

Near the metasedimentary rocks–orthogneiss contact and at the base of the orthogneiss, strongly deformed orthogneiss to mylonitic fabric are localized in a *c.*100 m thick zone. The mylonitic deformation is expressed in the orthogneiss as a linear alignment of fine recrystallized feldspar grain and quartz (Fig. 3-5d) and decimeter-sized NNE-trending tourmaline porphyroblasts (Fig. 3-5e). A boudinaged foliation has also been observed within the mylonite (Fig. 3-5f). When preserved C/S-fabrics on feldspar indicate top-to-the-north sense of the shear (Fig. 3-5g). Similar deformation, albeit less intense, is observed in the upper structural levels of the orthogneiss (Gessner *et al.*, 2001a). As for the metasedimentary rocks, top-to-the-S greenschist facies shear bands overprint preliminary top-to-the-N fabrics within mylonite (Figs. 3-5g & 3-5h). Near Goldağ peak the orthogneiss thrust via the same mylonite over the metasedimentary rocks which are folded into a recumbent SSW-verging antiform, consistent with apparent top-to-the-SSW movement (Fig. 3-4, cross section HG & fig. 3-6a). However the polarity and the short limb are unknown leading to a speculative interpretation (see below).

The microstructure in thin section observations has shows the same complex deformation within metasedimentary rocks. In the western most part, garnet inclusion trails in albite in pelitic gneiss show consistent top-to-the-S sense of shear (Fig. 3-6b). Contrasting shear criteria has been found near the orthogneiss within metasedimentary rocks. There, helicitic staurolite in textural equilibrium with chloritoid and chlorite, shows top-to-the-N movement (Sample T6, fig. 3-7a). Within the mylonite, mica fish also indicate top-to-the-N sense of shear (Sample GU8, Fig. 3-6c). Thin section observations revealed, as observed at the outcrop scale, top-to-the-S shear bands (Sample TE2, Fig. 3-6d).

A secondary  $S_2$  crenulation cleavage associated with NNE-trending foldings, overprints the primary  $S_1$  schistosity (Figs. 3-4 & 3-6e). Occasionally centimetric recumbent NNE-trending folds, subparallel to stretching lineation, affect metasedimentary rocks. Folds are interpreted as resulting from younger deformation that postdates juxtaposition of the orthogneiss and metasedimentary rocks.

**Legend**

*Mesozoic:*

- Cycladic blueschists unit

*Paleozoic / proterozoic ? :*

- marble
- Metasedimentary rocks (greenschist to lower amphibolite facies) (schist / calcshist / quartzite / marble intercalation)

*Neoproterozoic:*

- Orthogneiss & associated strike foliation
- Mica schist with marble lenses (amphibolite facies)

*Foliation dip angle:*

- 0-30°
- 31-61°
- > 61°

*stretching lineation:*

- dip angle: 0°
- 1-30°
- > 30°

*fold axis:*

- T gradient
- syncline
- anticycline
- anticycline recumbent
- sense of shear
- Strongly deformed to mylonitic contact
- pseudo-isograd (garnet-in)

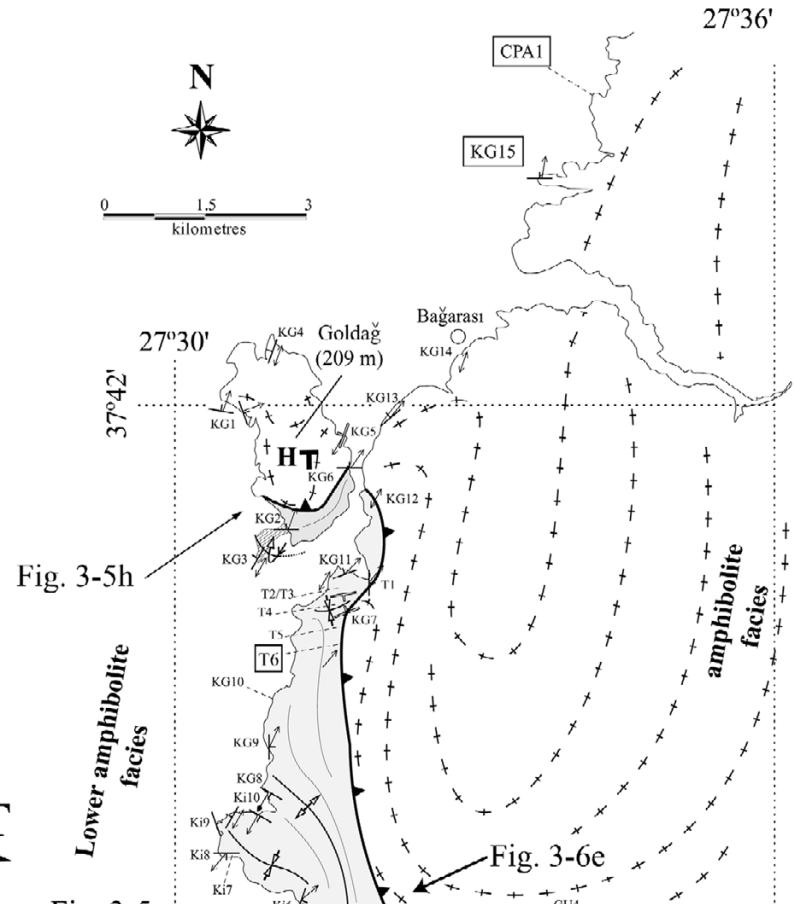
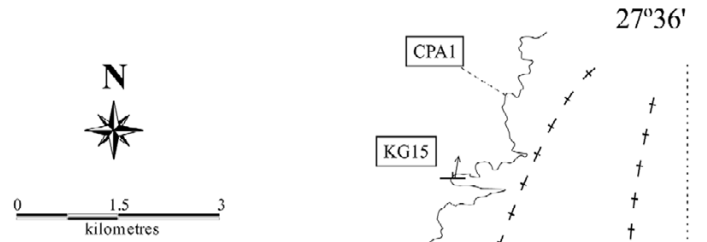


Fig. 3-5h

Fig. 3-5c

Fig. 3-6e

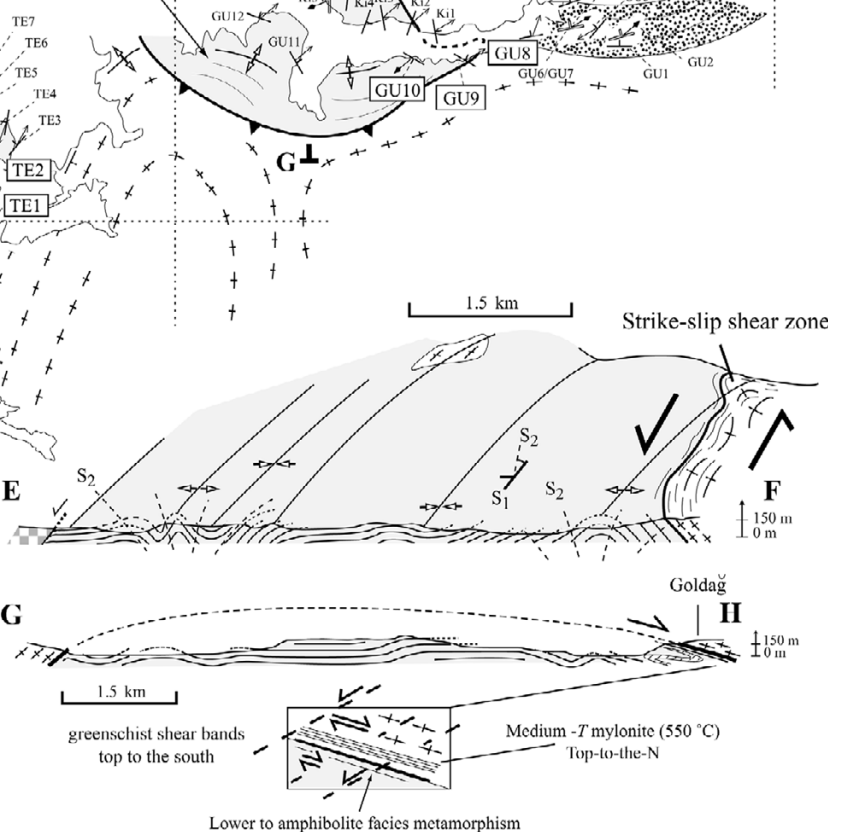
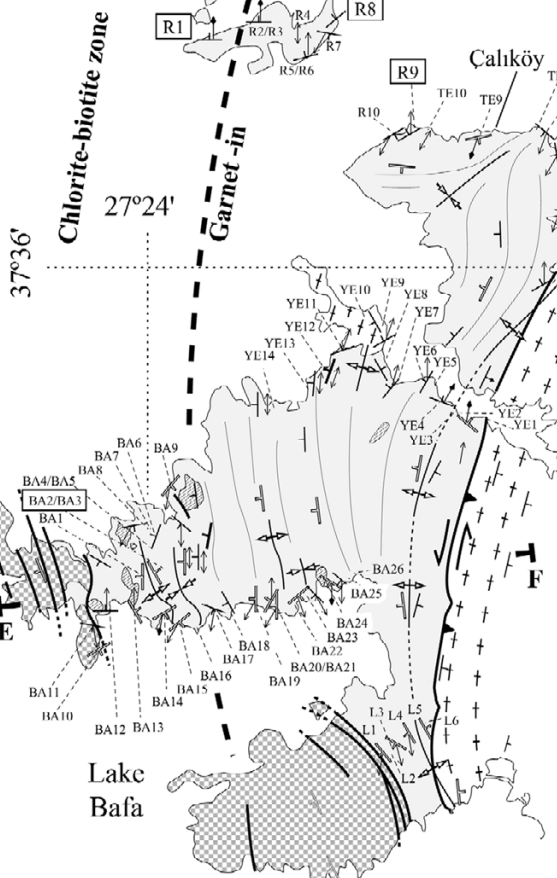


Fig. 3-4. Structural map of the western Menderes Massif between Bağarası and Lake Bafa modified after Schuiling (1962) and Taskin (1981). Localities of samples and figures are shown. Cross sections show the geometries of the contact between the orthogneiss of the Çine nappe and metasedimentary rocks along different directions. Temperature gradient and approximative metamorphic zones are also shown. Garnet-in isograd is considered as a “pseudo-isograd” since garnet occurrence strongly depends on bulk composition of samples (see discussion in text).

### **Northern and Eastern area**

In the northern part of the Çine Massif, metasedimentary rocks in enclaves in orthogneiss (south of Korçalı), has been described in detail by Régnier *et al.* (2003) (see also chapter 2). Synkinematic porphyroblasts revealed mainly top-to-the-N sense of shear. However, top-to-the-S fabrics are not absent and often associated with foliation boudinage and coaxial deformation (see fig. 2-6c). Nevertheless, we concluded that sense of shear overall was top-to-the-N in accord with the deformation in the orthogneiss.

In the area west of Dalama, north of Çine, within the northern central Çine Massif (Fig. 3-1), inclusion trails in rotated garnets in metasedimentary rocks (Sample EM2) are consistent with top-to-the-S sense of shear (Fig. 3-6f). Mineral parageneses, top-to-the-S fabrics and *P-T* conditions discussed latter in this work are similar to those found in the Selimiye nappe in the southern part.

In the eastern part of the Çine Massif reconnaissance mapping has shown that stretching lineations and folds overprinting the primary schistosity, associated with a  $S_2$  schistosity, have nearly the same trend as in the western part of the study area (Fig. 3-1). There, parageneses and rotated garnets record top-to-the-S shearing (Fig. 3-7c)

### **Primarily conclusions on structural observations**

In the western part of the Çine Massif, the mylonite near the contact orthogneiss/metasedimentary rocks is crucial for understanding the dynamics of this structurally complex area. Mylonitic orthogneiss contains evidence of a strong deformation during top-to-the-N movement. Presence of stretching-parallel tourmaline megablasts indicate the participation of an important fluid influx during this event. There is no disharmonic structure between orthogneiss and surrounding metasedimentary rocks and at least in the northern part shear sense criteria in metasedimentary rocks corroborate displacement of the orthogneiss northward. The geometry of the mylonite show special features. Indeed, in the southern part near Lake Bafa, the mylonite can be seen as a strike-slip shear zone whereas in the northern part the foliation is nearly horizontal overlying metasedimentary rocks (Fig. 3-4). Shear sense indicators are therefore consistent with overall

movement top-to-the-N and thrusting of orthogneiss over metasedimentary rocks (Fig. 3-6a). In this context apparent top-to-the-S thrusting near Goldağ peak is misleading (Fig. 3-6a).

The mylonite zone is however only expressed within orthogneiss and no evidence for a mylonite within metasedimentary rocks has been found. Moreover the presence of top-to-the-SSW criteria in the SW part (north of Lake bafa) complicate matters. One could conclude that two tectonic events have affected metasedimentary rocks in this area. However lack of mylonite within metasedimentary rocks support the idea of synkinematic mineral growth uniquely during top-to-the-N thrusting and loss of fluid. Mineralogic growth always results in volume increase and loss of fluid during prograde metamorphism. Thus, different senses of shear are interpreted as being due to strain partition rather than due to several deformation events. Note that top-to-the-SW criteria seems limited to the area where strike-slip shear zone is developed. Therefore first postulate that top-to-the-N thrusting is coeval with metamorphism everywhere within metasedimentary rocks even in the SW. Lack of disharmonic structures support this assumption but a detailed metamorphic study is necessary to constraint deformation history (see below). Finally all structure is overprinted by top-to-the-S greenschist shear bands.

Metasedimentary rocks in the northern part and eastern part show consistent top-to-the-S sense of shear and are likely correlated with metasedimentary rocks of the Selimiye nappe from a tectonic and metamorphic point of view (see below).

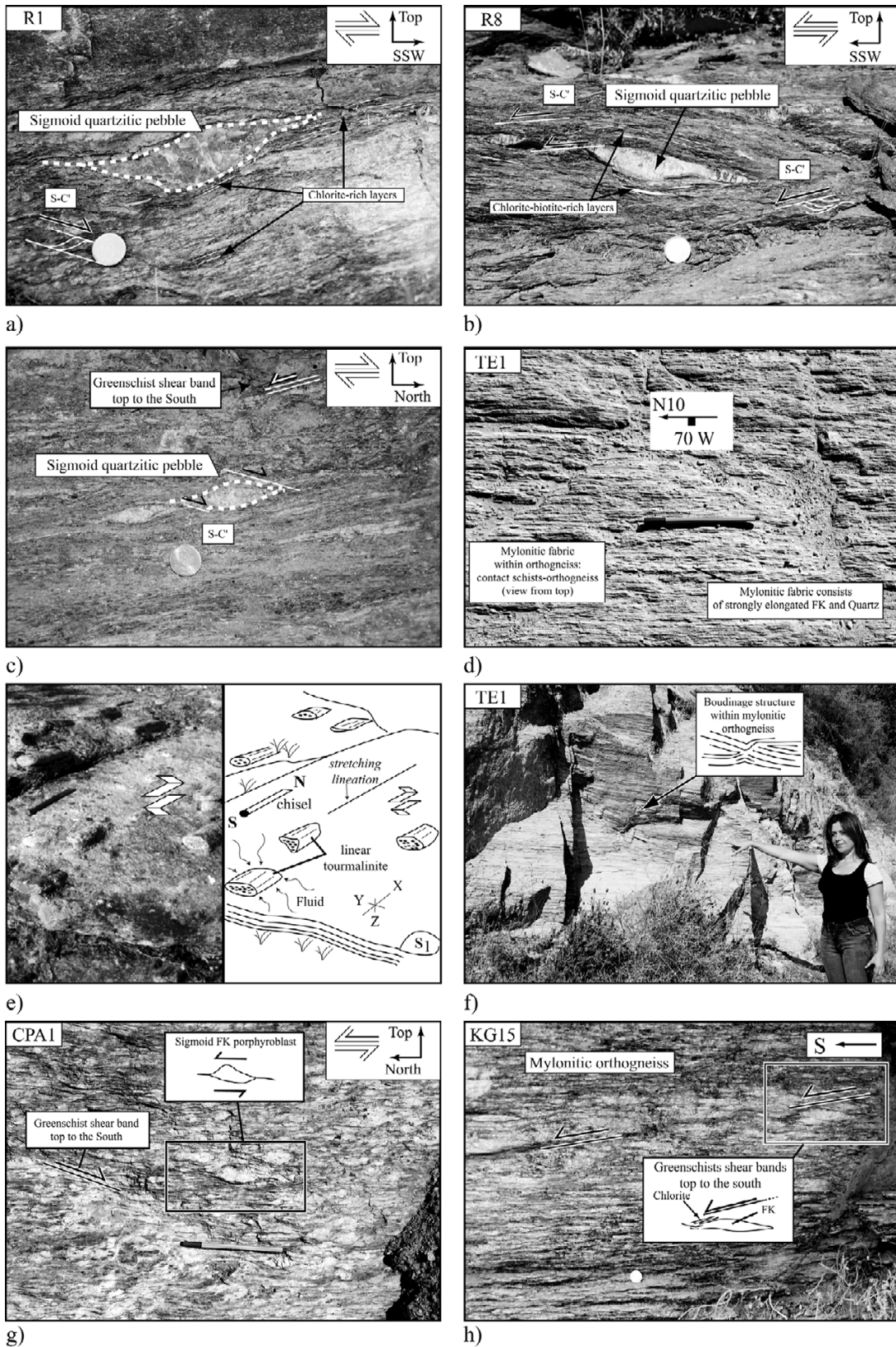


Fig. 3-5. Structural character of metasedimentary rocks and orthogneiss in the western Çine Massif. (a) Sample R1. Field photograph of sigmoid quartzitic pebble consistent with a top-to-the SSW movement. Note the presence of S-C' structure. (b) Same observation for the sample R8. (c) Contrasting top-to-the-N sigmoid quartz pebble within metasedimentary rocks near the orthogneiss. Note the presence of top-to-the-south greenschists shear bands. See figure 3-4 for location. (d) Field photograph of mylonitic orthogneiss near the contact with metasedimentary rocks (TE1). View from the top. (e) Field photograph and sketch showing parallel alignment of tourmalinite megablasts with mineral stretching lineation. Near the western margin of the orthogneiss. Chisel for scale. Sens of shear deduced from thin section. See figure 3-4 for location. (f) Field photograph of boudinage foliation within mylonitic orthogneiss. (g) and (h) Top-to-the-N sigmoid FK porphyroblast and associated top-to-the-S greenschist shear bands.

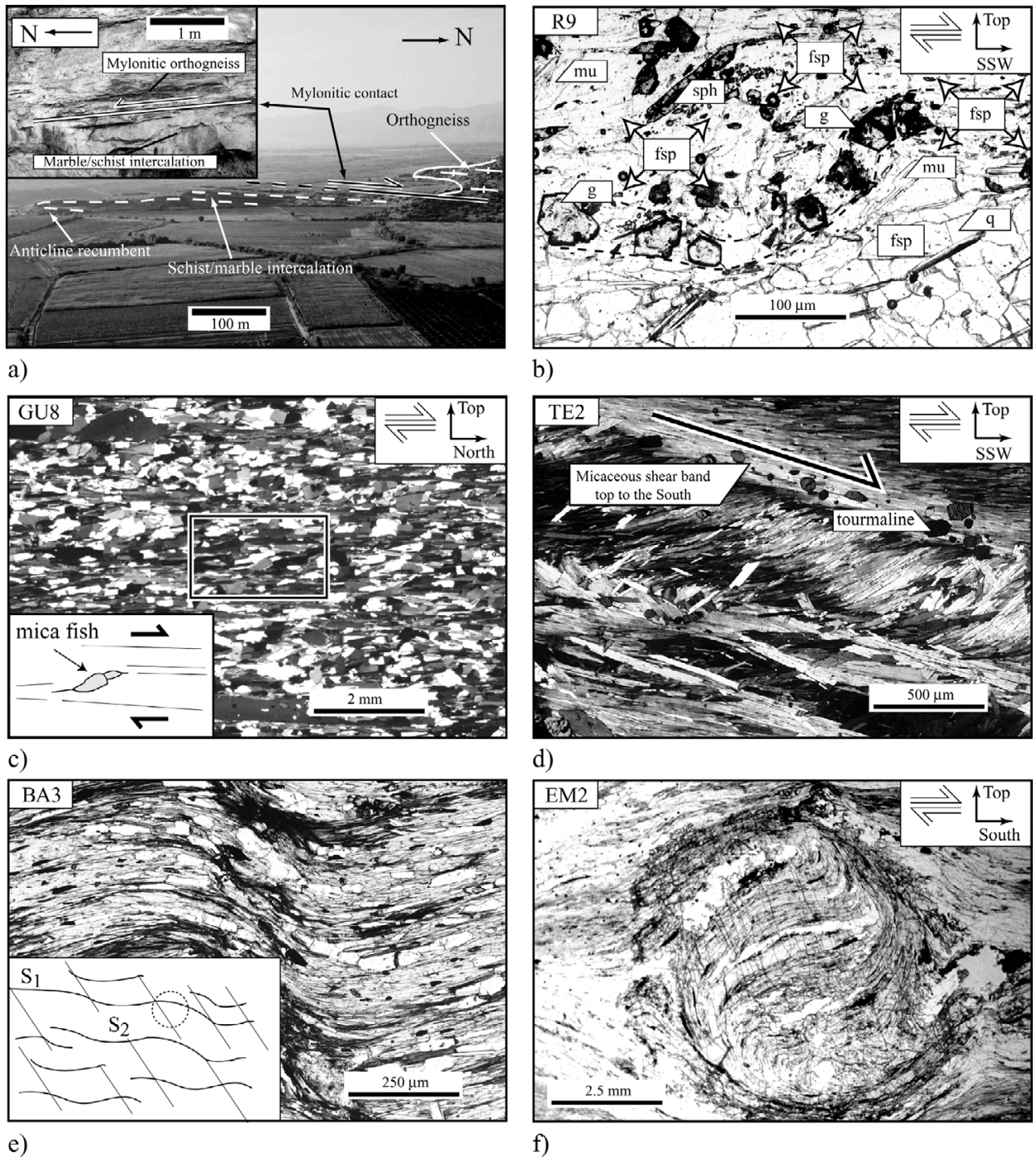


Fig. 3-6. Structural character of metasedimentary rocks and orthogneiss in the Çine Massif. (a) Field Photograph near Goldag peak. Mylonitic contact between orthogneiss and metasedimentary rocks. See figure 3-4 for location (b) Photomicrograph of schist from the western Çine Massif (R9) shows garnet inclusion trails in plagioclase (albite) with top-to-the-SSW sense of shear. Plane polarized light (PPL). (c) Photomicrograph of micaceous quartzite of the Çine nappe (GU8) shows mylonitic fabric with mica fish indicating top-to-the-N shearing. XPL. (d) Photomicrograph of mica schist near the contact with the orthogneiss (TE2). Micaceous shear bands indicate top-to-SSW sense of shear. Crossed polarized light (XPL). (e) Photomicrograph of schist from the western Çine Massif north of Lake Bafa (BA3). Crenulation cleavage  $S_2$  overprints main  $S_1$  schistosity. XPL. (f) Photomicrograph from metasedimentary rocks of the central Çine massif west of Dalama (EM2). Large garnet porphyroblast with helicitic inclusion trails indicate dextral, top-to-the-S rotation. PPL.

## SCOPE OF THE METAMORPHIC STUDY AND ANALYTICAL PROCEDURES

For this study 150 samples were analyzed, the bulk of which was collected in the western part of the Çine Massif near Lake Bafa (Fig. 3-1 & 3-4). Twelve samples were collected in the eastern Çine massif part near Karacasu (Fig. 3-1). Mineral parageneses do not allow a very precise mapping of mineral isograds. Meanwhile  $P$ - $T$  conditions of individual samples are estimated with the help of pseudosections calculated with THERMOCALC software (version 3.2.1). We used an internally consistent thermodynamic data set of Holland & Powell (1998) updated in May 2001. In addition, pressure and temperature estimations have been correlated with the phengitic substitution in muscovite (Wei & Powell, 2003, 2004).

Mineral analyses were obtained with a Jeol Superprobe (JXA 8900RL) undertaken at Johannes Gutenberg-Universität Mainz, Germany. The following operating conditions were applied: acceleration voltage of 15 kV, beam current of 15 nA, 20 s counting time per element. The following standards were used: wollastonite (Ca, Si), corundum (Al), pyrophanite (Ti), hematite (Fe), MgO (Mg), albite (Na), orthoclase (K), tugtupite (Cl), F-phlogopite (F), Cr<sub>2</sub>O<sub>3</sub> (Cr), rhodochrosite (Mn) and ZnS (Zn). Matrix correction was done with a ZAF procedure. The mineral analyses are considered to be accurate within a range of *c.* 3% (relative) on any given grain. Mineral formulae have been calculated using AX software (Holland, 2000) and are shown in Table 3-1. The remains of the rock chip used for the thin section was used for whole rock XRF analyses, also done in Mainz, to ensure maximum correlation between microprobe analyses and pseudosection calculations. Whole rock XRF analyses are given in wt % and normalized to mol % with Fe<sub>2</sub>O<sub>3</sub> recalculated to FeO<sub>total</sub> (Table 3-2). Mineral abbreviations used in text, figures and tables are adopted from Powell *et al.* (1998): als: aluminosilicate, amph: amphibole, and: andalusite; bi: biotite, cd: cordierite, chl: chlorite, ctd: chloritoid, ep: epidote, fsp: plagioclase, g: garnet, ilm: ilmenite, ky: kyanite, mu: muscovite, q: quartz, sill: sillimanite, sph: sphene, st: staurolite, zo: zoisite. Sample localities are shown on maps on Figures 3-1 and 3-4. Mineral parageneses are listed in Appendix 2 and activity models used for THERMOCALC calculations are described in Appendix 3.



## MINERAL CHEMISTRY OF METASEDIMENTARY ROCKS OF THE ÇİNE MASSIF

Garnets, attaining up to 5 mm in size, with exceptional grains exceeding one centimetre in diameter, are commonly almandine-rich ( $X_{alm}$  60–90) in both metapelites and calc-schists (Régner *et al.*, 2003). Other components vary in abundance: Mg ( $X_{prp}$  1–10), Mn ( $X_{sps}$  1–10) and Ca ( $X_{grs}$  2–30). Most garnet grains lack zoning (Sample EM2, Fig. 3-8a). If present, characteristic zoning patterns for garnets of the Çine Massif, sample KO6 from a metasedimentary enclave in the orthogneiss near Korçalı, show core to rim decrease of Ca and Mn and an increase of Mg and Fe (Fig. 3-8b). Similar zoning patterns are observed in samples from metasedimentary rocks of the Selimiye nappe near Selimiye (Sample SE12, Fig. 2-9a), and are further reported by Ashworth & Evirgen (1984) and Whitney & Bozkurt (2002).

Garnet inclusions in albite from a pelitic gneiss, common in the eastern part of the Çine Massif, display different zoning pattern, with core to rim increase in Ca and Fe, while Mn decreases and Mg remains constant (Sample R9, Fig. 3-8c) (Appendix 2). Ashworth & Evirgen (1984) reported similar patterns. In the metasedimentary units adjacent to the orthogneiss garnets are commonly retrograded to chlorite and pinitite (Fig. 3-7c, Appendix 2), while garnets from metasedimentary enclaves within the orthogneiss appear less altered. Similarly, biotite from the metasedimentary rocks is commonly chloritized (Ashworth & Evirgen, 1984). Primary chlorite occurs in most of the sample but secondary chlorite is ubiquitous crosscutting the main foliation or replacing garnet during kelyphytisation (e.g. sample Z12).

Muscovite forms a solid solution between paragonite, muscovite, celadonite and Fe-celadonite. As discussed in the following sections the phengitic substitution (Si content in T1 site) provides additional information for constraining pressure or temperature conditions of the parageneses studied.

Chloritoid is in textural equilibrium with biotite and chlorite (Samples SE3, T6, Z9; Figs. 2-4a, 3-7b, 3-7d), garnet-biotite–chlorite (Samples SE12, EM2, GU9, Z13; Figs. 2-4b, 3-9a & 3-9b), staurolite–chlorite (Sample T6; Fig. 3-7a), and as inclusion in garnet (Samples D6, EM2, GU9, GU10, KG3, KG6, Ki6, KO6, Z12; Figs. 3-9b, 3-9c; Appendix 2). On the basis of 6-oxygen structural formula, the mole fraction of Mg increases toward the orthogneiss from 0.135 ( $X_{Mg} = 0.135$ ) to 0.213 ( $X_{Mg} = 0.213$ ) for metasedimentary rocks of the Selimiye nappe (Régner *et al.*, 2003). In the western part (Samples T6, GU10, GU9) and in the eastern part (Sample Z12) mole fraction of Mg ranges from 0.16 to 0.19 ( $X_{Mg}$ ) (Table 1). There is no significant difference in the mole fraction of Mg between chloritoid as inclusion in garnet and at  $T_{max}$  (textural equilibrium in matrix). In the metasedimentary enclaves of the orthogneiss chloritoid inclusions in garnet have Mg-values up to 0.225 ( $X_{Mg}$ ) (Sample D6, Régner *et al.*, 2003).

Plagioclase composition is near albitic in lower grade rocks, and oligoclase–andesine at higher metamorphic grades (Table. 2-2 & 3-1). Significant zoning of plagioclase, oligoclase core and andesine rim, has been observed solely in calc-schists (Régnier *et al.*, 2003) but has been reported by Whitney & Bozkurt (2002) in metapelite. Furthermore, oligoclase is observed in apparent textural equilibrium with albite (peristerite gap, Ashworth & Evirgen, 1985; Régnier *et al.*, 2003).

Staurolite is in textural equilibrium with chloritoid and chlorite at  $T_{\max}$  in the western part of the Çine Massif (Sample T6; Fig. 3-7a). In a previous study, Régnier *et al.* (2003) have reported staurolite–chloritoid paragenesis (textural equilibrium) as inclusions in garnet south of Korçalı, but never at  $T_{\max}$  (c.f. in matrix). A small porphyroblast of staurolite is observed in equilibrium with chlorite and garnet (Sample GU10; Fig 3-9c). In both cases staurolite is enriched in Zn ( $\approx$  5 wt %). In comparison, a staurolite from the schist enclaves south of Korçalı has a significantly lower Zn content ( $\sim$  0.2 wt %) (Sample KO6 ; Fig. 3-1, Table 3-1).

Kyanite is a common phase in the schist enclaves south of Korçalı in metapelite (Sample D6; Régnier *et al.*, 2003), in equilibrium with staurolite–biotite (+ garnet). Sample GU1T provides the key paragenesis kyanite–biotite–garnet (without staurolite, fig. 3-5d). This study reports the first observations of kyanite in equilibrium with muscovite–ilmenite in the surrounding metasedimentary rocks (Selimiye nappe, samples Z7, Z8; Fig. 3-7d).

Amphibole in calc-schists near Selimiye is in equilibrium with garnet–biotite–zoisite–muscovite–plagioclase–chlorite–carbonate (Whitney & Bozkurt, 2002; Régnier *et al.*, 2003). Actinolite has been described within low-grade calc-schists near Milas (Fig. 3-1, Ashworth & Evirgen, 1985). In addition, near Çalıköy small calcic amphibole porphyroblasts were observed as inclusions in plagioclase in pelitic gneiss (Samples R9, TE9; Appendix 2). In the metasedimentary enclaves south of Korçalı amphibolite mostly consist of calcic amphibole and biotite ( $\pm$  epidote  $\pm$  sphene) (Samples GU4T, GU6T, GU8T, GU9T; Appendix 1). The compositional range of amphibole is shown on a Si vs. Mg/(Mg+Fe<sup>2+</sup>) diagram after Leake *et al.* (1997). Sample R9 plots near the transition ferrohornblende–magnesianhornblende, whereas sample GU6T is located near the transition magnesianhornblende–tschermakite indicating a higher Al content on the T1 tetrahedral site (Fig. 3-10; Table 3-1). Similar composition as in GU6T has been observed near the orthogneiss north of Selimiye (sample A11, Fig. 2-9f).

Zoisite and clinozoisite are common epidote phases in the calc-schists. Epidote also occurs in metapelite enriched in Fe<sup>3+</sup> and Ca (Samples T6, Z12, Appendix 2). Common accessory minerals are sphene, ilmenite, hematite, rutile, tourmaline, apatite and zircon. Some samples, e.g Z12, contain stilpnomelane overgrowing the main foliation, as a result of retrograde metamorphism or alteration.

## IMPLICATIONS OF MINERAL COMPOSITION AND PARAGENESES

The similar zoning patterns in garnets of the metasedimentary rocks of the Selimiye nappe and enclaves in the Çine orthogneiss has also been observed in the central Menderes Massif near Ödemiş (Ashworth & Evirgen, 1985). In some samples bulk rock chemistry controls zoning. The low Mg content of sample R9 is reflected in constant low Mg abundance across the grain. Ashworth & Evirgen (1984) also suggested that slow diffusion within plagioclase grains acting as hosts to garnets inclusions suppressed zoning.

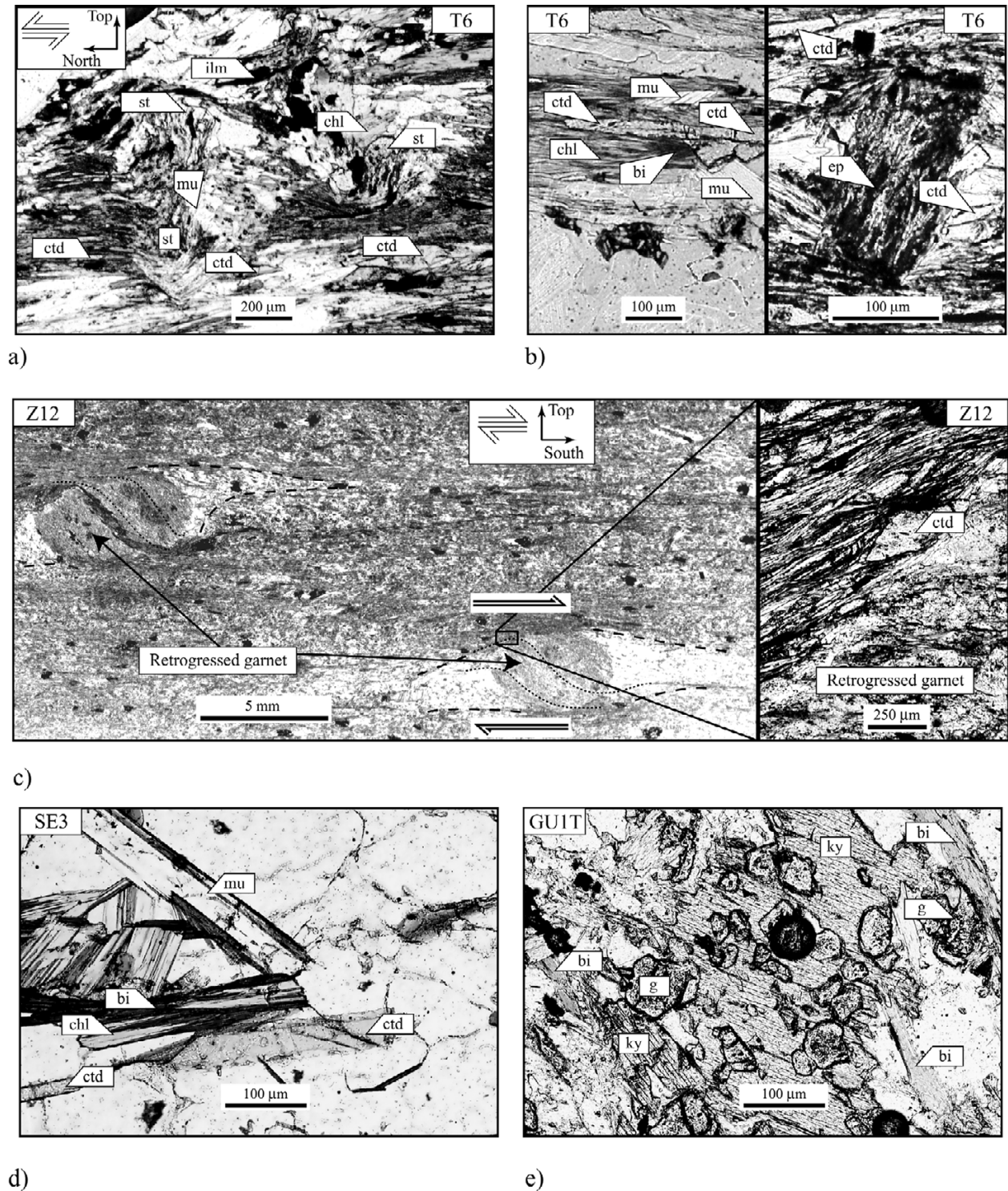
The relatively high abundance of Zn in synkinematic staurolite porphyroblasts is interpreted as preferential partition of Zn into staurolite, due to lack of suitable cation sites in other phases, rather than concentration in a relic grain during prograde metamorphism (Goodman, 1993). Zn-content may have stabilized staurolite at lower temperatures than pure Fe-staurolite, evident in sample GU10 where staurolite is in equilibrium with garnet and chlorite (Soto & Azañón, 1994). Indeed, in pure KFMASH system, the paragenesis staurolite–chlorite–garnet results from the breakdown of chloritoid (Spear & Cheney, 1989; Powell *et al.*, 1998). But nearby sample GU9 contains abundant chloritoid in equilibrium with garnet. However, staurolites of GU10 and T6 still contain enough Fe that its relative high Zn content likely does not have any effect on temperature calculation beyond the uncertainties of the thermodynamic data base (Worley & Powell, 2000).

The occurrence of garnet–biotite–kyanite paragenesis in metasedimentary enclaves south of Korçalı (sample GU1T) indicates conditions above 630 °C and 8 kbar in KFMASH system (Spear & Cheney, 1989; Powell *et al.*, 1998). Other parageneses in metasedimentary enclaves include biotite–kyanite–staurolite, conspicuously lacking chloritoid at  $T_{\max}$ . In contrast, the metasedimentary rocks east of the Çine Massif are characterized by chloritoid stable in the kyanite field (Sample Z7 & Z8).

The presence of chloritized biotite in low-grade metapelites complicates classic thermodynamic considerations. The projection of biotite in AFM diagram (+ mu + q + H<sub>2</sub>O) is so not suitable and misleading, preventing accurate paragenetic analysis via microprobe analyses.

The presence of actinolite in low-grade calc-schist, of hornblende (*sensu lato*) near the orthogneiss (Samples R9 & A11), or within upper amphibolite facies metasedimentary rocks (Samples GU5T, GU6T), shows a correlation with the Al content in the T1 tetrahedral site of calcic amphibole, expressed in the decreasing Si-number in the formula (Samples R9, GU6T; Fig. 3-10, Table 3-1). Due to the non-isobaric erosion level of this study area, the Al content in the T1 tetrahedral site can not easily be correlated with an increase of pressure or temperature, as proposed in models by Johnson & Rutherford (1989) and Blundy & Holland (1990). However, the Al content in the T1 site appears in

good agreement with the general increase of the  $P-T$  conditions through the orthogneiss (Régnier *et al.*, 2003).



The sequence of mineral parageneses in the metapelitic rocks around the Çine Massif displays always the same pattern: Chlorite–biotite (likely in kyanite stability field, cf sample Z7 and Z8) at low-grade, followed by chlorite–biotite–chloritoid or chloritoid–staurolite–chlorite, and garnet–biotite–chloritoid–chlorite at higher grade (Ashworth & Evirgen, 1984). These mineral isograds have been precisely mapped by Régnier *et al.*, (2003) in the Selimiye nappe. In the western part of the Çine Massif isograds mapping is nearly impossible because of the lack of suitable critical parageneses. However parageneses observed (Appendix 2) allow to proposed three main metamorphic zones: a chlorite-biotite zone, a garnet zone (lower amphibolite facies) and an amphibolite facies zone near the orthogneiss, more or less correlated with occurrence of staurolite in the sample GU10 (Fig. 3-4). This mapping is just given here in first approximation. Indeed, occurrences of garnet, staurolite, chloritoid and kyanite are controlled by the whole rock chemistry (c.f Al<sub>2</sub>O<sub>3</sub>, Mn content). Conspicuously absent in the metasedimentary rocks around the Çine Massif are cordierite–andalusite and garnet–cordierite parageneses (which are typical of a contact-type metamorphism). This strengthens evidence for a barrovian-type metamorphism. Similar Barrovian metamorphism and associated sequences of parageneses have been reported from the central Menderes Massif around Ödemiş (chloritoid, staurolite–kyanite, sillimanite, kyanite) by Evirgen & Ataman (1982), and south of Dermici (staurolite–andalusite–garnet–biotite, staurolite–garnet–kyanite–sillimanite, garnet–kyanite–sillimanite–biotite) by Candan & Dora (1993) .

Index minerals, the sequence of mineral parageneses, the paragenesis staurolite–chloritoid at  $T_{max}$  around the Çine massif and as inclusion in garnet of the metasedimentary enclaves, all point to a single metamorphism event affecting metasedimentary rocks of the Selimiye and Çine nappes. In accordance to Whitney & Bozkurt (2002) and Régnier *et al.* (2003) there is no evidence for polymetamorphism in the Menderes massif. This would imply similar ages for lower to upper amphibolite facies metamorphism.

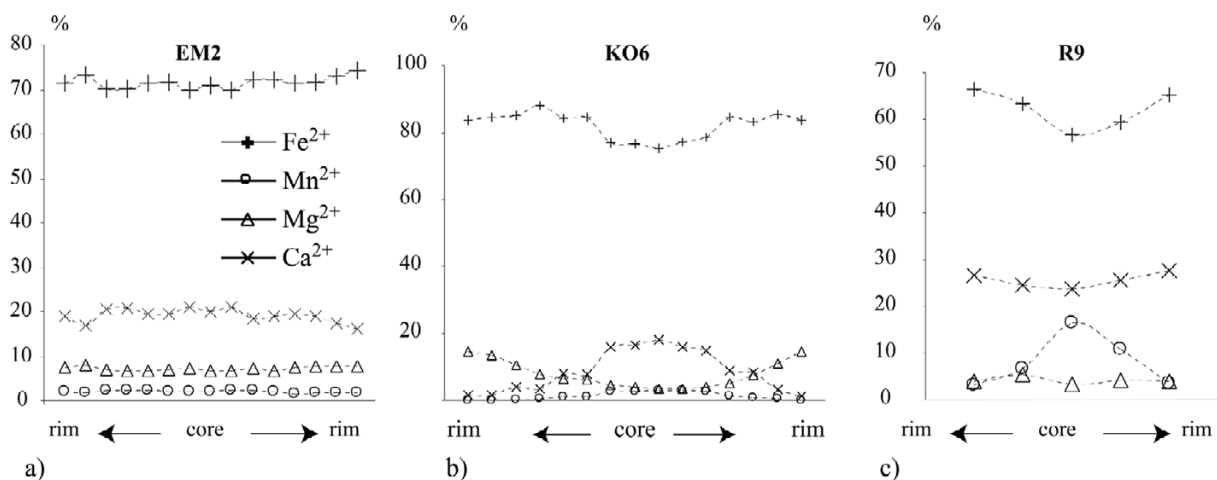


Fig. 3-8. Representative compositional transects of garnets of the Çine Massif. a) EM2 from the Selimiye nappe of the central Çine massif. b) KO6 from the metasedimentary enclave within the orthogneiss of the Çine nappe near Korçalı. c) R9: garnet inclusion in plagioclase from the western Çine Massif.

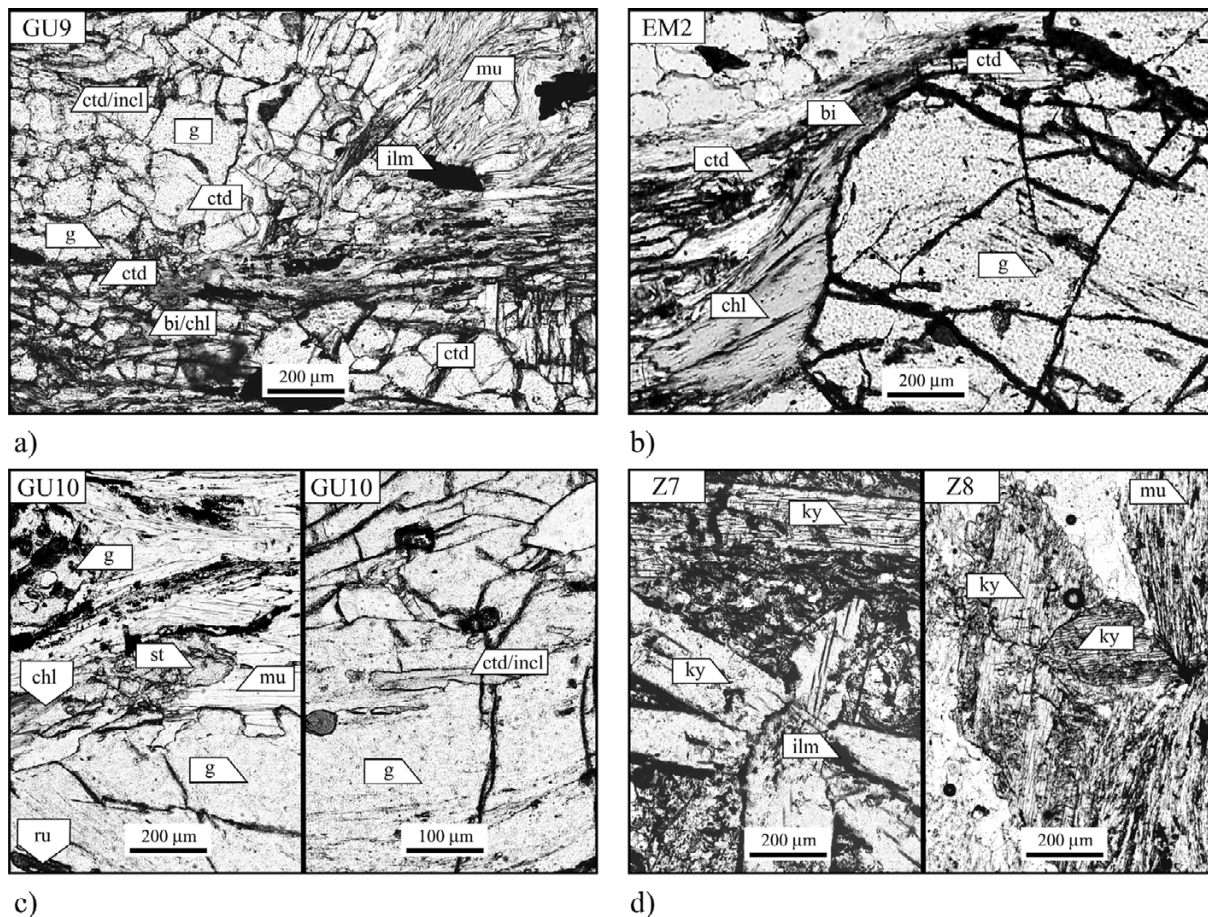


Fig. 3-9. Photomicrographs of mica schist samples from locations of Çine Massif. a) Sample GU9 (western zone): garnet-chlorite-biotite-chloritoid paragenesis. Chloritoid forms inclusions in garnet. Biotite and chlorite occur as traces. PPL. b) Sample EM2 (central zone): chlorite-biotite-garnet-chloritoid paragenesis. Biotite is in trace. PPL. c) Sample GU10 (western zone): staurolite-chlorite-garnet paragenesis (left) and chloritoid inclusion in garnet (right). PPL. d) Samples Z7, Z8 (eastern zone): kyanite-ilmenite-muscovite parageneses. Kyanite shown polysynthetic macles. PPL.

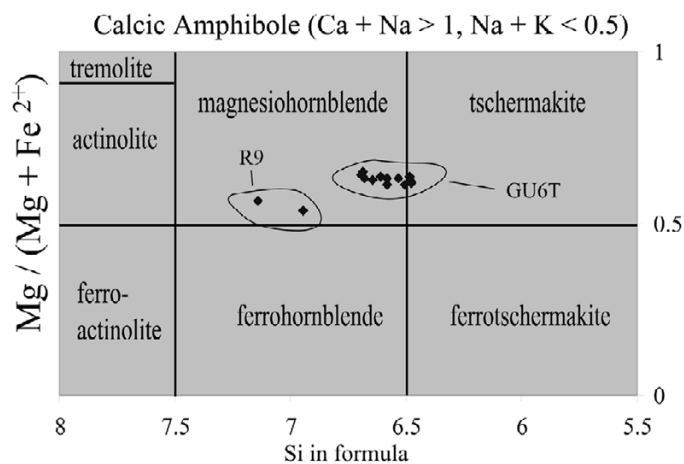


Fig. 3-10.  $Si^{total}$  versus  $Mg/(Mg + Fe^{2+})$  diagram of amphibole after Leake *et al.* (1997) of samples from the western Çine Massif (R9) and the metasedimentary enclave of the Çine nappe (GU6T). Lower amphibolite facies R9 plots near the transition ferrohornblende/magnesiohornblende and amphiboles from the upper amphibolite facies sample GU6T plots near the transition magnesiohornblende/tschermakite. The regional pressure and temperature increase correlates with Al content (8-Si) in the T1 tetrahedral site.

## PSEUDOSECTIONS AND P-T ESTIMATES

MnO is negligible on first approximation in all analysed samples lacking garnet. TiO<sub>2</sub> is relatively abundant, and mainly incorporated in ilmenite (e.g. sample SE12, Z12, Z8, T6, Table 3-1). White *et al.* (2000) show that large amounts of TiO<sub>2</sub> in metapelite have a restricted effect on KFMASH phase equilibria. Therefore, it is assumed at first approximation that all opaques are “in excess”.

Five representative samples (SE3, SE12, T6, Z12, GU1T) were selected for calculation of *P–T* pseudosections in the KFMASH (SE3), NCKFMASH (T6) or MnNCKFMASH (SE12, Z12, GU1T) systems. The NCKFMASH system is suitable in sample lacking garnet with epidote, albitic plagioclase and paragonite end-member participating in muscovite solid solution (sample T6). The MnNCKFMASH has been used when additional garnet phase occurs (SE12, Z12, GU1T). Indeed even weak additional MnO may have a strong influence on garnet growth (see below) and therefore can not be neglected (Droop & Harte, 1995; Tinkham *et al.*, 2001). XRF analyses listed in Table 3-2 show that K<sub>2</sub>O, Na<sub>2</sub>O and CaO are relatively low in the analysed samples, prohibiting usually, projection from muscovite or plagioclase in all the *P–T* space. Isopleths of phengitic substitution help in some cases to constrain pressure or temperature conditions (Wei & Powell, 2003, 2004). Additionally we used garnet isopleths (core) to constraint initial *P–T* conditions of garnet growth. For plagioclase the model 4T (Cī structure) of Holland & Powell (1992) was chosen, since the anorthite-component of plagioclase in this study does exceed An<sub>30</sub>. Other activity models used are listed in Appendix 3.

### Sample SE3

This sample from the chloritoid–biotite–chlorite zone of the Selimiye nappe north of Selimiye (Régner *et al.*, 2003) can be modelled in the KFMASH system (lack of garnet and weak participation of CaO, Na<sub>2</sub>O and MnO, Table 3-2). The high abundance of quartz (SiO<sub>2</sub> > 80 wt %) is due to the presence of quartz-rich layer in the remains of the rock chip used for the thin section. This is not problematic -from a thermodynamic point of view- since the pseudosection is projected from quartz, but we obviously lose some accuracy during XRF analysis. Within the metapelitic part of the chip, the paragenesis chloritoid–chlorite–biotite (+ mu + q + H<sub>2</sub>O) has been observed in thin section (Figs. 2-4a, 3-7d). *P–T* conditions in pseudosection for the observed chloritoid–chlorite–biotite (+ mu + q + H<sub>2</sub>O) paragenesis, are on order of 475-550 °C and 1–5 kbar (Fig. 3-11). However, the stability field size for this paragenesis may be wider because of the large uncertainties at low pressure and the failure of THERMOCALC to compute large Fe-rich field in KFMASH system (Roger Powell, written communication, 2003). Phengitic substitution (Si<sup>total</sup> in muscovite) ranges from 3.10 to 3.23 (Table 3-1) with an average around 3.15 (on 5 analyses in matrix). Therefore only the value of 3.10 for Si<sup>total</sup> in

muscovite is stable for the paragenesis observed. The AFM diagram plots whole rock composition at 4.5 kbar and 540 °C for  $Si^{total} = 3.10$  (Fig. 3-11, inset) and corresponding calculated phases. Phengitic substitutions with higher value are considered metastable. Possible interpretation is a  $P$ - $T$  path in decompression or/and heterogeneity of the bulk composition at small scale. Unfortunately chloritized biotite prevent any comparison between calculated and observed phases. However, it is interesting to note the occurrence of chlorite-chloritoid-garnet paragenesis around 5 kbar and 540 °C via the univariante reaction in KFMASH (Fig. 3-11):



Indeed, adjacent sample SE12 (see below) displays syn-kinematic garnet porphyroblasts in textural equilibrium with chlorite, biotite and chloritoid (Régnier *et al.*, 2003).  $P$ - $T$  conditions are so likely near the aluminosilicate triple point as already proposed by Régnier *et al.* (2003) but still with a large uncertainty (see also Fig. 2-10).

### Sample SE12

Sample SE12 was collected 1.5 km northward from SE3 (Appendices 1 & 2) and displays the following paragenesis: chlorite-biotite-garnet-chloritoid-muscovite-quartz (Fig. 2-4b). Plagioclase is rare ( $An_{14}$ ) and not in equilibrium with garnet or chloritoid (plagioclase-muscovite-quartz). Epidote is an accessory mineral (Table 3-1).  $P$ - $T$  conditions have been estimated via two pseudosections in NCKFMASH and MnNCKFMASH systems (Fig 3-12). In both systems, a part of pseudosections is not calculable at low  $T$  and medium  $P$ . This results from the fact that zoisite is not predicted as a stable phase. An additional phase such as paragonite-margarite and another activity model for Ca-rich plagioclase would allow us to calculate this area, but will not bring any substantial information since we are beyond the garnet stability field. In NCKFMASH the chloritoid-chlorite-garnet (+ mu + pl + q +  $H_2O$ ) paragenesis is stable around 8 kbar and 560 °C (Fig. 3-10a). In MnNCKFMASH the chloritoid-chlorite-garnet (+ mu + pl + q +  $H_2O$ ) paragenesis is stable around 6-8 kbar and 525-550 °C (Fig. 3-10b) emphasizing the importance of even small additional MnO for  $P$ - $T$  estimates. Stability of biotite with garnet, chlorite and chloritoid is not predicted in both systems. Phengitic substitution ranges from 3.00 to a maximum of 3.12 (Table 3-1), leading to maximum  $P$ - $T$  conditions around 7.5 kbar and 550 °C. However, the pressure is likely overestimated for two main reasons. Firstly, phengitic substitution average is here around 3.03 for muscovite (on 11 analyses in matrix) and so mainly correlated with low or medium pressure. Secondly, the grain size of garnets (around 0.5 cm; Fig. 2-4b) likely involves non negligible fractionation of the bulk rock composition. The lack of plagioclase in textural equilibrium with garnet may also result from fractionation of the bulk rock composition since the percentage of CaO and  $Na_2O$  in this sample is low (CaO=0.83 and  $Na_2O$ =1.54 in



mole %; Table 3-2). Ca will be mainly concentrated in garnet during nucleation and Na in muscovite (Table 3-2) preventing occurrence of plagioclase in equilibrium with garnet. Presence of sporadic paragonite may also be envisaged.

The garnet core composition from microprobe analysis yielded: almandine (68%), pyrope (5%), spessartine (5%) and grossular (22%) (Fig. 2-9a). This composition is considered as representing chemical conditions of initial garnet growth. Figure 3-12b displays calculated  $X_{\text{Fe-Mg-Ca}}$  isopleths for garnet (c.f.  $X_{\text{Fe}}=0.68$ ,  $X_{\text{Mg}}=0.05$ ,  $X_{\text{Ca}}=0.22$ ). Intersection of calculated isopleths lead to  $P$ - $T$  estimates around 8 kbar and 530 °C well correlated with maximum phengitic values. Maximum conditions of 8 kbar and 530 °C is therefore interpreted as representing  $P$ - $T$  conditions of initial garnet growth. In other words, keeping in mind a classic schema during barrovian-type metamorphism, these  $P$ - $T$  conditions would correspond to  $P_{\text{max}}$  before decompression and equilibrium at  $T_{\text{max}}$  in the matrix. We believe that  $P$ - $T$  conditions at  $T_{\text{max}}$  are likely those predicted in the KFMASH system (+ q + mu + H<sub>2</sub>O) for the univariante reaction: chloritoid + biotite Q' garnet + chlorite around 5 kbar and 540 °C (Figs. 2-10 or 3-11). The presence of biotite at  $T_{\text{max}}$  is in this case explicable. This also means that calculated pseudosections, when non negligible fractionation occurs due to garnet nucleation (whatever the system, KFMASH, NCKFMASH or MnNCKFMASH), will lead to  $P$ - $T$  conditions of initial garnet growth but unlikely those at  $T_{\text{max}}$ . Figure 3-12b shows a possible  $P$ - $T$  path for the sample SE12 (arrow) according to the remarks above.  $P$ - $T$  conditions at  $T_{\text{max}}$  are also more in agreement with the chlorite-biotite-chloritoid paragenesis observed in sample SE3 and described above.

P (kbar)

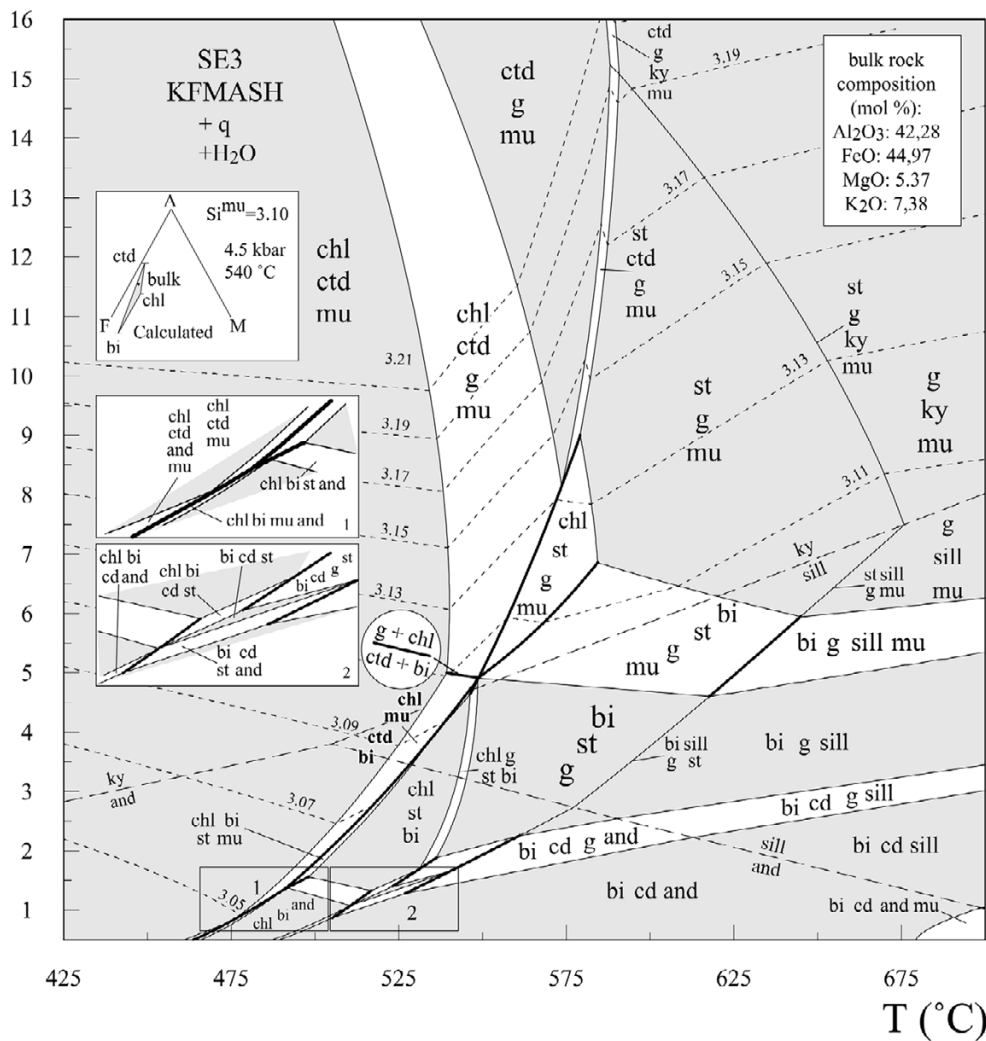


Fig. 3-11. Sample SE3 from the southern Selimiye nappe.  $P$ - $T$  pseudosection in KFMASH system (+ quartz +  $H_2O$ ) with detailed sections enlarged (insets). Note the position of the reaction  $ctd + bi = g + chl$  (using the updated (2001) data set of Holland & Powell (1998)). Phengitic substitution ( $Si^{total}$ ) ranges from 3.10 to 3.23 (Table 3-1),  $P$ - $T$  estimates for observed chlorite-biotite-chloritoid paragenesis are approximately 4.5 kbar and 540 °C for  $Si^{total}$  in muscovite = 3.10. Inset shows AFM diagram of calculated phases and bulk whole rock composition. Chloritized biotite prevent any representation of observed phase in AFM diagram. Muscovite with high Si value is considered metastable. Heterogeneity of bulk composition and/or  $P$ - $T$  path in decompression is envisaged.

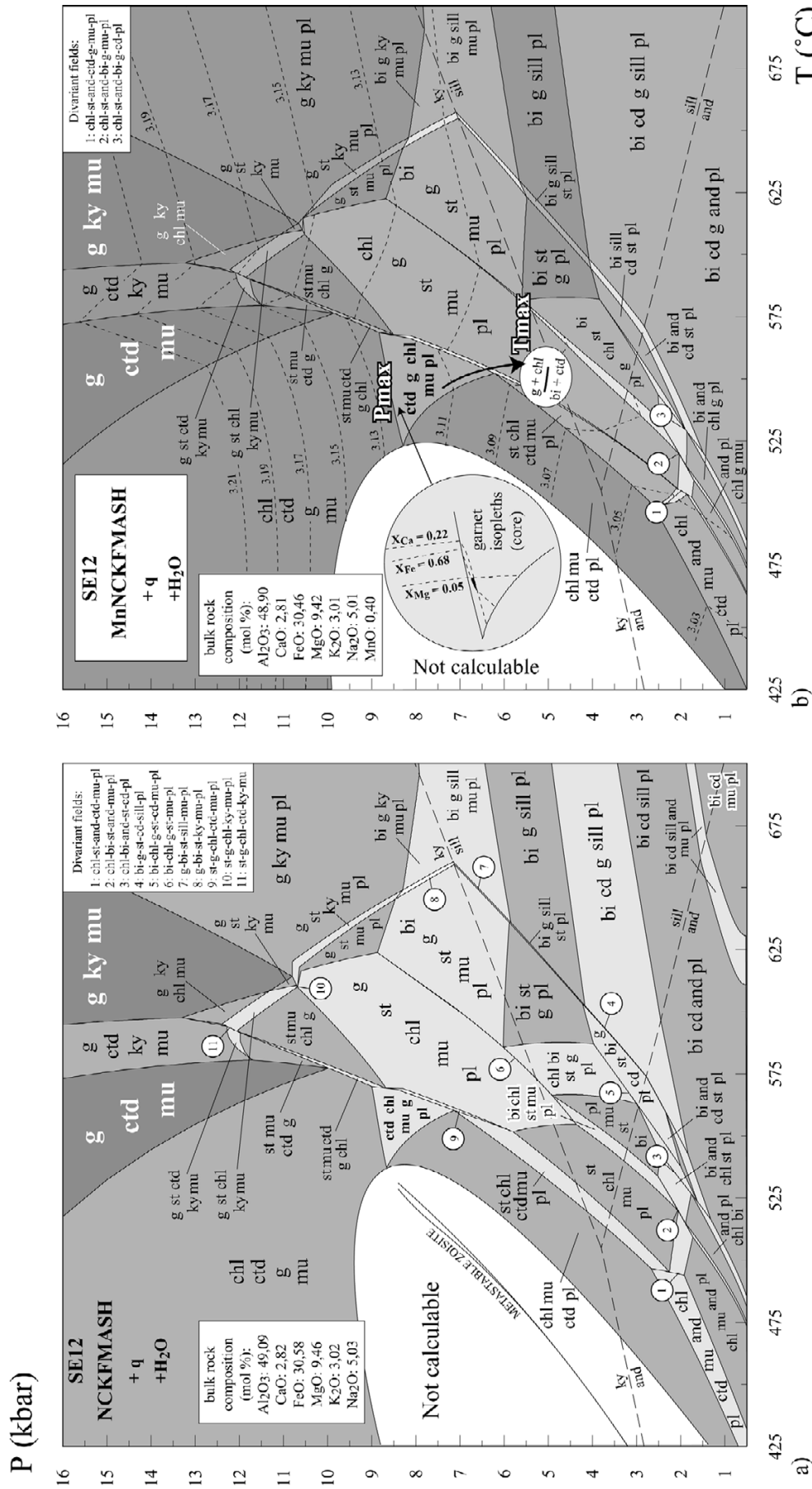


Fig. 3-12. Sample SE12 from the southern Selimiye nappe. a) *P-T* pseudosection in NCKFMASH system (+ quartz + H<sub>2</sub>O). Chloritoid-chlorite-garnet-plagioclase-muscovite paragenesis is stable around 8 kbar and 560 °C. b) *P-T* pseudosection in MnNCKFMASH system (+ quartz + H<sub>2</sub>O). Chloritoid-chlorite-garnet-plagioclase-muscovite paragenesis is now stable around 6–8 kbar and 525–550 °C. Phengitic substitution ranges form 3.00 to a maximum of 3.12 (Table 3-1), leading to maximum *P-T* conditions around 7.5 kbar and 550 °C. Approximately same *P-T* conditions are deduced from calculated/observed isopleths intersection for garnet core. Garnet growth in this sample likely involves fractionation of bulk rock composition leading to a paragenesis at *T*<sub>max</sub> more describable in KFMASH system. Pseudosection in MnNCKFMASH system is so suitable for initial *P-T* conditions of garnet growth whereas KFMASH system seems more suitable to explain the presence of biotite at *T*<sub>max</sub>. We propose a *P-T* path in decompression to explain the presence of biotite in textural equilibrium with garnet-chlorite-chloritoid in matrix.

P (kbar)

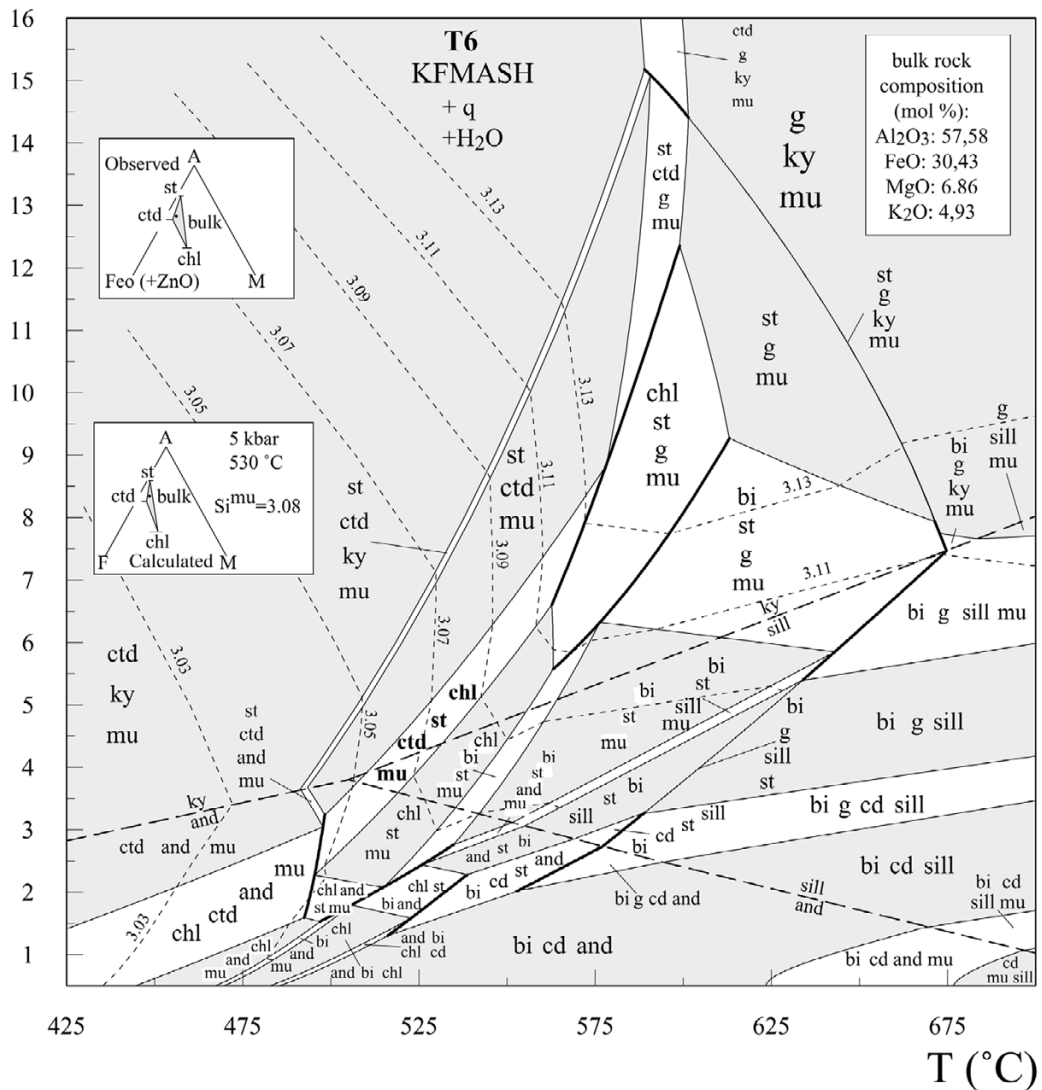
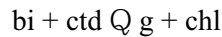


Fig. 3-13. Sample T6 from the western Çine Massif. *P-T* pseudosection in KFMASH system (+ quartz + H<sub>2</sub>O). Insets show AFM diagram of observed/calculated phases and bulk whole rock analyse. For staurolite FeO has been corrected from the amount of ZnO. Phengitic substitution ( $Si_{total}$ ) ranges from 3.00 to 3.13 (Table 3-1). *P-T* estimates for chlorite-staurolite-chloritoid are approximately 5 kbar and 530 °C for  $Si_{total}$  average in muscovite = 3.08. *P-T* pseudosection does not account for stability of observed chlorite-biotite-chloritoid paragenesis. Zoisite stability can not be calculated in this system (see Fig 3-14). Muscovite with high Si value is considered metastable. Heterogeneity of bulk composition and/or *P-T* path in decompression is envisaged.

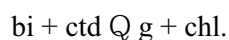
### Sample T6

This sample from the metapelitic rocks in the western part of the Çine Massif contains the following textural equilibria: chlorite–chloritoid–staurolite–muscovite–quartz, chloritoid–biotite–chlorite–muscovite–quartz, epidote–chloritoid–muscovite–quartz (Table 3-1 & Appendix 2). This sample mainly consists of chloritoid (mode of chloritoid around 80%). Plagioclase (An<sub>32</sub>) is rare and not in equilibrium with staurolite or epidote (plagioclase–muscovite–quartz). In the KFMASH

petrogenetic grid of Powell *et al.* (1998) stable parageneses chlorite–chloritoid–staurolite and chlorite–chloritoid–biotite are restricted to relatively low pressure by the reactions (see also Figure 2-10):



In the KFMASH grid of Spear & Cheney (1989) these parageneses are stable over a wider pressure range. Observations of natural assemblages corroborate the stability of chlorite–chloritoid–biotite paragenesis in andalusite and kyanite stability fields (Spear & Cheney, 1989; Likhanov *et al.*, 2001, 2004). The discrepancy between observed and calculated chlorite–chloritoid–biotite stability fields originates from the uncertainty of the location of the invariant point [cd, als] (Powell *et al.*, 1998) and the slope of the reaction  $\text{bi} + \text{ctd} \text{ Q } \text{g} + \text{chl}$ . To constrain pressure estimates the phengitic substitution of muscovite was calculated with THERMOCALC and correlated with microprobe analyses.  $\text{Si}^{\text{total}}$  in muscovite ranges from 3.00 to 3.13. Observed AFM diagram phases has been compared to calculated phases. A calculated AFM diagram using the bulk whole rock composition plots the chlorite-chloritoid-staurolite paragenesis at 530 °C and 5 kbar (Fig. 3-13), according to phengitic substitution average around 3.08 (Table 3-1). However the  $P$ – $T$  pseudosection in KFMASH does not show a stable field for chloritoid–biotite–chlorite. Possible reason is the whole rock composition which may change even at small scale. Because of the presence of plagioclase and epidote a NCKFMASH pseudosection was computed (Fig. 3-14). At moderate pressures there is little difference between KFMASH and NCKFMASH pseudosections.  $P$ – $T$  conditions for the stable chlorite–chloritoid–staurolite paragenesis are again approximately 530 °C and 5 kbar (Fig. 3-14a) and correlate well with the average of phengitic substitution ( $\text{Si}^{\text{total}} = 3.08$ ). The presence of Zn in staurolite may result in lower temperature estimates. Zoisite–chloritoid–chlorite–muscovite–plagioclase is stable at relatively high pressure for  $\text{Ab} = 70\%$  in plagioclase (Fig. 3-14b). But small scale variation of the bulk rock composition may cause the growth of epidote and plagioclase (e.g.  $\text{Fe}^{3+}$ ,  $\text{Ca}^{2+}$ ). Indeed  $\text{Fe}^{3+}$  is not taking into account in NCKFMASH system preventing any consideration about  $P$ – $T$  conditions for epidote growth. The critical paragenesis is considered to be chlorite–chloritoid–staurolite–muscovite–quartz (+ plagioclase not in equilibrium here) which corresponding to  $P$ – $T$  conditions in the kyanite field near the aluminosilicate triple point. Note that  $P$ – $T$  conditions are again near the reaction in KFMASH system:



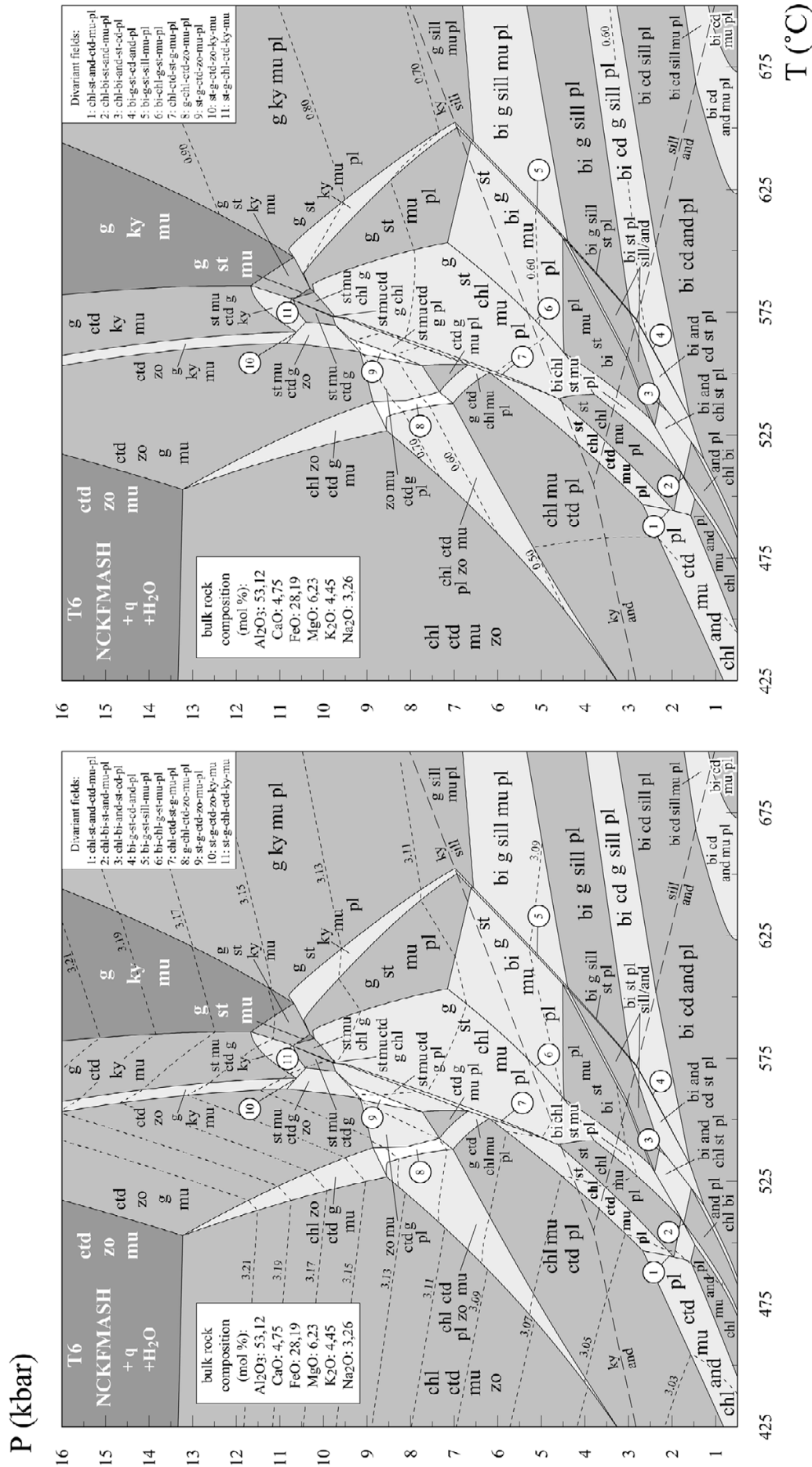


Fig. 3-14. Sample T6 from the western Çine Massif: a) *P-T* pseudosection in NCKFMASH system (+ quartz + H<sub>2</sub>O) with calculated isopleths for Si in muscovite. b) same pseudosection with calculated isopleths for plagioclase (albite content). Stability of observed chlorite-chloritoid-biotite-muscovite-quartz paragenesis is not predicted. *P-T* conditions for the stable chlorite-chloritoid-stauroilite-muscovite (+ plagioclase, not in equilibrium in thin section) paragenesis are around 530 °C and 5 kbar and correlate well with average of phengitic substitution (S<sub>total</sub> = 0.8). *P-T* conditions are so again near the reaction bi + ctd = g + chl in KFMASH system (see fig. 3-11).

## Sample Z12

This sample from the Selimiye nappe in the eastern part of the Çine Massif is characterized by strong retrogression of garnet to chlorite and pinitite (*sensu lato*). Small relics within retrogressed garnet reveal similar composition ( $X_{alm}=66$ ,  $X_{grs}=22$ ;  $X_{py}=6$ ;  $X_{spss}=5$ ; Table 3-1) to those obtained for garnet cores in SE12 or EM2 (Figs. 2-9a & 3-8a). A Possible interpretation is that Mn in core stabilize garnet at low temperature even after important retrogression. The observed parageneses are chlorite–chloritoid–garnet–biotite–muscovite–quartz and chloritoid–epidote–muscovite–quartz (Table 3-1 & Appendix 2). Chlorite and biotite occur as traces. Secondary chlorite replaces garnet during almost total kelyphitisation (pseudomorphose) at the outcrop scale. Though plagioclase was not observed in thin section, it may be present in the rock chip used for whole rock XRF analyses. With the given bulk rock composition (Table 3-2), chloritoid–garnet paragenesis without staurolite or kyanite does not exist in KFMASH system (calculated but not presented here). The more suitable system -as already noticed when garnet occurs- is in our case MnNCKFMASH (Fig. 3.15a). Biotite is still not predicted as stable phase. Then observed parageneses would correspond to the quadrivariant field: chlorite–chloritoid–garnet–zoisite (+ mu + q + H<sub>2</sub>O) without plagioclase, which ranges from 8 to 16 kbar (Fig. 3-15a). However Fe<sup>3+</sup> may stabilize epidote at medium pressure and lack of plagioclase might be due to fractionation of bulk rock composition during garnet nucleation (grain size around 0.5 cm; Fig. 3-7c). It is so difficult here to propose pressure estimate without phengitic substitution or garnet isopleths like for sample SE12. Table 3-1 displays phengitic values ranging from 3.12 to 3.17 (Si<sup>total</sup> in muscovite). This would involve pressure ranging from 7 to 10 kbar. Average of phengitic substitution in the matrix ( $T_{max}$ ) yield a value around 3.15 (on 9 analyses). The corresponding pressure would be 8.5 kbar for  $T_{max}$  temperature around 525 °C. Calculated/observed (core ?) garnet isopleths ( $X_{alm}=66$ ,  $X_{grs}=22$ ;  $X_{py}=6$ ;  $X_{spss}=5$ ; Table 3-1) yield  $P$ - $T$  conditions around 6-8 kbar and 525 °C (see intersection field; Fig. 3-15a). Finally almost total garnet kelyphitisation implies retrograde metamorphism beyond garnet field stability (large arrow; Fig. 3.15a).

## Sample GUIT

This sample from the metasedimentary enclaves in the Çine Massif SW of Korçalı contains the paragenesis garnet–kyanite–biotite and lacks staurolite (Fig. 3-7e). Muscovite only occurs as traces and oligoclase (An<sub>25</sub>, Table 3-1) is not zoned. The relative low K<sub>2</sub>O abundance prevents coexistence of biotite and muscovite everywhere in the  $P$ - $T$  space. As mentioned above  $P$ - $T$  conditions in KFMASH are likely around 630 °C and above 8 kbar (Spear & Cheney, 1989; Powell *et al.*, 1998). However, the whole rock analysis show non-negligible contents of Na<sub>2</sub>O and CaO (Table 3-2), so that a pseudosection in the MnNCKFMASH system (+ q + H<sub>2</sub>O) (Fig. 3-13b), indicates conditions of 8–9 kbar and above 630 °C according to the presence only in trace of muscovite (biotite-garnet-kyanite-

plagioclase ( $\pm$  muscovite) field). This is in good agreement with estimations of 600–630 °C and 8–11 kbar from the concomitant staurolite–biotite–kyanite zone south of Korçalı (Samples D1, D30, D42, Appendix 2). However between both zones an important isograd is crossed: the isograd staurolite-out. Indeed, corresponding univariante reaction in KFMASH system: staurolite + biotite = kyanite + garnet (Fig. 2-10) become a narrow biotite-garnet-staurolite-kyanite-plagioclase quadrivariant field in MnNCKFMASH at nearly same  $P$ - $T$  conditions.

### **Sample Z8**

This sample from the overlying metasedimentary rocks southwest of Karacasu contains synkinematic porphyroblasts of kyanite in textural equilibrium with muscovite, ilmenite and quartz (Fig. 3-9d, Appendix 2). The presence of previously unreported kyanite provides important constraints on the pressure estimation. A  $P$ - $T$  pseudosection can not be calculated since the sample lacks a suitable paragenesis in KFMASH. Whole rock analyses shows non-negligible content of  $\text{TiO}_2$  (Table 3-2), suggesting that most of FeO is incorporated in ilmenite, suppressing growth of other Al-Fe silicates. The most suitable system is likely KFMASHTO (White *et al.*, 2000). Phengitic substitution in muscovite is low ( $\text{Si}^{\text{total}} = 3.13$ , table 1) and on first approximation we assume pressure conditions similar to sample Z12.



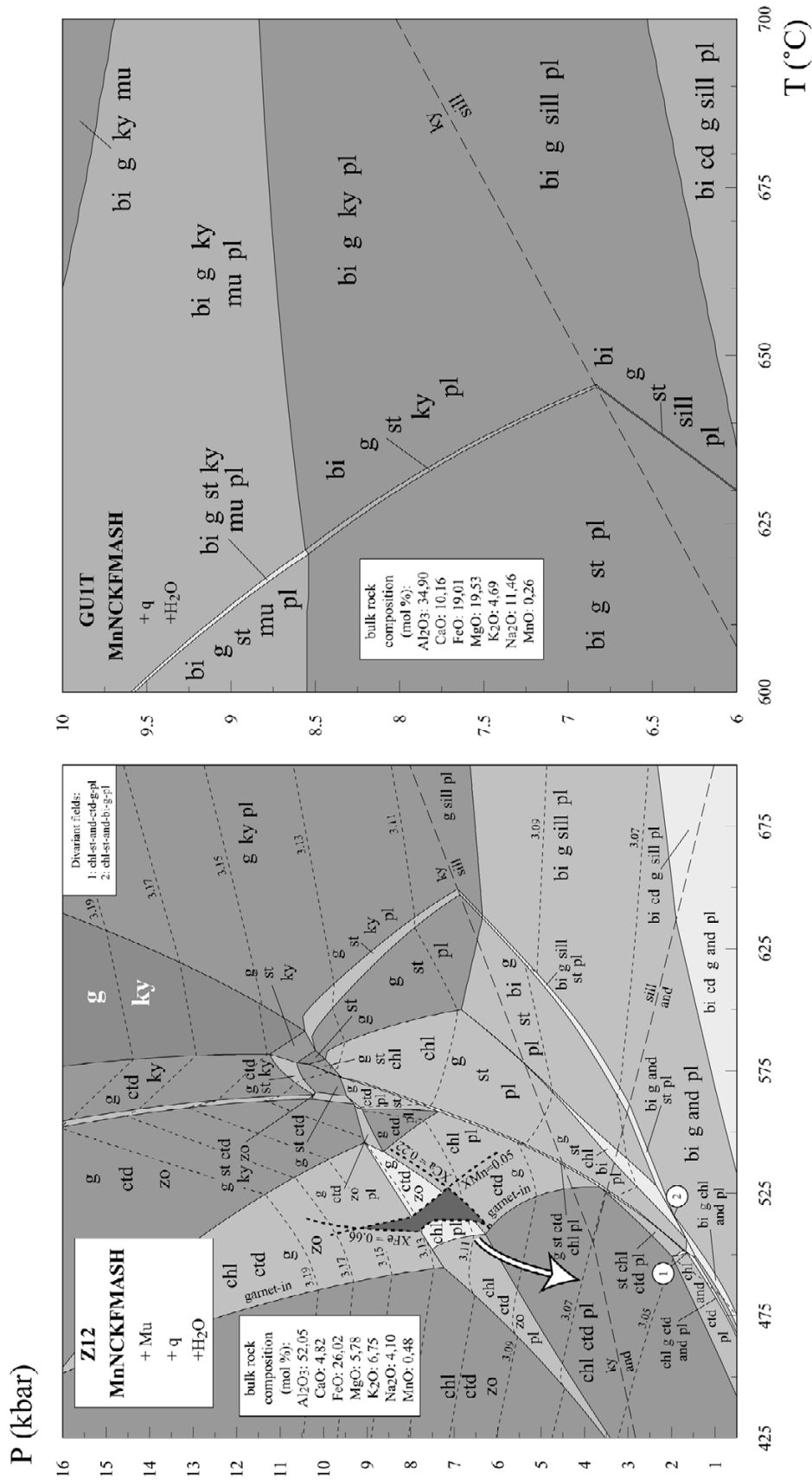


Fig. 3-15. a) Sample Z12 from the eastern Silimiye nappe near Karacasu. *P-T* pseudosection in MnNCKFMASH system (+ mu + quartz + H<sub>2</sub>O). According to the phengitic substitution average (Si<sup>total</sup> around 3.15, Table 3-1) and garnet-chloritoid-chlorite equilibrium, *P-T* estimates are on order of 8.5 kbar and 525 °C. Calculated-observed (core ?) garnet isopleths yield *P-T* conditions around 6-8 kbar and 525 °C (see intersection field). Retrogression produces almost complete kelyphitisation of garnet in chlorite-chloritoid-muscovite- (± plagioclase ± epidote) field (see arrow). b) Sample GUIT from the northern Çine nappe metasedimentary enclave. *P-T* pseudosection in MnNCKFMASH system (+ quartz + H<sub>2</sub>O). Traces of muscovite approximates pressure of 8-9 kbar at temperature above 630 °C. *P-T* estimations obtained in the staurolite-biotite-kyanite zone south of Korçali (Régner *et al.*, 2003) are so more or less similar. Note however that garnet-biotite-kyanite (± mu ± pl + q + H<sub>2</sub>O) paragenesis implies like in KFMASH system, total breakdown of staurolite (staurolite-out).

Table 3-1 (1/4). Single mineral analyses from different metamorphic zones of the Çine massif. Sample SE3: chloritoid-biotite-chlorite zone (Selimiye nappe). Sample SE12: chloritoid-garnet-chlorite zone (Selimiye nappe). GUIT : garnet-biotite-kyanite zone (Çine nappe). Samples T6, R9, GU10, GU9, & K16 (Selimiye nappe, western part). Sample Z12: garnet-biotite-chlorite-chloritoid zone (eastern part). Sample EM2: garnet-biotite-chlorite-chloritoid zone (Fig. 3-1, northern part). Mineral formulae have been calculated with AX software (Holland, 2000) except for staurolite. amph: amphibole; bi: biotite; chl: chlorite; GUIT: fsp; plagioclase; g: garnet; ilm: ilmenite; incl (fsp) inclusion in plagioclase; incl (g): inclusion in garnet; mu: muscovite; st: staurolite.

Sample	SE3	SE3	SE3	SE12	SE12	SE12	SE12	SE12	SE12	GUIT	GUIT	GUIT	T6	T6	T6	T6	T6	T6	T6	T6	T6	T6	T6	T6
Min	ctd	mu	mu	mu	chl	mu	mu	mu	fsp	g	g	g	mu	mu	mu	mu	mu	mu	chl	chl	chl	ctd	ctd	st
SiO <sub>2</sub>	24.83	46.97	48.22	48.85	37.93	24.51	44.96	47.36	47.33	59.90	38.26	38.90	37.58	61.11	61.36	47.34	45.64	45.14	24.82	23.93	24.87	24.69	28.26	
TiO <sub>2</sub>	-	0.27	0.30	0.31	0.02	0.04	0.11	0.35	0.27	0.01	0.10	0.04	1.39	0.03	0.01	0.27	0.30	0.21	0.04	0.13	-	0.10	0.23	
Al <sub>2</sub> O <sub>3</sub>	40.24	35.22	33.76	32.39	21.38	40.78	36.34	35.31	35.97	24.69	21.50	21.72	18.07	23.38	23.16	34.80	36.55	37.82	22.77	22.99	40.81	40.47	53.49	
Cr <sub>2</sub> O <sub>3</sub>	-	0.12	0.04	0.43	0.09	0.07	0.11	1.74	0.04	0.06	0.10	0.06	0.12	0.02	0.09	0.08	0.17	0.19	0.45	0.02	0.03	0.08	0.17	
Fe <sub>2</sub> O <sub>3</sub>	-	0.65	0.35	-	0.65	0.26	0.65	-	-	-	-	-	-	0.03	0.12	1.28	-	-	-	-	-	-	-	
FeO	24.57	1.36	1.65	1.95	33.89	22.74	26.31	1.11	0.97	-	30.57	30.34	14.29	-	0.49	0.85	0.72	27.86	28.03	23.33	23.40	8.53		
nO	-	-	-	-	-	Z	-	-	-	-	-	-	-	-	-	-	-	-	-	-	-	-	4.93	
MnO	0.51	0.02	0.03	-	0.93	0.10	0.06	0.01	0.03	-	1.00	0.97	0.08	0.03	0.03	-	-	0.05	0.03	0.15	0.14	0.02	-	
MgO	2.22	0.81	1.31	1.51	2.44	3.48	13.54	0.42	0.89	0.76	4.65	4.80	13.66	0.01	0.97	0.48	0.27	11.82	12.02	2.70	2.77	0.95		
CaO	-	0.09	-	0.11	4.78	-	0.01	0.06	0.01	3.01	4.25	4.59	0.05	5.20	5.27	0.03	-	0.03	0.14	0.03	0.03	0.04	0.04	
Na <sub>2</sub> O	-	1.19	0.93	0.86	0.01	0.06	1.43	1.18	1.66	9.89	0.04	0.03	0.20	8.56	8.34	0.96	1.32	1.63	0.02	0.01	0.02	0.01	-	
K <sub>2</sub> O	0.02	8.62	9.07	8.85	-	-	8.41	8.93	8.58	0.04	0.01	0.01	8.88	0.07	0.07	8.17	9.05	8.38	0.04	0.02	-	0.02	-	
Totals	92.39	95.32	95.67	95.26	102.12	92.01	88.00	95.32	95.62	97.79	100.47	101.46	94.33	98.43	98.45	94.41	94.37	94.40	88.01	87.21	91.94	91.71	96.61	
Oxygens	6	11	11	11	12	6	14	11	11	8	12	12	11	8	8	11	11	11	14	14	6	6	46	
Si	1.03	3.10	3.18	3.23	2.99	1.01	2.61	3.10	3.10	2.72	3.01	3.02	2.80	2.75	2.76	3.13	3.04	3.00	2.64	2.57	1.02	1.02	7.93	
Ti	-	0.02	0.02	0.02	-	-	0.01	0.02	0.01	-	0.01	-	0.08	-	-	0.01	0.02	0.01	-	0.01	-	-	0.05	
Al	1.96	2.74	2.62	2.52	1.98	1.98	2.87	2.74	2.78	1.32	1.99	1.99	1.59	1.24	1.23	2.72	2.87	2.96	2.86	2.92	1.98	1.97	17.70	
Cr	-	0.01	-	0.02	0.01	-	0.01	0.09	0.01	-	0.01	-	0.01	-	-	0.01	0.01	0.01	0.04	-	-	-	0.04	
Fe <sup>3+</sup>	-	0.03	0.02	-	0.04	0.01	0.03	-	-	-	-	-	-	-	-	0.06	-	-	-	-	-	-	-	
Fe <sup>2+</sup>	0.85	6.08	6.09	6.11	2.23	0.78	2.32	0.02	0.05	-	2.01	1.97	0.89	-	-	0.03	0.05	0.04	2.48	2.52	0.80	0.81	2.00	
Zn	-	-	-	-	-	-	-	-	-	-	-	-	-	-	-	-	-	-	-	-	-	-	1.02	
Mn	0.02	-	-	-	0.06	-	0.01	-	-	-	0.07	0.06	0.01	-	-	-	-	-	0.01	-	-	0.01	-	
Mg	0.14	0.08	0.13	0.15	0.29	0.21	2.13	0.04	0.07	-	0.54	0.56	1.52	-	-	0.10	0.05	0.03	1.87	1.93	0.17	0.17	0.40	
Ca	-	0.01	-	0.01	0.40	-	-	-	-	0.14	0.36	0.38	-	0.25	0.25	-	-	-	0.02	-	-	-	0.01	
Na	-	0.15	0.12	0.11	-	-	0.19	0.15	0.21	0.87	0.01	-	0.03	0.75	0.73	0.12	0.17	0.21	0.01	-	-	-	-	
K	0.00	0.73	0.76	0.75	-	-	0.72	0.75	0.72	-	-	-	0.85	-	-	0.69	0.77	0.71	0.01	-	-	-	-	
Sum	3.99	6.94	6.93	6.91	8.00	4.00	9.95	6.96	6.96	5.06	7.99	7.99	7.76	5.00	4.99	6.87	6.97	6.97	9.92	9.96	3.99	3.99	29.15	

Table 3-1 (2/4).

Sample	Min	T6	T6	T6	T6	T6	T6	T6	R9	R9	R9	R9	R9	R9	R9	R9	R9	R9	R9	Z12	Z12	Z12	Z12	Z12	Z12	Z12	Z12	Z12	Z12	Z12	Z12	Z12	Z12			
		st	st	st	st	st	ilim	ep	fsp	6.63	fsp	core	rtn	g	core	g	fsp	rim	fsp	rim	incl(fsp)	mu	amph	incl(fsp)	amph	cp	mu	mu	mu	mu	mu	chl	chl II			
SiO <sub>2</sub>	28.22	28.38	27.50	28.49	0.07	32.41	58.25	59.02	37.82	37.66	67.63	66.45	50.28	48.87	49.19	47.63	38.72	46.37	46.23	46.05	47.03	24.62	24.17													
TiO <sub>2</sub>	0.34	0.38	0.47	0.65	52.94	0.03	-	-	0.10	0.08	-	0.02	0.24	0.24	0.23	0.30	0.15	0.12	0.20	0.21	0.23	0.07	0.04													
Al <sub>2</sub> O <sub>3</sub>	54.25	53.71	50.99	53.41	0.03	18.22	24.70	24.82	21.11	21.31	19.54	19.56	26.89	27.59	10.16	12.03	28.35	33.68	34.37	33.46	33.64	22.79	22.82													
Cr <sub>2</sub> O <sub>3</sub>	0.06	0.08	1.75	0.09	0.14	0.39	0.32	-	0.09	0.06	0.12	0.01	0.67	0.04	0.06	0.05	0.06	0.03	0.02	0.62	0.06	0.11	0.12													
Fe <sub>2</sub> O <sub>3</sub>	-	-	-	-	-	11.33	0.02	0.09	-	-	0.49	0.07	0.06	0.92	1.38	1.93	6.18	1.65	1.12	1.28	0.66	-	-													
FeO	8.48	8.54	8.26	8.59	44.38	0.10	-	-	24.99	29.54	-	-	-	-	-	-	-	-	-	-	-	-	29.43													
ZnO	5.05	5.02	4.68	4.82	-	-	-	-	-	-	-	-	0.02	0.01	0.09	0.03	0.15	0.02	-	-	-	0.10	0.15													
MnO	0.04	0.08	-	0.08	0.26	0.06	0.04	-	7.14	1.37	0.07	-	0.02	0.01	0.09	0.03	0.15	0.02	-	-	-	0.01	0.15													
MgO	0.87	0.93	0.87	0.89	-	0.24	-	-	0.85	0.97	-	0.02	2.85	2.92	11.38	10.22	0.04	1.07	1.02	1.01	1.03	11.55	11.21													
CaO	0.02	-	0.17	0.01	0.02	12.63	6.52	6.60	8.13	9.23	0.29	0.36	0.12	-	8.07	7.94	23.13	0.01	0.01	0.10	0.01	0.05	0.02													
Na <sub>2</sub> O	-	-	-	-	0.03	0.06	7.53	7.64	0.05	0.04	11.63	11.40	0.33	0.45	1.30	1.53	0.02	0.56	0.85	0.63	0.73	-	-													
K <sub>2</sub> O	-	-	-	-	0.01	-	0.06	0.04	-	-	0.07	0.08	9.57	9.36	0.20	0.27	-	8.06	8.35	8.25	8.38	0.01	-													
Totals	97.33	97.11	94.69	97.03	97.86	75.48	97.45	98.22	100.28	100.26	99.83	97.97	93.91	92.12	97.64	97.57	96.87	92.22	92.61	92.11	92.67	88.27	87.96													
Oxygens	46	46	46	46	3	12.5	8	8	12	12	8	8	11	11	23	23	12.5	11	11	11	11	14	14													
Si	7.86	7.93	7.92	7.96	-	3.26	2.66	2.68	3.02	3.00	2.97	2.97	3.40	3.36	7.14	6.95	3.03	3.14	3.12	3.13	3.17	2.62	2.60													
Ti	0.07	0.08	0.10	0.14	1.02	-	-	-	0.01	0.01	-	-	0.01	0.01	0.03	0.03	0.01	0.01	0.01	0.01	0.01	0.01	-													
Al	17.81	17.68	17.30	17.59	-	2.16	1.33	1.33	1.99	2.00	1.01	1.03	2.15	2.23	1.74	2.07	2.61	2.69	2.74	2.68	2.68	2.86	2.89													
Cr	0.01	0.02	0.40	0.02	-	0.03	0.01	-	0.01	-	-	-	0.04	-	0.01	0.01	-	-	-	-	-	-	-													
Fe <sup>3+</sup>	-	-	-	-	-	-	-	-	-	-	0.02	-	-	0.05	0.15	0.21	0.36	0.08	0.06	0.07	0.03	-	-													
Fe <sup>2+</sup>	1.98	2.00	1.99	2.01	0.95	0.01	-	-	1.67	1.97	-	-	0.16	0.10	1.89	1.91	-	0.04	0.02	0.03	0.05	2.58	2.64													
Zn	1.04	1.04	0.99	0.99	-	-	-	-	-	-	-	-	-	-	-	-	-	-	-	-	-	-	-													
Mn	0.01	0.02	-	0.02	0.01	0.01	-	-	0.48	0.09	-	-	-	-	0.01	-	0.01	-	-	-	-	0.01	0.01													
Mg	0.36	0.39	0.37	0.37	-	0.04	-	-	0.10	0.12	-	-	0.29	0.30	2.46	2.22	0.01	0.11	0.10	0.10	0.10	1.84	1.79													
Ca	0.01	-	0.05	-	-	1.36	0.32	0.32	0.70	0.79	0.01	0.02	0.01	0.06	1.26	1.24	1.94	-	-	0.01	-	0.01	-													
Na	-	-	-	-	-	0.01	0.67	0.67	0.01	0.01	0.99	0.99	0.04	0.06	0.37	0.43	-	0.07	0.11	0.08	0.10	-	-													
K	-	-	-	-	-	-	-	-	-	-	-	-	0.83	0.82	0.04	0.05	-	0.70	0.72	0.72	-	-	-													
Sum	29.15	29.14	29.13	29.10	1.98	7.73	5.00	5.00	7.98	7.99	5.01	5.01	6.93	6.93	15.09	15.12	7.98	6.85	6.89	6.87	9.94	9.94														



Table 3-1 (4/4).

Sample Min	GU9		GU9		K16		K16		K16		EM2		EM2		EM2		EM2		EM2		GU6T		GU6T		GU6T			
	mu	g	core	rim	incl(g)	g	rim	bi	mu	fsp	rim	fsp	core	incl(g)	g	rim	chl	core	amph	rim	amph	core	rim	bi	fsp	rim	core	fsp
SiO <sub>2</sub>	47.14	37.68	37.96	37.96	24.51	37.13	37.90	36.81	46.40	67.96	68.29	47.41	24.51	24.52	24.45	24.68	37.32	37.49	24.58	45.10	45.83	39.53	59.16	39.53	59.16	45.83	63.28	-
TiO <sub>2</sub>	0.40	0.06	0.04	0.04	-	0.11	0.03	1.49	0.38	-	0.35	-	0.02	-	0.01	0.05	0.01	0.04	0.40	0.42	1.77	-	-	-	-	-	-	
Al <sub>2</sub> O <sub>3</sub>	34.41	21.20	20.95	41.23	21.11	21.59	18.99	19.28	35.51	18.99	19.33	32.11	40.77	40.67	40.57	40.07	21.05	21.15	23.08	12.56	12.56	16.74	24.84	16.74	24.84	12.56	22.29	
Cr <sub>2</sub> O <sub>3</sub>	0.14	0.04	0.07	0.09	0.09	0.09	0.05	0.08	0.10	0.52	-	0.60	0.07	0.06	0.07	0.08	0.10	0.05	0.12	0.41	0.50	0.06	-	0.50	0.06	-		
Fe <sub>2</sub> O <sub>3</sub>	-	-	-	-	-	-	0.02	-	-	0.04	0.07	0.22	0.02	-	-	0.43	-	1.93	1.62	1.62	-	0.08	0.08	-	0.08	0.08	-	
FeO	1.39	33.54	33.28	23.75	30.08	33.55	17.24	1.13	-	-	-	1.47	23.57	23.12	23.44	23.95	31.08	31.90	26.89	11.33	11.23	13.52	-	-	-	-	-	
nO	-	-	-	-	-	-	Z	-	-	-	-	-	-	-	-	-	-	-	-	-	-	-	-	-	-	-	-	
MnO	-	0.55	0.53	0.21	4.81	1.55	0.03	0.02	-	-	-	-	0.17	0.06	0.07	0.07	0.87	0.88	0.04	0.24	0.19	0.09	-	-	-	-	0.06	
MgO	0.70	1.83	1.83	2.88	1.43	2.23	10.89	0.65	0.02	0.02	-	1.47	3.08	3.05	3.00	2.82	1.78	1.91	12.50	11.23	11.70	13.62	-	-	-	-	-	
CaO	0.03	5.29	5.26	0.02	4.94	4.88	0.02	-	0.20	0.10	0.07	0.02	0.06	0.02	0.01	7.28	6.56	0.04	11.30	11.55	0.49	7.15	4.06	7.15	4.06	-		
Na <sub>2</sub> O	0.98	0.02	0.01	-	0.13	-	0.21	1.79	8.14	11.42	11.77	0.81	0.01	-	0.01	-	0.03	0.01	-	1.35	1.23	0.13	7.31	9.12	7.31	9.12	-	
K <sub>2</sub> O	8.61	0.01	-	0.02	0.01	-	8.77	8.14	0.06	0.06	0.06	8.65	-	0.01	-	0.02	0.01	-	0.02	0.55	0.51	7.54	0.08	7.54	0.08	0.10	-	
Totals	93.80	100.22	99.93	92.71	99.84	101.81	94.83	94.13	99.21	99.62	93.17	92.22	91.56	91.63	91.72	100.01	99.97	87.31	96.91	97.26	93.94	98.68	93.94	98.68	97.26	98.98	-	-
Oxygens	11	12	12	6	12	12	11	11	8	8	11	6	6	6	6	12	12	14	23	23	11	8	11	8	8	8	-	-
Si	3.15	3.02	3.04	1.00	3.00	2.99	2.76	3.09	3.00	3.00	3.20	1.01	1.01	1.01	1.02	2.99	3.00	2.62	6.61	6.68	2.92	2.67	2.92	2.67	6.68	2.82	-	
Ti	0.02	-	-	-	0.01	-	0.08	0.02	-	-	0.02	-	-	-	-	-	-	-	0.04	0.05	0.10	-	-	-	-	-	-	
Al	2.71	2.00	1.98	1.99	2.01	2.01	1.71	2.79	0.99	1.00	2.56	1.98	1.98	1.98	1.96	1.99	2.00	2.90	2.31	2.16	1.46	1.32	1.46	1.32	2.16	1.17	-	
Cr	0.01	-	0.01	-	0.01	-	0.01	0.01	0.02	0.02	0.03	-	-	-	-	0.01	-	-	0.01	0.01	0.05	0.03	-	-	-	-	-	
Fe <sup>3+</sup>	-	-	-	-	-	-	-	-	-	-	0.01	-	-	-	-	0.03	-	0.21	0.18	0.18	-	-	-	-	-	-	-	
Fe <sup>2+</sup>	0.08	2.25	2.23	0.81	2.03	2.21	1.08	0.06	-	-	0.08	0.81	0.80	0.81	0.83	2.08	2.14	2.40	1.39	1.37	0.83	-	-	-	-	-	-	
Zn	-	-	-	-	-	-	-	-	-	-	-	-	-	-	-	-	-	-	-	-	-	-	-	-	-	-	-	
Mn	-	0.04	0.04	0.01	0.33	0.10	-	-	-	-	-	0.01	-	-	-	0.06	0.06	-	0.03	0.02	0.01	-	-	-	-	-	-	
Mg	0.07	0.22	0.22	0.18	0.17	0.26	1.22	0.07	-	-	0.15	0.19	0.19	0.19	0.17	0.21	0.23	1.99	2.45	2.54	1.50	-	-	-	-	-	-	
Ca	-	0.45	0.45	-	0.43	0.41	-	-	0.01	0.01	0.01	-	-	-	-	0.63	0.56	-	1.78	1.81	0.04	0.35	0.19	0.04	0.35	0.19	-	
Na	0.13	-	-	-	0.02	-	0.03	0.23	0.98	1.00	0.11	-	-	-	-	0.01	-	0.38	0.35	0.02	0.64	0.79	0.02	0.64	0.79	0.02	0.64	
K	0.74	-	-	-	-	-	0.84	0.69	-	-	0.75	-	-	-	-	-	-	-	0.10	0.10	0.71	-	-	0.71	-	0.01	-	
Sum	6.90	7.98	7.97	4.00	8.00	8.00	7.73	6.96	4.99	5.01	6.91	4.00	3.99	4.00	4.00	8.00	8.00	9.92	15.32	15.30	7.61	4.99	7.61	4.99	15.30	4.99	-	

metapelite	GU1T*	SE3	SE12	T6	Z12	Z8
	Wt. %	Wt. %	Wt. %	Wt. %	Wt. %	Wt. %
SiO <sub>2</sub>	67.25	80.63	52.3	64.34	57.09	64.49
TiO <sub>2</sub>	0.90	0.69	1.14	1.03	1.08	1.50
Al <sub>2</sub> O <sub>3</sub>	13.56	6.43	24.54	18.15	21.86	20.79
Fe <sub>2</sub> O <sub>3</sub>	5.80	5.33	12.02	7.49	8.53	7.08
MnO	0.08	0.07	0.13	0.04	0.15	-
MgO	3.01	0.33	1.87	0.85	0.94	0.17
CaO	2.17	0.04	0.75	0.88	1.13	0.15
Na <sub>2</sub> O	2.69	0.22	1.53	0.65	1.02	0.30
K <sub>2</sub> O	1.67	1.03	1.42	1.43	2.61	1.81
P <sub>2</sub> O <sub>5</sub>	0.22	0.06	0.05	0.08	0.15	0.10
Fluid	1.79	2.31	4.044	3.65	5.04	3.62
Total	99.14	97.14	99.79	98.59	99.60	100.01

metapelite	GU1T*	SE3	SE12	T6	Z12	Z8
	Mol. %	Mol. %	Mol. %	Mol. %	Mol. %	Mol. %
SiO <sub>2</sub>	69.40	82.15	54.32	66.02	57.39	66.36
TiO <sub>2</sub>	0.70	0.53	0.89	0.79	0.82	1.16
Al <sub>2</sub> O <sub>3</sub>	8.25	3.86	15.02	10.98	12.95	12.61
FeOT	4.50	4.09	9.40	5.78	6.45	5.48
MnO	0.07	0.06	0.11	0.03	0.13	-
MgO	4.63	0.50	2.90	1.30	1.41	0.26
CaO	2.40	0.04	0.83	0.97	1.22	0.17
Na <sub>2</sub> O	2.69	0.22	1.54	0.65	0.99	0.30
K <sub>2</sub> O	1.10	0.67	0.94	0.94	1.67	1.19
P <sub>2</sub> O <sub>5</sub>	0.10	0.03	0.02	0.03	0.06	0.04
H <sub>2</sub> O	6.17	7.86	14.02	12.50	16.91	12.43
Total	100.00	100.00	100.00	100.00	100.00	100.00

\* pelitic gneiss

Table 3-2. Whole rock XRF analyses of selected samples of the Çine and Selimiye nappes of the western Menderes Massif. Analyses are given in weight % and normalized in mole % with Fe<sub>2</sub>O<sub>3</sub> recalculated to FeO total.

## P-T FIELD GRADIENT, NATURE OF TECTONIC CONTACT AND POSSIBLE ORIGIN OF BARROVIAN METAMORPHISM IN THE MENDERES MASSIF

In the western Çine massif metasedimentary enclaves in orthogneiss recorded temperatures of 600–640 °C and pressures around 8–10 kbar (e.g. Sample GU1T). Nearly the same  $P$ - $T$  estimates have been obtained south of Korçalı for samples D6, D1, D30, D42 (Chapitre 2) but in the staurolite stability field. Surrounding metasedimentary rocks yielded temperatures of 525–540 °C and 5–6 kbar (Samples T6). Albeit not precise, metamorphic zones shown an overall increase in  $P$ - $T$  conditions toward the orthogneiss. The contact between orthogneiss and surrounding schists is mylonitic. The syn-metamorphic character of this contact is outlined at least in northern part by helicitic top-to-the-N staurolite and sigmoid quartz pebbles. Shear sense criteria in mylonitic orthogneiss show same top-to-the-N sense of shear. Correlation between shearing and metamorphism lead to consider in this area, the presence of overall top-to-the-N movement and thrust of orthogneiss over metasedimentary rocks. In the SW part the deformation pattern is much more complicated by the presence of top-to-the-SW criteria. Absence of disharmonic structures would imply a possible partition of the strain, maybe related to the mylonite geometry (c.f. strike-slip shear zone, fig. 3-4). Another possibility is the correlation between widespread top-to-the-SW shear bands and local overprint of primarily top-to-the-N fabrics. Whatever the good interpretation it seems clear that top-to-the-N movement during lower amphibolite facies metamorphism characterize the NE part of this area. Temperature difference between sample T6 and GU1T in figure 3-3 would imply a “normal” temperature field gradient of *c.* 25 °C/km, according to the structural distance between both sample (around 5 km). The pressure is not well constrained but implies the presence of an inverted field gradient (prograde normal). Lateral distribution of isotherms in this area is likely complicated by an important fluid influx.

In the northern part, metasedimentary rocks in an enclave in orthogneiss (south of Korçalı), and orthogneiss everywhere in the Çine Massif revealed mainly top-to-the-N sense of shear with locally coaxial deformation (see fig. 2-6c). Top-to-the-N shear sense indicators are also expressed in the central Menderes Massif, where mylonitic foliation at the base of the orthogneiss has been described (Lips *et al.*, 2001).

In the southern Çine massif, the Selimiye nappe shown widespread evidence for a top-to-the-S displacement during prograde lower amphibolite facies metamorphism (Chapitre 2). Metasedimentary rocks behind the Selimiye shear zone shown the same deformation during a prograde amphibolite facies metamorphism. The difference of 2-3 kbar across the contact between orthogneiss/schists of the Çine nappe and metasedimentary rocks of the Selimiye nappe implies that approximately 7 km of crust is missing -notwithstanding thermodynamic uncertainties- throughout the Selimiye shear zone.

Metamorphic zones yielded overall increase of  $P$ - $T$  conditions toward the orthogneiss (chapter 2), from greenschist to amphibolite facies metamorphism.

In the area west of Dalama, north of Çine, within the northern central Çine Massif (Fig. 3-1), mineral parageneses (Sample EM2) of overlying schists and top-to-the-S fabrics are similar to those found in the Selimiye nappe. The same observations have been done in the eastern part where top-to-the-S fabrics are associated with garnet-biotite-chlorite-chloritoid parageneses and lower amphibolite facies metamorphism (sample Z12).

Figure 3-16 summarizes parageneses observed using AFM diagrams (KFMASH system). Indeed, we noticed during this work that only small differences occur in pseudosections using different chemical system. Only the garnet stability field strongly depends on the Mn content and for “normal” metapelite the system KFMASH can be used as a first approximation. Another important point concerns the stability field of chloritoid. Whatever the system, the chloritoid stability field in Al-rich metapelite is limited by the isograd chloritoid-out (breakdown of chloritoid) which constitutes a excellent thermometer (Wei & Powell, 2003). The same is true for the staurolite-out isograd (Fig. 3-16). Observed parageneses within the orthogneiss and in surrounding metasedimentary rocks (including the Selimiye nappe), plot in  $P$ - $T$  space near a line described as a “typical” geotherm for “normal” continental crust by Spear (p. 37–39, 1993). This is characteristic of Barrovian-type metamorphism. Chloritoid and chloritoid–staurolite inclusions in garnets from the Çine nappe (sample D6) provide valuable information of an likely earlier high-pressure garnet–chloritoid–staurolite paragenesis (Spear & Cheney, 1989; see also chapter 2) during metamorphism, and suggest a clockwise  $P$ - $T$ -path. Same clockwise  $P$ - $T$ -path has been proposed for metasedimentary rocks of the Selimiye nappe (Sample SE12).



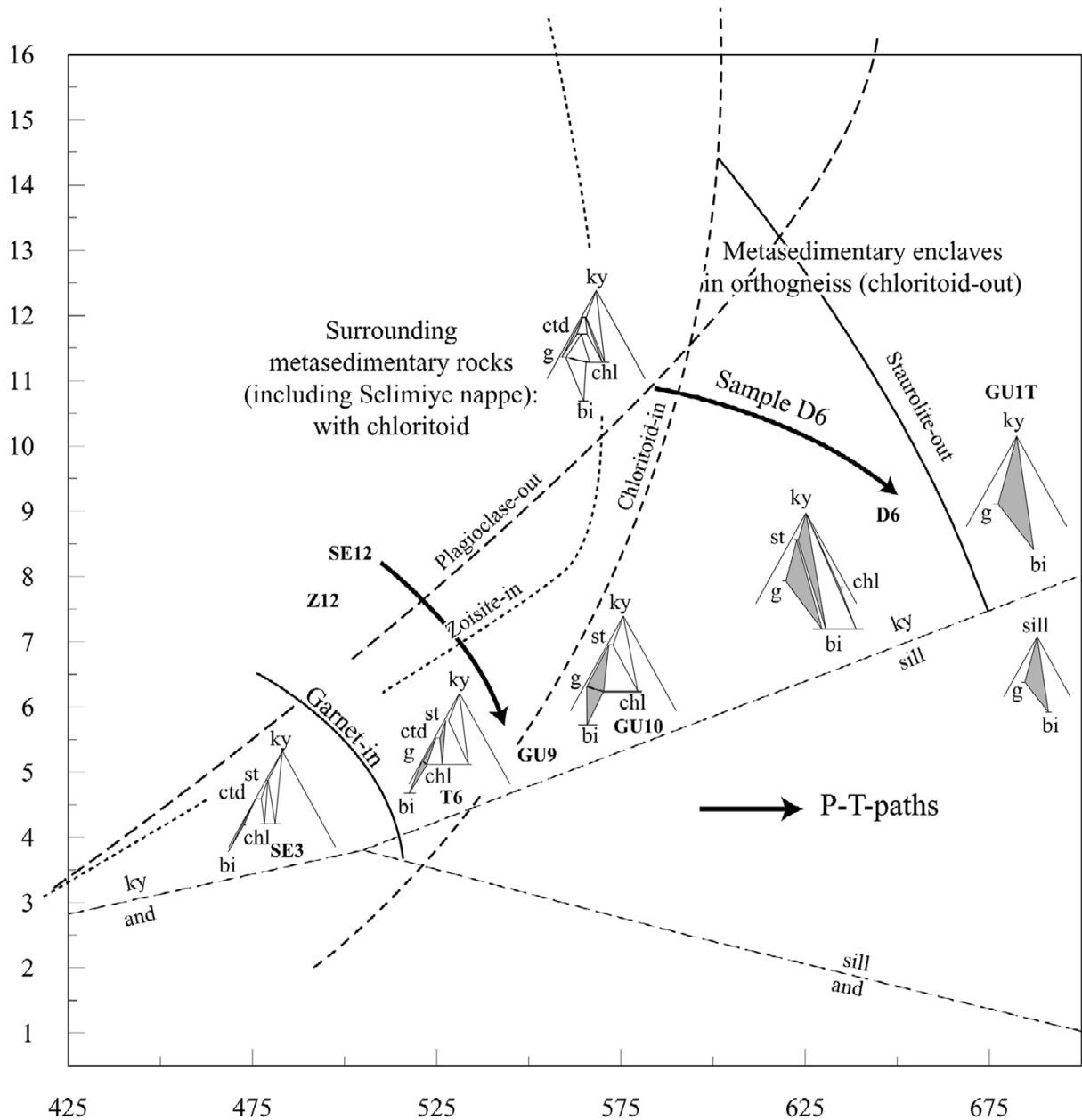


Fig. 3-16. Summary of parageneses observed in the Çine Massif. The system KFMASH has been chosen in order to simplify the representation of parageneses using calculated AFM diagrams (see also fig. 2-10). Parageneses observed are in grey. Sequence of parageneses describes a typical Barrovian field gradient. Chloritoid-in and staurolite-out isograds are well constrained whatever the system chosen for metapelite. Position of other isograds is specific to our own samples and will depend on whole rocks analyses. Clockwise *P-T*-path is deduced from pseudosections in chapitre 2 and 3. Surrounding metasedimentary rocks are characterized by the stability of chloritoid whereas metasedimentary enclaves shown total breakdown of this phase. Note the occurrence of sillimanite in the central Menderes Massif near Tire (Evirgen & Ataman, 1982) and in the North Menderes Massif, south of Dermici (Candan & Dora, 1993) (Bozdag nappe).

The occurrence of sillimanite in the central Menderes Massif near Tire (Evirgen & Ataman, 1982) and in the North Menderes Massif south of Dermici (Candan & Dora, 1993) within the Bozdağ nappe, are associated with top-to-the north shear criteria (Hetzl *et al.*, 1998), and concur with northward crustal thickening.

Although the deformation history is quite complex, metamorphic parageneses are consistent with a single metamorphic event. Figure 3-17 attempts to summarize our observations from a tectonical point of view taking as assumption that all parageneses are coeval. In this case overall top-to-the-N thrust of Çine orthogneiss would account for different sense of shear along different shear zone. Top-to-the-N sense of shear would occur within the orthogneiss whereas top-to-the-S would be expressed in overlying metasedimentary rocks. In lateral parts, accommodation of the deformation would be done via strike-slip shear zones (Fig. 3-17). Lack of evidence for polymetamorphism supports such a hypothesis. Indeed, if we assume an older age of metamorphism in the Çine nappe compared to the one observed in the overlying Selimiye nappe (with chloritoid), retrograde metamorphism in the chloritoid stability field would likely occur within metasedimentary enclaves of the Çine nappe. In contrast staurolite-kyanite-biotite parageneses did not show any retrograde overprinting metamorphism in chloritoid stability field (Note that there is still enough water within orthogneiss metasedimentary enclaves to allow this retrograde metamorphism).

In this context existence of an inverted field gradient (prograde inverse) described by Hetzel *et al.* (1998) near the Birgi-Bozdağ area (north of our this study, figs. 3-1 & 3-18a-c) with occurrence of sillimanite (and presumably cordierite in paragneiss or pyroxene-garnet-plagioclase in calc-silicate rocks) at the base of the Çine nappe, would explain by top-to-the-N thrusting. Moreover, this position, underlying Bozdağ nappe (see. Fig 3-2) is characterized by staurolite-kyanite-biotite and garnet-biotite parageneses, indicating a decrease in temperature across the nappe boundary (Hetzl *et al.*, 1998; Dora *et al.*, 2001). This succession describes a typical prograde inverse field gradient (Fig. 3-18) (e.g Scheuven, 2002). Nevertheless, Dora *et al.* (2001) and Ring *et al.* (2001) postulate that the inverted field gradient resulted from Eocene folding of a normal prograde field gradient.

South of Dermici Candan & Dora (1993) describe index mineral sequences which are consistent with Barrovian-type metamorphism and which are exposed along a normal prograde field gradient. Additionally, Régnier *et al.* (2003) reported a normal prograde erosion level near Selimiye. It seems plausible that the lower unit thrust during Barrovian-type metamorphism does not record real prograde inverse field gradient, however detailed isograd mapping is necessary to solve this problem in the Birgi-Bozdağ area.

Widespread greenschist shear bands are assumed related to top-to-the-S emplacement of Çine Bozdağ and Selimiye nappes during lower greenschist metamorphism via Bayındır nappe (Fig. 3-17). Finally, retrograde metamorphism is common in the Selimiye nappe as previously noticed by Ashworth & Evirgen (1984) and Régnier *et al.* (2003) and has to be correlated with an important tectonic event.

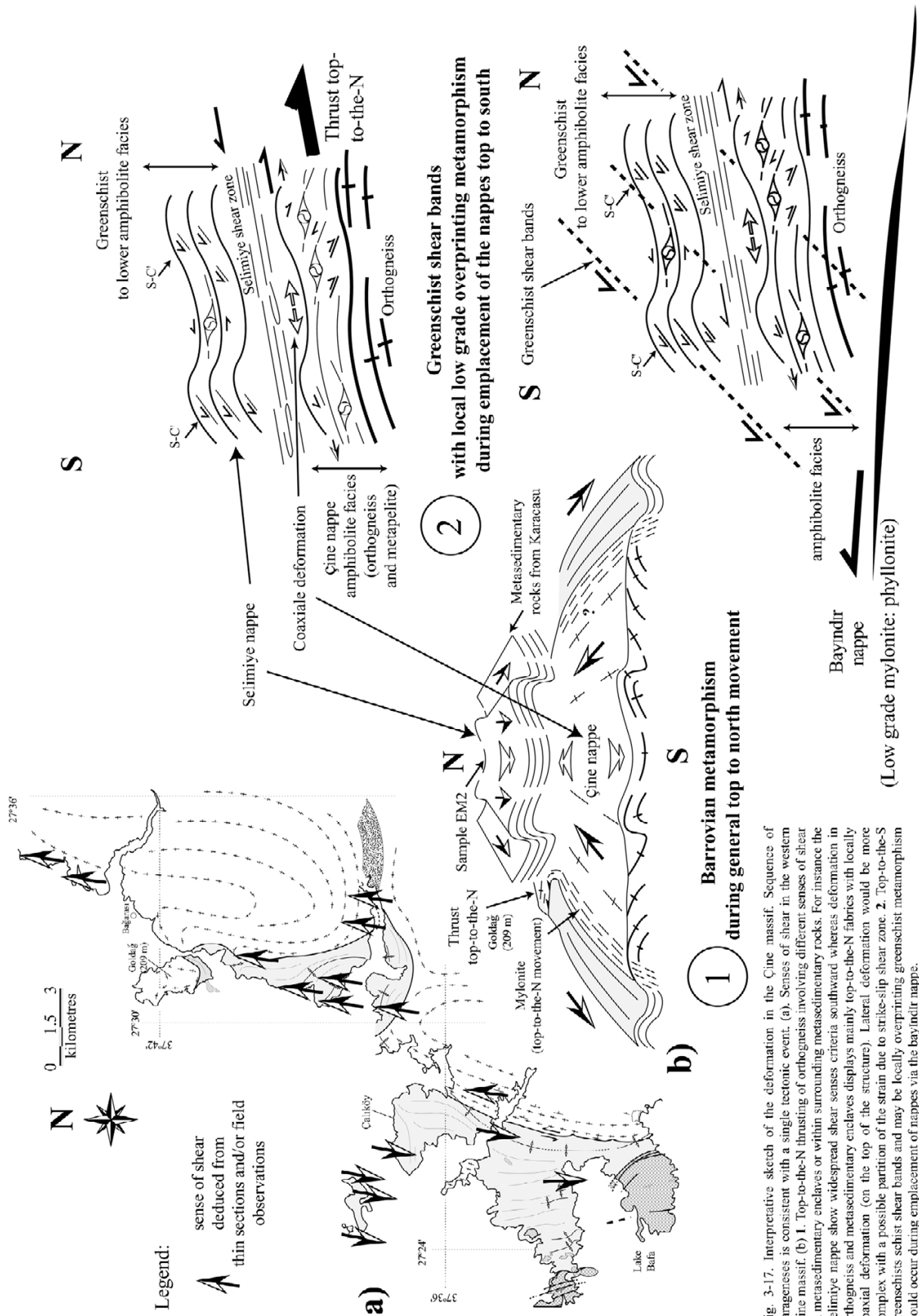


Fig. 3-17. Interpretative sketch of the deformation in the Çine massif. Sequence of parageneses is consistent with a single tectonic event. (a). Senses of shear in the western Çine massif. (b) 1. Top-to-the-N thrusting of orthogneiss involving different senses of shear in metasedimentary enclaves or within surrounding metasedimentary rocks. For instance the Seimiye nappe show widespread shear senses criteria southward whereas deformation in orthogneiss and metasedimentary enclaves displays mainly top-to-the-N fabrics with locally coaxial deformation (on the top of the structure). Lateral deformation would be more complex with a possible partition of the strain due to strike-slip shear zone. 2. Top-to-the-S greenschists schist shear bands and may be locally overprinting greenschist metamorphism would occur during employment of nappes via the bayındır nappe.

## DISCUSSION

Bozkurt & Park (1994) associated Barrovian metamorphism with Eocene burial of the Menderes Massif under the HP–LT blueschist unit and Lycian nappes, an interpretation which does not seem plausible since these nappes are typically cold during their exhumation. Rimmelé *et al.* (2003) argued for burial of the lower units of the Menderes Massif to a depth of at least 30 km during the closure of the Neo-Tethys (Northern branch). However, this study has not reported any evidence for a HP metamorphic overprinting. Régnier *et al.* (2003) correlate important retrograde metamorphism in the Selimiye nappe and greenschist facies shear zones in the Menderes Massif with thrusting of the HP–LT units onto the core series (Figs. 3-17b, 3-18b & 3-18c). Exhumation of lower structural levels has likely been initiated along the Bayındır nappe under lower greenschist facies conditions with top-to-the-S movement. However, in contrast to our study from the southern Çine massif (Régnier *et al.*, 2003 and chapter 2), the new evidence from the western part strongly suggests that amphibolite facies metamorphism throughout the Menderes Massif is coeval, implying that Barrovian metamorphism predated the nappe emplacement and HP–LT metamorphism (Fig. 3-18b; Güngör & Erdoğan, 2000).

Gessner *et al.* (2001a), Ring *et al.* (2001) and Gessner *et al.* (2004) suggested regional top-to-the-N deformation exclusively occur during Proterozoic amphibolite facies metamorphism, while Gessner *et al.* (2001a) additionally correlated regional top-to-the-S shearing under greenschist metamorphism during the Eocene. Data of the western Çine Massif presented in this study shown that such simplification is not suitable. Indeed, top-to-the-N deformation occurs during lower amphibolite facies metamorphism and top-to-the-S shearing has been observed in southern Çine nappe during amphibolite metamorphism. Moreover coaxial deformation is also present at the top of the orthogneiss unit (Régnier *et al.*, 2003). On the contrary, index minerals and deformation within Menderes Massif indicate that a major tectonic event, which resulted in the northward thrusting of Proterozoic orthogneiss onto lower units of the metasedimentary rocks prior to the Eocene (Hetzl *et al.*, 1998; Lips *et al.*, 2001; Fig. 3-18b). Top-to-the-N shearing would be accommodated in the underlying metasedimentary rocks (central Menderes Massif, Hetzel *et al.*, 1998; Ring *et al.*, 2001), while coaxial deformation prevails at the top of the orthogneiss. We infer fabrics indicating top-to-the-S shearing in the Selimiye nappe to be related to southward back-thrusting onto the Proterozoic orthogneiss (Fig. 3-17b & 3-18b). It should be noted that metamorphism in the upper metasedimentary unit of the thrust can involve a clockwise  $P$ – $T$  path as in the lower thrust unit if dissipated heating is taken in account (England & Molnar, 1993). Unloading implies decompression followed by heating of the upper unit while loading would be followed by heating in the lower unit (Spear, 1993). The only difference will be the presence of an inverted field gradient in the lower unit which has been described controversially near Birgi-Bozdağ area.

Régnier *et al.* (2003), Gessner *et al.* (2004) and Ring *et al.* (2004a) propose a Proterozoic age for amphibolite facies metamorphism, due to a SHRIMP zircon age of  $566 \pm 9$  Ma for a metagranite (only affected by greenschist shear bands) crosscutting regional-scale amphibolitic facies foliation in the orthogneiss. It seems plausible that protolith age for a part of metasedimentary rocks around the Çine Massif is older than previously assumed (Çağlayan *et al.*, 1980), Proterozoic instead of Paleozoic in age. Indeed, fossils of Paleozoic age in the Selimiye nappe (Devonian and Carboniferous), have been found (as usually) in very low grade schists. Alternatively, zircons from the metagranite could be inherited zircons. For instance if original melting occurred with a strong fluid participation temperatures attained will not be sufficiently high to cause rim overgrowth of zircon, so that some of this intrusions in the Çine Massif may be young. Rb–Sr and  $^{40}\text{Ar}$ – $^{39}\text{Ar}$  ages on mica yield Eocene ages within Çine and Selimiye nappe that are locally associated with a top-to-the-north displacement (Satır & Friedrichen, 1986; Hetzel & Reischmann, 1996), contrasting Gessner *et al.* (2004) and Ring *et al.* (2004a). Supporting a Tertiary age for amphibolite facies metamorphism are Eocene  $^{40}\text{Ar}$ – $^{39}\text{Ar}$  age on mica associated with top-to-the-N shearing in mylonitic granitic gneiss at the base of the Çine nappe (Lips *et al.*, 2001).  $^{40}\text{Ar}$ – $^{39}\text{Ar}$  ages can also be interpreted as true cooling ages. However, it appears unlikely for amphibolite facies metamorphism to take 500 Ma to cool below 400 °C. In addition, *in situ* monazite dating with the Th-Pb ion microprobe method yielded Eocene age for a part of the metasedimentary rocks of the Menderes Massif (Catlos *et al.*, 2002). All these remarks outline a serious geochronological problem which can not be solved, of course, only by a metamorphic study. However the possible existence of a major tectonic event before the Eocene and during the Tertiary, associated with top-to-the-N thrusting and Barrovian-type metamorphism, may have important implications on the paleocontinental reconstruction of the eastern Mediterranean domain, and could lend support to the idea of a Neo-Tethys (*sensu stricto*) branch south of the Menderes Massif (Stampfli, 2000).

## CONCLUSIONS

Parageneses observed in Proterozoic?–Paleozoic metasedimentary rocks of the southern Menderes Massif are indicative of a single Barrovian-type amphibolite facies metamorphism related to crustal thickening and northwards thrusting of the lower unit exposed in the Çine Massif. This could occur during pre-Eocene Tertiary. The emplacement of the lower nappes (Çine nappe, Bozdağ nappe, Selimiye nappe) postdated the main metamorphic event and was most likely initiated on the so-called Bayındır nappe under lower greenschist facies conditions. The Bayındır nappe can be interpreted as a major greenschist facies mylonitic shear zone developed at the base of the lower thrust nappe. Subsequently Late Eocene overthrusting of the HP–LT units following their exhumation resulted in retrograde metamorphism observed in the immediately underlying Selimiye nappe. The petrological data shows no evidence for burial of the lower units of the Menderes Massif to a depth of more than 30 km during closure of Neo-Tethys.

What remains to be solved are the cause and the age of the Barrovian metamorphism. Although early Tertiary age for widespread amphibolite facies metamorphism in the Menderes Massif is proposed here, this assumption needs to be substantiated by additional geochronological studies.

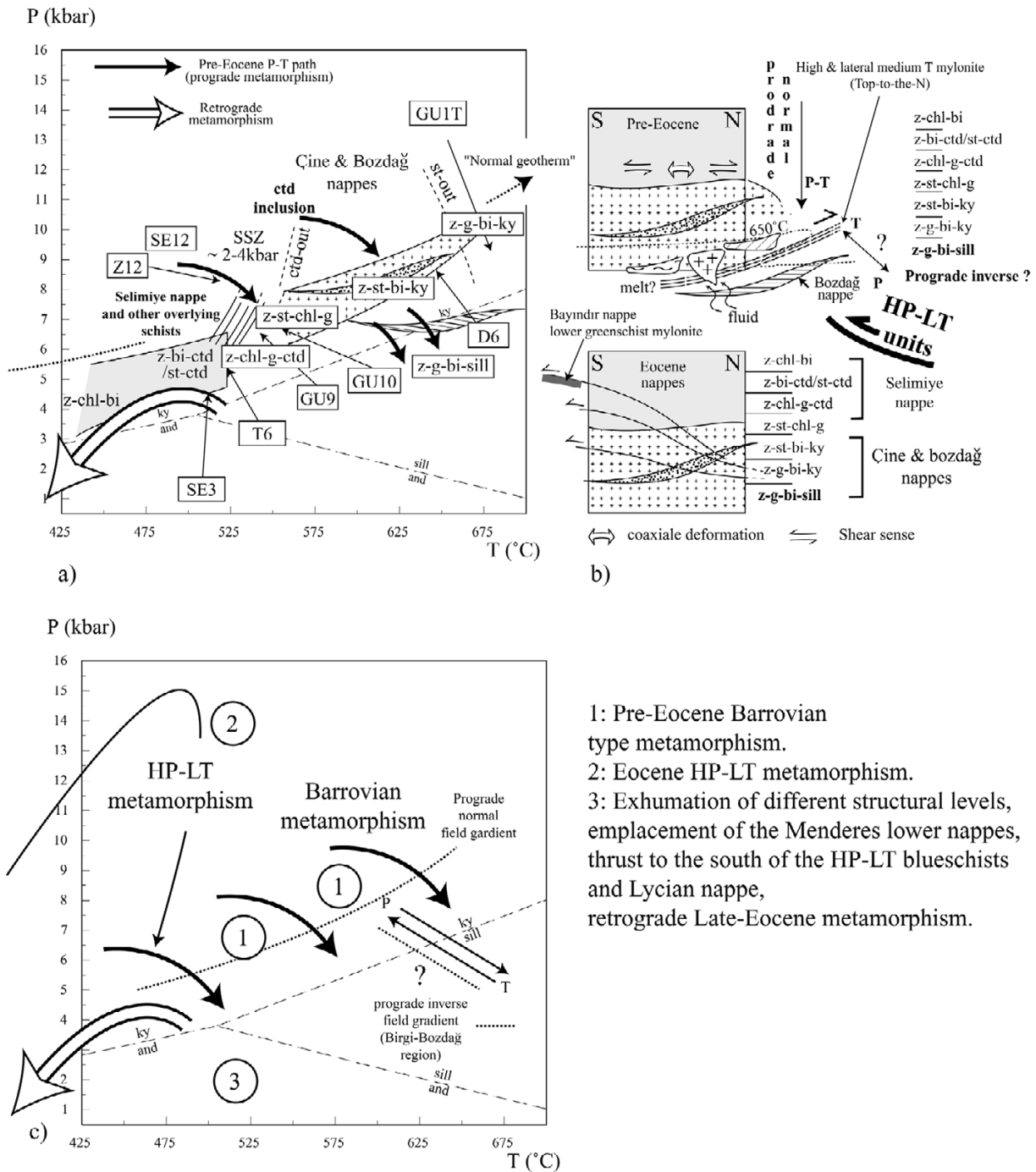


Fig. 3-18. Summary of parageneses encountered in the Çine Massif and sketch about timing of the different metamorphism in the Menderes Massif. a) Plot of different parageneses on a  $P$ - $T$  diagram according to  $P$ - $T$  estimates of Régnier *et al.* (2003) and this study (see also fig. 3-16). The different parageneses typically described a Barrovian field gradient (Spear, 1993). Chloritoid inclusion in Çine Massif garnet constrains clockwise  $P$ - $T$  path during thickening. Çine and Selimiye nappes are in tectonic contact via a jump of pressure on order of 2-4 kbar depending on the area. Selimiye nappe and surrounding schists in the western Çine Massif are characterized by  $P$ - $T$  condition in the chloritoid-kyanite field near triple aluminosilicate point. Çine nappe is characterized by  $P$ - $T$  conditions from the ctd-out isograd to the st-out isograd (biotite-garnet-kyanite field, sample GU1T). Retrograde metamorphism occurs mainly in Selimiye nappe. b) Sketch on the top: pre-Eocene Barrovian metamorphism. We propose overthrust to the north (see text for sense of shear) of Proterozoic orthogneiss (including the Çine nappe) on metasedimentary rocks, to explain Barrovian metamorphism (Hetzl *et al.*, 1998; Lips, 2001). Sketch on the bottom: syn to post-Eocene exhumation during closure of Neo-Tethys and emplacement of HP-LT units (blueschist unit and Lycian nappe) on the Menderes Massif. Parageneses from this study are also shown. Garnet-sillimanite-biotite paragenesis from Candan & Dora (1993). c)  $P$ - $T$  path history proposed in this study correlating emplacement of the HP-LT units over the Menderes Massif with the important retrogression observed in the Selimiye nappe. The hypothetical prograde inverse field gradient from the Birgi-Bozdağ region is also shown (Hetzl *et al.*, 1998; Dora *et al.*, 2001). See Fig. 3-1 for patterns. SSZ= Selimiye shear zone, Z= zone.



## Chapter 4

### Summary and general Conclusions

In Chapter 2, we put forward the theory that Barrovian-type metamorphism expressed within the core series of the Menderes Massif may result from a polyorogenic history. In other words we considered two distinct events and metamorphisms. The first one would occur during the Proterozoic involving the Çine and Bozdağ nappes with amphibolite facies metamorphism and associated top-to-the-N shearing. The second one would occur during the Eocene involving the Selimiye and Bayındır nappe, related to the closure of the northern Neo-Tethys branch and associated with top-to-the-S shearing during a single greenschist metamorphism. Meanwhile, the Selimiye nappe which effectively shows top-to-the-S sense of shear, recorded higher  $P$ - $T$  conditions -greenschist to lower amphibolite facies metamorphism- than those observed in the Bayındır nappe at the base of the lower thrust nappes. Additionally, part of the Çine nappe in the south showed amphibolite facies metamorphism associated with top-to-the-S shearing, making speculative the idea associating different sense of shear with different facies and ages of metamorphism.

As discussed in the Chapter 2,  $P$ - $T$  conditions in the Selimiye nappe contrast with those observed in the Çine nappe. The difference of  $P$ - $T$  conditions between the Çine and Selimiye nappes has been observed via paragenetic analyses and furthermore quantified from a thermodynamic point of view. Therefore the contact between the Çine and Selimiye nappes in the southern part is tectonic throughout the Selimiye shear zone and postdates the Barrovian-type metamorphism. These observations support the notion of nappes to describe the structure of present-day Menderes Massif. On the other hand, parageneses observed in both nappes are indicative of a single Barrovian-type amphibolite facies metamorphism. Petrological study showed a strong consistency of parageneses from greenschist to upper amphibolite facies metamorphism and point to a single event affecting metasedimentary rocks of the Selimiye and Çine nappes. No evidence has been found for a polymetamorphic history. There are therefore no petrological and tectonical reasons – according to our remark above concerning the sense of shear- to dissociate in age the metamorphism observed in the Selimiye nappe from the one observed in the Çine nappe.

It has been proposed by previous studies and in Chapter 2 that the actual structure observed in the Central Menderes Massif, which shows the presence of high-grade (Çine and Bozdağ nappes) on low-grade metamorphism rocks (Bayındır nappe), was initiated under lower greenschist metamorphism by top-to-south out-of-sequence thrusting during closure of the Neo-Tethys (northern

branch) in the Eocene. This model seems consistent on the whole with our observations but the Bayındır nappe could only be a major lower greenschist mylonitic shear zone at the base of the lower thrust nappes, inducing exhumation of previously existent Barrovian-type metamorphism.

In Chapter 3, evidence for top-to-the-N thrusting of orthogneiss over surrounding metasedimentary rocks has been found in the western part of the Çine Massif. *P-T* conditions during this top-to-the-N thrusting are around 530 °C and 5-6 kbar. Mineral parageneses are consistent with a Barrovian-type metamorphism and correspond to a lower amphibolite facies metamorphism as expressed by the presence of staurolite and chloritoid in textural equilibrium. This additional data make the interpretation of Proterozoic top-to-the-N versus Eocene top-to-the-S deformation respectively associated with amphibolite and greenschists metamorphism improbable. However presence of widespread top-to-the-S greenschist shear bands is in good agreement with previously proposed top-to-the-S emplacement of lower Menderes nappes (Çine, Bozdağ and Selimiye nappes) via the Bayındır nappe.

The idea that emplacement of the lower nappes is related to out-of-sequence thrusting during single greenschist metamorphism involving the Selimiye and Bayındır nappes is not supported by this study from a metamorphic point of view. As mentioned above the Selimiye nappe and overall surrounding metasedimentary rocks displayed higher *P-T* conditions than those observed in the Bayındır nappe (Phyllite of lower greenschist metamorphism). Moreover, out-of-sequence thrusting and associated metamorphism used by Ring *et al.* (1999a) and Gessner *et al.* (2001b) to describe the structure of the core series, would imply polymetamorphism in the directly underlying Çine or Bozdağ nappes and so retrograde parageneses in the chloritoid-garnet-chlorite stability field since the base of the Selimiye nappe records lower amphibolite facies *P-T* conditions. The lack of evidence for polymetamorphism, whatever the type within the metasedimentary rocks from the Çine nappes, argue for a single event. Within the Selimiye nappe no evidence for an inverted field gradient or for a single lower greenschist facies have been found. In contrast the metamorphic gradient around the Çine Massif is prograde normal from greenschist to amphibolite facies on the erosion level and unrelated to any thrust on the top. Therefore metamorphism in Çine Massif predates out-of-sequence thrusting (and associated greenschists shear bands) of Ring *et al.* (1999a) and Gessner *et al.* (2001b). Additionally evidence for a HP-LT metamorphism overprinting is nonexistent.

Deformation and petrological data are consistent with a top-to-the-N thrusting of orthogneiss over Bozdağ metasedimentary rocks related to a classic collisional chain metamorphism. Difference of sense of shear in surrounding metasedimentary rocks compared to those in the Çine or Bozdağ nappes is not in contradiction with a single event. Collisional chains show widespread evidence for back-thrusting shearing on the top of the structure during regional compression and thrusting (for instance

in the Himalayas; Brunel, 1986). Subsequently Late Eocene overthrusting of the HP–LT units would induce exhumation of the lower nappes (Çine nappe, Bozdağ nappe, Selimiye nappe) likely initiated on the so-called Bayındır nappe. Retrograde metamorphism observed mainly in the Selimiye nappe would result to top-to-the-S thrusting of upper and middle HP-LT units.

According to the geochronological problem outlined during this thesis, there are therefore two possible schemes: either Barrovian-type metamorphism is Proterozoic in age and so part of the sediments from surrounding metasedimentary rocks has to be Proterozoic in age too; or Barrovian-type metamorphism in Eocene of age (or Mesozoic since these ages are deduced from dating on mica). In the first case the structure observed now in the core series would correspond to a simple exhumation of proterozoic basement. In the latter it is possible -as outlined in Chapter 3- to envisage that Barrovian-type metamorphism associated with top-to-the-N thrusting would occur during closure of Neo-Tethys (*sensu stricto*, southern branch). This may have important implications on the paleocontinental reconstruction of the eastern Mediterranean domain. Indeed, possible presence of Neo-Tethys suture beneath the Lycean nappe may represent an oceanic closure during southward subduction involving for instance the presence of exotic block between Gondwana and the Taurid-block. An even more complex history could be envisaged but additional geochronological studies are necessary before doing so.

Whatever the assumption, the HP-LT metamorphism displayed by the overlying blueschist and Lycean nappe, has no relation with the observed parageneses in the core series. Moreover Barrovian-type metamorphism pre-date on the whole emplacement of the lower nappes.

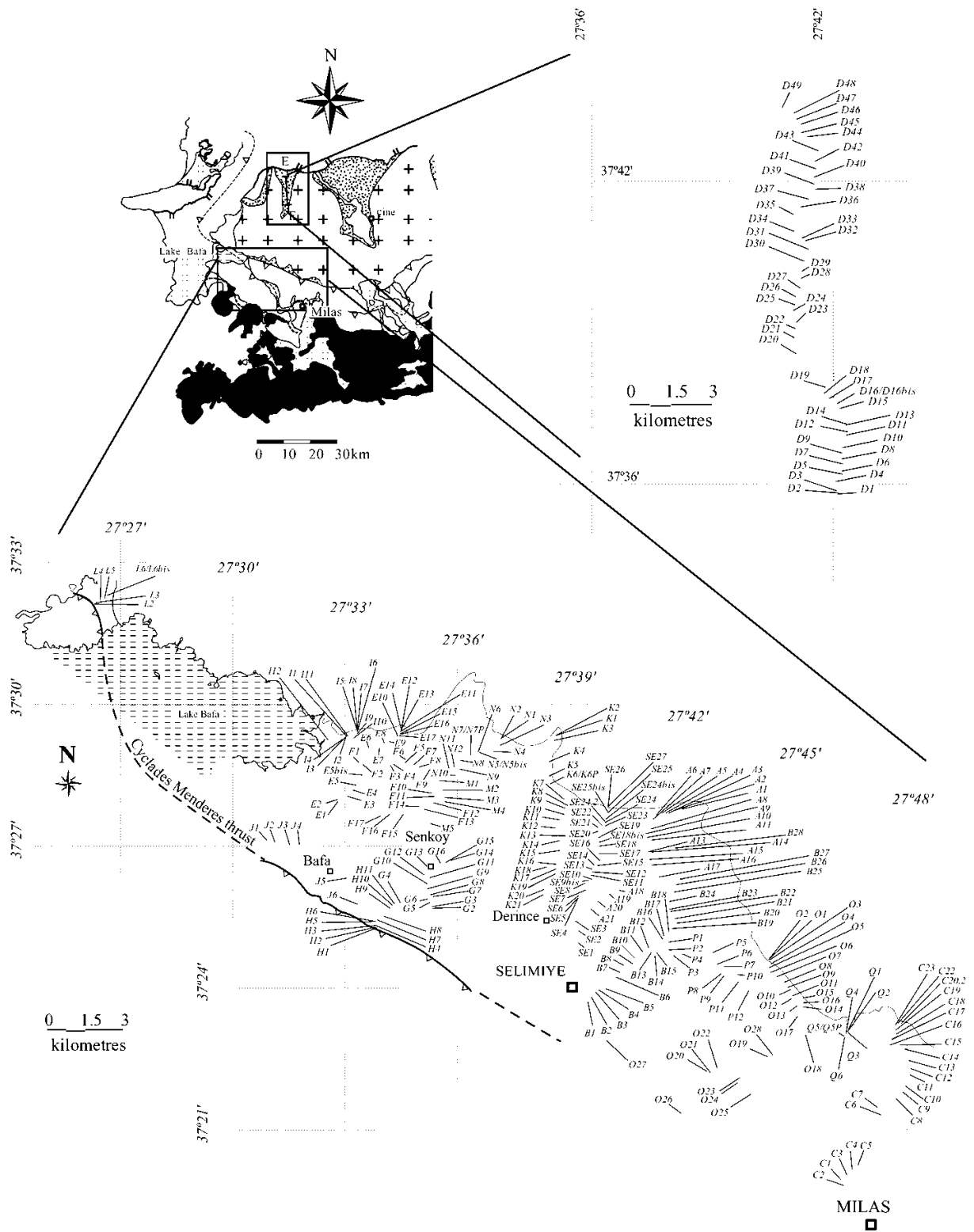
## **Recommendations for further study**

Despite the very fact that we did not make a success of dating mica and amphibole by  $^{40}\text{Ar}/^{39}\text{Ar}$  method, the few results that we have seems relatively promising. Indeed, preliminary results yielded Mesozoic ages on mica from the Çine nappe (*c.* 100 Ma). Within the Çine nappe amphiboles are also well preserved and albeit rich in calcium, they still display the presence of potassium. That would be a good starting point to perform dating by  $^{40}\text{Ar}/^{39}\text{Ar}$  method using [Ca, K]-amphibole. The other important point concerns the existence of an inverted field gradient (prograde inverse) described by Hetzel *et al.* (1998) near the Birgi-Bozdağ area in the central Menderes Massif. This area has to be mapped in detail from a metamorphic point of view in order to mark the boundary of the sillimanite-in isograd and to constrain the succession of parageneses. Generally, the northern most part of the Menderes Massif lack of any detailed metamorphic study. The correlation between metasedimentary rocks from the southern Menderes Massif and those outcropping in the northern part is therefore

complicated by the distance involved. Additional data from the northern most part is crucial for understanding of metamorphic history in the Menderes Massif.

# Appendix 1

Location of samples in chapter 2.



## Appendix 2 Parageneses of studied samples

<p>- absent 2 = secondary amph = amphibole and = andalusite ap = apatite bi = biotite carb = carbonate cd = cordierite chl = chlorite</p>	<p>ctd = chloritoid ep = epidote, zoisite fsp = feldspar g = garnet i = inclusions ky = kyanite mu = white mica op = opaque q = quartz</p>	<p>sill = sillimanite st = staurolite zi = zircon p... = main parageneses X &gt; 10 % O 1-10 % T &lt; 1 % R = retrograded garnet</p>
---	--	--

samples	N	E	q	fsp	mu	carb	chl	ctd	bi	g	st	ky	ep	amph	op	to	ap	zi
SE1	37°24'57.20"	27°39'13.50"	X	O	X	-	-	-	O	-	-	-	O	-	O	-	-	T
SE2	37°25'12.60"	27°39'14.30"	X	X	X	-	X(p1)	X(p1)	X(p1)	-	-	-	-	-	T	-	-	T
SE3	37°25'25.00"	27°39'20.20"	X	O	X	-	T(p1), 2	X(p1)	X(p1)	-	-	-	-	-	X	T	-	T
SE4	37°25'52.10"	27°39'12.00"	-	-	X	X	-	-	X(p1)	-	-	-	X(p1)	-	-	-	-	T
SE5	37°25'54.00"	27°39'13.00"	X	O	X	X	T(p1)	-	O(p1)	-	-	-	O(p1)	-	O	-	-	T
SE6	37°25'56.80"	27°39'13.60"	X	X	X	-	O(p3)	O(p1)	O(p2)	X(p1), T(p1), O(p3)	-	-	X(p1), T(p1)	-	O	-	-	T
SE7	37°26'5.00"	27°39'18.00"	X	X	X	T(p1)	X(p1)	-	X(p1)	X(p1)	-	-	X(p1), T(p1)	-	O	-	-	T
SE8	37°26'12.70"	27°39'23.90"	X	O	X	-	-	-	O(p1)	-	-	-	X(p1)	-	X	-	-	T
SE9	37°26'16.40"	27°39'29.70"	X	X	X	-	-	-	O	-	-	-	-	-	O	-	-	T
SE9 bis	37°26'16.40"	27°39'29.70"	X	X	X	-	2	-	X(p1)	-	-	-	-	-	O	-	-	T
SE10	37°26'18.00"	27°39'34.70"	X	X	X	-	2	-	O(p1)	O(p1)	-	-	T	-	O	-	-	T
SE11	37°26'23.07"	27°39'34.30"	X	O	X, T(p1)	-	X(p1), O(p2)	X(p1), T(p1), O(p3)	X(p1), O(p3)	X(p2), O(p3)	-	-	-	-	O	T	-	T
SE12	37°26'27.20"	27°39'36.80"	X	O	X	-	T(p1), 2	X(p1)	X(p1)	X(p1)	-	-	T	-	X	T	-	T
SE13	37°26'50.60"	27°39'35.60"	X	X	X	-	X(p1)	-	X(p1)	-	-	-	X(p1)	-	X	-	-	T
SE14	37°26'35.70"	27°39'38.60"	X	X	X	X	2p	-	X(p1)	X(p1)	-	-	X(p1), T(p1)	-	O	-	-	T
SE15	37°26'35.20"	27°39'44.50"	X	O	X	O	2p	-	O(p1)	X(p1)	-	-	X(p1), T(p1)	-	O	-	-	T
SE16	37°26'41.50"	27°39'47.50"	X	X	X	O, T(p1)	2	-	T(p1)	X(p1)	-	-	X(p1)	-	O	-	-	T
SE17	37°26'50.00"	27°39'47.50"	X	X	X, T(p1)	O	2	-	T(p1)	X(p1)	-	-	X(p1)	-	O	-	-	T
SE18	37°27'0.00"	27°39'47.50"	X	X	X	-	O(p1), 2	-	X(p1)	X(p1)	-	-	X(p1)	-	O	-	-	T
SE18bis	37°27'5.00"	27°39'47.50"	X	X	X	-	O(p1), T(p1), O(p2)	T(p1)	T(p1)	X(p1)	-	-	O(p1), T(p1)	-	X	-	-	T
SE19	37°27'10.70"	27°39'46.30"	X	X	X	-	2	-	X	-	-	-	-	-	X	-	-	T
SE20	37°27'18.60"	27°39'45.20"	X	X	X	-	-	-	O(p1)	O(p1)	-	-	-	-	X	-	-	T
SE21	37°27'23.60"	27°39'44.80"	X	X	X	-	-	-	X(p1)	X(p1)	-	-	-	-	O	T	-	T
SE22	37°27'26.80"	27°39'51.80"	X	X	X	-	-	-	X(p1)	O(p1)	-	-	-	-	O	T	-	T
SE23	37°27'25.80"	27°39'57.20"	X	X	X	-	-	-	X(p1)	O(p1)	-	-	-	-	O	O	-	T
SE24	37°27'30.00"	27°39'57.20"	X	O	X	-	-	-	X	-	-	-	-	-	T	-	-	T
SE24bis	37°27'30.00"	27°39'57.20"	X	O	X	-	-	-	X	-	-	-	-	-	T	-	-	T
SE25	37°27'42.60"	27°40'1.20"	X	X	X	-	-	-	X	-	-	-	-	-	T	O	-	T
SE25bis	37°27'42.60"	27°40'1.20"	X	X	X	-	-	-	X	-	-	-	-	-	T	O	-	T
SE26	37°27'50.00"	27°40'1.20"	X	X	X, T(p1)	-	T(p1)?, 2	-	X(p1)	X(p1)	-	-	-	-	T	T	-	T
SE27	37°27'50.00"	27°40'1.20"	X	-	X	-	-	-	O	-	-	-	-	-	T	X	-	-

samples	N	E	q	fsp	mu	carb	chl	ctd	bi	g	st	ky	ep	amph	op	to	ap	zi
A21	37°25'39.80"	27°38'34.30"	X	X	-	X(p1)	-	X(p1)	X(p1)	-	-	-	-	-	O	-	-	T
A20	37°25'49.90"	27°39'45.30"	X	O	-	X(p1)P2	-	X(p1)P2	X(p1)	-	-	-	T	-	X	-	-	T
A18	37°25'58.90"	27°40'3.40"	X	X	-	O(p1)	-	O(p1)	X(p2)	-	-	-	O(p1)O2	-	X	-	-	T
A18.1	37°26'1.00"	27°40'15.00"	X	O	-	O(p1).2	-	O(p1)	X(p2)	-	-	-	O	-	X	-	-	T
A17	37°26'18.40"	27°41'20.10"	X	O	-	O(p1).2	-	O(p1)P2	X(p1)	-	-	-	O(p1)O2	-	O	-	-	T
A16	37°26'35.80"	27°41'11.80"	X	O	-	O(p1)P2	-	X(p1)P2	X(p1)O2	-	-	-	O(p1)O2	-	O	-	-	T
A15	37°26'43.10"	27°41'19.00"	X	O	-	T(p1)P2	-	T(p1)P2	X(p1)	-	-	-	O(p1)O2	-	O	-	-	T
A14	37°26'52.40"	27°41'11.20"	X	X	-	X(p1)	-	X(p1)	X(p1)	-	-	-	-	-	X	-	-	T
A13	37°26'52.80"	27°41'5.60"	X	X	-	X(p1)	-	X(p1)	X(p1)	-	-	-	-	-	X	-	-	T
A11	37°27'10.80"	27°41'14.10"	X	X	X	X	2	O(p1)P2	O(p1)	-	-	-	X(p1)	-	O	-	-	T
A8	37°27'15.60"	27°41'11.90"	X	X	X	X	2	X(p1)	X(p1)	-	-	-	X(p1)	-	O	-	-	T
A5	37°27'21.70"	27°41'10.60"	X	X	X	X	-	X(p1).T10/g	X(p1)	-	-	-	-	-	O	X	-	T
A7	37°27'39.70"	27°41'18.90"	X	X	X	X	-	X(p1)	Tic1)	-	-	-	-	-	T	O	-	T
A5	37°27'41.70"	27°41'27.50"	X	X	X	X	-	X(p1)P2	O(p2)	-	-	-	-	-	T	T	-	T
A4	37°27'42.00"	27°41'33.70"	X	X	X	X	-	X	-	-	-	-	-	-	T	T	-	T
A3	37°27'41.90"	27°41'33.80"	X	X	X	X	-	X(p1)	Tic1)	-	-	-	-	-	T	T	-	T
A2	37°27'44.80"	27°41'47.00"	X	X	X	X	-	X	-	-	-	-	-	-	T	T	-	T
A1	37°27'46.90"	27°42'0.40"	X	X	X	X	-	X(p1)	O(p1)	-	-	-	-	-	T	T	-	T
samples	N	E	q	fsp	mu	carb	chl	ctd	bi	g	st	ky	ep	amph	op	to	ap	zi
B1	37°23'41.90"	27°39'29.10"	X	X	X	-	O(p1)	ctd	bi	g	st	-	ep	amph	op	to	ap	zi
B2	37°23'48.20"	27°39'34.70"	X	X	X	X	-	-	O(p1)	-	-	-	-	-	T	-	-	-
B3	37°23'54.90"	27°39'41.60"	X	O	X	X	X(p1)	-	O	-	-	-	-	-	T	-	-	-
B4	37°23'57.60"	27°39'46.44"	X	X	X	X	-	-	T(p1)	-	-	-	-	-	T	-	-	-
B5	37°23'58.90"	27°39'58.40"	X	X	X	X	-	-	X(p1)	-	-	-	-	-	O	-	-	-
B6	37°24'13.80"	27°40'14.50"	X	X	X	X	O(p1)	-	-	-	-	-	-	-	X	-	-	-
B7	37°24'20.00"	27°40'20.00"	X	T	X	X	-	-	O(p1)	-	-	-	-	-	O	T	-	-
B8	37°24'28.80"	27°40'26.10"	X	X	X	X	T	-	O(p1)	-	-	-	O(p1)	-	O	-	-	-
B9	37°24'31.00"	27°40'40.20"	X	X	X	X	-	-	O(p1)	-	-	-	-	-	X	-	-	-
B10	37°24'38.60"	27°40'43.20"	X	X	X	X	-	X(p1)	X(p1)	Tic1)	-	-	-	-	X	-	-	-
B11	37°24'46.60"	27°40'55.60"	X	O	X	-	O(p1)	O(p1)P2	O(p1)	O(p2)	-	-	-	-	O	-	-	-
B12	37°24'51.20"	27°41'15.90"	X	O	X	X	O(p1).2	-	O(p1)	Tic1)	-	-	-	-	O	-	-	-
B13	37°24'44.20"	27°41'19.90"	X	O	X	X	O(p1)?	-	O(p1)P2	X(p2)	-	-	O(p1)	-	O	-	-	-
B14	37°24'40.20"	27°41'16.20"	X	T?	X	X	-	-	X(p1)	-	-	-	O(p1)	-	O	-	-	-
B15	37°24'44.80"	27°41'19.00"	X	X	X	X	X(p1).2?	-	O(p1)	-	-	-	O(p1)	-	O	-	-	-
B16	37°25'2.10"	27°41'28.20"	X	X	X	X	-	-	X(p1)	-	-	-	O(p1)	-	O	-	-	-
B17	37°25'6.50"	27°41'30.40"	X	X	X	X	O(p1)	-	X(p1)	-	-	-	O(p1)	-	O	-	-	-
B18	37°25'12.00"	27°41'38.34"	X	X	X	X	Tic1)	-	O(p1)	X(p1)	-	-	O	-	O	-	-	-
B19	37°25'15.40"	27°41'44.30"	X	X	X	X	-	-	O	-	-	-	-	-	T	-	-	-
B20	37°25'22.80"	27°41'51.70"	X	X	X	X	-	-	T	-	-	-	-	-	O	-	-	-
B21	37°25'27.90"	27°41'47.80"	X	X	X	X	2	-	O(p1)	-	-	-	X(p1)	-	O	-	-	-
B22	37°25'37.10"	27°41'41.40"	X	X	X	X	-	Tic1)	X(p1)	T	-	-	O	-	O	-	-	-
B23	37°25'37.10"	27°41'41.40"	X	X	X	X	27	Tic1)	O(p1)	X(p1)	-	-	Tic1)	-	O	-	-	-
B23b	37°25'37.10"	27°41'41.40"	X	X	X	X	27	Tic1)	O(p1)	X(p1)	-	-	Tic1)	-	O	-	-	-
B24	37°25'40.00"	27°41'40.00"	X	X	X	X	-	X(p1)P2	O(p1)P2	X(p1)	-	-	Tic1)	-	O	-	-	-
B25	37°25'49.50"	27°41'39.40"	O	O	X	X	X(p1)	X(p1)P2	O(p1)P2	X(p1)	-	-	Tic1)	-	O	-	-	-
B25	37°26'1.60"	27°41'46.70"	X	X	X	X	-	X(p1)P2	O(p1)P2	X(p1)	-	-	O(p1)	-	O	-	-	-
B26	37°26'11.00"	27°41'50.50"	X	O	X	X	O(p1)	-	O(p1)	X(p1)	-	-	X(p1).T10/g	-	X	-	-	-
B27	37°26'18.10"	27°41'56.90"	X	-	X	X	-	-	O(p1)	X(p1)	-	-	X(p1).T10/g	-	X	-	-	-
B28	37°26'57.90"	27°41'49.20"	X	X	X	X	-	-	Tic1)	X(p1)	-	-	X(p1)	-	O	-	-	-

samples	N	Σ	c	fsf	mu	carb	chl	ctd	bl	g	st	ky	ep	amph	op	to	ap	zi
C1	37°19'57.33"	27°46'13.70"	X	?	X	-	O(p1)	-	X(p1)	-	-	-	-	-	T	-	-	T
C2	37°19'50.33"	27°46'18.00"	-	C?	-	X	-	-	T	-	-	-	-	-	T	-	-	-
C3	37°20'3.70"	27°46'23.20"	X	O	X	-	-	-	X	-	-	-	-	-	O	T	-	T
C4	37°20'10.53"	27°46'31.60"	X	?	X	-	-	-	X	-	-	-	-	-	O	T	-	T
C5	37°20'15.93"	27°46'41.10"	X	-	O	-	O(p1)	-	O(p1)	-	-	-	-	-	T	T	-	T
C6	37°21'19.43"	27°47'17.60"	X	O	X	-	O(p1)	-	X(p1)	-	-	-	-	-	T	T	-	T
C7	37°21'28.93"	27°47'12.10"	X	O	X	-	O(p1)	X(p1)	O	-	-	-	-	-	T	T	?	T
C8	37°21'39.53"	27°47'42.20"	X	X	X	-	?	-	O	-	-	-	-	-	T	-	-	T
C9F	37°21'48.13"	27°47'53.00"	X	X	X	-	X(p2)	-	O(p1)(p2)	O(p1)	-	-	-	-	O	-	-	T
C10P	37°21'56.73"	27°47'57.40"	X	X	X	-	X(p1)	-	O(p1)	O	-	-	T	-	O	O	-	T
C11	37°22'3.83"	27°48'4.63"	X	X	X	-	2	-	X(p1)	X(p1)	-	-	-	-	X	T	-	T
C11Bs	37°22'3.83"	27°48'4.63"	X	X	X	-	X(p1)	X(p1)	O(p1)	X(p1)	-	-	-	-	X	T	-	T
C12	37°22'17.93"	27°48'5.33"	X	X	X	-	O(p1), 2	-	O(p1)	X(p2)	-	-	?	-	X	T	-	T
C13	37°22'28.23"	27°48'2.53"	X	X	X, T(0)g	-	O(p1), 2	O(p1), T(0)g	O(p1)	X	-	-	-	-	X	T	-	T
C14	37°22'42.43"	27°47'58.60"	X	X	X	-	-	-	X	-	-	-	-	-	O	O	-	T
C15	37°22'47.53"	27°47'48.40"	X	O	X	-	-	-	X	-	-	-	-	-	O	-	-	T
C16	37°22'47.53"	27°47'31.70"	X	X	X	-	2	-	X	-	-	-	-	-	O	-	-	T
C17	37°22'56.13"	27°47'35.70"	X	O	X	-	2	-	X(p1)	X(p1)	-	-	-	-	O	T	-	T
C18	37°23'1.70"	27°47'42.60"	X	O	O	-	-	-	X	-	-	-	-	-	T	-	?	T
C19	37°23'7.93"	27°47'42.40"	X	O	X	-	2	-	X	-	-	-	-	-	O	O	-	T
C20.2	37°23'15.43"	27°47'50.60"	X	X	X	-	-	-	X	-	-	-	-	-	T	T	?	T
C21.5T	37°23'15.93"	27°47'50.70"	X	X	O	-	-	-	X	-	-	-	-	-	T	X	-	T
C22	37°23'15.93"	27°47'45.20"	X	X	X	-	-	-	X(p1)	-	-	-	-	-	T	-	-	T
C23	37°23'13.43"	27°47'41.50"	X	X	X	-	-	-	X	-	-	-	-	-	T	O	-	T



samples	N	E	q	fsp	nu	catr	chl	cid	bi	g	st	ky	ep	amph	op	to	ap	zi
D1	37°35'48.00"	27°42'7.30"	X	X	-	-	-	-	X(p1)	X(p1)	-	-	-	-	O	O	-	T
D1 bis	37°35'48.00"	27°42'7.30"	X	X	-	-	-	-	X	X(p1)	-	-	-	-	O	O	-	T
D2	37°35'49.30"	27°42'6.50"	X	X	-	-	2	-	X(p1)	X(p1)	-	-	-	-	O	O	-	T
D3	37°35'51.90"	27°42'4.60"	X	X	-	-	2	-	X(p1)(p2)	O(p2)	-	-	-	-	O	X	-	T
D3bis	37°35'51.90"	27°42'4.60"	X	X	-	-	2	-	X	X	-	-	-	-	O	X	-	T
D4P	37°36'2.90"	27°42'4.40"	X	X	-	-	-	T(0/g)	O(p2)(p3)	X(p1)(p2)	X(p1)(p3)	X(p1)	-	-	O	O	-	T
D5	37°36'11.70"	27°42'12.40"	X	X	-	-	-	T(0/g)	X(p2)(p3)	X(p1)(p2)(p3)	X(p1)(p2)	X(p1)(p2)	-	-	O	O	-	T
D6	37°36'15.30"	27°42'13.10"	X	X	-	-	-	T(0/g)	X(p2)(p3)	X(p1)(p2)(p3)	X(p1)(p2)	X(p1)(p2)	-	-	O	O	-	T
D7	37°36'23.80"	27°42'13.50"	X	O?	X	X	-	-	O(p1)	X(p1)	-	-	-	-	O	-	-	T
D7bis	37°36'23.80"	27°42'13.50"	X	O?	X	X	-	-	O(p1)	X(p1)	-	-	-	-	O	-	-	T
D8	37°36'29.90"	27°42'13.30"	X	X	-	-	-	T(0/g)	O(p2)(p3)	X(p1)	X(p1)(p2), T(0/g)	O(p3)	O(p2), T(0/g)	-	X	T	-	T
D9	37°36'36.70"	27°42'12.30"	X	O?	O	X	-	-	X(p1)(p2)	X(p1)	-	-	-	-	T	-	-	T
D10	37°36'43.20"	27°42'14.00"	X	X	-	-	-	T(0/g, 2)	X(p1), T(0/g)	X(p1)	-	-	-	-	X	T	-	T
D11	37°36'58.10"	27°42'16.60"	X	O	X	X	-	-	O(p1)	-	-	-	O(p1)	-	O	-	-	T
D12	37°37'2.00"	27°42'20.50"	X	X	-	-	-	-	X	-	-	-	-	-	O	-	-	T
D13	37°37'10.20"	27°42'18.20"	X	X	-	-	-	-	O(p1)	-	-	-	O(p1)	-	O	-	-	T
D14	37°37'11.20"	27°42'18.30"	X	X	-	-	-	-	O(p1)	X(p1)	-	-	O(p1)	-	O	O	-	T
D15	37°37'29.70"	27°42'9.50"	X	X	-	-	-	-	X(p1)	O(p1)	-	-	-	-	X	T	-	T
D16	37°37'35.60"	27°42'6.00"	X	X	-	-	-	-	X(p1)	X(p1)	-	-	-	-	O	T	-	T
D16bis	37°37'35.60"	27°42'6.00"	X	X	-	-	-	-	X(p1)(p2)	X(p1)	X(p1), T(0/g)	-	X?, T(0/g)	-	O	T	-	T
D17	37°37'41.70"	27°41'54.20"	X	O	X	-	-	-	O(p1)	-	-	-	O(p1)	-	O	-	-	T
D18	37°37'47.90"	27°41'46.70"	X	X	-	-	-	-	X(p1)	-	-	-	X(p1)	-	O	-	-	T
D19	37°37'55.20"	27°41'47.20"	X	X	-	-	-	T(0/g)	X(p1)	X(p1)	X(p1), T(0/g)	-	X(p1), T(0/g)	-	O	T	-	T
D20	37°38'35.10"	27°41'13.50"	X	X	-	-	-	-	X(p1)	X(p1)	-	-	-	-	O	-	-	T
D21	37°38'54.00"	27°41'1.40"	X	X	-	-	-	-	X	-	-	-	X(p1), T(0/g)	-	O	-	-	T
D22	37°39'4.50"	27°41'2.70"	X	T	-	-	-	-	T	-	-	-	-	-	O	-	-	T
D23	37°39'12.40"	27°41'5.10"	X	X	-	-	2	T(0/g)	X(p1)(p2)	X(p1)	X(p1)	X(p2), T(0/g)	?	-	O	-	-	T
D24	37°39'26.40"	27°41'6.90"	X	X	-	-	-	T(0/g, 2)	O(p2)(p3)	X(p1)(p3)	X(p1)(p2)	X(p1)	O	-	O	-	-	T
D25	37°39'33.00"	27°41'2.30"	X	X	-	-	-	T(0/g)	O(p2)(p3)	X(p1)(p3)	X(p1)(p2)	X(p1)	T(0/g)	-	O	O	-	T
D26	37°39'42.80"	27°41'3.20"	X	X	-	-	-	-	O(p1)(p2), T(0/g)	X(p2)	-	-	O(p1)	-	O	-	-	T
D27	37°39'53.20"	27°41'9.60"	X	X	-	-	2	-	X(p1)	X(p1)	-	-	-	-	O	-	-	T
D28	37°40'4.50"	27°41'11.90"	X	X	-	-	-	-	O(p1)	X(p1)	-	-	-	-	O	T	-	T
D29	37°40'13.00"	27°41'13.30"	X	X	-	-	2	-	X(p1)	X(p1)	-	-	-	-	O	T	-	T
D30	37°40'25.00"	27°41'15.60"	O	X	-	-	-	T(0/g)	O(p2)(p3)	X(p1)(p3)	X(p1)(p2)(p3)	X(p1)(p2)	-	O	O	-	-	T
D31	37°40'38.10"	27°41'22.50"	X	O	X	-	2	T(0/g)	O(p2)(p3), T(0/g)	X(p1)(p3)	X(p1)(p2)(p3), T(0/g)	X(p1)(p2)	T(0/g)	-	O	T	-	T
D32	37°40'48.40"	27°41'18.90"	X	X	-	-	-	-	O(p1)	X(p1)	-	-	-	-	O	T	-	T
D33	37°40'52.20"	27°41'13.10"	X	X	-	-	-	-	X(p1)	X(p1)	-	-	-	-	O	T	-	T
D34	37°41'0.20"	27°41'1.30"	X	X	-	-	2	-	X(p1)	X(p1)	-	-	-	-	O	T	-	T
D35	37°41'20.70"	27°40'58.60"	X	X	-	-	-	-	X(p1)	X(p1)	-	-	-	-	O	T	-	T
D36	37°41'29.40"	27°41'11.60"	X	X	-	-	-	-	X(p1)	X(p1)	-	-	-	-	O	T	-	T
D37	37°41'38.70"	27°41'22.40"	X	X	-	-	2	-	X(p1)	X(p1)	-	-	-	-	O	T	-	T
D38	37°41'50.20"	27°41'33.70"	X	X	-	-	-	-	O(p1)(p2)	X(p1)(p3)	X(p1)(p2)(p3)	X(p2)(p3)	-	-	O	O	-	T
D39	37°41'56.50"	27°41'31.30"	X	X	-	-	2	-	X(p1), T(0/g)	X(p1)	-	-	-	-	O	T	-	T
D40	37°42'4.50"	27°41'31.40"	X	X	-	-	2	-	X(p1)	X(p1)	-	-	-	-	O	T	-	T
D41	37°42'14.80"	27°41'33.30"	X	-	O	-	-	-	O	-	-	-	-	-	O	T	-	T
D42	37°42'23.70"	27°41'33.00"	X	X	-	-	-	T(0/g)	O(p1), T(0/g)	X(p1)(p2)	X(p1)(p2)	X(p2)	-	-	T	-	-	T
D43	37°42'36.20"	27°41'36.90"	X	X	-	-	-	-	O(p1)(p2), T(0/g)	X(p1)(p2)	X(p1)(p2)	X(p2)	-	-	X	T	-	T
D44P	37°42'52.80"	27°41'21.70"	X	O	X	-	2	-	O(p1)(p2), T(0/g)	X(p1)(p3)	X(p2)(p3)	X(p2)(p3)	-	-	X	T	-	T
D45	37°42'57.70"	27°41'12.30"	X	X	-	-	-	-	O(p1)(p2), T(0/g)	X(p1)(p3)	X(p1)(p2), T(0/g)	X(p2)(p3)	-	-	T	O	-	T
D46	37°43'7.80"	27°41'12.20"	X	X	-	-	-	-	X	X(p1)	-	-	-	-	T	X	-	T
D47	37°43'13.80"	27°41'6.30"	X	X	-	-	-	-	X(p1)	X(p1)	-	-	-	-	T	X	-	T
D48	37°43'27.70"	27°40'48.70"	X	X	-	-	-	-	X(p1)	T(p1)	-	-	-	-	T	X	-	T
D49	37°43'58.70"	27°40'57.10"	X	X	-	-	-	-	X(p1)	O(p1)	-	-	-	-	O	X	-	T
D50	37°43'57.10"	27°40'48.50"	X	X	-	-	-	-	X(p1)	O(p1)	-	-	-	-	O	X	-	T
D51	37°43'57.10"	27°40'48.50"	X	X	-	-	-	-	X(p1)	O(p1)	-	-	-	-	O	X	-	T
D51P	37°43'57.10"	27°40'48.50"	X	X	-	-	-	-	X(p1)	O(p1)	-	-	-	-	O	X	-	T
D52	37°43'59.00"	27°41'12.50"	X	X	-	-	-	-	X(p1)	O(p1)	-	-	-	-	O	O	-	T
D53	37°43'55.50"	27°41'28.30"	X	X	-	-	-	-	X	-	-	-	-	-	T	X	-	T
D54	37°44'15.90"	27°41'48.80"	X	X	-	-	-	-	X	-	-	-	-	-	T	X	-	T
D55	37°44'28.30"	27°41'44.10"	X	X	-	-	-	-	X	-	-	-	-	-	O	O	-	T
D56	37°44'33.20"	27°42'13.30"	O	X	-	-	-	-	X(p1), T(0/g)	X(p1)	-	-	X(p1), T(0/g)	-	O	O	-	T
D57	37°45'1.70"	27°42'48.00"	O	O	-	-	-	-	O(p1)	X(p1)	-	-	X	-	X	-	-	T
D58	37°45'32.10"	27°43'0.40"	X	X	-	-	-	-	O(p1)	X(p1)	X(p1)	O(p1)	-	-	X	X	-	T
D59	37°46'5.20"	27°42'56.30"	X	X	-	-	-	-	X	X(p1)	-	-	-	-	T	X	-	T
D59b	37°46'5.20"	27°42'56.30"	X	X	-	-	-	-	X	-	-	-	-	-	T	O	-	T

samples	N	E	q	fsp	nu	carb	chl	cld	bi	g	st	ky	ep	amph	op	to	ap	zi
L2E	37°32'5.00"	27°26'14.50"	X	X	X	-	X(p1)	-	O(p1)	-	-	-	-	-	O	to	-	T
L3	37°32'6.70"	27°26'16.20"	X	X	X	-	X(p1)	-	O(p1)	-	-	-	-	-	O	X	-	T
L4	37°32'11.00"	27°26'23.20"	X	O	X	-	X(p1)	-	T(p1)	T?	-	-	O(c1)	-	O	-	-	T
L5	37°32'12.50"	27°26'30.10"	X	O	X	-	27	-	O(p1)	-	-	-	-	-	T	-	-	T
L6F	37°32'12.50"	27°26'30.10"	X	X	X	-	X(p1)	-	T(p1)	O(p1)	-	-	-	-	T	X	-	T
samples	N	E	q	fsp	nu	carb	chl	cld	bi	g	st	ky	ep	amph	op	to	ap	zi
J1	37°27'7.30"	27°30'54.50"	X	X	X	-	chl	cld	bi	g	-	ky	ep	amph	op	to	ap	zi
J2	37°27'5.40"	27°31'7.70"	X	X	X	-	X(p1)	-	T(p1)	-	-	-	-	-	O	T	-	T
J3	37°27'1.50"	27°31'13.80"	X	X	X	-	X(p1)	-	O(p1)	-	-	-	-	-	O	T	-	T
J4	37°27'2.50"	27°31'14.7.10"	X	X	X	-	O(p1)	-	X(p1)	-	-	-	-	-	O	T	-	T
J5	37°26'19.30"	27°33'2.03"	X	X	X	-	X(p1)	-	O(p1)	-	-	-	-	-	X	T	-	T
J6	37°26'46.50"	27°33'19.80"	X	X	X	O	T	-	O(p1)	-	-	-	-	-	O	T	-	T
samples	N	E	q	fsp	nu	carb	chl	cld	bi	g	st	ky	ep	amph	op	to	ap	zi
H2	37°25'14.80"	27°33'47.80"	X	O	X	-	O(p1)	cld	bi	g	-	ky	ep	amph	op	to	ap	zi
H3	37°25'19.20"	27°33'47.80"	X	O	X	-	X(p1)	-	T(p1)	-	-	-	-	-	O	T	-	T
H4	37°25'19.80"	27°33'48.40"	X	O	X	-	X(p1)	-	X(p1)	-	-	-	-	-	O	T	-	T
H5	37°25'24.20"	27°33'42.50"	X	O	X	-	O(p1)	-	T(p1)	-	-	-	-	-	O	T	-	T
H6	37°25'24.70"	27°33'48.20"	X	O	X	-	X(p1)	-	T(p1)	-	-	-	-	-	T	T	-	T
H7	37°25'26.30"	27°33'52.20"	X	O	X	-	X(p1)	-	T(p1)	-	-	-	-	-	O	T	-	T
H8	37°25'30.90"	27°34'3.10"	X	O	X	-	O(p1)	-	T(p1)	-	-	-	-	-	O	T	-	T
H9	37°25'41.30"	27°34'12.00"	X	T?	X	-	O(p1)	-	O(p1)	-	-	-	-	-	T	T	-	T
H10	37°25'45.20"	27°34'16.10"	X	O	X	-	O(p1)	-	-	-	-	-	-	-	X	T	-	T
H11	37°25'46.80"	27°34'19.70"	X	O	X	-	X(p1)	-	O(p1)	-	-	-	-	-	X	T	-	T
samples	N	E	q	fsp	nu	carb	chl	cld	bi	g	st	ky	ep	amph	op	to	ap	zi
G2	37°25'41.30"	27°35'21.20"	X	X	X	-	T(p1),2	-	X(p1)	O(p1)	-	ky	ep	amph	op	to	ap	zi
G3	37°25'43.40"	27°35'20.20"	X	X	X	-	X(p1)	-	X(p1)	-	-	-	-	-	O	T	-	T
G4	37°25'48.50"	27°35'28.80"	X	X	X	-	O(p1)	-	X(p1)	-	-	-	-	-	X	T	-	T
G5	37°25'48.50"	27°35'15.30"	X	X	X	-	-	-	X	-	-	-	-	-	X	T	-	T
G6	37°25'52.60"	27°35'11.50"	X	X	X	-	-	-	O(p1)	-	-	-	-	-	X	T	-	T
G7	37°25'56.00"	27°35'21.60"	X	X	O	-	O(p1),2	-	O(p1)	-	-	-	-	-	O	T	-	T
G8	37°25'58.50"	27°35'17.70"	X	X	X, T(0/g)	-	T(p1), T(0/g), 2	-	X(p1)	X(p1)	-	-	-	-	O	T	-	T
G9	37°26'5.70"	27°35'12.00"	X	X	X	-	T(p1), 2	-	X(p1)	-	-	-	-	-	O	T	-	T
G10	37°26'12.30"	27°35'11.70"	X	X	X	-	O(p1), 2	-	X(p1)	-	-	-	-	-	O	T	-	T
G11	37°26'20.00"	27°35'16.40"	X	O	X	-	2	-	X(p1)	-	-	-	-	-	X	T	-	T
G12	37°26'27.20"	27°35'13.50"	X	O	X	-	T(p1), 2?	O(p1)	O(p1)	-	-	-	-	-	X	T	-	T
G13	37°26'32.90"	27°35'12.70"	X	O	X	-	X(p1)	-	O(p1)	-	-	-	-	-	O	T	-	T
G14	37°26'42.10"	27°35'50.20"	X	O	X	-	O(p1)	O(p1)	O(p1)	-	-	-	-	-	O	T	-	T
G15	37°26'59.30"	27°35'41.40"	X	X	X	-	T(p1)	-	O(p1)	-	-	-	-	-	X	T	-	T
G15	37°26'58.50"	27°35'32.70"	X	X	X	-	O(p1)	O(p1)	O(p1)	-	-	-	-	-	O	T	-	T

samples	N	E	q	fsp	nu	catr	chl	ctd	bi	g	st	ky	ep	amph	op	to	ap	zi
Q1egr	37°23'4.80"	27°45'24.30"	X	X	O	-	-	-	-	-	-	-	-	-	O	X	-	-
Q2	37°23'4.70"	27°45'24.30"	X	X	X	-	-	-	X	-	-	-	-	-	T	O	T	T
Q2 bis	37°23'4.70"	27°45'24.30"	X	X	X	-	-	-	X	-	-	-	-	-	T	X	T	T
Q3/Q3 bis	37°23'3.30"	27°45'25.30"	X	X	X	-	-	-	X	-	-	-	-	-	T	X	T	T
Q4	37°23'2.30"	27°45'21.70"	X	O	X	-	-	-	X	-	-	-	-	-	T	O	T	T
Q5	37°22'59.00"	27°45'18.40"	X	X	X	-	-	-	X(p1)	-	-	-	-	-	O	T	-	T
Q5	37°22'57.60"	27°45'15.70"	X	X	X	-	-	-	O(p1)	-	-	-	-	-	O	T	-	T
samples	N	E	q	fsp	nu	catr	chl	ctd	bi	g	st	ky	ep	amph	op	to	ap	zi
P1	37°24'58.30"	27°41'38.40"	X	O	O	-	-	-	bi	g	st	ky	ep	amph	op	to	ap	zi
P2	37°24'48.40"	27°41'38.50"	X	O	X, T(0/g)	-	O(p1), p2	T(p1)	X(p2)	g	st	ky	ep	-	X	-	-	T
P3	37°24'40.80"	27°41'46.30"	X	O	X	-	O(p1), 2	O(p2), T(0/g)	X(p1)	X(p1), p2	-	-	-	-	X	-	-	T
P4	37°24'43.10"	27°42'0.40"	X	X	X	X	X(p1)	-	X	-	-	-	T	-	O	T	-	T
P5	37°24'45.00"	27°42'48.10"	X	X	X	X	-	-	X(p1)	-	-	-	T(p1)	-	T	-	-	T
P6	37°24'30.40"	27°42'56.60"	X	O	O	-	2	-	T	-	-	-	T	-	O	-	-	T
P7	37°24'27.00"	27°43'7.40"	X	O	X, T(0/g)	-	T(p1), 2	X, T(0/g)	X(p1)	X(p1)	-	-	-	-	X	T	-	T
P8	37°24'18.30"	27°43'2.30"	X	T	T	-	-	-	T	-	-	-	-	-	O	-	-	T
P9	37°24'15.00"	27°43'6.00"	X	O	O	-	-	-	T	-	-	-	-	-	O	-	-	T
P10	37°24'17.10"	27°43'26.30"	X	O	X, T(0/g)	-	2	X, T(0/g)	X(p1)	X(p1)	-	-	T(0/g)	-	O	T	-	T
P11	37°24'7.60"	27°43'28.60"	O	X	O	X	T(p1)	-	O(p1)	-	-	-	O(p1)	-	T	-	-	T
P12	37°23'56.20"	27°43'45.50"	X	O	X, T(0/g)	-	T(p1)	O(0/g)	X(p1)	X(p1)	-	-	O(p1), T(0/g)	-	X	-	-	T
samples	N	E	q	fsp	nu	catr	chl	ctd	bi	g	st	ky	ep	amph	op	to	ap	zi
N1=gr	37°29'16.50"	27°37'10.30"	X	X	X	-	-	-	bi	-	-	-	ep	-	T	O	-	T
N2	37°29'16.40"	27°37'10.30"	X	X	X	-	-	-	X	-	-	-	-	-	T	T	-	T
N3	37°29'7.50"	27°37'8.70"	X	X	X	-	-	-	X	-	-	-	-	-	T	T	-	T
N4	37°28'59.70"	27°35'58.00"	X	O	X, T(0/g)	-	-	-	X	-	-	-	-	-	T	-	-	T
N5	37°28'58.50"	27°35'35.60"	X	X	X	X	-	-	O(p2)	-	-	-	O(p1), T(0/g)	-	O	-	-	T
N6bis	37°28'58.50"	27°35'35.60"	X	X	X	X	T(p1)	-	O(p2)	-	-	-	O(p1), p2	-	O	-	-	T
N6	37°28'59.60"	27°35'33.60"	X	X	X	X	X(p1)	-	O(p1)	-	-	-	X(p1)	-	O	-	-	T
N7p	37°28'55.90"	27°35'21.50"	X	X	X	X	X(p1)	T(0/g)	O(p1)	-	-	-	O(p1)	X(p1)	O	-	-	T
N7	37°28'55.90"	27°35'21.50"	X	X	X	X	X(p1), p2	T(0/g)	O(p1)	X(p1)	-	-	O(p1)	O	O	-	-	T
N8	37°28'48.50"	27°35'5.40"	X	X	X	X	2p	-	O(p2)	X(p2)	-	-	X(p1), p2	X(p1), p2	O	-	-	T
N9	37°28'37.30"	27°35'44.00"	X	O	X	-	2p	-	T(p1)	X(p1)	-	-	T(p1), T(0/g)	-	X	-	-	T
N10	37°28'33.00"	27°35'44.00"	X	O	X	X	2	X(p1)	T(p1)	-	-	-	O(p1)	-	O	-	-	T
N11	37°28'33.10"	27°35'44.00"	X	O	X, T(0/g)	-	2	X(p1), T(0/g)	O(p1)	O(p1)	-	-	-	-	O	-	-	T
N12	37°28'34.60"	27°35'45.20"	X	O	X	-	2	O(p1)	T(p1)	-	-	-	-	-	X	T	-	T
N12 bis	37°28'34.60"	27°35'45.20"	X	O	O	-	T(p1)	O(p1)	T(p1)	-	-	-	-	-	O	-	-	T

samples	N	E	q	fsp	ru	catd	chl	ctd	bi	g	sl	ky	ep	amph	op	to	ap	zi
E1	37°27'55.80"	27°32'48.30"	X	C	X	-	-	-	T	-	-	-	-	-	T	-	-	T
E2E	37°27'59.20"	27°32'48.90"	X	X	X	-	-	-	O	-	-	-	-	-	T	-	-	T
E3	37°28'03.00"	27°33'4.30"	X	C	X	-	O(p1), 2	X(p1)	X(p1)	-	-	-	-	-	O	-	-	T
E4	37°28'10.80"	27°33'13.50"	X	O	X	-	T(p), 2	X(p1)	T(p), 2	-	-	-	-	-	O	-	-	T
E5	37°28'17.10"	27°33'17.90"	X	X	X	-	T(p1), c2), 2	X(p1), p2)	X(p1)	-	-	-	O(p1)	-	O	-	-	T
E5 bis	37°28'30.10"	27°33'27.00"	X	X	X	-	X(p1), 2	-	X(p1), p2)	-	-	-	-	-	O	-	-	T
E6	37°29'15.10"	27°33'38.00"	X	X	X	-	T(p2), 2	-	O	-	-	-	-	-	O	-	-	T
E7	37°29'35.40"	27°33'55.20"	X	T	X	-	-	-	O	-	-	-	-	-	O	-	-	T
E7 2	37°29'33.40"	27°33'55.50"	X	X	X	-	-	-	O	-	-	-	-	-	O	-	-	T
E8	37°29'11.10"	27°34'2.60"	X	X	X	-	2	-	X(p1), p2)	-	-	-	T(p1)	-	X	-	-	T
E9	37°29'12.30"	27°34'11.70"	X	C	X	-	2	-	X	-	-	-	-	-	O	-	-	T
E10	37°29'19.00"	27°34'24.90"	X	C	X	-	-	-	X(p1), p2)	-	-	-	-	-	O	-	-	T
E11	37°29'29.30"	27°34'51.40"	X	C	X	-	-	-	X	-	-	-	-	-	T	-	-	T
E11 bis	37°29'29.30"	27°34'51.40"	X	C	X	-	-	-	X	-	-	-	-	-	T	-	-	T
E12	37°29'27.40"	27°34'30.40"	X	O	X	-	2	-	X(p1)	-	-	-	-	-	T	-	-	T
E13	37°29'25.10"	27°34'29.00"	X	X	X, T(0), 5	-	2	-	X(p1)	-	-	-	-	-	T	-	-	T
E14	37°29'27.00"	27°34'30.40"	X	X	X	-	2	-	X	-	-	-	-	-	T	-	-	T
E15	37°29'22.40"	27°34'28.90"	X	X	X	-	2	-	X	-	-	-	-	-	T	-	-	T
E16	37°29'21.80"	27°34'29.00"	X	X	X	-	2	-	X	-	-	-	-	-	T	-	-	T
E17	37°29'19.60"	27°34'27.90"	X	X	X	-	2	-	X	-	-	-	-	-	O	-	-	T
samples	N	E	q	fsp	ru	catd	chl	ctd	bi	g	sl	ky	ep	amph	op	to	ap	zi
F1	37°28'45.90"	27°33'22.10"	X	X	X	-	chl	ctd	X(p1)	-	-	ky	ep	amph	op	to	ap	zi
F2	37°28'43.30"	27°33'29.20"	X	X	X	-	2T	-	T(p1)	-	-	-	-	-	O	-	-	T
F3	37°28'41.90"	27°34'13.20"	X	C	X	-	-	-	X(p1), p2)	-	-	-	-	-	X	-	-	T
F4	37°28'43.60"	27°34'17.60"	X	C	X	-	-	-	X	-	-	-	-	-	O	-	-	T
F5	37°28'45.90"	27°34'36.80"	X	C	X	-	-	-	T(p1), p2)	-	-	-	-	-	O	-	-	T
F6	37°28'49.80"	27°34'36.70"	X	O	X	-	-	-	X(p1), 2	-	-	-	-	-	O	-	-	T
F7	37°28'43.10"	27°34'50.60"	X	O	X	-	O(p1), 2	O(p1)	X(p1), 2	-	-	-	-	-	O	-	-	T
F8	37°28'40.20"	27°34'58.90"	X	X	X	-	O(p1), 2	X(p1)	O(p1), 2	-	-	-	-	-	O	-	-	T
F9	37°28'35.60"	27°35'15.90"	X	X	X	-	T(p), 2	X(p1)	O(p1)	-	-	-	-	-	O	-	-	T
F10	37°28'27.20"	27°35'18.10"	X	X	X	-	-	-	X(p1), p2)	-	-	-	-	-	O	-	-	T
F11	37°28'27.00"	27°35'22.90"	X	X	X	-	O(p1), 2	-	X(p1), p2)	-	-	-	-	-	O	-	-	T
F12	37°27'54.70"	27°35'22.30"	X	X	X	-	O(p1), 2	-	X(p1), p2)	-	-	-	-	-	O	-	-	T
F13P	37°27'45.40"	27°35'8.14"	X	X	X	-	X(p2), 2	-	X(p1), p2), 2	-	-	-	-	-	O	-	-	T
F14	37°27'50.10"	27°34'58.40"	X	X	X	-	O(p1), 2	-	X(p1)	-	-	-	-	-	O	-	-	T
F15	37°27'40.40"	27°34'33.90"	X	X	X	-	X(p1), 2	-	O(p1), 2	-	-	-	-	-	O	-	-	T
F16	37°27'40.40"	27°34'11.80"	X	X	X	-	X(p1), 2	-	X(p1), 2	-	-	-	-	-	O	-	-	T
F17	37°27'38.00"	27°33'55.50"	O	C	X	-	-	-	O, 2	-	-	-	-	-	O	-	-	T
samples	N	E	q	fsp	ru	catd	chl	ctd	bi	g	sl	ky	ep	amph	op	to	ap	zi
I1=gr	37°29'19.90"	27°33'2.10"	X	X	X	-	chl	ctd	X(p1)	-	-	ky	ep	amph	op	to	ap	zi
I2	37°29'18.60"	27°33'1.80"	X	X	X, T(0), 5	-	2	-	O	-	-	-	-	-	O	-	-	T
I3	37°29'17.50"	27°33'2.00"	X	X	X	-	T(p2), 2	-	X(p1)	-	-	-	-	-	O	-	-	T
I4	37°29'15.30"	27°32'55.20"	X	O	X	-	T?, 2	-	X(p1), p2)	-	-	-	-	-	T	-	-	T
I5	37°29'25.50"	27°33'20.10"	X	X	X	-	-	-	X(p1)	-	-	-	-	-	T	-	-	T
I6 bis	37°29'25.50"	27°33'20.10"	X	X	O	-	-	-	X(p1)	-	-	-	-	-	T	-	-	T
I7	37°29'25.40"	27°33'19.90"	X	X	X	-	-	-	O	-	-	-	-	-	T	-	-	T
I8P	37°29'25.40"	27°33'19.90"	X	X	X	-	-	-	X(p1)	-	-	-	-	-	T	-	-	T
I9	37°29'22.70"	27°33'20.10"	X	O	X	-	2	-	X(p1)	-	-	-	-	-	T	-	-	T
I10	37°29'15.70"	27°33'13.90"	X	X	X	-	2	-	X(p1)	-	-	-	-	-	T	-	-	T
I11	37°29'18.70"	27°33'4.20"	X	X	X	-	2	-	X(p1)	-	-	-	-	-	T	-	-	T
I12	37°29'15.00"	27°32'52.70"	X	X	X	-	2	-	X(p1)	-	-	-	-	-	T	-	-	T
samples	N	E	q	fsp	ru	catd	chl	ctd	bi	g	sl	ky	ep	amph	op	to	ap	zi
M1	37°28'23.10"	27°35'31.40"	X	C	X	-	chl	ctd	X(p1)	-	-	ky	ep	amph	op	to	ap	zi
M2	37°28'10.90"	27°35'35.80"	X	X	X	-	T?, 2	-	O	-	-	-	-	-	O	-	-	T
M3	37°28'1.40"	27°35'40.10"	O	X	X	-	2	-	X(p1)	-	-	-	-	-	O	-	-	T
M4	37°27'55.10"	27°35'40.20"	X	X	X	-	T?, 2	-	X	-	-	-	-	-	O	-	-	T
M5	37°27'28.30"	27°35'17.40"	X	X	X	-	2	-	X	-	-	-	-	-	O	-	-	T

samples	N	E	q	isp	mu	carb	chl	ctd	bi	g	st:	sy	ep	amph	op	to	ap	zi
K1	37°29'19.80"	27°38'37.30"	X	X	X	-	-	-	X	-	-	-	T	-	-	-	-	T
K2	37°29'19.80"	27°38'37.30"	X	X	X	-	-	-	X	-	-	-	-	-	T	T	-	T
K3	37°29'13.80"	27°38'35.50"	X	X	X	-	-	-	X(p1)	X(p1)	-	-	-	-	T	-	-	T
K4	37°28'46.90"	27°38'26.90"	X	X	X	-	-	-	X	-	-	-	-	-	T	X	-	T
K5	37°28'28.40"	27°38'26.30"	X	X	X	-	-	-	X(p1), T(0/g)	X(p1)	-	-	-	-	O	-	-	T
K6(K6P)	37°28'18.60"	27°38'28.70"	X	X	X	-	2	-	X(p1)	X(p1)	-	-	-	-	O	T	-	T
K7	37°27'59.40"	27°38'50.20"	X	O	X	X	2	-	X(p1)	X(p1)	-	-	-	-	T	-	-	T
K7P	37°27'59.40"	27°38'50.20"	X	X	X	-	-	-	X	-	-	-	-	-	O	O	-	T
K8	37°27'51.40"	27°38'55.30"	X	X	X	-	2	-	X(p1)	T(p1)	-	-	-	-	O	O	-	T
K9	37°27'48.00"	27°38'51.90"	X	O	X, T(0/g)	-	2	-	X(p1)	X(p1)	-	-	-	-	O	O	-	T
K10	37°27'40.20"	27°38'50.20"	X	X	X	-	-	-	X	-	-	-	-	-	T	O	-	T
K11	37°27'33.20"	27°38'42.70"	X	O	X	-	2	-	X	-	-	-	-	-	T	O	-	T
K12P	37°27'22.70"	27°38'36.00"	X	X	X	-	2 T?	X(p1)	O(p1)	O(p1)	-	-	-	-	O	T	-	T
K12P bis	37°27'22.70"	27°38'36.00"	X	X	X, T(0/g)	-	2	O(p1), T(0/g)	T(p1)	X(p1)	-	-	O(p1), T(0/g)	-	X	T	-	T
K13	37°27'12.80"	27°38'52.60"	X	X	X, T(0/g)	-	2	T(0/g)	O(p1)	X(p1)	-	-	-	-	O	T	-	T
K14	37°27'16.70"	27°38'42.90"	X	O	X, T(0/g)	-	2	X(o1), T(0/g)	O(p1)	X(p1)	-	-	-	-	O	T	-	T
K15	37°26'49.20"	27°38'35.70"	X	O	X, T(0/g)	-	2	X(o1), T(0/g)	O(p1)	X(p1)	-	-	-	-	X	T	-	T
K16	37°26'30.80"	27°38'37.60"	O	X	X, T(0/g)	-	2	X(o1), T(0/g)	O(p1)	O(p1)	-	-	-	-	O	T	-	T
K17(K17 bis)	37°26'30.80"	27°38'37.60"	X	O	X	-	2	X(p1)	T	-	-	-	T(p1)	-	O	-	-	T
K18	37°26'33.40"	27°38'22.80"	X	X	X	-	-	-	O(p1)	X(p1)	-	-	-	-	O	-	-	T
K19	37°26'24.90"	27°38'37.10"	X	O	X, T(0/g)	-	2	X(o1), T(0/g)	O	-	-	-	-	-	X	T	-	T
K20	37°26'14.80"	27°38'18.60"	X	X	X	-	-	-	O	-	-	-	-	-	X	T	-	T
K21	37°25'58.00"	27°38'17.20"	X	O	X	-	-	-	T(p1)	-	-	-	-	-	X	-	-	T
samples	N	E	q	isp	mu	carb	chl	ctd	bi	g	st:	sy	ep	amph	op	to	ap	zi
O1	37°24'37.50"	27°44'19.70"	X	X	X	-	-	-	bi	g	st:	sy	ep	amph	op	to	ap	zi
O2	37°24'37.50"	27°44'19.70"	X	X	X	-	-	-	T	-	-	-	-	-	O	X	-	T
O3	37°24'36.30"	27°44'21.00"	X	X	X	-	-	-	X	-	-	-	-	-	T	O	-	T
O4	37°24'30.70"	27°44'21.70"	X	O	X, T(0/g)	-	-	-	X(p1)	X(p1)	-	-	-	-	T	O	-	T
O4 bis	37°24'30.70"	27°44'21.70"	X	O	X, T(0/g)	-	-	-	X(p1)	X(p1)	-	-	-	-	T	O	-	T
O5	37°24'26.10"	27°44'19.70"	X	O	X, T(0/g)	-	-	-	X(p1)	X(p1)	-	-	-	-	T	T	-	T
O6	37°24'20.00"	27°44'22.20"	X	O	X, T(0/g)	-	2	-	X(p1)	X(p1)	-	-	-	-	T	T	-	T
O7	37°24'14.40"	27°44'31.30"	X	O	X	-	-	-	X	-	-	-	-	-	O	-	-	T
O8	37°24'14.40"	27°44'31.30"	X	O	X, T(0/g)	-	2	-	X(p1)	X(p1)	-	-	-	-	T	T	-	T
O9	37°24'1.10"	27°44'49.10"	X	T	X	-	-	-	T	-	-	-	-	-	O	-	-	T
O10	37°23'58.20"	27°44'53.10"	X	O	X	-	-	-	X	-	-	-	-	-	T	O	-	T
O11	37°23'50.20"	27°44'56.20"	X	T	X	-	-	-	X	-	-	-	-	-	O	O	-	T
O12	37°23'46.60"	27°44'54.90"	X	O	X	-	2	-	X(p1)	X(p1)	-	-	-	-	O	T	-	T
O13	37°23'37.40"	27°45'3.40"	X	O	X	-	-	-	X(p1), 2	X(p1)	-	-	-	-	O	-	-	T
O14	37°23'36.10"	27°45'13.90"	X	O	X	-	2 T?	-	X	-	-	-	-	-	O	-	-	T
O15	37°23'47.50"	27°45'13.30"	X	X	X	-	-	-	X	-	-	-	-	-	O	X	-	T
O16	37°23'41.20"	27°45'13.60"	X	O	X	-	-	-	X(p1)	X(p1)	-	-	-	-	T	O	-	T
O17	37°23'24.00"	27°45'54.30"	X	X	X, T(0/g)	-	-	-	O(p1), 2	X(p1)	-	-	T(0/g)	-	X	O	-	T
O18	37°22'59.90"	27°45'17.40"	X	O	X	-	-	-	O(p1)	X(p1)	-	-	-	-	O	T	-	T
O23	37°22'36.90"	27°44'24.30"	O	O	X	O	X(p1)	X(p1)(p2)	O(p1)	-	-	-	O(p1)	-	O	-	-	T
O19	37°22'33.20"	27°44'15.90"	O	T	T	-	2	-	T	-	-	-	-	-	O	-	-	T
O20	37°22'14.60"	27°42'39.40"	O	O	X	-	-	-	O	-	-	-	-	-	X	-	-	T
O21	37°22'13.40"	27°42'44.60"	X	X	X	-	-	-	O(p1)	O(p1)	-	-	-	-	O	-	-	T
O22	37°22'18.40"	27°42'55.80"	X	X	X	-	-	-	O(p1)	O(p1)	-	-	-	-	O	T	-	T
O23	37°22'6.40"	27°43'31.70"	X	X	X	-	-	-	-	-	-	-	-	-	T	-	-	T
O24	37°21'59.70"	27°43'27.80"	X	X	X	-	-	-	O(p1)	O(p1)	-	-	-	-	O	-	-	T
O25	37°21'45.20"	27°43'49.00"	X	O	O	-	-	-	O(p1)	O(p1)	-	-	-	-	O	T	-	T
O26	37°21'21.50"	27°41'58.00"	X	O	X	-	-	-	O(p1)	O(p1)	-	-	-	-	T	T	-	T
O27	37°22'53.40"	27°35'59.10"	X	O	X	-	-	-	O(p1)	O(p1)	-	-	-	-	O	-	-	T

samples	N	E	q	fsp	rU	catc	chl	ctd	bl	g	st	ky	eo	ampn	op	lo	ap	zi
T1	37°40'35.10"	27°31'57.90"	X	X	X	-	2	-	X(p1)	X(p1)	-	-	-	-	X	-	-	T
T2	37°40'32.80"	27°31'29.00"	X	X	X	-	-	-	X	-	-	-	-	-	T	-	-	T
T3	37°40'32.80"	27°31'38.00"	X	X	X	-	-	-	O	-	-	-	-	-	T	-	-	T
T5	37°40'25.10"	27°31'35.10"	X	X	X	-	-	-	X	-	-	-	-	-	T	-	-	T
T6	37°40'22.30"	27°31'35.70"	X	O	X	-	O(p1), 2	X(p1), 2	T(p1)	-	O(p2)	-	O(p3)	-	X	T	-	T
samples	N	E	q	fsp	rU	catc	chl	ctd	bl	g	st	ky	eo	ampn	op	lo	ap	zi
BA1	37°33'32.10"	27°23'57.70"	X	O	X	-	2	-	O	-	-	-	eo	-	O	-	-	T
BA2	37°33'35.10"	27°24'18.90"	X	O	X	-	2	-	X	-	-	-	O	-	X	-	-	T
BA3	37°33'38.60"	27°24'14.20"	X	X	X	-	T(p1)	-	X(p1)	-	-	-	-	-	O	-	-	T
BA4	37°33'45.40"	27°24'21.50"	X	X	X	-	-	-	X	-	-	-	-	-	O	-	-	T
BA5	37°33'45.60"	27°24'15.60"	X	X	X	-	-	-	X(p1)	-	-	-	-	-	O	-	-	T
BA6	37°33'51.50"	27°24'14.50"	X	X	X	-	X(p1)	-	X(p1), f/isp	-	-	-	-	-	O	-	-	T
BA7	37°33'54.70"	27°24'10.10"	X	X	X	-	X(p1)	-	T(p1)	-	-	-	-	-	O	-	-	T
BA8	37°33'54.90"	27°24'10.10"	X	X	X	-	-	-	X	-	-	-	-	-	O	-	-	T
BA9	37°34'15.40"	27°24'14.14"	X	O	X	-	-	-	X	-	-	-	-	-	O	-	-	T
BA10P	37°32'55.30"	27°23'32.70"	T	-	-	-	-	-	-	-	-	-	-	-	-	-	-	-
BA11	37°33'18.00"	27°23'28.90"	X	O	X	-	X(p1)	-	X(p1)	-	-	-	X(p1)	-	X	T	-	T
BA12	37°33'13.30"	27°23'34.80"	X	X	X	-	T(f/isp)	-	X(p1)	-	-	-	-	-	O	-	-	T
BA13	37°33'17.10"	27°23'44.10"	X	X	X	-	O(p1), 2	-	X(p1)	-	-	-	T	-	O	-	-	T
BA14	37°33'12.30"	27°24'11.50"	X	X	X	-	O(p1)	-	X(p1)	-	-	-	O	-	X	-	-	T
BA15	37°33'7.90"	27°24'20.30"	X	X	X	-	T(p1)	-	X(p1)	-	-	-	-	-	O	-	-	T
BA16	37°33'4.70"	27°24'29.70"	X	X	X	-	X(p1), 2	-	X(p1)	A	-	-	-	-	O	-	-	T
BA17	37°33'12.90"	27°24'39.40"	X	X	X	-	T(p1), 2	-	X(p1)	-	-	-	-	-	O	-	-	T
BA18	37°33'13.10"	27°24'47.90"	X	X	X	-	-	-	T	-	-	-	-	-	X	-	-	T
BA19	37°33'15.80"	27°25'5.90"	X	X	X	-	2	-	O	-	-	-	-	-	X	-	-	T
BA20	37°33'14.30"	27°25'13.04"	X	X	X	-	T(p1), 2	-	O(p1)	-	-	-	-	-	X	-	-	T
BA21	37°33'12.70"	27°25'15.50"	X	X	X	-	T(p1), 2	-	X(p1)	-	-	-	-	-	X	-	-	T
BA22	37°33'17.20"	27°25'28.90"	X	X	X	-	T(p1), 2	-	T(p1)	-	-	-	O	-	X	-	-	T
BA23	37°33'20.30"	27°25'38.90"	X	X	X	-	X(p1)	-	T(p1)	-	-	-	-	-	X	-	-	T
BA24	37°33'23.80"	27°25'49.50"	X	X	X	-	T(p1), 2	-	T(p1)	A	-	-	-	-	O	-	-	T
BA25	37°33'25.00"	27°25'55.30"	X	X	X	-	T(p1), 2	-	O(p1)	-	-	-	-	-	O	-	-	T
BA26	37°33'28.10"	27°26'2.30"	X	X	X	-	-	-	O(p1)	-	-	-	-	-	X	-	-	T
samples	N	E	q	fsp	rU	catc	chl	ctd	bl	g	st	ky	eo	ampn	op	lo	ap	zi
GU1	37°37'24.70"	27°34'27.00"	X	X	X	-	T(p1), 2	-	O(p1)	X(p1)	-	-	O(p1)	-	O	-	-	T
GU2	37°37'29.10"	27°34'29.20"	X	O	X	-	-	-	O(p1)	-	-	-	O(p1)	-	X	-	-	T
GU3	37°37'33.60"	27°34'11.40"	X	O	O	-	-	-	T	-	-	-	-	-	O	-	-	T
GU3b	37°37'33.60"	27°34'11.40"	O	O	O	-	-	-	T	-	-	-	-	-	X	-	-	T
GU4	37°37'38.40"	27°33'55.50"	O	X	O	-	-	-	X	-	-	-	-	-	X	-	-	T
GU5	37°37'31.40"	27°34'0.10"	X	X	X	-	-	-	X	-	-	-	-	-	T	-	-	T
GU6	37°37'31.00"	27°33'54.20"	X	O	X	-	-	-	X	-	-	-	-	-	T	-	-	T
GU7	37°37'31.60"	27°33'49.20"	X	X	X	-	T(p1)	-	X(p1)	O(p1)	-	-	-	-	T	X	O	T
GU8	37°37'27.20"	27°33'55.70"	X	O	O	-	T(p1)	-	X	-	-	-	-	-	T	-	-	T
GU9	37°37'14.90"	27°32'54.30"	X	O	O	-	T(p1)	-	T(p1)	-	-	-	-	-	T	-	-	T
GU10	37°37'14.00"	27°32'20.20"	X	X	X	-	T(p1), 2	T(f/isp)	O(p1), 2	X(p1), 2	T(p2)	-	-	-	X	-	-	T
GU11	37°37'16.80"	27°31'15.10"	X	X	X	-	2	-	X(p1)	-	-	-	-	-	X	-	-	T
GU12	37°37'34.90"	27°30'50.50"	X	X	X	-	O(p1), 2	-	X(p1)	X(p1)	-	-	-	-	X	-	-	T

samples	N	E	q	fsp	nu	carb	chl	cld	bi	g	st	ky	ep	amph	op	ic	ap	zi
YE1	37°3443.20"	27°2722.10"	X	X	-	-	2	-	X	-	-	-	-	-	T	T	-	T
YE2	37°3444.10"	27°2713.30"	X	X	-	-	2	-	X	-	-	-	-	-	X	T	-	T
YE3	37°3450.10"	27°2731.30"	X	X	-	-	2	-	X	A	-	-	-	-	X	T	-	T
YE4P	37°3452.10"	27°2657.50"	X	X	-	-	2	-	O(p1)	X(p1)	-	-	-	-	X	T	-	T
YE5	37°3458.30"	27°2651.70"	X	X	-	-	T(c1), 2	-	O(p1)	O(p1)	-	-	-	-	O	T	-	T
YE6	37°353.20"	27°2643.40"	X	X	-	-	O(p1), 2	-	O	A	-	-	-	-	X	T	-	T
YE7	37°352.30"	27°2625.70"	X	X	-	-	2	-	X	A	-	-	-	-	X	T	-	T
YE7.2	37°352.30"	27°2625.70"	X	X	-	-	2	-	X	A	-	-	-	-	X	T	-	T
YE7.3	37°352.30"	27°2625.70"	X	X	-	-	T(c1), 2	-	O(p1)	-	-	-	-	-	O	T	-	T
YE8	37°3511.20"	27°2620.40"	X	X	-	-	O(p1), 2	-	X(p1)	-	-	-	-	-	O	T	-	T
YE9	37°3525.10"	27°2621.50"	X	X	-	-	O(p1), 2	-	O(p1)	A	-	-	-	-	O	T	-	T
YE10	37°3530.80"	27°2617.50"	X	X	-	-	2	-	O	-	-	-	-	-	T	T	-	T
YE11	37°3520.80"	27°2556.90"	X	X	-	-	2	-	O	-	-	-	-	-	O	T	-	T
YE12	37°356.30"	27°2543.10"	X	O	-	-	-	-	T	-	-	-	-	-	O	T	-	T
YE13	37°353.40"	27°2535.50"	X	X	-	-	O(p1), 2	-	O(p1)	-	-	-	-	-	O	T	-	T
YE14	37°3449.60"	27°254.20"	X	X	-	-	O(p1), 2	-	T(p1)	-	-	-	-	-	O	T	-	T
samples	N	E	q	fsp	nu	carb	chl	cld	bi	g	st	ky	ep	amph	op	ic	ap	zi
TE1	37°3552.00"	27°2757.10"	X	X	-	-	chl	cld	bi	g	st	ky	ep	amph	op	ic	ap	zi
TE2	37°3623.20"	27°2812.90"	X	X	-	-	2	-	O(p1)	-	-	-	-	-	O	T	-	T
TE3	37°3629.30"	27°2819.30"	X	X	-	-	X(c1), 2	-	O	A	-	-	-	-	X	T	-	T
TE4	37°3642.30"	27°2816.80"	X	X	-	-	O(p2), 2	-	O(p1)(p2), T(p)/fsp	X(p1), O(p)/fsp	-	-	-	-	O	T	-	T
TE5	37°3650.10"	27°283.20"	X	X	-	-	-	-	T(p1)	-	-	-	-	-	X	T	-	T
TE6	37°3655.40"	27°2758.00"	X	X	-	-	T(c1), 2	-	O(p1)(p2)	O(p2)	-	-	-	-	O	T	-	T
TE7	37°3658.90"	27°2758.30"	X	X	-	-	O(p1), 2	-	O(p1)	X(p1)	-	-	-	-	X	T	-	T
TE8	37°372.80"	27°2753.40"	X	X	-	-	2	-	O	-	-	-	-	-	O	T	-	T
TE9	37°3657.00"	27°2715.74"	X	X	-	-	T(c1), 2	-	O(p1)	O(p2), O(fsp)	-	-	-	-	O	T	-	T
TE10	37°3658.80"	27°2655.20"	X	X	-	-	X(p1), 2	-	O(p1), T(p)/fsp	O, O(fsp)	-	-	-	-	O	T	-	T
samples	N	E	q	fsp	nu	carb	chl	cld	bi	g	st	ky	ep	amph	op	ic	ap	zi
R1	37°3751.40"	27°2445.50"	X	O	-	-	2	-	O	-	-	-	-	-	O	T	-	T
R2	37°3752.40"	27°2456.00"	X	O	-	-	2	-	O	A	-	-	-	-	O	T	-	T
R3	37°3753.50"	27°2556.40"	X	O	-	-	2	-	X(p1)	X(c1)	-	-	-	-	X	T	-	T
R4/R4P	37°3751.80"	27°2526.30"	X	X	-	-	O(p1), T(p)/fsp	-	O(p1), T(p)/fsp	O, O(fsp)	-	-	-	-	O	T	-	T
R5	37°3736.30"	27°2544.00"	X	X	-	-	2	-	X	O, O(fsp)	-	-	-	-	X	T	-	T
R6	37°3737.20"	27°2550.80"	X	X	-	-	O(p1), T(p)/fsp	-	T(p1), T(p)/fsp	T(p)/fsp	-	-	-	-	O	T	-	T
R7	37°3745.50"	27°260.40"	X	X	-	-	X(p1), T(p)/fsp	-	O(p1), T(p)/fsp	T(p), T(p)/fsp	-	-	-	-	O	T	-	T
R8	37°3750.90"	27°2611.10"	X	X	-	-	X(c1), 2	-	X(p1)	O(p1), O(fsp)	-	-	-	-	O	T	-	T
R8P	37°3750.90"	27°2611.10"	X	X	-	-	X(c1), 2	-	X(p1)	O(p1), O(fsp)	-	-	-	-	O	T	-	T
R9	37°373.80"	27°2636.70"	X	X	-	-	X(p1), 2	-	X(p1)	O(p1), O(fsp)	-	-	-	-	O	T	-	T
R10	37°3659.60"	27°2628.20"	X	X	-	-	O(p1), 2	-	O(p1)	X(p1), O(fsp)	-	-	-	-	O	T	-	T
samples	N	E	q	fsp	nu	carb	chl	cld	bi	g	st	ky	ep	amph	op	ic	ap	zi
K11	37°3726.00"	27°3222.70"	X	X	-	-	chl	cld	bi	g	st	ky	ep	amph	op	ic	ap	zi
K12	37°3731.80"	27°3216.70"	X	X	-	-	-	-	O	-	-	-	-	-	O	T	-	T
K13	37°3722.00"	27°324.30"	X	X	-	-	-	-	X(p1)	X(c1)	-	-	-	-	O	T	-	T
K14	37°3729.40"	27°3151.70"	X	X	-	-	2	-	X(p1)	X(c1)	-	-	-	-	O	T	-	T
K15	37°3743.40"	27°3130.10"	X	X	-	-	O(p1), 2	-	X(p1)(p2)	O(p2)	-	-	-	-	O	T	-	T
K16	37°3745.60"	27°3120.70"	X	X	-	-	2	-	X(p1)	X(c1)	-	-	-	-	O	T	-	T
K17	37°3620.10"	27°3030.70"	X	X	-	-	O(p1), T(p)/fsp	-	X(p1)(p2), T(p)/fsp	X(p2), O(fsp)	-	-	-	-	O	T	-	T
K18	37°3623.00"	27°3028.00"	X	X	-	-	O(p1), T(p)/fsp	-	X(p1)(p2), T(p)/fsp	O(p2), O(fsp)	-	-	-	-	O	T	-	T
K19	37°3836.10"	27°3026.50"	X	X	-	-	X(p1), T(p)/fsp	-	X(p1), T(p)/fsp	O(p1), O(fsp)	-	-	-	-	O	T	-	T
K10	37°3840.90"	27°3054.60"	X	X	-	-	O(p1), 2	-	X(p1)	O(p1), O(fsp)	-	-	-	-	X	T	-	T

samples	N	E	g	fsp	mu	carb	chl	cid	bi	g	st	ky	ep	amph	op	to	ap	zi
KG1	37*4153.63*	27*3038.90"	X	X	X	-	-	-	O	-	-	-	-	-	O	X	O	T
KG2	37*4057.23*	27*317.70"	X	X	X	-	-	-	O	-	-	-	-	-	O	X	T	T
KG3	37*4070.93*	27*3049.90"	X	X	X	-	X(p1).2	T(0/g)	X(p1)	X(p1)	-	-	-	-	X	-	T	T
KG4	37*4223.83*	27*3133.30"	X	X	X	-	-	-	O	-	-	-	-	-	X	-	T	T
KG5	37*4142.19*	27*3139.00"	X	O	X	-	-	-	X	-	-	-	-	-	X	-	O	T
KG6	37*4127.33*	27*3144.90"	X	X	X	-	X(p1).2	T(0/g)	X(p1)	X(p1)	-	-	-	-	O	X	T	T
KG6bis	37*4127.33*	27*3144.90"	X	X	X	-	X(p1).2	T(0/g)	X(p1)	X(p1)	-	-	-	-	O	X	T	T
KG7	37*4022.43*	27*3141.00"	X	O	X	-	-	-	X	-	-	-	-	-	O	-	O	T
KG8	37*3846.53*	27*3059.80"	X	X	X	-	X(p1).2	-	X(p1)	O(p1)	-	-	-	-	O	-	T	T
KG9	37*3915.43*	27*3054.90"	X	X	X	-	X(p1).2	-	X(p1)	X(p1),0(fsp)	-	-	-	-	O	-	T	T
KG10P	37*3936.03*	27*3059.80"	X	X	X	-	X(p1).2	-	X(p1)	-	-	-	-	-	O	-	T	T
KG11	37*4037.53*	27*3142.00"	X	X	X	-	X(p1).2	-	X(p1)	-	-	-	-	-	O	-	O	T
KG12	37*4114.43*	27*3150.50"	X	X	X	-	-	-	X(p1)	X(p1)	-	-	-	-	X	-	T	T
KG13	37*4154.43*	27*3210.34"	X	X	X	-	-	-	O	-	-	-	-	-	O	-	T	T
KG14	37*4223.93*	27*3263.70"	X	X	X	-	-	-	O	-	-	-	-	-	O	-	T	T
KG15	37*4345.03*	27*3337.70"	X	X	X	-	-	-	X	-	-	-	-	-	O	-	T	T
CPA1	37*4425.43*	27*3413.50"	X	X	O	-	-	-	X	-	-	-	-	-	T	-	T	T
CPA2	37*4621.33*	27*3659.00"	X	X	X	-	-	-	O	-	-	-	-	-	T	-	T	T
samples	N	E	g	fsp	mu	carb	chl	cid	bi	g	st	ky	ep	amph	op	to	ap	zi
GU1T	37*4579.53*	27*3727.10"	X	X	T	-	2	-	bi	g	st	ky	ep	amph	op	to	ap	zi
GU2T	37*4570.43*	27*3715.30"	X	X	X	-	2	-	X(p1)	X(p1)	-	X(p1)	-	-	O	-	T	T
GU3T	37*4498.53*	27*3715.50"	X	X	X	-	-	-	X(p1)	O(p1)	-	-	-	-	T	-	T	T
GU4T	37*4418.93*	27*3713.60"	X	X	X	-	2	-	X(p1)	X(p1)	-	O(p1)	-	-	O	-	O	T
GU5T	37*4415.30*	27*3776.30"	X	X	X	-	2	-	X(p1)	O(p1)	-	-	-	-	O	-	T	T
GU6T	37*4394.13*	27*3657.90"	O	O	T	-	-	-	X(p1)	O(p1)	-	-	-	-	O	-	T	T
GU7T	37*4251.53*	27*3776.40"	X	X	X	-	2	-	X(p1)	X(p1)	-	-	O(p1)	-	O	X	O	T
GU8T	37*4272.60*	27*3730.90"	T	-	T	-	-	-	X(p1)	X(p1)	-	-	O(p1)	-	O	-	T	T
GU9T	37*4163.33*	27*3732.00"	T	-	T	-	-	-	T(p1)	-	-	-	-	-	-	-	-	-
GU10T	37*4412.33*	27*3720.70"	X	X	O	-	2	-	X(p1)	X(p1)	-	-	-	-	O	-	T	T
samples	N	E	g	fsp	mu	carb	chl	cid	bi	g	st	ky	ep	amph	op	to	ap	zi
KO1	37*4592.83*	27*4243.00"	X	X	O	-	-	-	bi	g	st	ky	ep	amph	op	to	ap	zi
KO2	37*4597.03*	27*3943.00"	X	X	X	-	-	-	T	O(p1)	-	-	O	-	T	-	-	-
KO3	37*4548.13*	27*3941.60"	X	X	X	-	-	-	X(p1)	O(p1)	-	-	-	-	O	-	-	-
KO4	37*462.90*	27*3943.80"	X	X	X	-	2	-	X(p1)	X(p1)	-	-	-	-	O	-	-	-
KO5	37*462.90*	27*3943.80"	X	X	X	-	-	-	X	-	-	-	-	-	O	-	-	-
KO6	37*467.00*	27*3950.10"	X	X	X	-	-	-	X(p1)	O(p1)	-	-	O(p1)	-	O	-	-	-
KO6b	37*461.90*	27*4322.00"	X	X	X	-	-	-	O(p1)	X(p1)	-	-	-	-	O	-	-	-
KO7	37*461.90*	27*4419.30"	X	X	X	-	-	-	X(p1)	X(p1)	-	-	-	-	O	-	-	-
samples	N	E	g	fsp	mu	carb	chl	cid	bi	g	st	ky	ep	amph	op	to	ap	zi
Z1	37*353.30*	28*3113.00"	X	X	O	-	-	-	bi	g	st	ky	ep	amph	op	to	ap	zi
Z2	37*3826.13*	28*3443.80"	X	X	X	-	X(p1)	-	T	-	-	-	O	-	O	-	-	-
Z3	37*3847.33*	28*3447.80"	X	X	X	-	O(p1).2	-	O(p1)	X(p1)	-	-	T	-	X	-	-	-
Z4	37*3856.33*	28*3454.90"	X	X	X	-	O(p1)E2).2	-	T(p2)	O(p1)	-	-	T	-	X	-	-	-
Z5	37*3862.93*	28*3474.60"	X	X	X	-	-	-	O	-	-	-	-	-	X	-	-	-
Z6	37*3829.03*	28*3359.00"	X	X	X	-	T(p1)	-	X(p1)	-	-	-	-	-	X	-	-	-
Z7	37*4021.53*	28*3257.00"	X	-	T	-	-	-	-	-	-	-	-	-	X	-	-	-
Z8	37*4021.33*	28*3322.90"	X	-	X	-	-	-	-	-	-	-	-	-	X	-	-	-
Z9	37*4025.73*	28*3348.80"	X	O	X	-	-	-	T(p1).2	-	-	-	-	-	X	-	-	-
Z10	37*5110.63*	28*3293.40"	X	X	X	-	2	-	X(p1)	X(p1)	-	-	-	-	O	-	-	-
Z11	37*4390.23*	28*4434.10"	X	X	O	-	T(p1).2	-	O(p1)	X(p1)	-	-	-	-	O	-	-	-
Z12	37*4432.53*	28*4511.50"	X	O	X.2	-	T(p1).2	X(p1)O2).T(0/g)	T(p1).2	R(p1)	-	-	O(p2)	-	X	-	-	-
Z13	37*4453.43*	28*4455.60"	X	O	X	-	2	X(p1)	T(p1)	O(p1)	-	-	O	-	X	-	-	-
Z14	37*4349.03*	28*4334.00"	X	O	O	-	-	-	T	O(p1)	-	-	-	-	X	-	-	-
Z15	37*4173.70*	28*4053.20"	X	O	X	-	2	-	O(p1)	X(p1)	-	-	-	-	-	-	-	-
Z16	37*4653.03*	28*4038.40"	X	X	X	-	2	-	T(p1)	X(p1)	-	-	-	-	O	-	-	-
samples	N	E	g	fsp	mu	carb	chl	cid	bi	g	st	ky	ep	amph	op	to	ap	zi
EM1	37*4548.43*	27*5010.24"	X	X	X	-	-	-	bi	X(p1)	-	-	T(0/g)	-	X	-	-	-
EM1b	37*4548.43*	27*5010.24"	X	X	X	-	-	-	T	X(p1)	-	-	O(p1)	-	X	-	-	-
EM2	37*4512.33*	27*5145.30"	X	O	X.1,T(0/g)	-	-	-	O(p1)	X(p1)	-	-	O(p1)	-	X	-	-	-
EM1P	37*4512.33*	27*5145.30"	X	X	X.1,T(0/g)	-	-	-	T	X	-	-	O(p1)	-	X	-	-	-

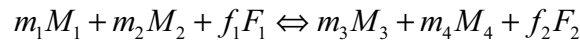


## Appendix 3

### Thermodynamic in petrology & THERMOCALC software

#### INTRODUCTION

Thermodynamic of solid solution is a large subject which involves mathematic, physic and mineralogy background. Because we used exclusively THERMOCALC software (Powell *et al.*, 1998) during this thesis work, we will present here a summary about thermodynamic principles and try to explain succinctly the method used by THERMOCALC to solve non linear equation. More details can be found for instance in Powell (1978), Holland & Powell (1985), Powell & Holland (1985), Powell & Holland (1988), Holland & Powell (1990), Holland & Powell (1998), Powell *et al.* (1998), and Will (1998*a*, 1998*b*). Consider the reaction involving  $M_1$ ,  $M_2$ ,  $M_3$ ,  $M_4$  end-members of minerals and  $F_1$ ,  $F_2$  fluids:



where  $m_1$ ,  $m_2$ ,  $m_3$ ,  $m_4$ ,  $f_1$ , and  $f_2$  are respectively the stoichiometric coefficients of minerals end-members and fluids. At the equilibrium the molar Gibbs free energy of reaction  $\Delta_r G_{ml}^{T,P}$  at T and P is:

$$\begin{aligned} \Delta_r G_{ml}^{T,P} &= \Delta_r H_{ml}^{T_0,P_0} - T \Delta_r S_{ml}^{T_0,P_0} + \int_{T_0}^T \Delta C_p dt - T \int_{T_0}^T \frac{\Delta C_p dt}{T} + \int_{P_0}^P \Delta V_{solid} dp \\ &+ RT \ln \frac{(a_{M_3})^{m_3} (a_{M_4})^{m_4} (a_{F_2})^{f_2}}{(a_{M_1})^{m_1} (a_{M_2})^{m_2} (a_{F_1})^{f_1}} = 0 \end{aligned} \quad (1)$$

with T in Kelvin and P in kbar:

$-\Delta_r H_{ml}^{T_0,P_0}$  molar enthalpy of reaction at  $T_0$  and  $P_0$  (1bar and 298 K) calculated via molar enthalpy of formation from minerals end-members and fluids ( $\text{kJ.mol}^{-1}$ ).

-  $\Delta_r S_{ml}^{T_0, P_0}$  molar entropy of reaction at  $T_0$  and  $P_0$  (1 bar and 298 K) calculated via molar entropy of minerals end-members and fluids ( $\text{kJ}\cdot\text{mol}^{-1}\cdot\text{K}^{-1}$ ).

-  $C_p$  heat capacity for each mineral end-member and fluid, usually:

$$C_p = c_1 + c_2 T + c_3 T^{-2} + c_4 T^{-\frac{1}{2}} \text{ (with } c_i = \text{constants and } T \text{ in K).}$$

-  $a$  activity of the different phases involved in the reaction. In our case the fluid phase is globally consist of  $F_1$  and  $F_2$  fluids (for example  $\text{CO}_2$  and  $\text{H}_2\text{O}$ ). The mineral  $M_3$  might belong to a global solid solution  $\varphi_{M_3}$  or can be the only end-member present in  $\varphi_{M_3}$  which imply in this case that  $a_{M_3} = 1$ . However, most of the time it is not true and  $\varphi_{M_3}$  consist of several end-members.

-  $R$  gas constant =  $0.0083143 \text{ kJ}\cdot\text{K}^{-1}\cdot\text{mol}^{-1}$ .

If the volume of solid phases are dependent of  $T$  and  $P$ , then:

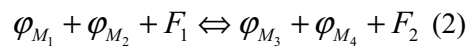
$$\int_{P_0}^P \Delta V_{solid} dp = \Delta \left[ P V_{1,298} \left( 1 + \alpha(T - 298) - \beta \frac{P}{2} \right) \right]$$

with:

- $V_{1,298}$  volume at 1 bar and 298 °K ( $\text{KJ}\cdot\text{kbar}^{-1}$ )
- $\alpha$  coefficient of thermal expansion ( $\text{K}^{-1}$ )
- $\beta$  coefficient of isothermal compressibility ( $\text{kbar}^{-1}$ )

## THERMOCALC SOFTWARE

The software THERMOCALC (Powell *et al.*, 1998) use internally consistent thermodynamic data set (Powell & Holland, 1985; Holland & Powell, 1985; Powell & Holland, 1988; Holland & Powell, 1990; Holland & Powell, 1998) which allows to determine uncertainties on phase equilibrium calculations summarized here. Consider the global equilibrium following:



where  $\varphi_{M1}$ ,  $\varphi_{M2}$ ,  $\varphi_{M3}$ , and  $\varphi_{M4}$  are this time solid solutions consist of several end-members. It is possible to write the equation (1) for all the possible reactions between the different end-members. Most of these reactions are linear combinations of other reactions, so that, for an  $m$  end-member,  $n$  component system ( $\text{SiO}_2$ ,  $\text{Al}_2\text{O}_3$  etc..) there are a total of  $C_{n+1}^m$  possible reactions (in general), only  $m-n$  of which are independent (Powell & Holland, 1988). Therefore THERMOCALC solve an independent set of reactions instead of the total number of reaction. Given the compositions of the phases whose end-members are involved in (2), and the activity-composition relationships for these phases, the solution of the independent set of reactions will be a non-linear line on a  $P$ - $T$  space. To generalize, considering an  $n$ -component model system, if phase  $k$  (solid solution) involves  $e_k$  end-members, then it involves  $e_k - 1$  compositional variables. For  $p$  solid solutions in the equilibrium, there will be

$$\sum_{k=1}^p e_k \equiv m \text{ end-members of phase, and } \sum_{k=1}^p e_k - 1 \equiv m - p \text{ composition variables. We have seen}$$

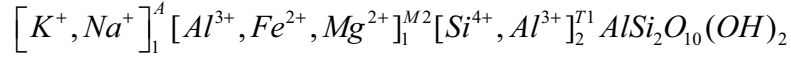
above that the number of reaction between the end-members that make up an independent set is  $m-n$ . Given that there is a non-linear equation for each reaction in the independ set, these relationships indicate how many unknowns can be solved for, and therefore how many must be set, because the  $m-n$  equations can only be solved for  $m-n$  unknowns. The number of things that have to be set in order for an equilibrium to be calculated can be represented in terms of degrees of freedom, equal to the number of unknowns,  $(m-p) + 2$  ( $P$  &  $T$ ) minus the number of equation  $m-n$ , given,  $n + 2 - p$ . So the number of degrees of freedom is just the variance. Setting unknowns may involve setting  $P$  and/or  $T$ , or setting compositional variables, as would be done, for example, in calculating composition isopleths on a  $P$ - $T$  diagram (Powell *et al.*, 1998).

## ACTIVITY-COMPOSITION RELATIONSHIP

In order to solve the set of equations resulting from (2), it is necessary to setup activity-composition relationship script for each solid solution involved. This imply to consider a general mineral formula and to recalculate the proportion of the different end-member which make up the interested phase. We will take here simple examples in order to illustrate the method which can be easily generalized to more complicated phases.

## Calcul of end-member proportions

Consider the white mica solid solution formula follows:



where A, M2, T1 are respectively the alkali, octahedral, and tetrahedral sites. The equilibrium of the charge leads to:

$$X_{Na}^A + X_K^A + X_{Al}^{M2} (3) + X_{Mg}^{M2} (2) + X_{Fe}^{M2} (2) + 2X_{Si}^{T1} (4) + 2X_{Al}^{T1} (3) + 3 + 2(4) + 12(-2) + 2 = 0 \quad (3)$$

where  $X_{element}^{site}$  is the molar fraction of the element in the considered site. Reducing (3) leads to:

$$X_{Al}^{M2} + 2X_{Si}^{T1} = 2$$

if  $x = X_{Si}^{T1}$  then  $X_{Al}^{M2} = 2(1-x)$  and  $X_{Al}^{T1} = 1-x$

if  $y = \left( \frac{Fe}{Fe + Mg} \right)^{M2}$  and  $z = \left( \frac{Na}{Na + K} \right)^A$  then  $X_{Fe}^{M2} = y(2x-1)$  and  $X_{Mg}^{M2} = 2 \left( x - \frac{1}{2} \right) (1-y)$

The problem following is to choose an independent set of end-members to describe our system. Since we have 3 compositional variables x, y, and z we need only four independent end-members (Powell *et al.*, 1998). According to the structural formula, white mica can be modeled in the system NKFMAH involving four end-members: muscovite (mu), paragonite (pa), celadonite (cel) and Fe-celadonite (fcel):

	A	M2	T1	
(mu): $KAl_3Si_3O_{10}(OH)_2$	K	Al	AlSi	$AlSi_2O_{10}(OH)_2$
(pa): $NaAl_3Si_3O_{10}(OH)_2$	Na	Al	AlSi	$AlSi_2O_{10}(OH)_2$
(cel): $KMgAlSi_4O_{10}(OH)_2$	K	Mg	Si <sub>2</sub>	$AlSi_2O_{10}(OH)_2$
(fcel): $KFeAlSi_4O_{10}(OH)_2$	K	Fe	Si <sub>2</sub>	$AlSi_2O_{10}(OH)_2$

the compositional matrix in term of molar fractions is:

	$X_{Na}^A$	$x_K^A$	$X_{Al}^{M2}$	$X_{Mg}^{M2}$	$X_{Fe}^{M2}$	$X_{Al}^{T1}$	$X_{Si}^{T1}$	
(mu)	0	1	1	0	0	0.5	0.5	
(pa)	1	0	1	0	0	0.5	0.5	(A)
(cel)	0	1	0	1	0	0	1	
(fcel)	0	1	0	0	1	0	1	

The transpose of A ( $A^T$ ) multiplied by the matrix proportion will give the matrix of the molar fraction:

$$\begin{pmatrix} 0 & 1 & 0 & 0 \\ 1 & 0 & 1 & 1 \\ 1 & 1 & 0 & 0 \\ 0 & 0 & 1 & 0 \\ 0 & 0 & 0 & 1 \\ 0.5 & 0.5 & 0 & 0 \\ 0.5 & 0.5 & 1 & 1 \end{pmatrix} \cdot \begin{pmatrix} P_{mu} \\ P_{pa} \\ P_{cel} \\ P_{fcel} \end{pmatrix} = \begin{pmatrix} X_{Na}^A = z \\ X_K^A = 1 - z \\ X_{Al}^{M2} = 2(1 - x) \\ X_{Mg}^{M2} = 2\left(x - \frac{1}{2}\right)(1 - y) \\ X_{Fe}^{M2} = y(2x - 1) \\ X_{Al}^{T1} = 1 - x \\ X_{Si}^{T1} = x \end{pmatrix}$$

$$\text{or } [A]^T \cdot [p] = [X_{element}^{site}]$$

then to solve  $[p]$ , the matrix  $[A]^T$  must be nonsingular, which imply that end-members chose are independents. In our case the solution of  $[p]$  is straightforward, but for more complex solid solution (for example amphibole) the solution can be quite more complicated. This can be however carried out using mathematical software as *mathematica* via nullspace fonction. Solving  $[p]$  give the proportions of each end-member in the white mica:

$$\begin{aligned} P_{pa} &= z \\ P_{mu} &= 1 - z - (2x - 1) \\ P_{cel} &= 2\left(x - \frac{1}{2}\right)(1 - y) \end{aligned}$$

$$P_{fcel} = y(2x-1)$$

### Activity models

Consider from the equation (1) the enthalpic molar of formation  $\Delta_f G_{ml}(M_3)^{T, P}$  of the end-member  $M_3$ . If  $M_3$  belongs to the global phase  $\varphi_{M_3}$ , the activity  $a_{M_3}^{\varphi_{M_3}} \neq 1$  and we have:

$$\Delta_f G_{ml}(M_3)^{T,P} = \Delta_f H_{ml}(M_3)^{T_0,P_0} - TS_{ml}(M_3)^{T_0,P_0} + \int_{T_0}^T Cp(M_3)dt - T \int_{T_0}^T \frac{Cp(M_3)dt}{T} + \int_{P_0}^P V_{ml}(M_3)dp + RT \ln(a_{M_3}^{\varphi_{M_3}}) = 0$$

or

$$\Delta_f G_{ml}(M_3)^{T,P} = \Delta_f G_{ml}(M_3)^{T_0,P_0} - (T - T_0)S_{ml}(M_3)^{T_0,P_0} + \int_{T_0}^T Cp(M_3)dt - T \int_{T_0}^T \frac{Cp(M_3)dt}{T} + \int_{P_0}^P V_{ml}(M_3)dp + RT \ln(a_{M_3}^{\varphi_{M_3}})$$

If  $\mu_{M_3}^{T,P} = \Delta_f G_{ml}(M_3)^{T,P}$  (chemical potential for  $M_3$  at  $T$  and  $P$ )

and

$$\mu_{M_3}^{*T,P} = \Delta_f G_{ml}(M_3)^{T_0,P_0} - (T - T_0)S_{ml}(M_3)^{T_0,P_0} + \int_{T_0}^T Cp(M_3)dt - T \int_{T_0}^T \frac{Cp(M_3)dt}{T} + \int_{P_0}^P V_{ml}(M_3)dp$$

(stantard state for  $M_3$  at  $T$  and  $P$ )

$$\text{then } \mu_{M_3}^{T,P} = \mu_{M_3}^{*T,P} + RT \ln(a_{M_3}^{\varphi_{M_3}})$$

If the solid solution  $\varphi_{M_3}$  is an ideal solution the activity  $a_{M_3}^{\varphi_{M_3}}$  will depend only on the entropy of configuration (Will, 1998a). However, if the mixing between the different end-members which make up the solid solution  $\varphi_{M_3}$  involves an excess energy, then a corrective term  $\gamma_{M_3}^{\varphi_{M_3}}$  need to be added and we have:

$$\mu_{M_3}^{T,P} = \mu_{M_3}^{*T,P} + RT \ln(a_{M_3}^{\varphi_{M_3}} \gamma_{M_3}^{\varphi_{M_3}})$$

with  $\gamma_{M_3}^{\varphi_{M_3}}$  the activity coefficient. The term  $a_{M_3}^{\varphi_{M_3}}$  will depend on the ideal mixing on site (entropy of configuration) and so on the  $X_{element}^{site}$  molar fractions of the elements in the considered sites. The term  $\gamma_{M_3}^{\varphi_{M_3}}$  will depend on the activity model and so on the proportion of the end-members involved in the solid solution  $\varphi_{M_3}$ , and on interaction parameters according to the activity model chosen. For instance if the solid solution  $\varphi_{M_3}$  consist of two end-members  $M_{31}$  and  $M_{32}$ , using a regular solution model we will have:

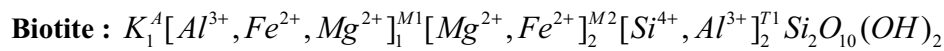
$$RT \ln \left( \gamma_{M_{31}}^{\varphi_{M_3}} \right) = (p_{M_{32}})^2 (w_{M_{31-32}})$$

$$RT \ln \left( \gamma_{M_{32}}^{\varphi_{M_3}} \right) = (p_{M_{31}})^2 (w_{M_{31-32}})$$

with  $w_{M_{31-32}}$  interaction parameter between the  $M_{31}$  and  $M_{32}$  (KJ/mol end-member). Other more complex solution model can be found in Will (1998a).

### Activity models used with THERMOCALC v3.1 for the KFMASH system

In addition to the solid solution minerals described below, the pure phases quartz, andalusite, sillimanite, kyanite, and an H<sub>2</sub>O fluid phase were used in calculations.



Biotite is modeled in the system KFMASH involving order-disorder of Fe and Mg between one M1 site and two M2 sites (Powell & Holland, 1999). There are four independent end-members: phlogopite (phl), annite (ann), eastonite (east), and the ordered end-member (obi). Biotite mixing is described by the following three variables:

$$x = \left( \frac{Fe^{2+}}{Fe^{2+} + Mg^{2+}} \right)^{tot} ; y = X_{Al}^{M1} ; N = 3 \left( x - X_{Fe}^{M2} \right)$$

Site fractions in terms of compositional variables are:

$$X_{Al}^{M1} = y; X_{Fe}^{M1} = x(1-y) + \frac{2N}{3}; X_{Mg}^{M1} = (1-y)(1-x) - \frac{2N}{3}; X_{Mg}^{M2} = (1-x) + \frac{N}{3};$$

$$X_{Fe}^{M2} = x - \frac{N}{3}$$

$$X_{Si}^{T1} = \frac{1-y}{2}; X_{Al}^{T1} = \frac{1+y}{2}$$

The ideal activities of end-members are expressed as:

$$a_{phl}^{ideal} = 4X_{Mg}^{M1} (X_{Mg}^{M2})^2 X_{Al}^{T1} X_{Si}^{T1}$$

$$a_{ann}^{ideal} = 4X_{Fe}^{M1} (X_{Fe}^{M2})^2 X_{Al}^{T1} X_{Si}^{T1}$$

$$a_{east}^{ideal} = X_{Al}^{M1} (X_{Mg}^{M2})^2 (X_{Al}^{T1})^2$$

$$a_{obi}^{ideal} = 4X_{Fe}^{M1} (X_{Mg}^{M2})^2 X_{Al}^{T1} X_{Si}^{T1}$$

The proportions of each end-member in the biotite phase are defined as:

$$P_{phl} = (1-x)(1-y) - \frac{2N}{3}$$

$$P_{ann} = x - \frac{N}{3}$$

$$P_{east} = y$$

$$P_{obi} = -xy + N$$

Non-ideality is expressed using symmetric formalism (Powell & Holland, 1993) with interaction parameters from Powell & Holland (1999) for KFMASH biotites. The interaction parameters are (KJ/mol end-member):

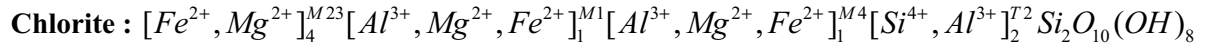
$$W_{phl-ann} = 9; W_{phl-east} = 10; W_{phl-obi} = 3; W_{ann-east} = -1; W_{ann-obi} = 6; W_{east-obi} = 10$$

Darkens Quadratic Formalism (DQF) parameter for the ordered end-member obi is (KJ/mol end-member):

$$I_{obi} = -10.73$$

(Powell & Holland, 2002; <http://www.earthsci.unimelb.edu.au/tpg/thermocalc/>)





Chlorite is modeled in the system FMASH involving four end-members: Al-free chlorite (afchl), clinocllore (clin), daphnite (daph) and amesite (ames) with:

$$x = \left( \frac{Fe^{2+}}{Fe^{2+} + Mg^{2+}} \right)^{tot} ; y = X_{Al}^{T2} ; N = \frac{X_{Al}^{M4} - X_{Al}^{M1}}{2}$$

Site fractions in terms of compositional variables are:

$$X_{Fe}^{M23} = x ; X_{Mg}^{M23} = 1 - x ; X_{Al}^{M1} = y - N ; X_{Fe}^{M1} = x(1 - y + N) ; X_{Mg}^{M1} = (1 - x)(1 - y + N)$$

$$X_{Al}^{M4} = y + N ; X_{Fe}^{M4} = x(1 - y - N) ; X_{Mg}^{M4} = (1 - x)(1 - y - N) ; X_{Al}^{T2} = y ; X_{Si}^{T2} = 1 - y$$

The ideal activities of end-members are expressed as:

$$a_{afchl}^{ideal} = (X_{Mg}^{M23})^4 X_{Mg}^{M1} X_{Mg}^{M4} (X_{Si}^{T2})^2$$

$$a_{clin}^{ideal} = 4 (X_{Mg}^{M23})^4 X_{Mg}^{M1} X_{Al}^{M4} X_{Al}^{T2} X_{Si}^{T2}$$

$$a_{daph}^{ideal} = 4 (X_{Fe}^{M23})^4 X_{Fe}^{M1} X_{Al}^{M4} X_{Al}^{T2} X_{Si}^{T2}$$

$$a_{ames}^{ideal} = (X_{Mg}^{M23})^4 X_{Al}^{M1} X_{Al}^{M4} (X_{Al}^{T2})^2$$

The proportions of each end-member in the chlorite phase are defined as:

$$P_{afchl} = 1 - y - N$$

$$P_{clin} = 2N - \left( \frac{2x}{5} \right) (3 - y)$$

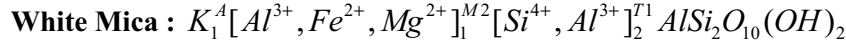
$$P_{daph} = \left( \frac{2x}{5} \right) (3 - y)$$

$$P_{ames} = y - N$$

Non-ideality is expressed using symmetric formalism (Powell & Holland, 1993) with interaction parameters from Holland *et al.* (1998) for FMASH chlorite. The interaction parameters are (KJ/mol end-member):

$$W_{afchl-clin} = 18 ; W_{afchl-daph} = 14.5 ; W_{afchl-ames} = 20 ; W_{clin-daph} = 2.5 ;$$

$$W_{clin-ames} = 18 ; W_{daph-ames} = 13.5$$



White mica is modeled in the system KFMASH involving three end-members : muscovite (mu), celadonite (cel) and Fe-celadonite (fcel). Ideal mixing is assumed (Massonne & Schreyer, 1987; Holland & Powell, 1998). The compositional variables are:

$$x = X_{Si}^{T1} ; y = \left( \frac{Fe^{2+}}{Fe^{2+} + Mg^{2+}} \right)^{tot}$$

Site fractions in terms of compositional variables are:

$$X_{Al}^{M2} = 2(1-x) ; X_{Fe}^{M2} = y(2x-1) ; X_{Mg}^{M2} = 2\left(x - \frac{1}{2}\right)(1-y) ; X_{Si}^{T1} = x ; X_{Al}^{T1} = 1-x$$

The ideal activities of end-members are expressed as:

$$a_{mu}^{ideal} = 4X_{Al}^{M2} X_{Al}^{T1} X_{Si}^{T1}$$

$$a_{cel}^{ideal} = X_{Mg}^{M2} \left( X_{Si}^{T1} \right)^2$$

$$a_{fcel}^{ideal} = X_{Fe}^{M2} \left( X_{Si}^{T1} \right)^2$$

The proportions of each end-member in the white mica phase are defined as:

$$P_{mu} = 2(1-x)$$

$$P_{cel} = 2\left(x - \frac{1}{2}\right)(1-y)$$

$$P_{fcel} = y(2x-1)$$

**Cordierite** :  $[Fe^{2+}, Mg^{2+}]_2^M Al_4 Si_5 O_{18} [\Omega, H_2O]_1^W$

Cordierite is modeled in the system FMASH involving three end-members: cordierite (crd), Fe-cordierite (fcrd) and hydrous cordierite (hcrd). Ideal mixing is assumed. The compositional variables and site fractions in terms of compositional variables are:

$$X_{Fe}^M = x ; X_{H_2O} = h ; X_{Mg}^M = 1 - x ; X_{\Omega}^W = 1 - h$$

The ideal activities and proportion of each end-member in the cordierite are expressed as:

$$a_{crd}^{ideal} = (X_{Mg}^M)^2 (X_{\Omega}^W) ; P_{crd} = 1 - (x + h)$$

$$a_{fcrd}^{ideal} = (X_{Fe}^M)^2 (X_{\Omega}^W) ; P_{fcrd} = x$$

$$a_{hcrd}^{ideal} = (X_{Mg}^M)^2 (X_{H_2O}^W) ; P_{hcrd} = h$$

**Staurolite** :  $[Fe^{2+}, Mg^{2+}]_4^M Al_{18} Si_{7.5} O_{48} H_4$

Staurolite is modeled in the system FMASH involving two end-members: Fe-staurolite (fst) and Mg-staurolite (mst). Ideal activities of end-members:

$$a_{fst}^{ideal} = (X_{Fe}^M)^4 ; a_{mst}^{ideal} = (X_{Mg}^M)^4$$

Non-ideality is expressed using symmetric formalism (Powell & Holland, 1993) with the interaction parameter (KJ/mol end-member):

$$W_{fst-mst} = -8$$

(<http://www.earthsci.unimelb.edu.au/tpg/thermocalc/>)

**Chloritoid**:  $[Fe^{2+}, Mg^{2+}]_1^M Al_2 Si O_5 (OH)_2$

Chloritoid is modeled in the system FMASH involving two end-members: Fe-chloritoid (fctd) and Mg-chloritoid (mctd). Ideal activities of end-members:

$$a_{fctd}^{ideal} = X_{Fe}^M ; a_{mctd}^{ideal} = X_{Mg}^M$$

Non-ideality is expressed using symmetric formalism (Powell & Holland, 1993) with the interaction parameter (KJ/mol end-member):

$$W_{fctd-mctd} = 1$$

(<http://www.earthsci.unimelb.edu.au/tpg/thermocalc/>)

**Garnet:**  $[Fe^{2+}, Mg^{2+}]_3^A Al_2 Si_3 O_{12}$

Garnet is modeled in the system FMAS involving two end-members: almandine (alm) and pyrope (py). Ideal activities of end-members:

$$a_{alm}^{ideal} = (X_{Fe}^A)^3 ; a_{py}^{ideal} = (X_{Mg}^A)^3$$

Non-ideality is expressed using symmetric formalism (Holland & Powell, 1998) with the interaction parameter (KJ/mol end-member):

$$W_{alm-py} = 2.5$$

### Activity models used with THERMOCALC v3.2.1 for the NCKFMASH system

We added plagioclase and zoisite as new phases in the NCKFMASH system. All other phases use similar activity models except for white mica and garnet. The pure phases quartz, andalusite, sillimanite, kyanite, and an H<sub>2</sub>O fluid phase were used as well in calculations.

**White Mica :**  $[K^+, Na^+]_1^A [Al^{3+}, Fe^{2+}, Mg^{2+}]_1^{M2} [Si^{4+}, Al^{3+}]_2^{T1} AlSi_2O_{10}(OH)_2$

White mica is modeled in the system NCKFMASH involving four end-members: paragonite (pa), muscovite (mu), celadonite (cel) and Fe-celadonite (fcel). The compositional variables are:

$$x = X_{Si}^{T1} ; y = \left( \frac{Fe^{2+}}{Fe^{2+} + Mg^{2+}} \right)^{M2} ; z = \left( \frac{Na^+}{Na^+ + K^+} \right)^A$$

Site fractions in terms of compositional variables are:

$$X_{Al}^{M2} = 2(1-x) ; X_{Fe}^{M2} = y(2x-1) ; X_{Mg}^{M2} = 2 \left( x - \frac{1}{2} \right) (1-y) ; X_{Si}^{T1} = x ; X_{Al}^{T1} = 1-x ; X_{Na}^A = z ;$$

$$X_K^A = 1-z$$

The ideal activities of end-members are expressed as:

$$a_{pa}^{ideal} = 4X_{Na}^A X_{Al}^{M2} X_{Al}^{T1} X_{Si}^{T1}$$

$$a_{mu}^{ideal} = 4X_K^A X_{Al}^{M2} X_{Al}^{T1} X_{Si}^{T1}$$

$$a_{cel}^{ideal} = X_K^A X_{Mg}^{M2} \left( X_{Si}^{T1} \right)^2$$

$$a_{fcel}^{ideal} = X_K^A X_{Fe}^{M2} \left( X_{Si}^{T1} \right)^2$$

The proportions of each end-member in the white mica phase are defined as:

$$P_{pa} = z$$

$$P_{mu} = 1 - z - (2x - 1)$$

$$P_{cel} = 2 \left( x - \frac{1}{2} \right) (1 - y)$$

$$P_{fcel} = y(2x - 1)$$

Non-ideality is expressed using symmetric formalism with the interaction parameters of Holland & Powell (1998; <http://www.esc.cam.ac.uk/astaff/holland/thermocalc.html>). The interaction parameters are (KJ/mol end-member):

$$W_{pa-mu} = 12 + 0.4P ; W_{pa-cel} = 14 + 0.2P ; W_{pa-fcel} = 14 + 0.2P$$

DQF parameter for the end-member paragonite is (KJ/mol end-member, P in Kbar):  $1.42 + 0.4P$

**Garnet:**  $[Fe^{2+}, Ca^{2+}, Mg^{2+}]_3^A Al_2 Si_3 O_{12}$

Garnet is modeled in the system CFMAS involving three end-members: almandine (alm), grossular (gr) and pyrope (py). Ideal activities of end-members:

$$a_{alm}^{ideal} = (X_{Fe}^A)^3 ; a_{gr}^{ideal} = (X_{Ca}^A)^3 ; a_{py}^{ideal} = (X_{Mg}^A)^3$$

Non-ideality is expressed using symmetric formalism (Worley & Powell, 1998) with the interaction parameter (KJ/mol end-member):

$$W_{gr-py} = 33$$

**Plagioclase :**  $[Na^+, Ca^{2+}]_1^A [Si^{4+}, Al^{3+}]_4^T O_8$

Plagioclase is modeled with the binary albite(ab)-anorthite(an) solution model 4T (C $\bar{1}$  structure) of Holland & Powell (1992). The compositional variable is:

$$x = \left( \frac{Na^+}{Na^+ + Ca^{2+}} \right)^4$$

Site fractions in terms of compositional variables are:

$$X_{Na}^A = x ; X_{Ca}^A = 1 - x ; X_{Si}^T = \frac{1}{2} + \frac{1}{4}x ; X_{Al}^T = \frac{1}{2} - \frac{1}{4}x$$

The ideal activities of end-members are expressed as:

$$a_{ab}^{ideal} = \frac{256}{27} (X_{Na}^A) (X_{Al}^T) (X_{Si}^T)^3$$

$$a_{an}^{ideal} = 16 (X_{Ca}^A) (X_{Al}^T)^2 (X_{Si}^T)^2$$

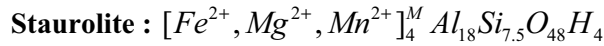
Regular solution model interaction parameter, from Worley & Powell (1998) is (KJ/mol):

$$W_{ab-an} = 5.5$$

DQF parameter for the end-member anorthite is (KJ/mol end-member, T in Kelvin): 4.31 - 0.00217T

## Activity models used with THERMOCALC v3.2.1 for the MnNCKFMASH system

MnO is assumed mainly concentrated in staurolite, chloritoid and garnet. All other phases use similar activity models (see NCKFMASH system). The pure phases quartz, andalusite, sillimanite, kyanite, and an H<sub>2</sub>O fluid phase were used as well in calculations.



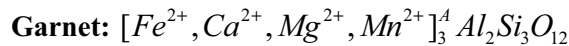
Staurolite is modeled in the system MnFMASH involving three end-members: Fe-staurolite (fst), Mg-staurolite (mst) and Mn-staurolite (mnst). Ideal activities of end-members:

$$a_{fst}^{ideal} = (X_{Fe}^M)^4 ; a_{mst}^{ideal} = (X_{Mg}^M)^4 ; a_{mnst}^{ideal} = (X_{Mn}^M)^4$$

Non-ideality is expressed using symmetric formalism (Powell & Holland, 1993) with the interaction parameter (KJ/mol end-member):

$$W_{fst-mst} = -8$$

(<http://www.earthsci.unimelb.edu.au/tpg/thermocalc/>)



Garnet is modeled in the system MnCFMAS involving four end-members: almandine (alm), grossular (gr), pyrope (py) and spessartine (spss). Ideal activities of end-members:

$$a_{alm}^{ideal} = (X_{Fe}^A)^3 ; a_{gr}^{ideal} = (X_{Ca}^A)^3 ; a_{py}^{ideal} = (X_{Mg}^A)^3 ; a_{spss}^{ideal} = (X_{Mn}^A)^3$$

Non-ideality is expressed using symmetric formalism (Worley & Powell, 1998; Wood et al., 1994) with the interaction parameter (KJ/mol end-member):

$$W_{gr-py} = 33 ; W_{py-spss} = 4.5$$

**Chloritoid:**  $[Fe^{2+}, Mg^{2+}, Mn^{2+}]_1^M Al_2SiO_5(OH)_2$

Chloritoid is modeled in the system MnFMASH involving three end-members: Fe-chloritoid (fctd), Mg-chloritoid (mctd) and Mn-chloritoid (mnctd). Ideal activities of end-members:

$$a_{fctd}^{ideal} = X_{Fe}^M ; a_{mctd}^{ideal} = X_{Mg}^M ; a_{mnctd}^{ideal} = X_{Mn}^M$$

Non-ideality is expressed using symmetric formalism (Powell & Holland, 1993) with the interaction parameter (KJ/mol end-member):

$$W_{fctd-mctd} = 1$$



## References

- Ashworth, J. R. & Evirgen, M. M., 1984. Garnet and associated minerals in the southern margin of the Menderes Massif, Southwest Turkey. *Geological Magazine*, **121**, 323–337.
- Ashworth, J. R. & Evirgen, M. M., 1985. Plagioclase relations in pelites, central Menderes Massif, Turkey; I, The peristerite gap with coexisting kyanite. *Journal of Metamorphic Geology*, **3**, 207-218.
- Blundy, J. D. & Holland, T. J. B., 1990. Calcic amphibole equilibria and a new amphibole-plagioclase geothermometer. *Contribution to Mineralogy and Petrology*, **104**, 208–224.
- Bozkurt, E. & Park, R. G., 1994. Southern Menderes Massif; an incipient metamorphic core complex in western Anatolia, Turkey. *Journal of Geological Society of London*, **151**, 213–216.
- Bozkurt, E. & Park, R. G., 1997. Microstructures of deformed grains in the augen gneisses of southern Menderes Massif (western Turkey) and their tectonic significance. *Geologische Rundschau*, **86**, 103–119.
- Bozkurt, E., Park, R. G. & Winchester, J. A., 1993. Evidence against the core/cover interpretation of the southern sector of the Menderes Massif, west Turkey. *Terra Nova*, **5**, 445–451.
- Brunel, M., 1986. Ductile thrusting in the Himalayas: shear sense criteria and stretching lineations. *Tectonics*, **5**, 247-265.
- Çağlayan, M. A., Öztürk, E. M., Öztürk, S., Sav, H. & Akat, U., 1980. Some new data for southern Menderes Massif structural interpretation (in Turkish with English Abstract). *Geological Engineering of Turkey*, **10**, 9-19.
- Candan, O. & Dora, O. Ö., 1993. Application of Schreinemakers' method to a metamorphic area located at the northern flank of Menderes Massif (Western Turkey). *Bulletin of the Geological Society of Greece*, **28**, 169–186.
- Candan, O. & Dora, Ö.O., 1998. The generalised map of Menderes Massif. Department of Geological Engineering, Dokuz Eylül University Bornova, İzmir.
- Candan, O., Dora, Ö.O., Oberhänsli, R. *et al.*, 2001. Pan-African high-pressure metamorphism in the basement of the Menderes Massif, western Anatolia, Turkey. *International Journal of Earth Sciences*, **89**, 793-811.
- Catlos, E. J., Cemen, I., Isik, V. & Seyitoglu, G., 2002. In situ timing constraints from the Menderes Massif, Western Turkey. *Geological Society of America*, 2002 Fall Meeting.
- Collins, A. S. & Robertson, A. H. F., 1997. Lycian melange, southwest Turkey: An emplaced Cretaceous accretionary complex. *Geology*, **25**, 255-258.
- Collins, A. S. & Robertson, A. H. F., 1998. Process of late Cretaceous to late Miocene episodic thrust-sheet translation in the Lycean Taurides. *Journal of the Geological Society*, London, **155**, 759-772.

Collins, A. S. & Robertson, A. H. F., 1999. Evolution of the Lycian Allochthon, western Turkey, as a north-facing Late Palaeozoic–Mesozoic rift and passive continental margin. *Geological Journal*, **34**, 107–138.

Collins, A. S. & Robertson, A. H. F., 2003. Kinematic evidence for Late Mesozoic–Miocene emplacement of the Lycian Allochthon over the Western Anatolide Belt, SW Turkey. *Geological Journal*, **38**, 295–310.

Compagnoni, R., 1977. The Sesia-Lanzo Zone; high pressure-low temperature metamorphism in the austroalpine continental margin. *Rendiconti della Società Italiana di Mineralogia e Petrologia*, **33**, 335–374.

Dannat, C. & Reischmann, T., 1999. Single zircon ages of migmatites from the Menderes Massif, SW Turkey. *Journal of Conference Abstracts*, **4**, 805.

Dannat, C., 1997. Geochemie, Geochronologie und Nd-Sr-Isotopie der granitoiden Kerngneise des Menderers Massivs, SW-Türkei. PhD thesis, Johannes Gutenberg-Universität, Mainz.

De Graciansky, P. C., 1966. Le massif cristallin du Menderes (Taurus occidental, Asie Mineure); un exemple possible de vieux socle granitique remobilisé. *Revue de Géographie Physique et de Géologie Dynamique*, **8**, 289–306.

Dora, O. Ö., Candan, O., Kaya, O., Koray, E. & Dürr, S., 2001. Revision of "Leptite-gneisses" in Menderes Massif: a supracrustal metasedimentary origin. *International Journal of Earth Sciences*, **89**, 836–851.

Droop, G. T. R. & Harte, B., 1995. The effect of Mn on the Phase Relations of Medium-Grade Pelites: Constraints from Natural Assemblages on Petrogenetic Grid Topology. *Journal of Petrology*, **36**, 1549–1578.

England, P. & Molnar, P., 1993. The interpretation of inverted metamorphic isograds using simple physical calculations. *Tectonics*, **12**, 145–157.

Evirgen, M. M. & Ashworth, J. R., 1984. Andalusitic and kyanitic facies series in the central Menderes Massif, Turkey. *Neues Jahrbuch fuer Mineralogie*, **5**, 219–227.

Evirgen, M. M. & Ataman, G., 1982. Etude du métamorphisme de la zone centrale du Massif de Menderes; Isogrades, pressions et température. *Bulletin de la Société Géologique de France*, **24**, 309–319.

Faure, G. & Powell, J. L., 1972. Strontium isotope geology. *Springer-Verlag. Berlin, Heidelberg and New York*, 188 pp.

Foster, D. A. & John, B. E., 1999. Quantifying tectonic exhumation in an extensional orogen with thermochronology: examples from the southern Basin and Range province, in Ring, U., et al. eds. Exhumation processes: Normal faulting, ductile flow and erosion. *Geological Society of London Special Publication*, **154**, 343–364.

Gessner, K., Piazzolo, S., Güngör, T., Ring, U., Kröner, A. & Passchier, C. W., 2001a. Tectonic significance of deformation patterns in granitoid rocks of the Menderes nappes, Anatolide belt, southwest Turkey. *International Journal of Earth Sciences*, **89**, 766-780.

Gessner, K., Ring, U., Passchier, C. W. & Güngör, T., 2001b. How to resist subduction: Eocene post-high-pressure emplacement of the Cycladic blueschist unit onto the Menderes nappes, Anatolide belt, western Turkey. *Journal of Geological Society of London*, **158**, 769-780.

Gessner, K., Ring, U., Johnson, C., Hetzel, R., Passchier, C. W. & Güngör, T., 2001c. An active bivergent rolling-hinge detachment system; central Menderes metamorphic core complex in western Turkey. *Geology*, **29**, 611-614.

Gessner, K., Collins, A. S., Ring, U. & Güngör, T., 2004. Structural and thermal history of poly-orogenic basement: U-Pb geochronology of granitoid rocks in the southern Menderes Massif, Western Turkey. *Journal of the Geological Society, London*, **161**, 93-101.

Goodman, S., 1993. Survival of zircon staurolite to upper amphibolite facies metamorphic grade. *Mineralogical Magazine*, **27**, 736-739.

Güngör, T. & Erdoğan, B., 2001. Emplacement age and direction of the Lycian nappes in the Söke-Selçuk region, western Turkey. *International Journal of Earth Sciences*, **89**, 874-882.

Hetzel, R. & Reischmann, T., 1996. Intrusion age of Pan-African augen gneisses in the southern Menderes Massif and the age of cooling after Alpine ductile extensional metamorphism. *Geological Magazine*, **133**, 505-572.

Hetzel, R., Romer, R. L., Candan, O. & Passchier, C. W., 1998. Geology of the Bozdağ area, central Menderes Massif, SW Turkey; Pan-African basement and Alpine deformation. *Geologische Rundschau*, **87**, 394-406.

Holland, T. J. B. & Blundy, J. D., 1994. Non-ideal interactions in calcic amphiboles and their bearing on amphibole-plagioclase thermometry. *Contributions to Mineralogy and Petrology*, **116**, 433-447.

Holland, T. J. B. & Powell, R., 1985. An internally consistent thermodynamic dataset with uncertainties and correlations: 2. Data and results. *Journal of Metamorphic Geology*, **3**, 343-370.

Holland, T. J. B. & Powell, R., 1990. An enlarged and updated internally consistent thermodynamic dataset with uncertainties and correlations: the system  $K_2O-Na_2O-CaO-MgO-MnO-FeO-Fe_2O_3-Al_2O_3-TiO_2-SiO_2-C-H_2-O_2$ . *Journal of Metamorphic Geology*, **8**, 89-124.

Holland, T. J. B. & Powell, R., 1992. Plagioclase feldspars: Activity-composition relations based upon Darken's quadratic formalism and Landau theory. *American Mineralogist*, **77**, 53-61.

Holland, T. J. B. & Powell, R., 1998. An internally consistent thermodynamic data set for phases of petrological interest. *Journal of Metamorphic Geology*, **16**, 309-343.

Holland, T. J. B., 2000. AX: A program to calculate activities of mineral end members from chemical analyses which uses the activity models outlined in Holland & Powell (1998). <http://www.esc.cam.ac.uk/astaff/holland/ax.html>.

Holland, T. J. B., Baker, J. & Powell, R., 1998. Mixing properties and activity-composition relationships of chlorite in the system MgO-FeO-Al<sub>2</sub>O<sub>3</sub>-SiO<sub>2</sub>-H<sub>2</sub>O. *European Journal of Mineralogy*, **10**, 395-406.

Işık, V. & Tekeli, O., 2001. Late orogenic crustal extension in northern Menderes Massif (western Turkey): evidence for metamorphic core complex formation. *International Journal of Earth Sciences*, **89**, 757-765.

Johnson, M. C. & Rutherford, M. J., 1989. Experimental calibration of the aluminium-in-hornblende geobarometer with application to long Valley caldera (California) volcanic rocks. *Geology*, **17**, 837-841.

Leake, B. E., Woolley, A. R., Arps, C. E. S. *et al.*, 1997. Nomenclature of amphiboles: report of the subcommittee on amphiboles of international mineralogical association, commission on new minerals and mineral names. *Canadian Mineralogist*, **35**, 219-246.

Likhanov, I. I., Reverdatto, V. V. & Selyatitskiĭ, A. Y., 2004. Petrogenetic Grid for Ferruginous-Aluminous Metapelites in the K<sub>2</sub>O-FeO-MgO-Al<sub>2</sub>O<sub>3</sub>-SiO<sub>2</sub>-H<sub>2</sub>O System. *Doklady Earth Sciences*, **394**, 46-49.

Likhanov, I. I., Reverdatto, V. V., Sheplev, V. S., Vershinin, A. E. & Kozlov, P. S., 2001. Contact metamorphism of Fe- and Al-rich graphitic metapelites in the Transangarian region of the Yenisei Ridge, eastern Siberia, Russia. *Lithos*, **58**, 55-80.

Lips, A. L. W., Cassard, D., Sözbilir, H., Yilmaz, H. & Wijbrans, J. R., 2001. Multistage exhumation of the Menderes Massif, western Anatolia (Turkey). *International Journal of Earth Sciences*, **89**, 781-792.

Loos, S. & Reischmann, T., 1999. The evolution of the southern Menderes Massif in SW Turkey as revealed by zircon dating. *Journal of Geological Society of London*, **156**, 1021-1030.

Malavieille, J., 1987. Extensional shearing deformation and kilometer-scale "a" type folds in a cordilleran metamorphic core complex (Raft River Mountains, Northwestern Utah). *Tectonics*, **6**, 423-448.

Massonne, H. J. & Schreyer, W., 1987. Phengite geobarometry based on the limiting assemblage with K-feldspar, phlogopite, and quartz. *Contributions to Mineralogy and Petrology*, **96**, 212-224.

McDougall, I. & Harrison, T. M., 1988. Geochronology and thermochronology by the <sup>40</sup>Ar/<sup>39</sup>Ar method. *Oxford University Press, New York*.

Monod, O., Maluski, H., Monié, P. & Akkök, R., 1996. Schistes bleus du Trias supérieur en Turquie du NW: comment s'est fermée la Paléo-Tethys ? *16th Réunion des Sciences de la Terre*, **10-11**, Orléans, France, Abstract, 43.

Oberhänsli, R., Candan, O., Dora, Ö. O. & Dürr, S. H., 1997. Eclogites within the Menderes Massif, western Turkey. *Lithos*, **41**, 135-150.

Oberhänsli, R., Monié, P., Candan, O., Warkus, F. C., Partzsch, J. H. & Dora, Ö. O., 1998. The age of blueschist metamorphism in the Mesozoic cover series of the Menderes Massif. *Schweizerische Mineralogische und Petrographische*, **78**, 309-316.

Oberhänsli, R., Partzsch, J. H., Candan, O. & Çetikaplan, M., 2001. First occurrence of Fe-Mg carpholite documenting a high-pressure metamorphism in metasediments of the Lycian Nappes, SW Turkey. *International Journal of Earth Sciences*, **89**, 867–873.

Okay, A. İ. & Monié, P., 1997. Early Mesozoic subduction in the Eastern Mediterranean: evidences from Triassic eclogite in northwest Turkey. *Geology*, **25**, 595-598.

Okay, A. İ., 2000. Was the Late Triassic orogeny in Turkey caused by the collision of an oceanic plateau?, in: E. Bozkurt, J.A. Winchester, J.D.A. Piper (Eds.), Tectonics and magmatism in Turkey and surrounding Area. *Geological Society of London Special Publication*, **173**, 25-41.

Özer, S. & Sözbilir, H., 2003. Presence and tectonic significance of Cretaceous rudist species in the so-called Permo-Carboniferous Göktepe Formation, central Menderes metamorphic massif, western Turkey. *International Journal of Earth Sciences*, **92**, 397–404.

Özer, S., Sözbilir, H., Özkar, İ., Tokar, V. & Sari, B., 2001. Stratigraphy of Upper Cretaceous-Palaeogene sequences in the southern and eastern Menderes Massif (western Turkey). *International Journal of Earth Sciences*, **89**, 852–866.

Pognante, U., 1989. Tectonic implications of lawsonite formation in the Sesia Zone (Western Alps). *Tectonics*, **162**, 219-227.

Powell, R. & Holland, T. J. B., 1985. An internally consistent thermodynamic dataset with uncertainties and correlations: 1. methods and a worked example. *Journal of Metamorphic Geology*, **3**, 327-342.

Powell, R. & Holland, T. J. B., 1988. An internally consistent dataset with uncertainties and correlations: 3: applications to geobarometry, worked examples and a computer program. *Journal of Metamorphic Geology*, **6**, 173-204.

Powell, R. & Holland, T. J. B., 1993. On the formulation of simple mixing models for complex phases. *American Mineralogist*, **78**, 1174–1180.

Powell, R. & Holland, T. J. B., 1994. Optimal geothermometry and geobarometry. *American Mineralogist*, **79**, 120-133.

Powell, R. & Holland, T. J. B., 1999. Relating formulations of the thermodynamics of mineral solid solutions: Activity modelling of pyroxenes, amphiboles, and micas. *American Mineralogist*, **84**, 1–14.

Powell, R., 1978. Equilibrium thermodynamics in petrology. Harper and Row, London, 284p.

Powell, R., Holland, T. J. B. & Worley, B., 1998. Calculating phase diagrams involving solid solutions via non-linear equations, with examples using THERMOCALC. *Journal of Metamorphic Geology*, **16**, 577-588.

Régnier, J.-L., Ring, U., Passchier, C. W., Gessner, K. & Güngör, T., 2003. Contrasting metamorphic evolution of metasedimentary rocks from the Çine and Selimiye nappes in the Anatolide belt, western Turkey. *Journal of Metamorphic Geology*, **21**, 699–721.

Ridley, J., 1984. The significance of deformation associated with blueschist-facies metamorphism on the Aegean island of Syros. In: The geological evolution of the eastern Mediterranean, Dixon, J. E., Robertson, A. H. F. (eds). *Geological Society of London Special Publication*, **17**, 545-550.

Rimmelé, G., Oberhänsli, R., Goffé, B., Jolivet, L., Candan, O. & Cetinkaplan, M., 2003. First evidence of high-pressure metamorphism in the “Cover Series” of the southern Menderes Massif. Tectonic and metamorphic implications for the evolution of SW Turkey. *Lithos*, **71**, 19-46.

Ring, U. & Brandon, M. T., 1994. Kinematic data for the Coast Range fault and implications for exhumation of the Franciscan complex. *Geology*, **22**, 735-738.

Ring, U. & Layer, P. W., 2003. High-pressure metamorphism in the Aegean, eastern Mediterranean: Sequential accretion from the Late Cretaceous until the Miocene to Recent. *Tectonics* (in press).

Ring, U., 1995. Horizontal contraction or horizontal extension?: Heterogeneous Late Eocene and Early Oligocene general shearing during blueschist- and greenschist-facies metamorphism at the Pennine-Austroalpine boundary zone in the Western Alps. *Geologische Rundschau*, **84**, 843-859.

Ring, U., Gessner, K., Güngör, T. & Passchier, C. W., 1999a. The Menderes Massif of western Turkey and the Cycladic Massif in the Aegean; do they really correlate? *Journal of the Geological Society, London*, **156**, 3-6.

Ring, U., Laws, S. & Bernet, M., 1999b. Structural analysis of a complex nappe sequence and late-orogenic basins from the Aegean Island of Samos, Greece. *Journal of Structural Geology*, **21**, 1575-1601.

Ring, U., Brandon, M. T., Willett, S. & Lister, G. S., 1999c. Exhumation processes. In: Exhumation Processes: Normal faulting, ductile flow and erosion, Ring, U., Brandon, M. T., Lister, G. S., Willett, S. (eds). *Geological Society of London Special Publication*, **154**, 1-28.

Ring, U., Willner, A. & Lackmann, W., 2001. Stacking of nappes with different Pressure-Temperature paths: an example from the Menderes nappes of western Turkey. *American Journal of Science*, **301**, 912-944.

Ring, U., Buchwaldt, R. & Gessner, K., 2004a. Pb/Pb dating of garnet from the Anatolide belt in western Turkey: Pan-African metamorphism related to the collision of Angara with Gondwana. *Zeitschrift Deutsche Geologische Gesellschaft (in press)*.

Ring, U., Johnson, C., Hetzel R. & Gessner, K., 2004b. Tectonic denudation of an Alpine collision belt: The symmetry of cooling patterns and extensional faults in the Anatolide belt of western Turkey. *Geological Magazine (in press)*.

Ring, U., Thomson, S. N. & Bröcker, M., 2003. Fast extension but little exhumation: The Vari detachment in the Cyclades, Greece. *Geological Magazine*, **140**, 245-252.

Satır, M. & Friedrichsen, H., 1986. The origin and evolution of the Menderes Massif, W-Turkey: A rubidium/strontium and oxygen isotope study. *Geologische Rundschau*, **75**, 703–714.

Scheuven, D., 2002. Metamorphism and microstructures along a high-temperature metamorphic field gradient: the north-eastern boundary of the Královský hvozd unit (Bohemian Massif, Czech Republic). *Journal of Metamorphic Geology*, **20**, 413–428.

Schuilung, R. D., 1962. On petrology, age and structure of the Menderes migmatite complex (SW-Turkey). *Bulletin of the Mineral Research and Exploration Institute of Turkey*, **58**, 71-84.

Şengör, A. M. C., 1979. Mid-Mesozoic closure of Permo-Triassic Tethys and its implications. *Nature*, **279**, 590-593.

Şengör, A. M. C. & Yilmaz, Y., 1981. Tethyan Evolution of Turkey: a plate tectonic approach. *Tectonophysics*, **75**, 181-241.

Şengör, A. M. C., 1987. Cross faults and differential stretching in their hanging walls in regions of low-angle normal faulting: examples from western Turkey. In: Coward, M.J., Dewey, J.F., Hancock, P.L. (eds) Continental extensional tectonics. *Geological Society of London Special Publications*, **28**, 405-473.

Şengör, A. M. C., Satır, M. & Akkök, R., 1984. Timing of tectonic events in the Menderes Massif, western Turkey; implications for tectonic evolution and evidence for Pan-African basement in Turkey. *Tectonics*, **3**, 693-707.

Sherlock, S., Kelley, S., Inger, S., Harris, N. & Okay, A., 1999.  $^{40}\text{Ar}$ - $^{39}\text{Ar}$  and Rb-Sr geochronology of high-pressure metamorphism and exhumation history of the Tavsanli Zone, NW Turkey. *Contributions to Mineralogy and Petrology*, **137**, 46-58.

Soto, J. I. & Azañón, J. M., 1994. Zincian staurolite in metabasites and metapelites from the Betic Cordillera (SE Spain). *Neues Jahrbuch für Mineralogie: Abhandlungen*, **168**, 109–126.

Spear, F. S. & Cheney, J. T., 1989. A petrogenetic grid for pelitic schists in the system  $\text{SiO}_2$ - $\text{Al}_2\text{O}_3$ - $\text{FeO}$ - $\text{MgO}$ - $\text{K}_2\text{O}$ - $\text{H}_2\text{O}$ . *Contributions to Mineralogy and Petrology*, **101**, 149-164.

Spear, F. S., 1993. *Metamorphic Phase Equilibria and Pressure-Temperature-Time Paths*, 799 p. *Mineralogical Society of America*, Washington, D. C.

Stampfli, G. M. & Borel, G. D., 2002. A plate tectonic model for the Paleozoic and mesozoic constrained by dynamic plate boundaries and restored synthetic oceanic isochrons. *Earth and Planetary Science Letters*, **196**, 17-33.

Stampfli, G. M., 2000. Tethyan oceans, in: E. Bozkurt, J.A. Winchester, J.D.A. Piper (Eds.), *Tectonics and magmatism in Turkey and surrounding Area. Geological Society of London Special Publication*, **173**, 163-185.

Stampfli, G. M., Mosar, J., De Bono, A. & Vavasis, I., 1998. Late Paleozoic, early Mesozoic plate tectonics of the Western Tethys. *Bulletin of the Geological Society of Greece*, **32**, 113-120.

Taşkın, I., 1981. Bafa Gölü Kuzevbatisinin Jeolojisi: Graduate thesis, 28 p., Geology Department of Dokuz Eylül University, Izmir, Turkey.

Tinkham, D. K., Zuluaga, C. A. & Stowell, H. H., 2001. Metapelite phase equilibria modeling MnNCKFMASH: The effect of variable  $\text{Al}_2\text{O}_3$  and  $\text{MgO}/(\text{MgO}+\text{FeO})$  on mineral stability. *Geological Materials Research*, **3**, 1–42.

Wei, C. & Powell, R., 2003. Phase relations in high-pressure metapelites in the system KFMASH ( $\text{K}_2\text{O}-\text{FeO}-\text{MgO}-\text{Al}_2\text{O}_3-\text{SiO}_2-\text{H}_2\text{O}$ ) with application to natural rocks. *Contributions to Mineralogy and Petrology*, **145**, 301-315.

Wei, C. & Powell, R., 2004. Calculated Phase Relations in High-Pressure Metapelites in the System NKFMAASH ( $\text{Na}_2\text{O}-\text{K}_2\text{O}-\text{FeO}-\text{MgO}-\text{Al}_2\text{O}_3-\text{SiO}_2-\text{H}_2\text{O}$ ). *Journal of Petrology*, **45**, 183-202.

Wheeler, J. & Butler, R. W. H., 1994. Criteria for identifying structures related to true crustal extension in orogens. *Earth and Planetary Science Letters*, **117**, 457-474.

White, R. W., Powell, R., Holland, T. J. B. & Worley, B. A., 2000. The effect of  $\text{TiO}_2$  and  $\text{Fe}_2\text{O}_3$  on metapelitic assemblages at greenschist and amphibolite facies conditions: mineral equilibria calculations in the system  $\text{K}_2\text{O}-\text{FeO}-\text{MgO}-\text{Al}_2\text{O}_3-\text{SiO}_2-\text{H}_2\text{O}-\text{TiO}_2-\text{Fe}_2\text{O}_3$ . *Journal of Metamorphic Geology*, **18**, 497–511.

Whitney, D. L. & Bozkurt, E., 2002. Metamorphism history of the southern Menderes Massif, Western Turkey. *Geological Society of America Bulletin*, **114**, 829–838.

Will, T. M., 1998a. Phase Equilibria in Metamorphic Rocks-Thermodynamic Background and Petrological Applications. Springer-Verlag, Berlin Heidelberg New York, 315p.

Will, T. M., 1998b. Phase Diagrams and their application to determine Pressure-Temperature Paths of Metamorphic Rocks. *Neues Jahrbuch für Mineralogie: Abhandlungen*, **174**, 103-130.

Will, T., Okrusch, M., Schmädicke, E. & Guoli, C., 1998. Phase relations in the greenschist-blueschist-amphibolite-eclogite facies in the system  $\text{Na}_2\text{O}-\text{CaO}-\text{FeO}-\text{MgO}-\text{Al}_2\text{O}_3-\text{SiO}_2-\text{H}_2\text{O}$  (NCFMASH), with application to metamorphic rocks from Samos, Greece. *Contributions to Mineralogy and Petrology*, **132**, 85-102.

Wood, B.J., Hackler, R.T., & Dobson, D.P., 1994 Experimental determination of Mn-Mg mixing properties in garnet, olivine and oxide. *Contributions to Mineralogy and Petrology*, **115**, 438-448.

Worley, B. & Powell, R., 1998. Singularities in NCKFMASH ( $\text{Na}_2\text{O}-\text{CaO}-\text{K}_2\text{O}-\text{FeO}-\text{MgO}-\text{Al}_2\text{O}_3-\text{SiO}_2-\text{H}_2\text{O}$ ). *Journal of Metamorphic Geology*, **16**, 169–188.

Worley, B. & Powell, R., 2000. High-precision relative thermobarometry; theory and a worked example. *Journal of Metamorphic Geology*, **18**, 91–101.